Universidad de Huelva

Departamento de Física Aplicada

Propiedades interfaciales y equilibrio de fase de mezclas fluidas mediante simulación Monte Carlo

Memoria para optar al grado de doctor
presentada por:

Francisco José Martínez Ruiz

Fecha de lectura: 30 de noviembre de 2015

Bajo la dirección del doctor:

Francisco Jiménez Blas

Huelva, 2015

Universidad de Huelva

Facultad de Ciencias Experimentales
Departamento de Física Aplicada

Propiedades interfaciales y equilibrio de fase de mezclas fluidas mediante simulación Monte Carlo

Memoria que para optar al grado de Doctor presenta

Francisco José Martínez Ruiz

Director: Dr.Felipe Jiménez Blas

Huelva, 2015

A Currito y Carmen con todo mi corazón

Agradecimientos

La felicidad por la obra terminada, y el alivio por poner punto y final a un viaje, que durante cinco años ha envuelto mi día a día, resulta en agradecimientos mucho más que retóricos hacia quienes la han hecho posible. Pero la felicidad y el alivio son estados, en ocasiones efímeros, que podrían arrojar dudas sobre la durabilidad del sentimiento de gratitud que generan. No dudes del mío Felipe, mi Director y amigo. La deuda que tengo contigo rebasa sobradamente la relación con esta tesis doctoral. Mi gratitud Felipe solamente puede expresarse con pobreza en unas líneas de texto. Como Director de mi tesis doctoral te debo, ciertamente, más de lo que corresponde usualmente por el desempeño de tal cometido académico. Has tenido capacidad de convicción, has aportado didáctica y claridad para ver los caminos de integración adecuados en el arduo trabajo de la simulación molecular, y sobre todo, una inmensa capacidad de trabajo para ayudarme a sacar este proyecto adelante. Precisamente esa didáctica sobre simulación, ofrecida en los momentos compartidos de las reuniones de la Ponencia de Física para la prueba de acceso a la Universidad, fue la que me atrapó en esta aventura. En unas de esas charlas de café llegamos al pacto de iniciar la tesis doctoral para disfrutar, para pasarlo bien haciendo ciencia, y así ha sido, he disfrutado, y el resultado del trabajo refleja la mano de un gran maestro. Gracias y un fuerte abrazo.

Es imposible imaginarse un trabajo de este tipo en solitario, así que me gustaría compartirlo con los profesores D. Luis García MacDowell (Universidad Complutense de Madrid), D. Iñaki Moreno-Ventas Bravo (Departamento de Geología - Universidad de Huelva) y D. Bruno Mendibouret (Laboratoire des Fluides Complexes et leurs Réservoirs - Université de Pau). Gracias por vuestra ayuda y generosidad. Para un humilde profesor de instituto ha sido todo un privilegio intelectual del que muy pocos pueden disfrutar. A Iñaki en especial. . . gracias amigo.

Valga también mi más sincero agradecimiento al Prof. D.Manuel Martínez Piñeiro (Departamento de Física Aplicada de la Universidad de Vigo), al Prof. D. Carlos Vega de las Heras (Departamento de Química Física de la Universidad Complutense de Madrid), a la Prof.ª Dña. Amparo Galindo Carbajo (Departamento de Ingeniería Química - Imperial College, Londres) y al Dr. D. José Manuel Míguez (Laboratoire des Fluides Complexes et leurs Réservoirs - Université de Pau), por sus oportunas discusiones y aportaciones en la elaboración de los artículos de los que se compone este trabajo de tesis.

Si alguien me ha causado admiración docente es el Prof. D. Enrique de Miguel Agustino (Departamento de Física Aplicada de la Universidad de Huelva). Fue mi profesor de física estadística cuando era estudiante de Físicas en Sevilla y posteriormente en los cursos de doctorado. Su claridad se refleja en sus pizarras, en sus artículos, y como no, en sus códigos Monte Carlo. Le debo una parte de mi formación en física estadística, y le agradezco que sus artículos hayan sido claras guías para mi trabajo. Iniciarse en el mundo de la programación de Monte Carlo no es precisamente fácil, e inicialmente sus códigos han supuesto todo un referente de programación Fortran. Gracias.

En el panorama actual, de pesimismo educativo, gusta encontrarse con mentes jóvenes que toman el relevo de la Ciencia, así que a Jesús Algaba (Departamento de Física Aplicada de la Universidad de Huelva) y a José Matías Garrido (Universidad de Concepción - Chile) os deseo mucha suerte en vuestro camino de vida . . . en lo que esté en mi mano tendréis mi ayuda. Gracias por vuestras frescas ideas y sutiles aportaciones.

Cuando uno se aproxima al horizonte de sucesos de depositar la tesis doctoral llega el momento de las revisiones ortográficas y gramaticales, y encontrar a una persona que quiera leerse una tesis de simulación y física estadistica no siempre es fácil. A D. José Ramon del Pino Ruiz (Asesor del Centro del Profesorado de Alcalá de Guadaíra) le agradezco la tarea realizada y siento que la lectura no haya sido precisamente literaria.

Al Prof. D. José Enrique García González (Dpto. De Filología Inglesa (Lengua Inglesa) - Universidad de Sevilla) le agradezco que haya ejercido una tutela académica en *background*. Gracias Jose por tener siempre las palabras adecuadas para el momento en que lo necesitaba. Al final la *losa doctoral* salió a flote.

Mis deudas no acaban aquí. En el año 2003 iniciaba mis estudios de los cursos de doctorado en la Universidad de Huelva, y el Prof. D. Juan Pedro Bolívar Raya (Grupo de Investigación Física de Radiaciones y Medio Ambiente de la Universidad de Huelva) me abría de par en par las puertas del Departamento de Física Aplicada. Quizás, sin ese gesto, hoy no estaría presentando esta tesis. Permíteme Juan Pedro agradecerte el que me hayas mostrado qué es hacer investigación, y aunque la vida marcó otros caminos, hoy me siento muy orgulloso de la formación que me distes. Un abrazo Juan Pedro con todas mis fuerzas.

A todos los miembros del Departamento de Física Aplicada de la Universidad de Huelva con quien he compartido estos años, gracias.

Para Carmen, mi mujer, no tengo palabras suficientes de agradecimiento . . . muchos besos

Curro Martínez
Huelva, 2015

Índice de contenidos

Capítulo 1

Motivación y objetivos

La comprensión, desde un punto de vista molecular , del equilibrio de fases y las propiedades interfaciales de sistemas condensados ha crecido enormemente en las últimas décadas. En este sentido, la combinación de diferentes técnicas de simulación en el marco de la Mecánica Estadística nos va a permitir entender, desde un punto de vista microscópico, cómo la parametrización del modelo molecular determina el comportamiento macroscópico de un determinado sistema [1]

Hoy en día se puede determinar el diagrama de fases completo y las propiedades interfaciales de un determinado modelo haciendo uso de la simulación molecular. Esto es posible, no solamente debido al vertiginoso aumento de la potencia computacional asociado al extraordinario desarrollo del hardware, sino también al gran número de técnicas y algoritmos que se han desarrollado en estos últimos años [2, 3]. Además de las simulaciones en los colectivos tradicionales, existe una gran variedad de técnicas que permiten determinar la coexistencia de fases, así como la energía libre de las mismas. Entre todas ellas destacar la integración termodinámica, la integración de Gibbs-Duhem, y cálculos de energía libre, como el uso del Expanded Ensamble, el método de inserción de la partícula de prueba (test-particle insertion), el método del cristal de Einstein (fases sólidas) o en el caso de la determinación de propiedades interfaciales el Test-Area, para calcular la tensión superficial mediante simulación de fases fluidas en coexistencia directa [4].

El estudio de fluidos inhomogéneos, desde los días de las primeras teorías macroscópicas propuestas por Laplace y Young hasta llegar a las teorías funcionales de la densidad que se usan actualmente, tiene una larga historia [5]. Desafortunadamente, la comprensión a nivel molecular de las propiedades interfaciales, como anchura interfacial, adsorción y tensión superficial entre otras, es muy limitada, especialmente si la comparamos con el conocimiento actual de sistemas homogéneos. Esto es especialmente cierto en el caso de moléculas con interacciones intermoleculares complejas, como el caso de cadenas moleculares y sistemas asociantes. El conocimiento preciso de las propiedades interfaciales es esencial en el diseño de procesos de enorme interés industrial, biológico y comercial: detergentes (surfactantes y solubilización de sustancias), producción de alimentos (coloides y emulsiones), industria de cosméticos (fases estructuradas) y dispositivos optoelectrónicos (cristales líquidos) entre otros [6]. Los fundamentos teóricos de las interfases están bien consolidados desde el punto de vista de la Mecánica Estadística. El formalismo de los funcionales de la densidad ha sido descrito en detalle por diferentes autores [7, 8]. Pese a todo ello, existen pocos funcionales capaces de predecir cuantitativamente el comportamiento interfacial de sistemas reales complejos y sus mezclas.

La determinación de los perfiles de la densidad (variación de la densidad con la distancia a la interfase) o la anchura de interfases (región del espacio en la que existe una variación significativa de la densidad) es relativamente sencilla desde el punto de vista de una simulación. En cambio, el cálculo de la tensión superficial es mucho más exigente computacionalmente hablando. Hasta hace poco, el método estándar (y casi único) utilizado para su evaluación era el cálculo del tensor de presiones del sistema inhomogéneo [9]. Aunque este método se puede aplicar a sistemas sencillos, es particularmente difícil de implementar en sistemas moleculares complejos. En los últimos 10 años se han propuesto métodos alternativos para la determinación de la tensión superficial desde un punto de vista termodinámico (WIM (wandering interface method) [10], Area-Sampling [11], Expanded Ensamble [12]), incluyendo la técnica del Test-Area [4]. Especial relevancia cobra la aportación de MacDowell y Blas [13, 14] extendiendo y mejorando el método de Janeček [15] para determinar las correcciones de largo alcance de sistemas moleculares, obteniéndose de este modo ventajas computacionales frente al método original.

1.1 Objetivos

El trabajo de este trabajo de tesis doctoral se desarrolla en el seno del Grupo de Investigación de Física de Líquidos Complejos (FILICO) perteneciente al Departamento de Física Aplicada y desde 2015 al Laboratorio de Simulación Molecular y Química Computacional, CIQSO-Centro de Investigación en Química Sostenible. El grupo de investigación cuenta con una dilatada experiencia en las diferentes técnicas y formalismos mencionados en la breve introducción anterior.

En una fase previa de definición del trabajo, durante el año 2010, se decide que el trabajo de tesis sea una transición suave de las líneas de trabajo iniciadas en el grupo de investigación dentro de la simulación molecular mediante técnicas de Monte Carlo (MC). Así que el punto de arranque de esta tesis es precisamente la extensión del método de MacDowell y Blas [14] para la evaluación de las correcciones de largo alcance (LRC), en unión con la técnicas termodinámicas del Test-Area (TA) o Volume Perturbation (VP) [16], al estudio de las propiedades interfaciales de diferentes sistemas inhomogéneos, concretamente mezclas binarias de modelos esféricos sencillos y modelos simplificados de cadenas moleculares flexibles. Se inicia así un trabajo previo de programación para extender códigos MC desarrollados en el grupo de investigación, o creación de códigos nuevos como es el caso de un código para mezclas de moléculas esféricas sencillas que interaccionan bajo el potencial discontinuo de square-well. Además se decide implementar, en los códigos MC, el cálculo de las componentes microscópicas del tensor de presiones (virial) tanto para el potencial de Lennard-Jones (LJ) como para el potencial de square-well (SW).

Por tanto los problemas a resolver se enfocan hacia la determinación de propiedades interfaciales y equilibrios de fase de mezclas binarias y de cadenas flexibles, haciendo uso de la simulación Monte Carlo. Nuestro interés es determinar el efecto de parámetros microscópicos del potencial (en los modelos de LJ y de SW), tales como el tamaño molecular, la energía dispersiva, y el rango de la interacción, sobre las propiedades interfaciales, especialmente sobre la tensión superficial, pero también sobre otras propiedades de interés, como el tensor de presiones, la anchura interfacial, etc. El periodo de tiempo, de diseño y programación de códigos MC, permitió ir definiendo la elección de los sistemas a estudiar, tanto por su interés como por acotar el problema con unos objetivos de tesis realistas en el tiempo.

Cabe mencionar también, que la gran experiencia del grupo en diferentes versiones del formalismo SAFT (Teoría Estadística de Fluidos Asociantes) colocó el punto de arranque, de cada uno de los sistemas de estudio, en una posición claramente ventajosa. Aunque el objetivo de este trabajo de tesis es calcular propiedades interfaciales mediante simulación Monte Carlo, el conocimiento del equilibrio de fases es esencial para ello. Se ha podido disponer de los datos del equilibrio de fases de las mezclas de estudio, sin duda una poderosa herramienta a disposición del doctorando, especialmente útil, tanto para preparar cuidadosamente los sistemas para la simulación en coexistencia directa, como para chequear los resultados obtenidos mediante las diferentes metodologías utilizadas.

A continuación se presentan los objetivos de la tesis divididos en tres grandes bloques, de forma que cada uno de estos bloques se ha dividido en tareas realistas que han constituido la guía por la que ha transitado el proceso de investigación:

Obj 1. Revisar, aplicar y extender las correcciones de largo alcance para la determinación de propiedades interfaciales en sistemas inhomogéneos.

- **Obj 1-a.** Extender la versión mejorada por MacDowell y Blas [13,14] de las correcciones de largo alcance de Janeček [15], para el potencial de Lennard-Jones, sobre el cálculo de las componentes microscópicas del tensor de presiones usando la ruta mecánica (virial), en el contexto de la elección de Irving-Kirkwood.
- **Obj 1-b.** Determinar las componentes macroscópicas del tensor de presiones mediante la ruta termodinámica basada en perturbaciones de volumen propuesta por de Miguel y Jackson [16] con objeto de validar y comparar la implementación de las correcciones de largo alcance mediante la ruta mecánica.
- **Obj 1-c.** Evaluar la tensión interfacial haciendo uso de tres metodologías en simulaciones en coexistencia directa vapor-líquido: integración de la diferencia de los perfiles microscópico de las componentes del tensor de presiones (método Irving-Kirkwood), direfencia entre las componentes macroscópicas del tensor de presiones (ruta perturbativa) y Test-Area.
- **Obj 1-d.** Analizar el efecto de la distancia de corte y las correcciones de largo alcance sobre las propiedades de coexistencia.
- **Obj 1-e.** Comprender el efecto de la contribución impulsiva de la presión debido a la discontinuidad que aparece al cortar el potencial de interacción intermolecular, así como las consecuencias de no tener en cuenta esta contribución en la evaluación de las componentes microscópicas del tensor de presiones.

Obj 2. Determinación de la tensión interfacial fluido-fluido en mezclas binarias de modelos esféricos sencillos

- **Obj 2-a.** Extender los **Obj 1.a** , **Obj 1.b** y **Obj 1.c** al caso de mezclas binarias que interaccionan mediante potenciales Lennard-Jones y que exhiben, no solamente equilibrio líquido-vapor, sino también líquido-líquido. La consecución de este objetivo nos permitirá afrontar el estudio de problemas más ambiciosos. El primer paso será la implementación en nuestros, códigos de programación dedicados a moléculas esféricas, el escenario de mezclas de dos o más componentes junto con el procedimiento de MacDowell y Blas para las correcciones de largo alcance en interfases planas fluido-fluido.
- **Obj 2-b.** Utilizar la aproximación Soft-SAFT, basada en la teoría termodinámica perturbativa de Wertheim [17–20] y desarrollada por Blas and Vega [21,22], para calcular el

diagrama de fases completo de las mezclas binaria objeto de estudio. El conocer el diagrama de fase previamente a la simulación de Monte Carlo posee un doble interés. Por un lado, la simulación bajo condiciones de coexistencia directa precisa conocer una imagen fiel de la coexistencia que envuelve al sistema en las condiciones termodinámicas para las que se diseñan las simulaciones, en particular las densidades y composiciones de los componentes en las fases implicadas. Por otro lado, chequear la validez de las metodologías de simulación Monte Carlo implementadas para mezclas binarias.

Obj 2-c. Simular interfases planas líquido-vapor de diferentes mezclas esféricas Lennard-Jones y considerar la dependencia de diferentes propiedades interfaciales, como densidades de coexistencia, perfiles de densidad, anchura interfacial y tensión superficial, en función de los diferentes parámetros moleculares y diferentes condiciones termodinámicas, como presión, temperatura y/o composición de la mezcla.

Obj 2-d. Considerar interfases planas líquido-líquido de mezclas esféricas Lennard-Jones seleccionado mezclas binarias que exhiban inmiscibilidad líquido-líquido eligiendo adecuadamente los valores de los parámetros de interacción cruzados. Analizar el comportamiento interfacial de mezclas binarias que exhiben diferentes tipos de equilibrio líquido-líquido, concretamente un tipo III de acuerdo con la clasificación de Scott y Konynenburg.

Obj 2-e. Analizar mezclas binarias de esferas que interaccionan mediante el potencial de pozo cuadrado (SW). El estudio de sistemas que interaccionan con potenciales SW no precisará el uso de correcciones de largo alcance puesto que el potencial tiene un rango limitado, pero si una implementación en los códigos del cálculo de las componentes microscópicas del tensor de presiones.

Obj 2-f. Determinar el diagrama de fases de las mezclas SW objeto de estudio haciendo uso de la aproximación SAFT-VR.

Obj 3. Determinación de propiedades interfaciales de modelos simplificados de cadenas moleculares que interaccionan mediante potenciales de Lennard Jones y de pozo cuadrado (square-well).

Obj 3-a. Determinar propiedades interfaciales de cadenas flexibles de monomeros Lennard-Jones mediante simulación directa de la interfase líquido-vapor. En estas simulaciones se tendrán en cuenta las correcciones inhomogéneas de largo alcance en su versión mejorada por MacDowell y Blas [13, 14] de las correcciones de largo alcance de Janeček [15], válidas tanto para sistemas moleculares esféricos Lennard-Jones como para sistemas de cadenas moleculares rígidas y flexibles. Utilizar la metodología Test-Area para determinar la tensión superficial.

Obj 3-b. Comparar los resultados de cadenas flexibles de monomeros Lennard-Jones con datos de la literatura de cadenas rígidas de la misma longitud con objeto de analizar el efecto de la longitud de cadena y flexibilidad sobre las propiedades interfaciales.

Obj 3-c. Simular el equilibrio líquido-vapor en cadenas de monomeros, totalmente flexibles, que interaccionan bajo el potencial de square-well (SW) con objeto de estudiar el comportamiento de propiedades interfaciales en función de la temperatura y el tamaño molecular.

Obj 3-d. Utilizar la metodología WIM (Wandering Interface Method) desarrollada por MacDowell and Bryk (2007) [10] como un método elegante de cálculo de la tensión superficial en una gran cantidad de sistemas complejos, para determinar la tensión superficial en cadenas de monomeros SW.

Obj 3-e. Determinar la presión de vapor en el equilibrio líquido-vapor de cadenas SW (especialmente en el caso de cadenas largas) de forma indirecta mediante la combinación de la simulación Monte Carlo y la integración termodinámica, así como estimar la incertidumbre asociada a la integración termodinámica haciendo uso del *método sintético* propuesto por de Miguel (2008) [12].

Obj 3-f. Explorar relaciones de escalado universal para correlacionar cadenas moleculares, que interaccionan bajo el potencial intermolar de Lennard-Jones o de square-well, con diferentes grados de flexibilidad de la cadena.

1.2 Organización de la memoria de tesis

Este trabajo de tesis queda organizado en dos apartados principales. En la Parte I se exponen los fundamentos teóricos y las metodologías utilizadas. Al presentarse la memoria como compendio de artículos, la intencionalidad de esta primera parte es aclarar aspectos, tanto conceptuales como metodológicos, que simplemente se citan en las publicaciones, o bien son tratados de una forma más general. Se ha redactado, intencionadamente, con un estilo especialmente didáctico, concibiendo esta memoria como un documento útil en el cual futuras personas, que se incorporen al grupo de investigación, encuentren un material donde puedan tener una visión clara, y de conjunto, de algunas de las metodologías de simulación Monte Carlo que se están tanto utilizando como extendiendo, así como de la bibliografía básica de referencia.

En la Parte II se recogen las publicaciones (capítulos 10 al 15) en los que se exponen los resultados relativos a los objetivos propuestos anteriormente. Estas publicaciones se han formateado conforme al estilo tipográfico de esta tesis, siendo copias fieles de las publicaciones. Es por lo que se indica en cada uno de estos capítulos la referencia bibliográfica, autores y afiliaciones. Finalmente se exponen las conclusiones finales (capítulo 16) de este trabajo de tesis junto a posibles líneas futuras de continuidad del mismo.

Parte I

Fundamentos teóricos y metodología

Capítulo 2

Fundamentos básicos de la Mecánica Estadística

La Mecánica Estadística representa uno de los cuerpos de doctrina centrales de la Química Física. Su papel es el de servir de conexión entre la visión microscópica y la visión macroscópica de la Termodinámica. La descripción microscópica es de gran precisión y abundante en el detalle. Demasiado abundante cuando se trata de determinar el comportamiento de un sistema macroscópico. Por el contrario, la Termodinámica adopta una perspectiva esencialmente empírica, de modo que bastan unas pocas variables, fácilmente medibles, para caracterizar el estado termodinámico. La Mecánica Estadística sirve de nexo entre ambas descripciones, de manera que permite utilizar la información detallada de la imagen microscópica para pronosticar el comportamiento termodinámico.

2.1 Principios fundamentales

El postulado fundamental de la mecánica estadística (también conocido como postulado de equiprobabilidad de los microestados) establece que: dado un sistema en equilibrio todos los microestados compatibles con un macroestado dado son igualmente probables.

Este postulado es necesario porque permite concluir que para un sistema en equilibrio, el estado termodinámico (macroestado) que puede resultar de un gran número de microestados es también el macroestado más probable del sistema.

La termodinámica estadística se basa en la suposición fundamental de que todas las posibles configuraciones de un sistema dado, que satisfacen condiciones de contorno, tales como la energía, el volumen,y el número de partículas, son igualmente probables de ocurrir. El objetivo pues es el de comprender e interpretar las propiedades macroscópicas de la materia en términos de sus partículas constituyentes y de las interacciones entre ellas.

La receta estadística es, en principio, bien simple. Debe tomarse una muestra representativa de los estados posibles del sistema y determinar las propiedades promedio para la misma. El problema consiste en asegurar la representatividad de la muestra o, como se denomina en este contexto, la ergodicidad del procedimiento.

Admitiendo que las partículas de nuestro sistemas obedecen las leyes de las mecánica clásica, sabemos que para caracterizar un estado microscópico, de un sistema de N partículas, necesitaremos

f coordenadas generalizadas $q_1, \cdots, q_f$ y f momentos generalizados $p_1, \cdots, p_f$, siendo f el número de grados de libertad del sistema y estando definida la energía total por el Hamiltoniano del sistema

$$\mathcal{H}(p,q) = \sum_{i=1}^{f} \frac{p_i^2}{2m} + \mathcal{U}(q) \tag{2.1}$$

donde el primer término corresponde a la energía cinética de las partículas y $\mathcal{U}(q)$ es la energía de interacción total del sistema.

Dado que estamos utilizando una descripción clásica del sistema y que en la Mecánica Clásica las coordenadas generalizadas q_i y los momentos generalizados p_i son variables continuas, lo que la Mecánica Estadística va a postular para cada sistema macroscópico es una función densidad de probabilidad para las variables coordenadas y momentos generalizados, es decir una *densidad de probabilidad* en el espacio de las fases [23]. Así pues, en el caso más general va a postular una función de la forma

$$\rho(q_i, p_i; t) = \rho(q, p; t) \tag{2.2}$$

de manera que, por la definición de densidad de probabilidad,

$$\rho(q_i, p_i; t) dq_1, \cdots, dq_f \; dp_1, \cdots, dp_f \equiv \rho(q,p;t) dq dp \tag{2.3}$$

representa la probabilidad de que en un instante t dado, el sistema se encuentre en un pequeño volumen del espacio fásico:

$$dpdq \equiv dq_1, \cdots, dq_f \; dp_1, \cdots, dp_f \tag{2.4}$$

alrededor del punto (q,p). De acuerdo con esta definición, $\rho(q,p;t)$ deberá, en todo instante, cumplir la condición de normalización

$$\int dpdq \; \rho(q,p;t) = 1 \tag{2.5}$$

Esta idea de asociar a cada macroestado de un sistema un conjunto de microestados con una distribución de probabilidades es debida a Josiah Williard Gibbs (a finales del siglo XIX). Gibbs introduce el concepto de colectivo, asamblea de sistemas o *ensemble* (anglicismo muy difundido). Un colectivo es un conjunto formado por un número muy grande de sistemas, todos los cuales se encuentran en el mismo estado termodinámico. La idea es que esta colección de sistemas representen una muestra apropiada de todos los estados microscópicos y, por lo tanto, sus propiedades promedio sean las del sistema promedio ideal. El método de los colectivos de Gibbs garantiza de antemano la ergodicidad y, además, proporciona ecuaciones analíticas muy útiles de las propiedades termodinámicas.

El punto de conexión inicial entre la descripción macroscópica y la microscópica que vamos a necesitar consiste en identificar la energía interna del sistema tal y como se define termodinámicamente con el total de la energía que poseen las partículas que componen nuestro modelo a escala microscópica. Si consideramos una variable que, como sucede con la energía, es función de las coordenadas y momentos generalizados $A(p,q)$. A cada macroestado le corresponde un número muy grande de microestados en los que en general los valores de q y p son distintos, por lo tanto también los es $A(p,q)$. La Mecánica Estadística establece que los valores de los parámetros macroscópicos que definen el estado de un sistema son iguales a los valores medios, sobre el conjunto de microestados asociados, de la correspondiente magnitud microscópica. Es decir que el valor de A en el sistema macroscópico en un instante t es

$$\langle A(t) \rangle = \int dpdq \; \rho(q,p;t) \; A(q,p) \tag{2.6}$$

Este promedio también podría contemplarse como un promedio temporal

$$\overline{A(t)} = \lim_{x\to\infty} \frac{1}{t} \int A(t')dt' \tag{2.7}$$

Establecer la igualdad entre estas dos declaraciones es precisamente lo que Paul y Tania Ehrenfest [24] bautizaron como hipótesis ergódica en su artículo de 1911. Un cierto folklore establecería, en una naciente mecánica estadística, que la relación entre teoría y experimento se fundamenta en la hipótesis que dice que *"promedios temporales y promedios de ensemble coinciden en el límite de tiempos muy largos"*. Esta equivalencia, aunque razonable, no puede considerarse como trivial y ha sufrido numerosas reformulaciones, como su versión moderna en el teorema de Birkhoff [25], siendo realmente complejo establecer si un sistema es o no ergódico. Aún así, la hipótesis es asumida en el estudio de sistemas, mediante simulación molecular, en el marco de la mecánica estadística del equilibrio [3].

2.2 Ensembles y funciones de partición

A partir de ahora centraremos la discusión en sistemas que se encuentran en equilibrio, por lo que la función densidad de probabilidad de la Eq.(2.2) puede considerarse independiente del tiempo, y el estado termodinámico de un sistema puede establecerse dando valor a tan solo tres variables termodinámicas: una elegida de cada una de las tres parejas $\{N, \mu\}$ (número de partículas o potencial químico), $\{V, p\}$ (volumen o presión), y $\{E, T\}$ (energía interna o temperatura). Cada pareja está formada por una variable extensiva y otra intensiva. Existen, por lo tanto, ocho formas diferentes de definir el estado termodinámico de los sistemas que forman el ensemble. Las más relevantes son:

- (N, V, E), que da lugar al ensemble microcanónico,
- (N, V, T), que define el ensemble canónico,
- (N, p, T), del ensemble isobárico e isotérmico,
- (μ, V, T), del ensemble gran canónico.

En cada ensemble, juega un papel fundamental el concepto de función de partición como objeto que va a contener toda la información estadística del mismo. La función de partición dependerá de las tres variables que fijan el macroestado del ensemble, existiendo una relación privilegiada entre dicha función y el potencial termodinámico definido por la terna de variables que fijan el macroestado, lo que da lugar a un nexo de unión fundamental entre los estados microscópicos y el macroestado correspondiente.

A continuación haremos una revisión breve, y de carácter axiomática, de las funciones de partición de los ensembles utilizados, pudiendo acudir para deducciones detalladas a manuales de referencia de Mecánica Estadística (por ejemplo Ref. [23], [26], [27], [28]).

2.2.1 El ensemble canónico

La densidad de probabilidad para un sistema de N partículas interaccionando, en el ensemble NVT, viene dada por

$$\rho(\mathbf{r}^N, \mathbf{p}^N) = \frac{\exp\left[-\beta\mathcal{H}(\mathbf{p}^N, \mathbf{r}^N)\right]}{N!h^{3N}}\, {Q_{NVT}}^{-1} \tag{2.8}$$

y la función de normalización o función de partición

$$Q_{NVT} = \frac{1}{N!h^{3N}} \int d\mathbf{p}^N d\mathbf{r}^N \exp\left[-\beta \mathcal{H}(\mathbf{p}^N, \mathbf{r}^N)\right] \tag{2.9}$$

donde h corresponde a la constante de Planck que aparece en el límite semiclásico de la mecánica cuántica, ya que para cada grado de libertad i, el principio de incertidumbre nos impone que

$$\Delta p_i \Delta q_i \geq h \tag{2.10}$$

y por tanto, la máxima resolución para definir un microestado en el espacio fásico es el volumen h^f, para un sistema con f grados de libertad. El parámetro β se relaciona con el inverso de la temperatura, $\beta = (K_B T)^{-1}$, siendo K_B la constante de Boltzmann.

Si A es un observable, expresado en función de las coordenadas y momentos, su promedio en el ensemble podemos evaluarlo como

$$\langle A \rangle_{NVT} = \frac{\int d\mathbf{p}^N d\mathbf{r}^N A(\mathbf{p}^N, \mathbf{r}^N) \exp\left[-\beta \mathcal{H}(\mathbf{p}^N, \mathbf{r}^N)\right]}{\int d\mathbf{p}^N d\mathbf{r}^N \exp\left[-\beta \mathcal{H}(\mathbf{p}^N, \mathbf{r}^N)\right]} \tag{2.11}$$

En el colectivo canónico la conexión entre la Mecánica Estadística y la Termodinámica se establece a partir de la relación

$$F = -k_B T \ln Q_{NVT} \tag{2.12}$$

siendo F la energía libre de Helmholtz, es decir, el potencial termodinámico correspondiente al sistema con N , V y T fijos.

La conexión resulta de gran utilidad al poder relacionar los potenciales termodinámicos con otras variables termodinámicas mediante la trans formada de Legendre. Dado que F es la transformada de Legendre de la energía interna considerando T y V como variables independientes ($F = U - TS$), y teniendo en cuenta el hecho de que F, al igual que otros potenciales termodinámicos, es una función de estado y por tanto tiene diferencial exacta, podemos obtener relaciones de gran utilidad en el cálculo de propiedades termodinámicas, como por ejemplo la presión del sistema

$$P = -\left(\frac{\partial F}{\partial V}\right)_T \tag{2.13}$$

Ahora bien, dado que la energía podemos expresarla como la suma de una contribución cinética (dependiente de los momentos) y una contribución del potencial (dependiente de las coordenadas), la función de partición puede ser factorizada como un producto

$$Q_{NVT} = \frac{1}{N!h^{3N}} \int d\mathbf{p}^N \exp\left[-\beta \mathcal{K}(\mathbf{p}^N)\right] \int d\mathbf{r}^N \exp\left[-\beta \mathcal{U}(\mathbf{r}^N)\right] = Q^{id}_{NVT} Q^{ex}_{NVT} \tag{2.14}$$

La integración sobre los momentos puede resolverse analíticamente, lo que nos permite expresar la función de partición como

$$Q_{NVT} = \frac{V^N}{N!\Lambda^{3N}} Q^{ex}_{NVT} \tag{2.15}$$

siendo el factor $\Lambda = (h^2/2\pi m k_B T)^{1/2}$ la longitud de onda traslacional de de Broglie, y la parte en exceso (o configuracional) de la función de partición

$$Q^{ex}_{NVT} = \frac{1}{V^N} \int d\mathbf{r}^N \exp\left[-\beta \mathcal{U}(\mathbf{r}^N)\right] \tag{2.16}$$

Esta separación de la función de partición hace que en general el cálculo del promedio $\langle A \rangle$ pueda dividirse en dos contribuciones: una cuya integración sobre los momentos nos proporciona la contribución de gas ideal al promedio, y otra cuya integración sobre las coordenadas nos proporciona la contribución configuracional al promedio

$$\langle A \rangle^{c}_{NVT} = \frac{\int d\mathbf{r}^N A(\mathbf{r}^N) \exp\left[-\beta \mathcal{U}(\mathbf{r}^N)\right]}{\int d\mathbf{r}^N \exp\left[-\beta \mathcal{U}(\mathbf{r}^N)\right]} \tag{2.17}$$

Nuestro problema entonces se reduce a realizar integrales del tipo Eq. (2.17). La dificultad radica en la integración de funciones $A(\mathbf{r}^N)$. Solamente en muy pocos casos este tipo de integrales multidimensionales, sobre las coordenadas de las partículas, pueden ser calculadas. Acudir a métodos tradicionales de cuadraturas tiene un coste computacional simplemente prohibitivo, unido a que además la función densidad de probabilidad solamente toma valores significativos en un subconjunto muy reducido del espacio fásico [3]. Es precisamente en la resolución de este tipo de integrales donde las técnicas basadas en métodos de Monte Carlo muestran su potencia.

2.2.2 El ensemble isobárico e isotérmico

En el ensemble isobárico e isotérmico el número total de partículas N, la presión P, y la temperatura T son constantes. La función de partición en el ensemble NPT puede escribirse como

$$Q_{NPT} = \int dV \exp(-\beta PV) Q_{NVT} \tag{2.18}$$

y la versión equivalente a la ecuación Eq. (2.17) para el cálculo de promedios

$$\langle A \rangle_{NPT} = \frac{\int dV \exp(-\beta PV) \int d\mathbf{r}^N A(\mathbf{r}^N, V) \exp\left[-\beta \mathcal{U}(\mathbf{r}^N)\right]}{\int dV \exp(-\beta PV) \int d\mathbf{r}^N \exp\left[-\beta \mathcal{U}(\mathbf{r}^N)\right]} \tag{2.19}$$

Es conveniente reconsiderar la formulación de la función de partición Q_{NVT}, para hacer explícita la participación del volumen V en la definición del estado del sistema. Para ello reescribimos el problema en coordenadas escaladas $(\mathbf{s}^N; L)$, donde $\mathbf{s}^N = \mathbf{r}^N/L$. Si asumimos que el sistema está definido por una caja de aristas L_x, L_y, L_z, el escalamiento se define como $s_{i\alpha} = r_{i\alpha}/L_\alpha$ con $\alpha = x, y, z$ e $i = 1 \cdots N$. Introduciendo el escalamiento en la Eq. (2.15), y teniendo en cuenta que $d\mathbf{r}^N = V^N d\mathbf{r}^N$, tenemos

$$Q_{NVT} = \frac{V^N}{N! \Lambda^{3N}} \int_0^1 \cdots \int_0^1 d\mathbf{s}^N \exp\left[-\beta \mathcal{U}(\mathbf{s}^N; L)\right] \tag{2.20}$$

Consideraremos que nuestro sistema, de volumen V y de paredes móviles, está inmerso dentro de otro sistema formado por un reservorio de gas ideal y en el límite en el que el tamaño de este reservorio tiende a infinito. En las condiciones de este límite termodinámico, pequeños cambios en el volumen de nuestro sistema no afectarán a la presión P del reservorio y puede demostrarse [3] que la función de partición del ensemble NPT puede escribirse como

$$Q_{NPT} = \frac{\beta P}{N! \Lambda^{3N}} \int dV\ V^N \exp(-\beta PV) \int d\mathbf{s}^N \exp\left[-\beta \mathcal{U}(\mathbf{s}^N; L)\right], \tag{2.21}$$

donde el factor βP tiene la función de hacer que Q_{NPT} sea adimensional. Consecuentemente, la integral sobre las coordenadas de las partículas de la Eq. (2.19) se transforma ahora en una integral sobre una caja unidad (Ω)

$$\langle A \rangle_{NPT} = \frac{\int V^N dV \exp(-\beta PV) \int_\Omega d\mathbf{s}^N A(\mathbf{s}^N, V) \exp\left[-\beta \mathcal{U}(\mathbf{s}^N; L)\right]}{\int V^N dV \exp(-\beta PV) \int_\Omega d\mathbf{s}^N \exp\left[-\beta \mathcal{U}(\mathbf{s}^N; L)\right]} \tag{2.22}$$

En el mismo esquema general del límite que acabamos de ver, la diferencia entre la energía libre del sistema total (reservorio más el subsistema de volumen V con N partículas) y el reservorio en ausencia del subsistema es lo que se conoce como energía libre de Gibbs G, y la conexión entre función de partición y potencial termodinámico queda establecida por

$$G = -k_B T \ln Q_{NPT} \tag{2.23}$$

La densidad de probabilidad, de encontrar al sistema en una configuración definida por $\mathbf{s}^N$ y un volumen V, cumplirá que

$$\begin{aligned} \rho(V;\mathbf{s}^N) &\propto V^N \exp(-\beta PV) \exp\left[-\beta \mathcal{U}(\mathbf{s}^N;L)\right] \\ &= \exp\left\{-\beta \left[\mathcal{U}(\mathbf{s}^N;L) + PV - N\beta^{-1} \ln V\right]\right\} \end{aligned} \tag{2.24}$$

2.2.3 El ensemble gran canónico

En el ensemble gran canónico el potencial químico μ, el volumen V, y la temperatura T son constantes, pasando ahora a ser el número de partículas N una variable. La función de partición en el ensemble μVT puede demostrarse [3] que puede escribirse término de coordenadas escaladas como en el apartado anterior

$$Q_{\mu VT} = \sum_{N=0}^{\infty} \exp[\beta N \nu] Q_{NVT} = \sum_{N=0}^{\infty} \frac{\exp(-\beta\mu N) V^N}{N! \Lambda^{3N}} \int d\mathbf{s}^N \exp\left[-\beta \mathcal{U}(\mathbf{s}^N)\right] \tag{2.25}$$

donde Q_{NVT} viene dada de forma similar a la Eq. (2.20). Ahora la densidad de probabilidad, de encontrar al sistema en una configuración definida por $\mathbf{s}^N$ y un valor del número de partículas N, cumplirá que

$$\rho(N;\mathbf{s}^N) \propto \frac{\exp(-\beta\mu N) V^N}{N! \Lambda^{3N}} \exp\left[-\beta \mathcal{U}(\mathbf{s}^N)\right] \tag{2.26}$$

La conexión con su potencial termodinámico (o energía libre) queda establecida por

$$\Omega = -k_B T \ln Q_{\mu VT} \tag{2.27}$$

Capítulo 3

Simulación molecular mediante método de Monte Carlo

Bajo el término genérico de simulación molecular se engloban tanto técnicas computacionales basadas en Monte Carlo (MC) como en dinámica molecular (DM). El principal objetivo de la simulación molecular es ofrecer resultados exactos a problemas de la mecánica estadística por encima de alternativas aproximadas.

Lo que caracteriza a la simulación molecular frente a otros métodos computacionales, y aproximativos, es que las coordenadas son determinadas de acuerdo a rigurosos cálculos de energías y fuerzas intermoleculares, pudiendo determinar propiedades macroscópicas mediante la evaluación exacta de un modelo teórico del comportamiento molecular. La palabra clave, de la descripción ofrecida por estas técnicas, es "exacta". Es decir, los resultados de una simulación están condicionados por la naturaleza del modelo teórico utilizado. Consecuentemente, la comparación de sus resultados con experimentos, o con resultados de teorías, suponen un test de la precisión del modelo, por lo que discrepancias entre medidas experimentales y datos de simulación molecular deben atribuirse sin ambigüedad a fallos en el modelado del comportamiento molecular. También, se muestra interesante una visión en la cual la simulación molecular puede servir para resolver discrepancias entre medidas experimentales tomadas en condiciones especialmente críticas.

En sesenta años, desde la primera simulación MC de un líquido diseñada por Metropolis et al. (1953) [29] sobre una computadora MANIAC, o la primera implementación en DM de potenciales de esferas duras, por parte de Alder y Wainwright (1957,1959), la simulación molecular ha ido siempre de la mano de la vertiginosa historia de la computación (desarrollo de hardware, códigos de programación, redes, ...). Bien sea mediante el desarrollo de códigos propios, el uso de códigos comerciales, o códigos open source, el horizonte actual se muestra realmente fascinante, como por ejemplo el escenario que ofrece la programación sobre GPU (Graphics Processing Units). El cálculo de las energías de los pares de interacciones entre moléculas consume normalmente la mayoría del esfuerzo computacional, y la eficiencia, en la paralelización necesaria, es posible gracias al nuevo paradigma computacional que suponen las arquitecturas de cálculo paralelo de las actuales GPUs, y como esa paralelización puede expresarse mediante lenguajes de alto nivel como C++ o FORTRAN.

En este capítulo, se abordan las bases teóricas de la simulación molecular mediante el método de Monte Carlo, como estrategia estocástica para la resolución de integrales multidimensionales del tipo de la Eq. (2.17), haciendo especial énfasis en los métodos y algoritmos utilizados en este trabajo.

En este sentido los algoritmos van a depender del ensemble elegido para la simulación.

El esquema de Monte Carlo utilizado, en nuestras simulaciones de fluidos, se resume básicamente en que las transiciones entre diferentes estados o configuraciones del sistema se alcanzan mediante una secuencia que pasa por: (a) la generación de una configuración de prueba de forma aleatoria; (b) la evaluación de un criterio de aceptación mediante el cálculo de la variación de enegía y otras propiedades en la configuración de prueba; y (c) la comparación del criterio de aceptación con un número aleatorio, aceptando o rechazando la configuración de prueba.

Es importante recalcar que no todos los estados generados supondran una contribución significativa a las propiedades configuracionales del sistema. Para determinar de forma precisa las propiedades del sistema será necesario muestrear adecuadamente aquellos estados que supongan una contribución significativa. En este sentido jugará un papel fundamental el concepto de cadena de Markov, como secuencia de muestreo en la cual el resultado de la configuración de prueba depende exclusivamente del estado anterior. Es decir, en una cadena de Markov, un nuevo estado será aceptado solamente si es más favorable que el estado presente.

3.1 La técnica de Monte Carlo y el muestreo Metropolis

En un esquema de integración basado en métodos deterministas, por ejemplo un método numérico de cuadraturas basado en la regla de Simpson, el número total de puntos (n) en el que hay que evaluar el integrando de la integral definida sobre un volumen V

$$I = \int_V f(x)dx \tag{3.1}$$

será igual a m^{DN}, siendo m el número de puntos equiespaciados en el que se divide cada eje de coordenadas en el dominio de V, y DN es la dimensionalidad del espacio de configuración. La computación sobre ese número de puntos en simplemente inviable.

En un primer esquema de integración de Monte Carlo (que podríamos denominar de "fuerza bruta") los m puntos los tomaríamos de forma aleatoria pero todos igualmente probables, es decir, en base a una distribución de probabilidad uniforme. La integral puede así estimarse como

$$I = \int_V f(x)dx = V\langle f\rangle \pm V\sqrt{\frac{\langle f^2\rangle - \langle f\rangle^2}{m-1}} \tag{3.2}$$

donde $\langle f\rangle = \dfrac{1}{m}\sum_i^m f(x_i)$ y $\langle f^2\rangle = \dfrac{1}{m}\sum_i^m f^2(x_i)$

Fijémonos, por ejemplo, que en un método de cuadratura mediante la regla de Simpson la estimación del error de truncamiento depende de la dimensionalidad de la integral como $\epsilon \sim m^{-4/d}$, con lo cual, para una cota máxima del error, m y el tiempo de computación aumentan exponencialmente con la dimensionalidad, puesto que $m \sim (1/\epsilon)^{d/4}$. Sin embargo, en el esquema de Monte Carlo el error es puramente estadístico, de forma que cuando $m \to \infty$ tenemos que, de acuerdo al teorema del límite central, el error converge según $\epsilon \sim m^{-1/2}$, siendo independiente de la dimensionalidad. Por lo tanto al aumentar la dimensionalidad, el método de Monte Carlo se muestra más eficiente (para $d > 8$ es más ventajoso que una estrategia Simpson).

Retomando nuestro objetivo, el promedio de la propiedad termodinámica $\langle A(\mathbf{r}^N)\rangle$ podría obtenerse por evaluación de la siguiente integral sobre $3N$ grados de libertad en un sistema de N partículas

$$\langle A(\mathbf{r}^N)\rangle_{NVT} = \int d\mathbf{r}^N A(\mathbf{r}^N)\rho_{NVT}(\mathbf{r}^N) \tag{3.3}$$

donde $\rho_{NVT}(\mathbf{r}^N)$ es la probabilidad de obtener una configuración $\mathbf{r}^N$ la cual depende de la energía potencial U de dicha configuración.

$$\rho_{NVT}(\mathbf{r}^N) = \frac{\exp\left[-\beta\mathcal{U}(\mathbf{r}^N)\right]}{\int d\mathbf{r}^N \exp\left[-\beta\mathcal{U}(\mathbf{r}^N)\right]} \tag{3.4}$$

La solución a plantear mediante Monte Carlo sería generar un número muy grande de configuraciones (N_{trial}) de $\mathbf{r}^N$ de forma aleatoria y reemplazar la integración por una suma sobre un número finito de configuraciones, de forma que la Eq. (3.3) se convierte en

$$\langle A(\mathbf{r}^N)\rangle_{NVT} = \frac{\sum\limits_{i}^{N_{trial}} A_i(\mathbf{r}^N)\exp\left[-\beta\mathcal{U}_i(\mathbf{r}^N)\right]}{\sum\limits_{i}^{N_{trial}} \exp\left[-\beta\mathcal{U}_i(\mathbf{r}^N)\right]} \tag{3.5}$$

En la práctica, la ejecución simple del método de Monte Carlo para evaluar Eq. (3.3) es altamente ineficiente debido a que la elección de la estrategia de muestreo, basada en seleccionar configuraciones de forma aleatoria y con la misma probabilidad, deja pasar muchas configuraciones en las cuales el factor de Boltzmann toma valores muy pequeños. Tales configuraciones suman una contribución muy pequeña al promedio. Como consecuencia, para obtener una aproximación adecuada del promedio necesitaríamos muestrear sobre un número prohibitivamente grande de configuraciones. Por lo tanto tendremos que restringir el muestreo de la función a aquellas regiones del espacio configuracional del sistema que contribuyan de forma significativa a la integral, surgiendo así el concepto de importancia del muestreo (*"importance sampling"*).

El concepto de *"importance sampling"* consiste básicamente en muestrear según una distribución de probabilidad no uniforme en el dominio de V. Para ello sea $g(x)$ una función densidad de probabilidad tal que $g(x) \geq 0$ y $\int_V g(x)dx = 1$, de manera que la Eq. (3.2) puede escribirse como

$$I = \int_V g(x)\frac{f(x)}{g(x)}dx = V\left\langle \frac{f}{g}\right\rangle \pm V\sqrt{\frac{\left\langle \left(\frac{f}{g}\right)^2\right\rangle - \left\langle \frac{f}{g}\right\rangle^2}{m-1}} \tag{3.6}$$

La esencia del método es determinar una función densidad de probabilidad $g(x)$ tal que el cociente $f(x)/g(x)$ sea una función suave y lo más constante posible en el dominio de integración V. Si por ejemplo $g(x) = 1/V$ recuperamos el método de cuadratura de Monte Carlo de "fuerza bruta", por lo que lo interesante es que $g(x)$ "mimetize" a $f(x)$.

Aplicando estas consideraciones a la Eq. (3.3) tenemos que

$$\langle A(\mathbf{r}^N)\rangle_{NVT} = \int d\mathbf{r}^N \left[\frac{A(\mathbf{r}^N)\rho_{NVT}(\mathbf{r}^N)}{g(\mathbf{r}^N)}\right] g(\mathbf{r}^N) \tag{3.7}$$

y enlazamos esta filosofía con el método propuesto por Metropolis et al. (1953) [29], para muestrear la función de Boltzmann, donde para la función g se hace la elección $g(\mathbf{r}^N) \equiv \rho_{NVT}(\mathbf{r}^N)$. En el método Metropolis se generan estados con una probabilidad $\exp\left[-\beta\mathcal{U}(\mathbf{r}^N)\right]$ y cada uno de ellos cuenta igualmente, en contraste con el método simple de Monte Carlo donde los estados se generan con la misma probabilidad asignandoles un peso igual a $\exp\left[-\beta\mathcal{U}(\mathbf{r}^N)\right]$.

Sin embargo, generar puntos en el espacio configuracional con una probabilidad relativa proporcional al factor de Boltzmann no es un problema trivial. A diferencia de la situación planteada en la Eq. (3.6), donde a priori conocemos la probabilidad de muestrear un punto en un volumen $d\mathbf{r}^N$ alrededor de $\mathbf{r}^N$, es decir conocemos tanto $\exp\left[-\beta\mathcal{U}(\mathbf{r}^N)\right]$ como $\int d\mathbf{r}^N \exp\left[-\beta\mathcal{U}(\mathbf{r}^N)\right]$ (función de partición del sistema), ahora únicamente conocemos $\exp\left[-\beta\mathcal{U}(\mathbf{r}^N)\right]$; esto es, conocemos solamente la probabilidad relativa de visitar los diferentes puntos del espacio configuracional. La dificultad estriba en encontrar un método para generar una secuencia de estados aleatorios tales que al final de la simulación cada estado haya sido muestreado con la probabilidad adecuada.

Resulta, que es posible hacer esto sin necesidad de calcular el factor de normalización de $\rho_{NVT}(\mathbf{r}^N)$, es decir, la función de partición. La secuencia se generará según una cadena de Markov, siendo ésta la esencia del algoritmo implementado en el código de simulación Monte Carlo.Una cadenas de Markov se caracterizan por la "falta de memoria": el resultado del siguiente paso en la evolución de un sistema depende solamente del estado actual de dicho sistema y es independiente de la historia del mismo.

LLamemos $\mathbf{\Gamma}_j$ al estado en el que se encuentra el sistema en el paso j de una secuencia de estados, definido por las coordenadas $\{\mathbf{r}^N\}_{(j)}$. Si después de una secuencia de $(n-1)$ pasos se tiene la secuencia de estados $\mathbf{\Gamma}_0, \mathbf{\Gamma}_1, \ \ldots \ , \mathbf{\Gamma}_{n-1}$, la probabilidad de que el sistena vaya al estado $\mathbf{\Gamma}_n$ en el paso siguiente está dada por la probabilidad condicional $P(\mathbf{\Gamma}_n|\mathbf{\Gamma}_{n-1}, \ \ldots \ \mathbf{\Gamma}_0)$ y si la secuencia sigue una cadena de Markov tenemos

$$P(\mathbf{\Gamma}_n|\mathbf{\Gamma}_{n-1}, \ \ldots \ \mathbf{\Gamma}_0) = P(\mathbf{\Gamma}_n|\mathbf{\Gamma}_{n-1}) \tag{3.8}$$

La probabilidad de transición entre dos estados la denotaremos como $\pi_{mn} = P(\mathbf{\Gamma}_m|\mathbf{\Gamma}_n)$, donde los índices m, n indican dos de los posibles estados $\mathbf{\Gamma}$, no dos pasos de la secuencia. Obviamente, estas probabilidades de transición son elementos de una matriz estocástica $\mathbf{\Pi} = \{\pi_{ij}\}$.

Entonces, la cadena de Markov se generará a partir de un microestado de partida y una prescripción de las probabilidades de transición $\{\pi_{ij}\}$. Esta cadena de Markov genera una distribución de probabilidad, de modo que la probabilidad de que $\mathbf{\Gamma}_i$ aparezca en la cadena sería

$$P(\mathbf{\Gamma}_i) = \lim_{n\to\infty} \frac{N_i}{n} \tag{3.9}$$

donde N_i es el número de veces que la cadena pasó por $\mathbf{\Gamma}_i$.

Ahora debemos establecer las condiciones que debe de cumplir la probabilidad de transición π_{ij} para que después de un "tiempo" de la cadena suficientemente largo la distribución resultante $P(\mathbf{\Gamma}_i)$ sea estacionaria y converja en particular a la distribución de Boltzmann.

La probabilidad de transición $\pi_{mn} = P(\mathbf{\Gamma}_m|\mathbf{\Gamma}_n)$ debe satisfacer:

1. $\pi_{mn} > 0$, para todo $\mathbf{\Gamma}_m, \mathbf{\Gamma}_n$

2. para todo $\mathbf{\Gamma}_n$

$$\sum_n \pi_{mn} = 1 \tag{3.10}$$

3. para todo par de conjuntos de microestados $\Omega_n = \{\mathbf{\Gamma}_n\}$ y $\Omega_m = \{\mathbf{\Gamma}_m\}$ debe existir al menos un $\mathbf{\Gamma}_n \in \Omega$, y un $\mathbf{\Gamma}_m \in \Omega_m$, tal que $\pi_{mn} > 0$

Las dos primeras condiciones resultan de que π_{mn} es una probabilidad. La tercera condición no es sino otra forma de imponer la ergodicidad de la cadena de Markov.

En el comienzo de la cadena de Markov, el sistema se encuentra en un microestado $\mathbf{\Gamma}_0$. En ese instante, la distribución de probabilidad será simplemente $P(\mathbf{\Gamma}) = \delta_{\Gamma,\Gamma_0}$. En pasos sucesivos dicha distribución irá cambiando hasta converger a la deseada. Podemos pensar por lo tanto en una distribución de probabilidad que sea función del paso o "tiempo" de la cadena, $P(\mathbf{\Gamma}, t)$. La variación de la distribución en el "tiempo" se puede describir mediante la ecuación

$$\frac{dP(\mathbf{\Gamma}, t)}{dt} = -\sum_m \pi_{nm} P(\mathbf{\Gamma}_n, t) + \sum_m \pi_{mn} P(\mathbf{\Gamma}_m, t) \tag{3.11}$$

donde el primer término de la derecha es la probabilidad de "salir" de $\mathbf{\Gamma}_n$ y el segundo de "entrar" en $\mathbf{\Gamma}_n$, aceptando un "tiempo" continuo si la cadena tiene un número suficientemente grande de pasos. La solución estacionaria de esta ecuación implica queda

$$\sum_m \pi_{nm} P(\mathbf{\Gamma}_n, t) = \sum_m \pi_{mn} P(\mathbf{\Gamma}_m, t) \tag{3.12}$$

de donde haciendo uso de la condición de la Eq.(3.10) resulta

$$P(\mathbf{\Gamma}_n) = \sum_m \pi_{mn} P(\mathbf{\Gamma}_m) \tag{3.13}$$

que es la condición de probabilidad invariante o estacionaria que debe poseer $P(\mathbf{\Gamma}_n)$. Aunque esta ecuación puede reemplazarse por una condición aún más fuerte que se conoce como *condición de balance detallado* o *reversibilidad microscópica*

$$\pi_{mn} P(\mathbf{\Gamma}_m) = \pi_{nm} P(\mathbf{\Gamma}_n) \tag{3.14}$$

ya que puede comprobarse que sumando sobre todos los estados m y haciendo uso de la Eq. (3.10) podemos recuperar la Eq. (3.13) en cuestión.

Metropolis et al. (1953) [29] mostraron una elección para la matriz de probabilidad de transición, que satisfaciendo las Eq.(3.10) y Eq.(3.13), permite la construcción de una trayectoria en el espacio fásico en el emsemble canónico

$$\pi_{mn} = \begin{cases} \alpha_{mn} & si \quad \dfrac{P(\mathbf{\Gamma}_n)}{P(\mathbf{\Gamma}_m)} \geq 1, \; m \neq n \\[2ex] \alpha_{mn} \left(\dfrac{P(\mathbf{\Gamma}_n)}{P(\mathbf{\Gamma}_m)} \right) & si \quad \dfrac{P(\mathbf{\Gamma}_n)}{P(\mathbf{\Gamma}_m)} < 1, \; m \neq n \end{cases} \tag{3.15}$$

donde α_{mn} representa la probabilidad de seleccionar una configuración de prueba Γ_n cuando el sistema se encuentra en Γ_m (con la restricción de simetría $\alpha_{mn} = \alpha_{nm}$). Si la probabilidad del nuevo estado es mayor que la del estado anterior, entonces el nuevo estado es aceptado con una probabilidad α_{mn}, mientras que en el caso contrario la probabilidad de transición dependerá además del cociente $P(\mathbf{\Gamma}_n)/P(\mathbf{\Gamma}_m)$: cuanto más pequeño es este cociente menor es la probabilidad de pasar de Γ_m a Γ_n.

Además debemos de contemplar una probabilidad distinta de cero de permanecer en el mismo estado $(m = n)$ dada por

$$\pi_{mm} = 1 - \sum_{n \neq m} \pi_{mn} \tag{3.16}$$

En un proceso de Monte Carlo, una nueva configuración de prueba puede obtenerse por desplazamiento (del centro de masas), intercambio, eliminación o adición de una molécula. En el caso de sistemas moleculares también se podrán contemplar reorientaciones aleatorias de las moléculas. Por ejemplo, generemos una configuración de prueba haciendo un desplazamiento aleatorio centro de masas de una molécula (i), desde su posición $\mathbf{r}_i^m$ a un punto vecino con posión $\mathbf{r}_i^n$ dentro de un cubo C centrado en la posición antigua. Con un número muy grande pero finito de nuevas posiciones N_{trial}, donde todas son igualmente probables, puede definirse α_{mn} para la molécula (i) como

$$\alpha_{mn} = \begin{cases} 1/N_{trial} & si \quad \mathbf{r}_i^n \in C, \\ \\ 0 & si \quad \mathbf{r}_i^n \notin C \end{cases} \tag{3.17}$$

La naturaleza exacta de la probabilidad de transición dependerá del ensemble elegido pero siempre involucrará la evaluación de la energía de la nueva configuración generada y su comparación con la energía del estado actual. Notar también que si la nueva configuración es rechazada, entonces la configuración presente pasa a contabilizarse como una nueva configuración.

3.2 El algoritmo Metropolis en el ensamble NVT

La implementación del algoritmo Metropolis pasa por la generación de un movimiento de prueba y el cálculo del cambio de energía $\Delta\mathcal{U} = \mathcal{U}_n - \mathcal{U}_m$:

- Si $\Delta\mathcal{U} \leq 0$, entonces $P(\mathbf{\Gamma}_n)/P(\mathbf{\Gamma}_m) \geq 1$ y se acepta el movimiento.
- Si $\Delta\mathcal{U} > 0$, $P(\mathbf{\Gamma}_n)/P(\mathbf{\Gamma}_m) < 1$ y el movimiento se acepta con una probabilidad $P(\mathbf{\Gamma}_n)/P(\mathbf{\Gamma}_m) = \exp(-\beta\Delta\mathcal{U})$. Se genera un número aleatorio ξ, con probabilidad uniforme en $(0, 1)$, y se acepta el movimiento si $\exp(-\beta\Delta\mathcal{U}) \geq \xi$.

El procedimiento se resume definiendo la probabilidad de aceptación como

$$\min\left[1, \exp(-\beta\Delta\mathcal{U})\right] \tag{3.18}$$

Una simulación Monte Carlo es diseñada por ciclos. En cada ciclo, se intenta un desplazamiento para cada molécula (elegida aletoriamente o de forma secuencial) y se aplica el criterio de aceptación. El tamaño del cubo C controla la fracción de movientos de prueba que son aceptados. Por lo tanto, se define el párametro de simulación δr_{max} (desplazamiento máximo permitido en un movimiento de prueba) con objeto de controlar la tasa de movimientos aceptados. El desplazamiento de la molécula i se lleva a cabo mediante la suma de un vector $\mathbf{v}$, generado aletoriamente con probabilidad uniforme en el intervalo $[-1, 1]$, a la posición original de la partícula

$$\mathbf{r}_{i,new} = \mathbf{r}_{i,old} + \delta r_{max}\mathbf{v} \tag{3.19}$$

La experiencia indica que una tasa de aceptación del $40\% - 50\%$ es aceptable para una simulación de Monte Carlo. Un disminución del valor de δr_{max} tendrá como consecuencia un aumento de la tasa de aceptación pero el espacio fásico será muestreado lentamente y las configuraciones aceptadas estarán altamente correlacionadas. Por el contrario, un aumento de δr_{max} conllevará que un mayor número de configuraciones no sean aceptadas y a una peor exploración del espacio fásico.

3.3 El algoritmo Metropolis en el ensamble NPT

El algoritmo para el ensamble NPT puede plantearse como una simple modificación sobre el algoritmo NVT. Además de intentar deplazamientos de moléculas los cuales son aceptados o rechazados dependiendo del valor de $\Delta\mathcal{U}$, se llevarán a cabo fluctuaciones de volumen con objeto de mantener constante la presión del sistema. El volumen se tratará como una coordenada adicional. Estos cambios de volumen se pueden asumir de V_m a un valor $V_n = V_m + \Delta V$, donde ΔV es una magnitud aleatoria uniformemente distribuida en el intervalo $[-\Delta V_{max}, +\Delta V_{max}]$. Las sucesivas configuraciones se generarán siguiendo el esquema propuesto en las Eqs. (3.15) y (3.16), con una probabilidad de que el sistema se encuentre en una configuración concreta dada por la Eq. (2.24). Así pués, para las fluctuaciones de volumen la probabilidad de aceptación vendrá dada por

$$\min\left[1, \exp\left\{-\beta\left[\Delta\mathcal{U} + P\Delta V - N\beta^{-1}\ln(V_n/V_m)\right]\right\}\right] \tag{3.20}$$

En este trabajo el volumen ha sido muestreado únicamente en la dirección z, haciendo cambios en L_z, y manteniendo constante la sección transversal, L_xL_y.

Los desplazamientos de moléculas se llevarán a cabo manteniendo el volumen del sistema constante; y consecuentemente, la probabilidad de aceptación de estos movimientos será la misma dada por la Eq. (3.18) para el ensamble NVT.

3.4 Condiciones de contorno periódicas y condición de mínima imagen

Una de las limitaciones de las simulaciones, tanto en MC como en DM, es el tamaño del sistema objeto de estudio. La pregunta de cuán grande tiene que ser un sistema relativamente pequeño para que los resultados concuerden con el comportamiento descrito por un experimento, o una teoría, no tiene respuesta única. Por un lado tenemos que sopesar el tiempo de computación que requiere el cálculo de las energías de interacción de las moléculas; el corazón de una simulación MC, ya que como hemos visto, esta información es utilizada para aceptar o no aceptar una determinada configuración del sistema. En principio, para un sistema de N moléculas, el tiempo de computación del doble bucle, en el algoritmo utilizado en este cálculo, es proporcional N^m, siendo m el número de interacciones. En el caso de una interacción aditiva por pares es proporcional a N^2. Reducir o eliminar esta dependencia con N^2 será uno de los problemas de los algoritmos en los códigos de simulación.

Por otro lado, si estamos interesados en la simulación del seno de un fluido (conocido como “bulk”) debemos minimizar los efectos de condiciones de contorno o paredes del entorno de simulación, ya que las moléculas en contacto con una pared experimentan fuerzas bastante diferentes a la de la fase que se pretende simular. El problema de estos efectos de superficie se puede resolver aplicando condiciones de contorno periódicas (PBC) [2,3,28,30]. La caja cúbica de simulación se replica a través del espacio para formar una red infinita. De este modo, la caja central es representativa de un *bulk* y está rodeada de réplicas de sí misma. Hay dos consecuencias de esta periodicidad. La primera es que cada una de las N moléculas de la caja central tiene una imagen, en la misma posición relativa, en cada una de las cajas réplica. Cuando una molécula abandona la caja central, su correspondiente imagen entra en la caja central desde la cara opuesta. De esta forma el número de moléculas se conserva durante la simulación. Después de cada movimiento Monte Carlo de una partícula, tienen que examinarse las coordenadas, y si se encuentra que una molécula se ha movido fuera de la caja de simulación sus coordenadas tienen que ser ajustadas. Si por ejemplo, la coordenada x debe estar entre 0 y L_x, donde L_x es el tamaño de la caja en la dirección x, las pruebas son: si $x_i \geq L_x$ entonces se reemplaza x_i por $x_i - L_x$, y si $x_i < 0$ entonces se reemplaza por $x_i + L_x$.

La segunda consecuencia de las PBC es la dificultad que introduce en el cálculo de la energía. Si consideramos un potencial aditivo por pares, la contribución a la energía de una molécula incluirá la interacción de dicha molécula con todas la de la caja de simulación. Habrá $N-1$ términos en la suma. Sin embargo, en principio, se deben incluir también todas las interacciones con las moléculas de las cajas vecinas. Esta tarea supondría un número infinito de términos y por supuesto es inviable. Para una función de energía potencial de corto alcance , se puede restringir esta suma haciendo una aproximación. Se considera a la molécula como centro de una región del mismo tipo y tamaño que la caja de simulación. Esta molécula interacciona con todas las moléculas cuyo centro se encuentre dentro de esta región, es decir, con las imágenes periódicas más cercanas de las otras $N-1$ moléculas. A esta técnica se le denomina *criterio de mínima imagen* [2, 3, 28, 30]. La implementación del criterio de mínima imagen en el cálculo de la interacción dentro del código de simulación es sencilla. Por ejemplo, si la distancia x_{ij} entre pares de moléculas $x_{ij} > L_x/2$ entonces se reemplaza x_{ij} por $x_{ij} - L_x$, y si $x_{ij} < L_x/2$ entonces se reemplaza x_{ij} por $x_{ij} + L_x$.

En el criterio de mínima imagen el cálculo de la energía implica una serie de términos de interacción, concretamente, $N(N-1)/2$. Este cálculo es costoso computacionalmente para sistemas de un orden de párticulas a partir de $\sim 10^3$. Así que existe una aproximación adicional, que mejora sustancialmente la situación, que consiste en el *truncamiento del potencial*. Supondremos que el potencial intermolecular se hace cero a partir de una cierta distancia que denominaremos distancia o radio de corte r_c ("cutoff"). Durante la simulación solamente se evaluarán las energías debidas a moléculas que se encuentren a una distancia inferior a r_c (ver Fig. 3.1).

En una caja de simulación de lado L, el número de vecinos considerados se reducirá en un factor de aproximadamente $4\pi r_c^3/3L^3$ (en el caso de que $r_c = L/2$, se reduciría en un factor de $\approx 1/2$). La introducción de un cutoff esférico supone una perturbación pequeña al sistema. Es importante puntualizar que el mayor valor que podríamos tomar sería $r_c = L/2$ ya que de lo contrario se violaría la condición de mínima imagen.

Objeto de otras secciones de este trabajo será tratar los problemas derivados del uso de un r_c; básicamente: la generación de una discontinuidad en la función del potencial, y la necesidad de utilizar correcciones de largo alcance de la energía como consecuencia de no tener en cuenta las interacciones desde el r_c a ∞.

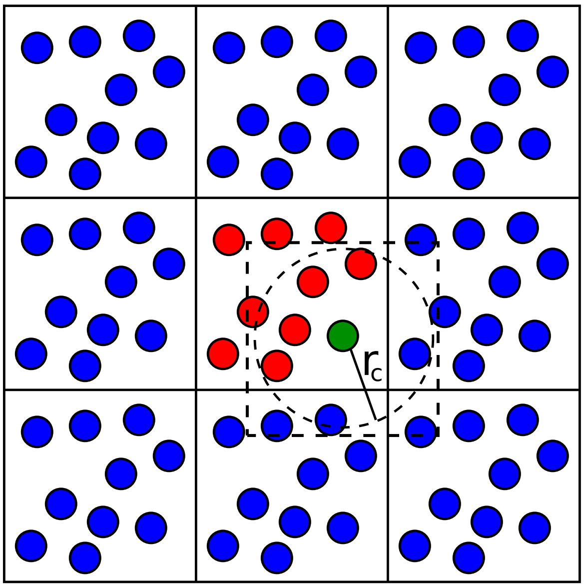

Figura 3.1: Criterio de mínima imagen en un sistema de dos dimensiones. La caja central contiene 10 moléculas (9 en rojo y una en verde que es sobre la que calcularemos la interacción). La caja de trazo discontinuo construida en torno al centro de la molécula, representada en color verde, también contiene 10 moléculas (5 rojas pertenecen a la caja de simulación y 4 azules son imágenes). La circunferecia de trazo discontinuo representa la distancia r_c a la que se trunca el potencial.

3.5 La lista de vecinos

En el apartado anterior hemos visto como disminuir el tiempo de computación en el cálculo de la energía, ya que las contribución de a la energía de una molécula no se hace teniendo en cuenta las $N-1$ restantes, sino un número menor. Sin embargo, para saber qué moléculas están a una distancia mayor que el r_c, debemos examinar, en cada paso de computación, la distancia entre todos los pares de moléculas. El tiempo de computación de esta comprobación se escala proporcional a N^2. Para reducir este tiempo de computación, Verlet (1967) [31] propuso un método basado en un sistema de lista de vecinos de cada partícula, que se refresca cada cierto número de pasos, en una MD de 864 partículas interaccionando bajo un potencial de Lennard-Jones . El método supone que los vecinos con los cuales interactúa la molécula i, o sea, aquellas que están dentro de la esfera de radio r_c no varían mucho entre paso y paso de integración.

Para ello eligiremos un rádio de corte $r_l > r_c$, y construimos para cada molécula una lista indexada de moléculas que caen dentro de esta región de radio de corte r_l. La creación de la lista de vecinos involucra dos matrices en el código de la simulación. Una que llamaremos *NLIST* y que contiene todos los vecinas de cada una de las N moléculas (de un tamaño de aproximadamente $4\pi N\rho r_l^3/6$). Y otra que denominaremos $NPOINT$ (de tamaño N) donde almacenaremos la posición (entendida como índice) del último vecino de la molécula i en $NLIST$. Para cada molécula, el valor de $NLIST$ nos permite la indexación de las moléculas vecinas. Así pues, los índices de las moléculas vecinas a la molécula i estarían comprendidos entre $NPOINT(i-1)+1$ y $NPOINT(i)$ (ver Fig. 3.2).

La ventaja de la lista es que no es necesario actualizarla después de cada paso Monte Carlo (traslación, cambios de volumen,...). La elección de r_l se hará de tal manera que forme una capa alrededor de r_c, de modo que entre actualización y actualización de la lista garanticemos que ninguna

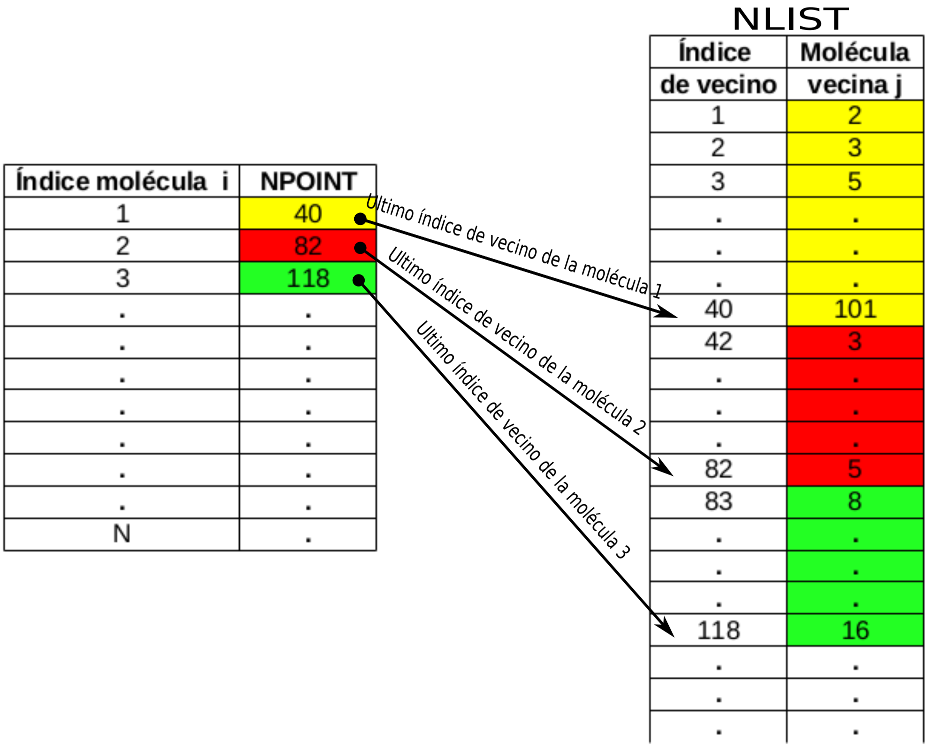

Índice molécula i	NPOINT
1	40
2	82
3	118
.	.
.	.
.	.
.	.
.	.
.	.
.	.
N	.

NLIST

Índice de vecino	Molécula vecina j
1	2
2	3
3	5
.	.
.	.
.	.
40	101
42	3
.	.
.	.
.	.
82	5
83	8
.	.
.	.
.	.
118	16
.	.
.	.
.	.

Figura 3.2: Ejemplificación de la construcción de la lista de vecinos.

molécula, efectuando movimientos Monte Carlo, pueda penetrar a través de dicha capa hacia la esfera de cutoff r_c. Por ejemplo, como puede verse en la Fig.3.3, la molécula 2 en su desplazamiento Monte Carlo no podrá ser vecina de la molécula central 1 antes de que la lista de vecinos sea actualizada.Es decir, que $r_l - r_c$ se ajustará de manera que coincida el máximo desplazamiento que puedan sufrir las moéculas. Al inicio de la simulación se construye por primera vez la lista, conteniendo todos los pares de vecinos que se encuentran a una distancia r_l entre ellos, y la lista se reconstruye a intervalos.

El ahorro con este método es significativo para sistemas de entre 500 a 5000 partículas, para los cuales el tiempo por paso de simulación baja prácticamente a la mitad (ver Ref. [2]). Para sistema de entre 100 a 200 partículas los cambios no son sustanciales, mientras que para sistemas de más de 5000 partículas se emplean métodos más eficientes, como el link-cell-list [2].

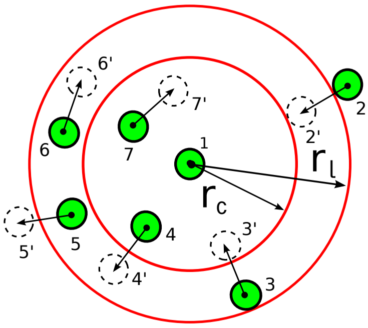

Figura 3.3: Esfera cutoff de radio r_c y capa, alrededor de la molécula, de radio r_l.

3.6 Promedios y errores en la simulación

La estimación de los promedios en el emsemble, obtenidos en una simulación, están sujetos a incertidumbres estadísticas debido a su carácter probabilístico. Sin embargo, no podemos usar como estimación del error la desviación estándar de la magnitud evaluada durante la simulación, ya que configuraciones próximas están correlacionadas. En general, una forma de estimar dicho error es evaluando la magnitud en intervalos de pasos de Monte Carlo en los que las configuraciones estén práctimente descorrelacionadas.

Los promédios en una simulación de Monte Carlo son solamente acumulados después de un periodo de equilibración. Si N es el número de moléculas, una simulación Monte Carlo se organiza en ciclos (o movimientos), donde se efectúan N intentos de movimientos de moléculas (traslaciones y/o rotaciones, algún cambio de volumen, una reconstrucción de una cadena de átomos que forma una molécula, etc) . Después de un número de ciclos de equilibración la simulación sigue sobre un número N_{run} de ciclos que denominaremos de producción. De antenamo no conocemos el número de ciclos de equilibración y debe determinase mediante un número de ensayos previos (por ejemplo representando la densidad, o su perfil, frente al número de ciclos). Alternativamente, es usual descartar un gran número de ciclos para tener un mayor margen de seguridad en la equilibración del sistema (por ejemplo en una simulación de 5×10^6 ciclos tomar los 10^6 primeros de equilibración).

Si estuviéramos en un experimento real, el error $\epsilon(\mathcal{A})$ asociado con la medida de la magnitud $\mathcal{A}$ es estimado mediante la repetición del experimento un número n de veces. De forma que la varianza correspondiente vendría dada por

$$var(\mathcal{A}) \equiv \sigma^2(\mathcal{A}) = \frac{1}{n}\sum_{k=1}^{n}(\mathcal{A}_k - \langle\mathcal{A}\rangle)^2 \tag{3.21}$$

donde $\mathcal{A}_k$ es el resultado después de la k-ésima medida y $\langle\mathcal{A}\rangle$ es el valor medio sobre el conjunto de las medidas. El error $\epsilon(\mathcal{A})$ se suele asociar a la desviación standard, $\sigma(\mathcal{A})$ (definida como la raiz cuadrada de la varianza), de forma que si $\epsilon(\mathcal{A}) = \sigma(\mathcal{A})$ existirá un 67% de probabilidad de que una medida individual esté comprendida entre $\langle\mathcal{A}\rangle$ y $\langle\mathcal{A}\rangle \pm \epsilon(\mathcal{A})$. En el caso de que tomaramos $\epsilon(\mathcal{A}) = 2\sigma(\mathcal{A})$ hablaríamos de un 97%.

Haciendo una comparación con un experimento real, una forma de estimar el error podría ser el promediar sobre n simulaciones independientes que comiencen desde diferentes configuraciones iniciales, estando formada cada una de estas simulaciones por un número N_{run} de ciclos de Monte Carlo. Pero, en la práctica de la simulación, la estimación del error se realiza desde una única simulación dividida en un número n_b de bloques, cada uno de ellos compuesto por un número de ciclos $N_b = N_{run}/nb$ [2,3,28,30]. El promedio de la magnitud A calculado sobre cada bloque vendría dado por

$$\langle\mathcal{A}\rangle_b = \frac{1}{N_b}\sum_{i=1}^{N_b}\mathcal{A}_i \tag{3.22}$$

donde la suma corre solamente sobre las configuraciones del bloque b. Los promedios sobre cada bloque pueden utilizarse para estimar la varianza

$$\sigma_b^2 = \sigma^2(\langle\mathcal{A}\rangle_b) = \frac{1}{n_b}\sum_{i=1}^{n_b}(\langle\mathcal{A}\rangle_b - \langle\mathcal{A}\rangle_{run})^2 \ \propto N_b^{-1} \tag{3.23}$$

Obviamente $\langle\mathcal{A}\rangle_{run} = 1/N_{run}\sum_{i=1}^{N_{run}}\langle\mathcal{A}\rangle_i$ y concidiría exactamente con el promedio $\langle\mathcal{A}\rangle$ en el ensemble si fuera posible $N_{run}\to\infty$. La varianza expresada en la Eq. (3.23) es inversamente proporcional a N_b cuando este valor se hace lo suficientemente grande, así como los bloques se convierten en estadísticamente no correlacionados. Pero como se puede ver, σ_b^2 depende del número de bloque en que hayamos dividido la simulación, por lo que sería interesante obtener esta misma varianza para un único bloque que constituya la simulación completa. Resulta que un buen estimador de esta varianza es

$$\sigma^2(\langle\mathcal{A}\rangle_{run}) \approx \frac{1}{n_b - 1}\sigma_b^2 \tag{3.24}$$

, insistiendo en un número de ciclos N_b suficientemente grande, de forma que la estimación del error se hace insensible al número de bloques utilizados cuando el tamaño de éstos es suficientemente grande [2, 3]. Por supuesto, esta estimación del error será válida siempre y cuando la propiedad pueda obtenerse como un promedio en el ensamble de la simulación.

Errores muy grandes en la simulación pueden indicar que no se ha alcanzado la equilibración, que la métodologia no es la adecuada para la determinación de cierta propiedad, o simplemente que es irrealizable por alguna razón (por ejemplo correlaciones introducidas por grandes fluctuaciones cerca del punto crítico).

3.7 Unidades reducidas

Una posible elección de unidades para potenciales por pares de la forma $\mathcal{U}(r) = \epsilon f[r/\sigma]$, que además ha sido la empleada en nuestras simulaciones, es tomar σ como unidad de longitud y ϵ como unidad de energía. Con esta elección podemos definir el resto de magnitudes utilizadas en la simulación en unidades reducidas (denotadas mediante el superíndice *) como: $U^* = U\epsilon^{-1}$ para la energía, $P^* = P\sigma^3\epsilon^{-1}$ para la presión, $\rho^* = \rho\sigma^3$ para la densidad, $T^* = k_B T\epsilon^{-1}$ para la temperatura y $\gamma^* = \gamma\sigma^2\epsilon^{-1}$ para la tensión superficial.

La razón más importante para utilizar unidades reducidas es que muchas combinaciones de ρ, T, ϵ y σ corresponden todas al mismo estado en unidades reducidas. Es lo que se conoce como ley de los estados correspondientes. Si no usamos unidades reducidas es imposible, por ejemplo, encontrar equivalencias entre dos simulaciones. Por supuesto, un resultado de simulación en unidades reducidas puede trasladarse a unidades reales.

Otro motivo para el uso de unidades reducidas es puramente computacional. Si trabajamos con unidades reales podemos encontrarnos con valores de magnitudes que durante el cálculo pueden ser mucho mayores o mucho menores que 1. Operaciones sucesivas de multiplicación en coma flotante que impliquen estas cantidades pueden dar lugar a desbordamientos.

Capítulo 4

Potenciales intermoleculares

El cálculo de la energía potencial (o fuerzas) debido a las interacciones intermoleculares es, sin duda, lo que más tiempo computacional consume y un paso crucial en cualquier simulación. En general la energía potencial de un sistema de N partículas interaccionando se calcula según

$$\mathcal{U} = \sum_i u_1(r_i) + \sum_i \sum_{j>i} u_2(r_i, r_j) + \sum_i \sum_{j>i} \sum_{k>j>i} u_3(r_i, r_j, r_k) + \ldots \tag{4.1}$$

donde el primer término representa el efecto de un campo externo y el resto de los términos las interacciones entre las partículas, por ejemplo, el término u_2 es el potencial entre pares de partículas, u_3 entre tripletes, etc. Típicamente se asume que solamente las interacciones entre dos cuerpos son importantes, situación denominada como potencial aditivo por pares, y la Eq. (4.1) se trunca después del segundo término de forma que la energía total para un sistema de N partículas es

$$\mathcal{U} = \frac{1}{2} \sum_{i=1}^{N} \sum_{j=1}^{N} u_{ij} = \frac{1}{2} \sum_{i=1}^{N} U_i \tag{4.2}$$

Una de las decisiones fundamentales, en el estudio de fluidos en simulación, es la elección de potenciales que sean capaces de reproducir tanto la termodinámica como otras propiedades del sistema, dado que las propiedades de bulk de las sustancias son resultado de las propiedades de las moléculas individuales e interacciones entre ellas. Las funciones de energía potencial son empíricas y contienen tanto fuerzas de atracción como de repulsión. En la teoría básica, debida a London, se establece que en los potenciales, la parte de atracción, varía con la inversa de la potencia sexta de la separación entre moléculas, mientras que exponentes más altos controlan la parte repulsiva. En este sentido, para moléculas neutras sin puentes de hidrógeno ni otro tipo de interacción especial, Mie (1903) propone una expresión para representar esta situación

$$u_{ij}(r) = ar^{-n} - br^{-6} \tag{4.3}$$

Un caso especial de este potencial para $n = 12$ es el propuesto por Lennard-Jones (1924). Es evidente que para simular fases condensadas de la materia, y la mayor parte de las transiciones de fases, son necesarias las fuerzas atractiva entre partículas. Existen muchos modelos de potenciales atractivos por pares, pero es sin duda uno de los potenciales más ampliamente utilizados para modelar la interacción de van del Waals, tanto en MC como en MD. Hablar del este potencial es hablar de partículas con carga neta nula que interactúan de forma isotrópica y no discriminatoria. Además, ya que la energía de interacción entre las moléculas no solamente depende de sus separaciones sino también de sus orientaciones, y cuando sea necesario de sus conformaciones, es posible calcular la interacción de van der Waals entre moléculas usando un modelo en el cual la interacción se calcula como la suma de todos los pares de "sites" en las dos moléculas (site model).

Desde los primeros estudios sistemáticos relizados por Verlet [31] en la década de los sesenta hasta la actualidad, la cantidad de artículos que utilizan el potencial de Lennard-Jones resulta ser realmente abrumadora, lo que refleja la importancia de este potencial en el desarrollo de metodologías de simulación. Nos encontramos por ejemplo con trabajos que han constituido los cimientos de la simulación molecular, como el de Nicolas et al.(1979) [32] que recopila y revisa datos para la ecuación de estado del fluido de Lennard-Jones de una década de trabajos de simulación en MD y MC, o la revisión posterior realizada por Johnson et al.(1993) [33]; nombres que resuenan en el corpus fundamental de las lecturas obligadas en la formación de todo simulador de sistemas interfaciales, como Chapela et al.(1977) [34], Walton et al. (1983) [35], Nijmeijer et al.(1988) [36], Holcomb et al.(1993) [37], Mecke et al.(1997) [38], . . . Un potencial que se ha mostrado esencial en el estudio de problemas asociados a la determinación de propiedades de sistemas inhomogéneos (densidades de coexistencia y propiedades interfaciales) como tamaño finito del sistema, area interfacial (Chen (1995) [39]) o truncamiento de las interacciones. Sobre este último aspecto, Trokhymchuk and Alejandre [9] presentan una brillante y completa discusión sobre los efectos del truncamiento de las interacciones para pequeños valores del radio de corte, en simulaciones en MD y MC.

En este capítulo repasamos aspectos esenciales del potencial de Lennard-Jones haciendo especial hincapié en las consecuencias del truncamiento del mismo. Como es sabido, el truncamiento del potencial tiene consecuencias inmediatas sobre las propiedades de los líquidos: densidad de coexistencia de la fase líquida, presión de vapor y especialmente la tensión interfacial. En el caso de sistemas homogéneos se efectúan sencillas correcciones bajo el supuesto de que la función de distribución radial es igual a 1, para distancias superiores al radio de corte del potencial, y que la densidad de todos los componentes no depende de la posición. En el caso de sistemas inhomogéneos las correcciones de "bulk" no reflejan el hecho de que las correcciones de largo alcance de la energía para una molécula en la fase líquida son diferentes a las de una molécula en la fase vapor, o en otras palabras, la contribución de largo alcance para la fuerza actuando sobre una molécula en la región interfacial no es tenida en cuenta.

Los métodos para minimizar la influencia del truncamiento del potencial, en simulaciones de sistemas inhomogéneos, se han ido refinando desde los primeros trabajos de Chapela et al.(1977) [34], Holcomb et al.(1993) [37] o Blokhuis et al. (1995)), orientados a obtener correcciones de cola para la tensión interfacial, hasta la necesidad de incluir correcciones de largo alcance (LRC) inhomogéneas en los algoritmos de cálculo de la energía interna con objeto de obtener, por ejemplo, perfiles de la densidad que correspondieran a un modelo de potencial no truncado, en el marco conceptual abierto por los trabajos de Guo y Lu (1997) o Mecke et al.(1997) [38]. Sin embargo, aunque el algoritmo propuesto para las LRC inhomogéneas por Mecke et al.(1997) [38] ofrece mejores resultados en comparación con simulaciones sin LRC, a temperaturas altas ofrece resultados que no son independientes del radio de corte. Janeček (2006) [15] retoma este problema obteniendo expresiones correctas para la energía, la fuerza y el virial, para sistemas inhomogéneos con interfases planas. Posteriormente MacDowell y Blas (2009) [14] adaptan el método de Janeček de forma que las correcciones de largo alcance pueden expresarse como un potencial efectivo de largo alcance aditivo por pares más un autotérmino, de forma que estas correcciones se puedan implementar de una forma sencilla en el código de simulación.

Una segunda parte de este capítulo se dedica a abordar aspectos fundamentales del potencial de square-well (SW). Es un modelo que ha sido extensamente estudiado tanto en simulación como mediante métodos de mecánica estadística, mostrándose simple y apropiado para testear teorías de fluidos. Las referencias sobre simulación de sistemas SW simples son abundantes, tanto en número como en métodos: simulaciones MC y MD de una fase para diferentes rangos de la interacción [40–43], coexistencia líquido-vapor mediante diferentes métodos de simulación (MD [44–46] , Gibbs Ensamble MC [47], Gran Canonico MC [48], . . .), determinación de la tensión superficial [49]. . .

En este capítulo se analizan también algunas implicaciones que un potencial discontinuo SW presenta a la hora de calcular la presión. Una aproximación para calcular la presión en sistemas con potenciales SW, en una simulación MC, es evaluar el virial (ruta mecánica), el cual puede expresarse en términos de solapamientos bajo escalamientos de las distancias intermoleculares (compresiones y expansiones virtuales). Trabajos como los de E. de Miguel y G. Jackson (2006) [50] o P.E. Brumby et al. [51], ambos aplicados a sistemas de esferas duras, muestran los elementos básicos de un escalamiento isotrópico para evaluar tanto la presión de un sistema bulk como las componentes del tensor de presiones, y que podemos extrapolar a sistemas SW. Comprender los detalles de este tipo de cálculos, a nivel computacional en sistemas bulks, es fundamental para tener una adecuada perspectiva y posteriormente poder extender estos detalles al cálculo de las componentes del tensor de presiones en un sistema inhomogéneo, es por lo que el desarrollo de esta apartado se presenta con un marcado carácter didáctico.

4.1 El potencial de Lennard-Jones

La expresión para el potencial de Lennard-Jones (LJ) está dada por la expresión

$$u_{ij}^{LJ}(r) = 4\epsilon_{ij}\left[\left(\frac{\sigma_{ij}}{r}\right)^{12} - \left(\frac{\sigma_{ij}}{r}\right)^{6}\right] \tag{4.4}$$

donde r es la distancia entre dos moléculas i y j , los parámetros ajustables, ϵ_{ij} y σ_{ij}, representan respectivamente la profundidad del pozo de potencial, y la distancia en la que el potencial entre moléculas es cero. Este potencial está constituido por un término repulsivo de corto alcance, que modeliza el solapamiento de nubes electrónicas, función de la potencia r^{-12} y término atractivo debido a las fuerzas de van der Waals que es función de r^{-6}. Si tenemos tipos de moléculas diferentes, por ejemplo el caso de mezclas binarias, entonces estos parámetros están asociados a la interacción entre moléculas de distinto tipo.

En este trabajo, usamos las conocidas reglas de combinación de Lorentz-Berthelot, en las que los parámetros para las interacciones entre moléculas diferentes se obtienen en función de los parámetros de interacción de las especies puras de tipo i $(\epsilon_{ii}, \sigma_{ii})$, y de tipo j $(\epsilon_{jj}, \sigma_{jj})$, según

$$\sigma_{ij} = \frac{\sigma_{ii} + \sigma_{jj}}{2} \tag{4.5}$$

y

$$\epsilon_{ij} = (\epsilon_{ii}\epsilon_{jj})^{1/2} \tag{4.6}$$

Evidentemente, en el caso de sistemas puros diremos que $\epsilon_{ij} = \epsilon$ y $\sigma_{ij} = \sigma$.

Estas reglas de combinación propuestas por Lorentz en 1881, motivado por una media aritmética de colisión de esferas duras, y por Berthelot en 1889 como un media geométrica de los parámetros de energía de moléculas diferentes con débiles argumentos físicos, son las más antiguas de las aproximaciones utilizadas, y aunque el que se hayan mostrado inadecuadas para la descripción de propiedades de mezclas [52] , también han sido hasta ahora las más utilizadas.

Es en la década de los 50 en los trabajos de Reed [53] [54] donde podemos encontrar como la conocida regla de Berthelot puede obtenerse teniendo en cuenta el potencial de ionización y el tamaño molecular en la teoría de London para fuerzas dispersivas, hecho que es descrito posteriormente en la bibliografía como la base teórica de esta regla de combinación [55] [56]. Idea que es utilizada por algunos autores para obtener reglas de combinación en aquellos casos en los que la media geométrica se muestra inadecuada. En la teoría de London [57, 58] la energía de dispersión entre dos moléculas esféricas i y j separadas por una distancia r_{ij} está dada por la expresión

$$\phi_{ij} = -\frac{3}{2}\frac{\alpha_{0,i}\,\alpha_{0,j}}{(4\pi\epsilon_0)^2 r_{ij}^6}\,\frac{h\nu_i\nu_j}{h(\nu_i+\nu_j)} \tag{4.7}$$

donde h es la constante de Planck, ϵ_0 es la permitividad en el vacío, $\alpha_{0,i}$ y $\alpha_{0,j}$ son la polarizabilidad electrónica de las moléculas i y j; ν_i y ν_j las frecuencias fundamentales (correspondientes a las moléculas , consideradas como un oscilador de electrones). London indica que para moléculas simples $h\nu_i \approx I_i$, el potencial de ionización, con lo cual la (4.7) toma la forma

$$\phi_{ij} = -\frac{3}{2}\frac{\alpha_{0,i}\,\alpha_{0,j}}{(4\pi\epsilon_0)^2 r_{ij}^6}\,\frac{I_i\,I_j}{I_i+I_j} \tag{4.8}$$

Por ejemplo, Hudson y McCoubrey [58, 59] obtienen una regla de combinación relacionando el término atractivo del potencial de Lennard-Jones con la energía de dispersión de London; relación que para la interacción entre moléculas del mismo tipo resulta

$$\phi_{ii} = -\frac{3}{4}\frac{\alpha_{0,i}^2}{(4\pi\epsilon_0)^2 r_{ii}^6} I_i = -4\pi\epsilon_{ii}\left(\frac{\sigma_{ii}}{r_{ii}}\right)^6 \tag{4.9}$$

Obteniendo $\alpha_{0,i}$ y sustituyendo en la Eq. (4.8) $\alpha_{0,i}$ y $\alpha_{0,j}$ tenemos

$$\epsilon_{ij} = 2\frac{\sigma_{ii}^3\sigma_{jj}^3}{\sigma_{ij}^6}\,\frac{(I_iI_j)^{1/2}}{I_i+I_j}(\epsilon_{ii}\epsilon_{jj})^{1/2} \tag{4.10}$$

de forma que el término que representa la interacción entre moléculas de distinto tipo ϵ_{ij} queda expresado en función de las profundidades del pozo de potencial para la interacción entre moléculas del mismo tipo. Aún así tenemos una dependencia con σ_{ij} que es un parámetro desconocido y debemos elegir una regla de combinación. Hudson y McCoubrey [58, 59] asumen la regla de Lorentz $\sigma_{ij} = (\sigma_{ii}+\sigma_{jj})/2$ de forma que la regla de combinación para ϵ_{ij} toma la forma

$$\epsilon_{ij} = 2^7\frac{\sigma_{ii}^3\sigma_{jj}^3}{(\sigma_{ii}+\sigma_{jj})^6}\,\frac{(I_iI_j)^{1/2}}{(I_i+I_j)}(\epsilon_{ii}\epsilon_{jj})^{1/2} \tag{4.11}$$

La media geométrica de la regla de Berthelot está contenida en la (4.10) en el caso de que los tamaños moleculares y los potenciales de ionización de i y j sean los mismos.

4.1.1 Truncamiento del potencial

Para las simulaciones de este trabajo se ha utilizado un potencial esféricamente truncado a la distacia de corte r_c, definido por

$$u_{ij}(r) = u_{ij}^{LJ}(r)\;[1-\Theta(r-r_c)] = \begin{cases} u_{ij}^{LJ}(r) & r \le r_c \\ 0 & r > r_c \end{cases}\;, \tag{4.12}$$

donde $\Theta(x)$ es la función salto de Heaviside.

Como el potencial no es cero para distancias mayores que las del radio de corte r_c, el truncamiento introduce un error en el cálculo de la energía de interacción, por lo que para minimizarlo se introducen correcciones de largo alcance a la Eq. (4.4)

$$U_i = \sum_{j \in r_c^{(i)}} u_{ij} + U_i^{LRC} \tag{4.13}$$

En las simulaciones Monte Carlo, el potencial se calcula durante la simulación y el truncamiento tiene consecuencias inmediatas en el cálculo de la presión. Truncar el potencial según la Eq. (4.12) da lugar a la aparición de una fuerza adicional, de tipo impulsivo, debido a la propia discontinuidad en la distancia de corte r_c. Los trabajos de Trokhymchuk y Alejandre [9], y más recientemente de Miguel y Jackson [16], insisten en la importancia de evaluar esta contribución impulsiva en el tratamiento de fluidos inhomogéneos, y como debe incluirse en el virial si se utiliza una ruta mecánica para el cálculo de las componentes del tensor de presiones. La fuerza intermolecular asociada al potencial de interacción intermolecular $u(r)$, entre dos moléculas separadas una distancia r, está dada por $\mathbf{f} = f(r)\hat{\mathbf{r}}$, con $f(r) = -(du/dr)$ y $\hat{\mathbf{r}}$ es el vector unitario entre las dos moléculas interactuantes. Por lo tanto el valor de la fuerza que se obtiene de un potencial truncado de forma simple $u_{ST}(r)$, como el expresado en Eq.(4.12), es

$$f_{u_{ST}}(r) = f_{LJ}(r)\big[1 - \Theta(r - r_c)\big] + u_c\,\delta(r - r_c) \tag{4.14}$$

donde $f_{LJ}(r) = -(du_{LJ}/dr)$ es el valor de la fuerza asociada al potencial intermocular de LJ, $u_c = u_{LJ}(r_c)$ el valor del potencial de LJ en $r = r_c$ y $\delta(x)$ es la función δ de Dirac. El segundo sumando de la Eq. (4.14) representa el valor del la fuerza impulsiva (atractiva), el cual no es precisamente despreciable [3] y puede suponer una contribución significativa a la presión [16]. Para sistemas homogéneos esta contribución, que llamaremos P_{imp} , puede hacerse explícita. Para ello tendremos en cuenta que, en el caso de sistemas en los cuales la interacción sea aditiva por pares, la presión macroscópica puede escribirse como

$$P = \langle \rho k_B T \rangle + \left\langle \frac{1}{3V} \sum_{i=1}^{N-1} \sum_{j=i+1}^{N} \mathbf{r}_{ij} \cdot \mathbf{f}_{ij} \right\rangle \tag{4.15}$$

donde $\rho = N/V$ es la densidad de número de paríprops, k_B la constante de Boltzmann, T es la temperatura, $\mathbf{r}_{ij}$ es el vector intermolecular entre pares de moléculas, y $\mathbf{f}_{ij}$ la fuerza intermolecular. Como puede verse en la Eq. (4.14), el cálculo de la contribución impulsiva requiere evaluar computacionalmente $\delta(r - r_c)$, para lo cual usaremos la aproximación discreta

$$\delta(r - r_c) = \lim_{\Delta r_c \to \infty} \frac{\Theta(r - r_c) - \Theta(r - r_c - \Delta r_c)}{\Delta r_c} \tag{4.16}$$

donde Δr_c es un parámetro fijo. Teniendo en cuenta la Eq. (4.15) y la aproximación de Eq. (4.16), la contribución de la fuerza impulsiva puede evaluarse como

$$P_{imp} = \frac{1}{3V} \left\langle \sum_{i=1}^{N-1} \sum_{j=i+1}^{N} \mathbf{r}_{ij} \cdot \mathbf{f_{imp}} \right\rangle = \frac{1}{3V} r_c u_c \lim_{\Delta r_c \to \infty} \frac{\langle n(r_c^+) \rangle}{\Delta r_c} \tag{4.17}$$

donde $\langle n(r_c^+) \rangle$ es el promedio de pares de moléculas entre r_c y $r_c + \Delta r_c$. En las simulaciones de este trabajo se ha utilizado una capa con $\Delta r_c = 0.005\sigma$ para determinar $\langle n(r_c^+) \rangle$. La expresión dada en la

Eq. (4.17) no pierde generalidad y será adaptada posteriormente para su aplicación en el cálculo de las componentes del tensor de presiones para sistemas inhomogéneos.

Conviene puntualizar que un potencial truncado y una fuerza truncada no son equivalentes [9], [16]. En las simulaciones de dinámica molecular es la fuerza la que se calcula durante la simulación y es común tratar con sistemas en los cuales las fuerzas están esféricamente truncadas de forma simple (no desplazadas o non shifted), calculadas como

$$f_{ST}(r) = f_{LJ}(r)\big[1 - \Theta(r - r_c)\big] \tag{4.18}$$

Así que integrando Eq. (4.18) obtenemos la expresión correspondiente para el potencial

$$u_{f_{ST}}(r) = \{u_{LJ}(r) - u_c\}\left[1 - \Theta(r - r_c)\right] \tag{4.19}$$

Si comparamos la Eq. (4.12) con la Eq. (4.19), podemos observar que corresponden, respectivamente, a un potencial esféricamente truncado (ST) y a un potencial esféricamente truncado y desplazado (STS). Diferentes formas de truncar el potencial (ST o STS) dan lugar a cambios en el diagrama de fases, los cuales no pueden ser ignorados a la hora de determinar densidades de coexistencia o propiedades interfaciales, o cuando queremos hacer comparaciones con otros trabajos de la literatura. En este último sentido, el trabajo de Trokhymchuk y Alejandre [9] recoge la gran dispersión de datos en la literatura en resultados de densidades de coexistencia y tensión superficial debido a dos hechos: las simulaciones en MC o en MD no han tenido en cuenta diferencias en el potencial, o bien, la contribución de la fuerza impulsiva no ha sido tenida en cuenta en el cálculo de la presión (MC) o las fuerzas (MD). Obviamente, las diferencias entre los dos modelos de potencial, ST y STS, serán tanto menores cuanto mayor sea el r_c, ya que en el límite de $r_c \to \infty$ ambos potenciales se aproximarán al potencial sin truncar de la Eq. (4.4); aunque las formas de aproximarse a este límite sean diferentes, ya que en un potencial STS tenemos cambios en la profundidad del pozo, mientras que en un potencial ST simplemente despreciamos el potencial para $r > r_c$.

4.1.2 Correcciones de largo alcance homogéneas para la energía y la presión

En este trabajo se han utilizado correcciones de largo alcance homogéneas en simulaciones NPT, de fases de bulk (líquido y vapor), necesarias para la construcción de interfases vapor-líquido de mezclas binarias de moléculas LJ. Como vimos en la Eq. (4.13), el hecho de no considerar las interacciones al cortar el potencial de interacción para $r > r_c$ introduce un error, tanto en la energía total del sistema como en la presión , que para sistemas homogéneos será de tipo sistemático. Evidentemente, este error se reducirá al aumentar el r_c. Por otro lado, si usamos condiciones de contorno periódicas y un radio de corte $r_c < L/2$, donde L es la longitud de la caja de simulación, solamente será necesario considerar la interacción de una molécula dada i con la imagen periódica más cercana de las otras moléculas j. La corrección de este error sistemático consistirá en la suma de una contribución de cola (u_{tail}) a la energía total del sistema. La deducción la corrección (u_{tail}) para un fluido Lennard-Jones puede verse en las Refs. [3], [2], [30] y la adaptamós aquí para el caso de mezclas binarias. Asumiendo que las interacciones son aditivas por pares podemos descomponer al energía del sistema según

$$\mathcal{U} \equiv U_{N_A N_B} = U^{AA} + U^{BB} + U^{AB} \tag{4.20}$$

donde

$$\begin{aligned} U^{AA} &= \sum_{1\leq i<j\leq N_A} u_{AA,ij} \\ U^{BB} &= \sum_{1\leq i<j\leq N_B} u_{BB,ij} \\ U^{AB} &= \sum_{i=1}^{N_A}\sum_{j=1}^{N_B} u_{BB,ij} \end{aligned} \tag{4.21}$$

Y podremos expresar la energía configuracional media como la suma:

$$\langle \mathfrak{U} \rangle = \langle U^{AA} \rangle + \langle U^{BB} \rangle + \langle U^{AB} \rangle \tag{4.22}$$

Para la deducción haremos uso de la función de distribución de n-partículas $\rho^{(n)}$, que nos da la probabilidad de encontrar n partículas en las posiciones $\mathbf{r}_1, \mathbf{r}_2, \ldots, \mathbf{r}_n$ independientemente de las $N-n$ partículas restantes

$$\rho^{(n)}(\mathbf{r}^n) = \frac{N!}{(N-n)!}\int \rho_N(\mathbf{r}^N) d\mathbf{r}_{n+1}\ldots d\mathbf{r}_N \tag{4.23}$$

donde $\rho_N(\mathbf{r}^N)$ corresponde la densidad de probabilidad definida en Eq. (2.8), siendo la condición de normalización

$$\int \rho^{(n)}(\mathbf{r}^n) d\mathbf{r}^n = \frac{N!}{(N-n)!} \tag{4.24}$$

La función $\rho^{(n)}$ nos permite para magnitudes del tipo

$$X_n(\mathbf{r}_1, \mathbf{r}_2, \ldots, \mathbf{r}_N) = \sum_{1\leq i_1<i_2<\ldots<i_n\leq N} f(\mathbf{r}_{i_1}, \mathbf{r}_{i_2}, \ldots, \mathbf{r}_{i_n}) \tag{4.25}$$

calcular sus promedios

$$\begin{aligned} \langle X_n \rangle &= \sum_{1\leq i_1<\ldots<i_n\leq N} \langle f(\mathbf{r}_{i_1}, \mathbf{r}_{i_2}, \ldots, \mathbf{r}_{i_n}) \rangle = \frac{N!}{n!(N-n)!}\langle f(\mathbf{r}_1, \mathbf{r}_2, \ldots, \mathbf{r}_n) \rangle \\ \langle X_n \rangle &= \frac{N!}{n!(N-n)!}\int f(\mathbf{r}_1, \mathbf{r}_2, \ldots, \mathbf{r}_n)\rho_N(\mathbf{r}^N) d\mathbf{r}_1\ldots d\mathbf{r}_N \end{aligned} \tag{4.26}$$

Integrando sobre las partículas $n+1$, $n+2, \ldots$,N y haciendo uso de Eq. (4.23), tenemos

$$\langle X_n \rangle = \frac{1}{n!}\int f(\mathbf{r}^n)\rho^{(n)}(\mathbf{r}^n) d\mathbf{r}^n \tag{4.27}$$

Para funciones que dependen de las coordenadas de dos partículas, como es el caso de un potencial aditivo por pares, tenemos que $n=2$ y la Eq. (4.27) se reduce a

$$\langle X_2 \rangle = \frac{1}{2}\int f(\mathbf{r}_1, \mathbf{r}_2)\rho^{(2)}(\mathbf{r}_1, \mathbf{r}_2) d\mathbf{r}_1 d\mathbf{r}_2 \tag{4.28}$$

Por otro lado, en física estadística se define la función de correlación para n partículas como

$$g_n(\mathbf{r}^n) = \frac{\rho^{(n)}(\mathbf{r}^n)}{\rho^{(1)}(\mathbf{r}_1)\dots\rho^{(1)}(\mathbf{r}_n)} \tag{4.29}$$

que para un sistema homogéneo se simplifica en $\rho^{(n)}(\mathbf{r}^n) = \rho^n g_n(\mathbf{r}^n)$, donde $\rho \equiv \rho^{(1)} = N/V$. Para $n = 2$ tenemos que $\rho^{(2)}(\mathbf{r}_1, \mathbf{r}_2) = \rho^2 g(\mathbf{r}_1, \mathbf{r}_2)$, donde $g(\mathbf{r}_1, \mathbf{r}_2) = g(\mid \mathbf{r}_1 - \mathbf{r}_2 \mid) \equiv g(r_{12})$, o simplemente $g(r)$, es la denominada función de distribución radial.

En una mezcla binaria uno debe distinguir entre diferentes tipos de moléculas al considerar la pareja de interacción. Por lo tanto, esto nos lleva a tener que definir tres funciones de distribución: $\rho^{(2)}_{AA}$, $\rho^{(2)}_{BB}$ y $\rho^{(2)}_{AB}$, que describen las correlaciones entre moléculas de las mismas especies (AA o BB) y entre moléculas de diferentes especies (AB). Con lo cual

$$\begin{aligned}
\rho^{(2)}_{AA}(\mathbf{r}_1, \mathbf{r}_2) &= \rho_A^2\, g_{AA}(\mathbf{r}_1, \mathbf{r}_2) = \frac{N_A^2}{V^2}\, g_{AA}(r_{12}) \\
\rho^{(2)}_{BB}(\mathbf{r}_1, \mathbf{r}_2) &= \rho_B^2\, g_{BB}(\mathbf{r}_1, \mathbf{r}_2) = \frac{N_B^2}{V^2}\, g_{BB}(r_{12}) \\
\rho^{(2)}_{AB}(\mathbf{r}_1, \mathbf{r}_2) &= \rho_A \rho_B\, g_{AB}(\mathbf{r}_1, \mathbf{r}_2) = \frac{N_A\, N_B}{V^2}\, g_{AB}(r_{12})
\end{aligned} \tag{4.30}$$

Teniendo en cuenta la forma de calcular el promedio expresada en la Eq. (4.28) y las expresiones de Eq. (4.30) , cada uno de los sumandos de la energía configuracional media de Eq. (4.22) toman ahora la forma

$$\begin{aligned}
\langle U^{II} \rangle &= \frac{N_I^2}{2V} \int_0^\infty 4\pi r^2 u_{II}(r) g_{II}(r) dr, \qquad I = A, B \\
\langle U^{AB} \rangle &= \frac{N_A\, N_B}{2V} \int_0^\infty 4\pi r^2 u_{AB}(r) g_{AB}(r) dr
\end{aligned} \tag{4.31}$$

Las correcciones que pretendemos calcular se darán asumiendo que para $r > r_c$ se tiene que $g_{AA} \cong g_{BB} \cong g_{AB} \cong 1$. Teniendo en cuenta las Eqs. (4.31), los diferentes sumandos de las corrección $\langle \mathfrak{U}_{tail} \rangle = \langle U^{AA}_{tail} \rangle + \langle U^{BB}_{tail} \rangle + \langle U^{AB}_{tail} \rangle$ vendrán dados, en unidades reducidas al componente A, por las siguientes expresiones

$$\langle U^{AA*}_{tail} \rangle = \frac{N_A^2}{2V^*} \int_{r_c^*}^\infty 4\pi r^{*2} u^*_{AA}(r^*) dr^* = \frac{8\pi N_A^2}{V^*} \left[\frac{1}{9 r_c^{*9}} - \frac{1}{3 r_c^{*3}} \right] \tag{4.32}$$

$$\langle U^{BB*}_{tail} \rangle = \frac{N_B^2}{2V^*} \int_{r_c^*}^\infty 4\pi r^{*2} u^*_{BB}(r^*) dr^* = \frac{8\pi N_B^2}{V^*} \frac{\epsilon_{BB}}{\epsilon_{AA}} \left(\frac{\sigma_{BB}}{\sigma_{AA}} \right)^6 \left[\frac{1}{9 r_c^{*9}} \left(\frac{\sigma_{BB}}{\sigma_{AA}} \right)^6 - \frac{1}{3 r_c^{*3}} \right] \tag{4.33}$$

$$\langle U^{AB*}_{tail} \rangle = \frac{N_A N_B}{2V^*} \int_{r_c^*}^\infty 4\pi r^{*2} u^*_{AB}(r^*) dr^* = \frac{16\pi N_A N_B}{V^*} \frac{\epsilon_{AB}}{\epsilon_{AA}} \left(\frac{\sigma_{AB}}{\sigma_{AA}} \right)^6 \left[\frac{\left(\frac{\sigma_{AB}}{\sigma_{AA}} \right)^6}{9 r_c^{*9}} - \frac{1}{3 r_c^{*3}} \right] \tag{4.34}$$

Con la adición de estas correcciones homogéneas a la energía deben de contemplarse también correcciones homogéneas a la presión, y no incluir en el código de computación la correción impulsiva a la presión dada por Eq. (4.17) ya que está contenida de manera natural. Dicho de otro modo, si cortamos el potencial y no hacemos LRC , tenemos una discontinuidad que hay que tener en cuenta al calcular la presión. Pero si cortamos el potencial y hacemos LRC, tenemos un potencial pseudocontinuo al añadir la cola, y por lo tanto, la contribución de la presión de LRC elimina la discontinuidad. Una vez demostradas las expresiones para las correcciones a la energía, la obtención de las LRC para la presión es trivial. Si partimos de la expresión dada por Eq. (4.15) para la presión macroscópica, el segundo sumando contiene el virial que denominaremos W

$$W = \frac{1}{3}\sum_{i=1}^{N-1}\sum_{j=i+1}^{N}\mathbf{r}_{ij}\cdot\mathbf{f}_{ij} = -\frac{1}{3}\sum_{i=1}^{N-1}\sum_{j=i+1}^{N} w(r_{ij}) \tag{4.35}$$

donde la función $w(r)$ es

$$w(r_{ij}) = r_{ij}\frac{du(r_{ij})}{dr_{ij}} \tag{4.36}$$

Al ser el virial W una función aditiva por pares, podemos descomponerlo de manera que su promedio será

$$\langle W\rangle = \langle W^{AA}\rangle + \langle W^{BB}\rangle + \langle W^{AB}\rangle \tag{4.37}$$

Igual que hemos hecho con la energía calcularemos estos promedios haciendo uso de la Eq. (4.28) y las expresiones de Eq. (4.30)

$$\begin{aligned}\langle W^{II}\rangle &= -\frac{1}{3}\frac{N_I^2}{2V}\int_0^\infty 4\pi r^2 w_{II}(r)g_{II}(r)dr, \qquad I = A, B\\ \langle W^{AB}\rangle &= -\frac{1}{3}\frac{N_A\,N_B}{2V}\int_0^\infty 4\pi r^2 w_{AB}(r)g_{AB}(r)dr\end{aligned} \tag{4.38}$$

Teniendo en cuenta la relación entre el virial y el potencial, dada en la Eq. (4.36), la aproximación para la función de distribución radial y trabajando en unidades reducidas del componente A, tenemos

$$\frac{\langle W_{tail}^{AA*}\rangle}{V^*} = \frac{16\pi}{3}\frac{N_A^2}{2V^{*2}}\left[\frac{2}{3}\frac{1}{r_c^{*9}} - \frac{1}{r_c^{*3}}\right] \tag{4.39}$$

$$\frac{\langle W_{tail}^{BB*}\rangle}{V^*} = \frac{16\pi}{3}\frac{N_B^2}{2V^{*2}}\frac{\epsilon_{BB}}{\epsilon_{AA}}\left(\frac{\sigma_{BB}}{\sigma_{AA}}\right)^6\left[\frac{2}{3}\left(\frac{\sigma_{BB}}{\sigma_{AA}}\right)^3\frac{1}{r_c^{*9}} - \frac{1}{r_c^{*3}}\right] \tag{4.40}$$

$$\frac{\langle W_{tail}^{AB*}\rangle}{V^*} = \frac{32\pi}{3}\frac{N_A N_B}{V^*}\frac{\epsilon_{AB}}{\epsilon_{AA}}\left(\frac{\sigma_{AB}}{\sigma_{AA}}\right)^6\left[\frac{2}{3}\left(\frac{\sigma_{AB}}{\sigma_{AA}}\right)^3\frac{1}{r_c^{*9}} - \frac{1}{r_c^{*3}}\right] \tag{4.41}$$

De manera que la corrección homogénea a la presión para la mezcla binaria vendrá dada por

$$P^{LRC-HOM} = \frac{\langle W_{tail}^{AA*}\rangle}{V^*} + \frac{\langle W_{tail}^{BB*}\rangle}{V^*} + \frac{\langle W_{tail}^{AB*}\rangle}{V^*} \tag{4.42}$$

4.1.3 Correcciones de largo alcance para sistemas inhomogéneos

En este trabajo se hacen uso de las LRC inhomogéneas propuestas por Janeček (2006) [15], y su adaptación por MacDowell y Blas (2009) [14]. Las correcciones de Janeček de largo alcance U_i^{LRC}, entre la partícula i y todas las demás que están más alejadas que $r_c^{(i)}$, se llevan a cabo bajo las siguientes condiciones de partida:

1) Es un procedimiento válido para interfases planas, de modo que la inhomogeneidad del sistema existe a lo largo de z. Ahora bien, Dentro de planos con coordenada z constante asumimos que

el sistema es homogéneo, con lo cual $\rho(\mathbf{r}) \equiv \rho(z)$. Se divide la caja de simulación en "slabs", de anchura Δz, paralelos a la interfase y se asume que $\rho(z_k)$, la densidad en el slab k (que por convenio se encuentra entre $z_k - \dfrac{\Delta z}{2}$ y $z_k + \dfrac{\Delta z}{2}$), es constante. De esta forma el término de la corrección de largo alcance dependerá unicamente de la posición z y puede expresarse como una suma de contribuciones de todos los slabs (ver Fig. 4.1):

$$U_i^{LRC}(z_i) = \sum_{k=1}^{n_s} \Delta u_{i.k}^{LRC}(z_i, z_k) \tag{4.43}$$

2) Se asume que la función de distribución radial entre partículas i y k, localizadas entre z_i y z_k, es igual a la unidad. Por lo tanto, el promedio de la energía de interacción debido al largo alcance $(r > r_c)$ se calcula con la expresión habitual

$$\Delta u_{i,k}^{LRC}(z_i, z_k) = \int_V u(r)\, \rho(z_k)\, dV \tag{4.44}$$

Bajo estas condiciones, la expresión final de la contribución de energía de largo alcance para la molécula i, obtenida por Janeček es

$$U_i^{LRC}(z_i) = \sum_{k=1}^{n_s} w(|z_i - z_k|)\, \rho(z_k)\, \Delta z \tag{4.45}$$

donde la función $w(\xi) = w(|z_i - z_k|)$ viene dada por

$$w(\xi) = \begin{cases} 4\pi\epsilon\sigma^2 \left[\dfrac{1}{5}\left(\dfrac{\sigma}{r_c}\right)^{10} - \dfrac{1}{2}\left(\dfrac{\sigma}{r_c}\right)^{4}\right] & \xi \le r_c \\[2ex] 4\pi\epsilon\sigma^2 \left[\dfrac{1}{5}\left(\dfrac{\sigma}{\xi}\right)^{10} - \dfrac{1}{2}\left(\dfrac{\sigma}{\xi}\right)^{4}\right] & \xi > r_c \end{cases} \tag{4.46}$$

En la expresión del método de Janeček se vislumbra el obstaculo computacional de obligar a calcular explícitamente el perfil de la densidad del sistema y a actualizarlo en cada movimiento Monte Carlo. Además, la implementación del método perturbativo Test-Área, para calcular la tensión superficial, implica una ambigüedad a la hora de calcular el nuevo perfil de la densidad, ya que, aunque se obliga

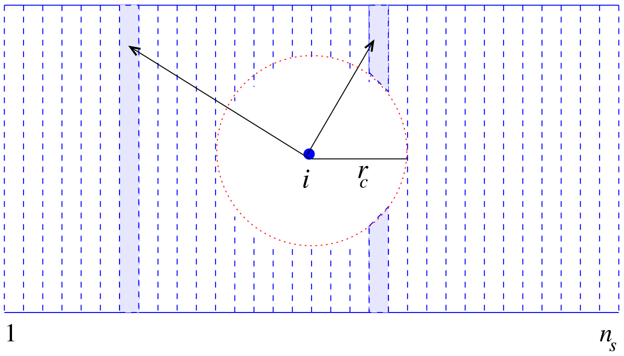

Figura 4.1: $\Delta u_{i.k}^{LRC}(z_i, z_k)$ representa la energía de interacción entre la partícula i y aquellas partículas pertenecientes al slab k y fuera del radio de corte r_c.

a que el volumen total del sistema permanezca constante, la longitud de la caja L_z varía, y por tanto, el número de slabs n_s o la anchura de los mismos, δz. Es por lo que posteriormente MacDowell y Blas (2009) [14] proponen que formalmente la Eq. (4.45) se debe escribir como

$$U_i^{LRC}(z_i) = \int_{-\infty}^{+\infty} \rho(z)\, w(|z - z_i|)\, dz \tag{4.47}$$

con $w(|z - z_i|)$ definida como en la Eq. (4.46). La energía total del sistema debido a las LRC se puede expresar fácilmente como

$$U^{LRC} = \frac{1}{2}\sum_{i=1}^{N} U_i^{LRC}(z_i) = \frac{1}{2}\sum_{i=1}^{N} \int_{-\infty}^{+\infty} \rho(z)\, w(|z - z_i|)\, \rho(z)\, dz \tag{4.48}$$

donde el factor $1/2$ se introduce para no calcular doblemente los pares de interacciones. Con respecto a la expresión de Janeček supone hacer un tratamiento de modo continuo, y además no limitarnos a calcular la interacción de largo alcance para $r > r_c$ dentro de la caja de simulación, sino extender la interacción para $z \to \pm\infty$. MacDowell y Blas proponen hacer uso de la definición formal de la densidad $\rho(z)$ instantánea en términos de la función δ de Dirac, de modo que

$$\rho(z) = C \sum_{j=1}^{N} \delta(z - z_j) \tag{4.49}$$

donde C es una constante de normalización. Teniendo en cuenta que $\int d\mathbf{r}\, \rho(z) = N$, y usando la simetría de problema, podemos escribir

$$\rho(z) = \frac{1}{A} \sum_{j=1}^{N} \delta(z - z_j) \tag{4.50}$$

donde A es el área interfacial en el plano $x - y$, y z_j es la coordenada z de la molécula j.

Dado que en este trabajo se utilizan las LRC inhomogéneas en sistemas Lennard Jones binarios expandimos la Eq.4.48, de forma que en la suma sobre las N moléculas del sistema distinguimos, mediante los índices $\alpha = A, B$ y $\beta = A, B$, los dos tipos de moléculas de un sistema con N_A moléculas tipo A y N_B moléculas tipo B

$$U^{LRC} = \frac{1}{2}\sum_{\alpha}\sum_{i=1}^{N_\alpha} U_i^{LRC}(z_i) = \frac{1}{2}\sum_{\alpha}\sum_{i=1}^{N_\alpha}\sum_{\beta} \int_{-\infty}^{+\infty} \rho_\beta(z)\, w(|z - z_i^\alpha|)\, dz \tag{4.51}$$

Ahora incorporamos a la ecuación anterior la definición de la densidad dada por la Eq. 4.50, de forma que

$$U^{LRC} = \frac{1}{2}\sum_{\alpha}\sum_{i=1}^{N_\alpha}\sum_{\beta} \int_{-\infty}^{+\infty} \frac{1}{A}\sum_{j=1}^{N_\beta} \delta(z - z_j^\beta)\, w(|z - z_i^\alpha|)\, dz = \frac{1}{2A}\sum_{i=1}^{N}\sum_{j=1}^{N} w(|z_i^\alpha - z_j^\beta|) \tag{4.52}$$

Reescribimos el sumatorio sobre los índices i y j en una suma de pares y un autotérmino, de manera que la expresión anterior queda

$$U^{LRC} = \frac{1}{A}\sum_{i=1}^{N-1}\sum_{j=i+1}^{N} w(|z_i^\alpha - z_j^\beta|) + \frac{1}{2A}\sum_{i=1}^{N} w(0) \tag{4.53}$$

siendo $w(0) = w(|z_i^\alpha - z_i^\alpha|)$ y pudiendose también escribir el autotérmino como

$$\frac{1}{2A}\sum_{i=1}^{N} w(0) = \frac{1}{2A}\sum_{\alpha}\sum_{i=1}^{N_\alpha} w_{\alpha\alpha}(0) = \frac{1}{2A}\sum_{i=1}^{N_A} w_{AA}(0) + \frac{1}{2A}\sum_{i=1}^{N_B} w_{BB}(0) \tag{4.54}$$

Escribir las LRC según la Eq.4.53 supone claras ventajas, ya que como comentan MacDowell y Blas (2009) [14] se trata de una expresión exacta que no precisa de discretización, y corresponde a la suma de una especie de potencial efectivo aditivo por pares que es evaluado dentro de la condición de mínima imagen a lo largo del eje z. Además es una expresión fácil de implementar en un código MC, ya que no es preciso calcular instantáneamente el perfil de la densidad. Aunque comentan los autores que en un escenario donde se usa $r_c = 3\sigma$ más LRC se obtienen tiempos de computación similares a un $r_c = 4\sigma$. Así que esta implementación es una alternativa viable siempre y cuando el tiempo de CPU no sea una cuestión crítica.

4.2 El potencial de square-well

El potencial de interacción entre dos moléculas SW de especies i y j a una distancia r está dado por

$$u_{ij}^{SW}(r) = \begin{cases} +\infty & r < \sigma_{ij} \\ -\epsilon_{ij} & \sigma_{ij} < r < \lambda_{ij}\sigma_{ij} \\ 0 & r > \lambda_{ij}\sigma_{ij} \end{cases} \tag{4.55}$$

donde ϵ_{ij} es la profundidad de pozo y λ_{ij} es el parámetro que fija rango de la interacción o anchura del pozo ($\lambda_{ij} = 1.5\sigma_{ij}$ en nuestro trabajo). El diámetro de esfera dura σ_{ij} y la energía de interación ϵ_{ij} entre moléculas i y j, están dados por las Eq. (4.5) y (4.6) respectivamente, y la anchura del pozo por

$$\lambda_{ij} = \frac{\sigma_{ii}\lambda_{ii} + \sigma_{jj}\lambda_{jj}}{\sigma_{ii} + \sigma_{jj}} \tag{4.56}$$

Para este potencial, el radio de corte de viene dado por $\lambda_{ij}\sigma_{ij}$, de manera que el número de moléculas N_{ji} a una distancia entre r y $r + dr$ de una molécula central i está relacionado con la función de distribución radial $dN_{ji} = 4\pi\rho_j\, g_{ji}(r)r^2dr$.

A diferencia del potencial de LJ, en el potencial de SW no tenemos que truncar interacciones ni aplicar correcciones de largo alcance, pero un potencial discontinuo no está exento de problemas y es un potencial que debe ser tratado con especial cautela. A la complejidad que ya de hecho presentan las discontinuidades a nivel computacional, se le añade la asimetría del potencial ante compresiones y expansiones de volumen con importantes implicaciones en el cálculo de la presión [50, 51]. Por ejemplo, si nos fijamos en la parte de esfera dura del potencial SW en $r = \sigma_{ij}$, cuando el sistema es comprimido, uno puede muestrear la contribución configuracional de la presión, pero cuando el sistema se expande solamente podemos obtener la contribución ideal.

4.2.1 Determinación del virial en el potencial SW

El problema inmediato que se plantea es el cálculo del promedio sobre el ensemble correspondiente del término del virial W dado en la Eq. (4.35), ya que ahora el cálculo de $w(r_{ij}) = r_{ij}(du(r_{ij})/dr_{ij})$

implica que debemos evaluar la derivada en $r_{ij} = \sigma_{ij}$ y $r_{ij} = \lambda_{ij}\sigma_{ij}$, donde el potencial de interacción es discontinuo. En este cálculo es más efectivo partir del uso de la función

$$e^{-\beta u(r_{ij})} = \begin{cases} 0 & r_{ij} < \sigma_{ij} \\ e^{\beta\epsilon_{ij}} & \sigma_{ij} < r_{ij} < \lambda_{ij}\sigma_{ij} \\ +1 & r_{ij} > \lambda_{ij}\sigma_{ij} \end{cases} \tag{4.57}$$

la cual puede expresarse en términos de funciones salto de Heaviside de la siguiente forma

$$e^{-\beta u(r_{ij})} = \Theta(r_{ij} - \sigma_{ij})\, e^{\beta\epsilon_{ij}} - \Theta(r_{ij} - \lambda_{ij}\sigma_{ij})\, e^{\beta\epsilon_{ij}} + \Theta(r_{ij} - \lambda_{ij}\sigma_{ij}) \tag{4.58}$$

ya que si tenemos en cuenta que

$$\frac{d}{dr}\left(e^{-\beta u(r_{ij})}\right) = -\beta\, e^{-\beta u(r_{ij})}\frac{du(r_{ij})}{dr_{ij}} \tag{4.59}$$

tendremos que

$$e^{-\beta u(r_{ij})}\frac{du(r_{ij})}{dr_{ij}} = -k_B T\left[e^{\beta\epsilon_{ij}}\,\frac{d\Theta(r_{ij}-\sigma_{ij})}{dr_{ij}} - e^{\beta\epsilon_{ij}}\,\frac{d\Theta(r_{ij}-\lambda_{ij}\sigma_{ij})}{dr_{ij}} + \frac{d\Theta(r_{ij}-\lambda_{ij}\sigma_{ij})}{dr_{ij}}\right] \tag{4.60}$$

Como la derivada de la función de Heaviside no es más que la función δ-Dirac, la ecuación anterior puede expresarse como

$$e^{-\beta u(r_{ij})}\frac{du(r_{ij})}{dr_{ij}} = -k_B T\left[e^{\beta\epsilon_{ij}}\,\delta(r_{ij}-\sigma_{ij}) - \left(e^{\beta\epsilon_{ij}} - 1\right)\,\delta(r_{ij}-\lambda_{ij}\sigma_{ij})\right] \tag{4.61}$$

de forma que obtenemos así una expresión sencilla que como veremos a continuación nos va a permitir evaluar la derivada $du(r_{ij})/dr_{ij}$ en las dos discontinuidades del potencial SW [60]. Transportando este resultado a la expresión para el virial tendremos que

$$\begin{aligned}\langle W\rangle &= \frac{1}{3}\left\langle \sum_{i=1}^{N-1}\sum_{j=i+1}^{N} r_{ij}\left(-\frac{du(r_{ij})}{dr_{ij}}\right)\right\rangle = \\ &= \frac{k_BT}{3}\left\langle \sum_{i=1}^{N-1}\sum_{j=i+1}^{N} r_{ij}e^{\beta u(r_{ij})}\left\{e^{\beta\epsilon_{ij}}\,\delta(r_{ij}-\sigma_{ij}) - \left(e^{\beta\epsilon_{ij}}-1\right)\,\delta(r_{ij}-\lambda_{ij}\sigma_{ij})\right\}\right\rangle = \\ &= \frac{k_BT}{3}\left\langle \sum_{i=1}^{N-1}\sum_{j=i+1}^{N} r_{ij}e^{\beta u(r_{ij})}e^{\beta\epsilon_{ij}}\,\delta(r_{ij}-\sigma_{ij}) + \sum_{i=1}^{N-1}\sum_{j=i+1}^{N} r_{ij}e^{\beta u(r_{ij})}\left(1-e^{\beta\epsilon_{ij}}\right)\,\delta(r_{ij}-\lambda_{ij}\sigma_{ij})\right\rangle\end{aligned} \tag{4.62}$$

Obtenemos así una expresión de tipo formal en términos de funciones δ-Dirac, aunque tal y como ya vimos en el apartado 4.1.1 la presencia de estas funciones no es cómoda. Desde el punto de vista computacional debemos obtener las contribuciones impulsivas debido a $r_{ij}\delta(r_{ij}-\sigma_{ij})$ y $r_{ij}\delta(r_{ij}-\lambda_{ij}\sigma_{ij})$. En el caso de $r_{ij}\delta(r_{ij}-\sigma_{ij})$ la derivada solo está definida para $r_{ij} = {\sigma_{ij}}^{+}$ (por la derecha), ya que desde el punto de vista de la mecánica estadística, y obviamente desde la simulación MC, no tiene sentido físico la situación en que la distancia intermolecular de dos esferas duras sea $r_{ij} < \sigma_{ij}$, ya que se encuentran solapando y por tanto no existe la derivada en $r_{ij} = {\sigma_{ij}}^{-}$. Sin embargo si podemos definir la derivada del potencial en $r_{ij} = (\lambda_{ij}\sigma_{ij})^{-}$ y en $r_{ij} = (\lambda_{ij}\sigma_{ij})^{+}$. Con estas consideraciones es posible vislumbrar que en la evaluación de la expresión dada por la Eq. (4.62) van a aparecer tres contribuciones, de forma que

$$\langle W\rangle = \langle W^{\sigma^+}\rangle + \langle W^{(\lambda\sigma)^-}\rangle + \langle W^{(\lambda\sigma)^+}\rangle \tag{4.63}$$

Si queremos evaluar la Eq. (4.62) en la primera discontinuidad tenemos que aproximarnos de manera que $r_{ij} = {\sigma_{ij}}^{+}$ y tendremos, a falta de evaluar la δ-Dirac, que

$$\left\langle \sum_{i=1}^{N-1} \sum_{j=i+1}^{N} r_{ij} e^{\beta u(r_{ij})} e^{\beta \epsilon_{ij}}\, \delta(r_{ij} - \sigma_{ij}) \right\rangle = \left\langle \sum_{i=1}^{N-1} \sum_{j=i+1}^{N} r_{ij}\, \delta(r_{ij} - \sigma_{ij}) \right\rangle \tag{4.64}$$

Si ahora hacemos uso de la definición de la función δ-Dirac en términos de la derivada de la función de Heaviside [49,50] (ver Eq. (4.16)), tenemos que si r_{ij} es tal que $\sigma_{ij} < r_{ij} < \sigma_{ij} + \Delta r_{ij}$ con $\Delta r_{ij} \to 0^{+}$

$$\delta(r_{ij} - \sigma_{ij}) \approx \frac{1}{\Delta r_{ij}} \tag{4.65}$$

Si $\Delta r_{ij} \to 0^{+}$ entonces $r_{ij} \to \sigma_{ij}^{+}$, y podemos hacer la aproximación

$$\left\langle \sum_{i=1}^{N-1} \sum_{j=i+1}^{N} r_{ij}\, \delta(r_{ij} - \sigma_{ij}) \right\rangle \approx \left\langle \sum_{i=1}^{N-1} \sum_{j=i+1}^{N} r_{ij} \frac{1}{\Delta r_{ij}} \right\rangle \approx \frac{\sigma_{ij}}{\Delta r_{ij}} \left\langle \sum_{i=1}^{N-1} \sum_{j=i+1}^{N} 1 \right\rangle \tag{4.66}$$

donde $\left\langle \sum_{i=1}^{N-1} \sum_{j=i+1}^{N} 1 \right\rangle$ representa el promedio, sobre el ensemble correspondiente, del número de pares de moléculas que se encuentran separadas una distancia entre σ_{ij} y $\sigma_{ij} + \Delta r_{ij}$ con $\Delta r_{ij} \to 0^{+}$ y que denotaremos como $\langle n(\sigma^{+}) \rangle$, y obtendremos la contribución

$$\langle W^{\sigma^{+}} \rangle = \frac{K_B T}{3} \frac{\langle n(\sigma^{+}) \rangle}{\frac{\Delta r_{ij}}{\sigma_{ij}}} \tag{4.67}$$

Este mismo procedimiento lo seguimos para evaluar la Eq. (4.62) en la segunda discontinuidad, pero ahora tendremos dos situaciones posibles según nos aproximemos por la izquierda en $r_{ij} = (\lambda_{ij}\sigma_{ij})^{-}$ o por la derecha en $r_{ij} = (\lambda_{ij}\sigma_{ij})^{+}$. Para ver más claramente dichas situaciones expandimos el segundo sumatorio en la forma

$$\begin{aligned} &\left\langle \sum_{i=1}^{N-1} \sum_{j=i+1}^{N} r_{ij} e^{\beta u(r_{ij})} (1 - e^{\beta \epsilon_{ij}})\, \delta(r_{ij} - \lambda_{ij}\sigma_{ij}) \right\rangle = \\ = &\left\langle \sum_{i=1}^{N-1} \sum_{j=i+1}^{N} r_{ij} e^{\beta u(r_{ij})}\, \delta(r_{ij} - \lambda_{ij}\sigma_{ij}) \right\rangle - \left\langle \sum_{i=1}^{N-1} \sum_{j=i+1}^{N} r_{ij} e^{\beta u(r_{ij})} e^{\beta \epsilon_{ij}}\, \delta(r_{ij} - \lambda_{ij}\sigma_{ij}) \right\rangle \end{aligned} \tag{4.68}$$

Si observamos la procedencia del término $(1 - e^{\beta \epsilon_{ij}})$, recordando la Eq. (4.57), podemos decir que es igual que $(e^{-\beta u(\lambda_{ij}\sigma_{ij})^{+})} - e^{-\beta u(\lambda_{ij}\sigma_{ij})^{-})})$ [61]. Esta matización resulta importante ya que, por ejemplo, al acercarnos a la discontinuidad por la derecha real realmente en la expresión formal de la Eq. (4.68) solamente el primer término es evaluable, y de igual forma el segundo término será el implicado a la hora de acercarnos a la discontinuidad por la izquierda. Por tanto, si nos acercamos a la discontinuidad por la derecha nos quedaremos con el primer término de la Eq. (4.68) y tendremos en cuenta que $e^{\beta u(r_{ij})} = 1$, por lo que siguiendo el mismo procedimiento que para obtener Eq. (4.66) resulta

$$\left\langle \sum_{i=1}^{N-1} \sum_{j=i+1}^{N} r_{ij} e^{\beta u(r_{ij})}\, \delta(r_{ij} - \lambda_{ij}\sigma_{ij}) \right\rangle \approx \frac{\lambda_{ij}\sigma_{ij}}{\Delta r_{ij}} \left\langle \sum_{i=1}^{N-1} \sum_{j=i+1}^{N} 1 \right\rangle = \lambda_{ij} \frac{\langle n(\lambda\sigma^{+}) \rangle}{\frac{\Delta r_{ij}}{\sigma_{ij}}} \tag{4.69}$$

donde ahora $\left\langle \sum_{i=1}^{N-1}\sum_{j=i+1}^{N} 1\right\rangle$ representa el promedio, sobre el ensemble correspondiente, del número de pares de moléculas que se encuentran separadas una distancia entre $\lambda_{ij}\sigma_{ij}$ y $\lambda_{ij}\sigma_{ij}+\Delta r_{ij}$ con $\Delta r_{ij}\to 0^+$ y que hemos denotado como $\left\langle n(\lambda\sigma^+)\right\rangle$, permitiéndonos el resultado de la Eq. (4.69) obtener la contribución $\langle W^{(\lambda\sigma)^+}\rangle$ en la Eq. (4.63). Para evaluar la discontinuidad por la izquierda de nuevo seguimos un procedimiento idéntico, teniendo en cuenta que $e^{\beta u(r_{ij})}=e^{-\beta\epsilon_{ij}}$ en el segundo sumando de la Eq. (4.68). Además, como $\Delta r_{ij}\to 0^-$ cuando evaluemos la δ-Dirac $\Delta r_{ij}<0$ y por tanto

$$\left\langle \sum_{i=1}^{N-1}\sum_{j=i+1}^{N} r_{ij}\delta(r_{ij}-\lambda_{ij}\sigma_{ij})\right\rangle \approx \left\langle \sum_{i=1}^{N-1}\sum_{j=i+1}^{N} r_{ij}\frac{\Theta(r_{ij}-\lambda_{ij}\sigma_{ij})-\Theta(r_{ij}-[\lambda_{ij}\sigma_{ij}-|\Delta r_{ij}|])}{-|\Delta r_{ij}|}\right\rangle$$
$$\approx \left\langle \sum_{i=1}^{N-1}\sum_{j=i+1}^{N} r_{ij}\frac{-1}{-|\Delta r_{ij}|}\right\rangle \approx \frac{\lambda_{ij}\sigma_{ij}}{|\Delta r_{ij}|}\left\langle \sum_{i=1}^{N-1}\sum_{j=i+1}^{N} 1\right\rangle = \lambda_{ij}\frac{\left\langle n(\lambda\sigma^-)\right\rangle}{\frac{|\Delta r_{ij}|}{\sigma_{ij}}} \tag{4.70}$$

Si incorporamos los resultados de las Eqs. (4.66), (4.69) y (4.70) en la Eq. (4.63) y tenemos en cuenta Eq. (4.15) obtenemos una expresión para la presión macroscópica en un sistema SW

$$P=\left\langle \rho k_B T\right\rangle+\frac{K_BT}{3V}\left[\frac{\left\langle n(\sigma^+)\right\rangle}{\frac{|\Delta r_{ij}|}{\sigma_{ij}}}+\lambda_{ij}\frac{\left\langle n(\lambda\sigma^+)\right\rangle}{\frac{|\Delta r_{ij}|}{\sigma_{ij}}}-\lambda_{ij}\frac{\left\langle n(\lambda\sigma^-)\right\rangle}{\frac{|\Delta r_{ij}|}{\sigma_{ij}}}\right] \tag{4.71}$$

4.2.2 Determinación de la presión de un sistema homogeneo SW mediante escalamiento isotrópico

Finalmente nos encontramos con el problema computacional de calcular los promedios de pares de moléculas $\left\langle n(\sigma^+)\right\rangle$, $\left\langle n(\lambda\sigma^+)\right\rangle$ y $\left\langle n(\lambda\sigma^-)\right\rangle$ en los cocientes incrementales con $|\Delta r_{ij}|\to 0$ de la Eq. (4.71). A continuación se presenta una esquema basado en el cálculo de pares de solapamientos que ocurren en el sistema cuando llevamos a cabo cambios isotrópicos de coordenadas de las moléculas [50, 51] y cuya comprensión nos servirá para abordar de forma sencilla la metodología empleada para el cálculo de las componentes del tensor de presiones para un potencial discontinuo SW en el apartado 5.3.2.

Por ejemplo, evaluar $\left\langle n(\lambda\sigma^+)\right\rangle$ es calcular el número medio de pares de moléculas que se encuentran separadas una distancia r_{ij} de tal manera que $\lambda_{ij}\sigma_{ij}<r_{ij}<\lambda_{ij}\sigma_{ij}+\Delta r_{ij}$, y que es igual al número de pares de moléculas que se solapan cuando se hace una disminución isotrópica de volumen con un cambio $\xi_1=-|\Delta V|/V$, escogiendo un valor de ξ_1 de modo que si las distancias antes del solapamiento son $r_{ij}=\lambda_{ij}\sigma_{ij}+\Delta r_{ij}$, después sean $r_{ij}{}'=\lambda_{ij}\sigma_{ij}$. Por tanto, esta disminución de volumen de V a $V'=V-|\Delta V|$ equivale a una transformación de escalamiento de la distancia relativa entre pares de moléculas según

$$r_{ij}{}'=(1-|\xi_1|)^{1/3}r_{ij} \tag{4.72}$$

y relación entre Δr_{ij} y ξ_1 viene dada por

$$\frac{\Delta r_{ij}}{\lambda_{ij}\sigma_{ij}}=\frac{1}{(1-|\xi_1|)^{1/3}}-1 \tag{4.73}$$

Puesto que $|\xi_1| \ll 1$ tenemos que $(1-|\xi_1|)^{-1/3} \simeq 1 + 1/3\,|\xi_1|$, y por tanto la relación entre Δr_{ij} y ξ_1 puede aproximarse por

$$\frac{\Delta r_{ij}}{\sigma_{ij}} = \frac{\lambda_{ij}}{3}|\xi_1| \tag{4.74}$$

Si denominamos $P_{\lambda\sigma^+}$ a la componente de la presión macroscópica, debido a la contribución impulsiva en $r_{ij} = \lambda_{ij}{\sigma_{ij}}^+$, podemos evaluarla haciendo uso de la relación dada en la Eq. (4.74), según

$$P_{\lambda\sigma^+} = \lim_{\Delta r_{ij}\to 0} \frac{K_B T}{3V} \lambda_{ij} \frac{\langle n(\lambda\sigma^+)\rangle}{\frac{|\Delta r_{ij}|}{\sigma_{ij}}} = \lim_{\xi_1 \to 0} \frac{K_B T}{V} \frac{n(\xi_1)}{|\xi_1|} \tag{4.75}$$

donde $n(\xi_1)$ representa el número de pares de moléculas que solapan.

Pero, ¿qué ventaja nos ofrece el hacer el escalamiento isotrópico?. La respuesta es que básicamente el método implica un escaso esfuerzo computacional. Si trabajamos en unidades reducidas la transformación de escalamiento dada por la Eq. (4.72) se expresa como ${r_{ij}}'^{*} = (1-|\xi_1|)^{1/3} r^*_{ij}$, y existirá solapamiento si se se cumple la condición necesaria ${r_{ij}}^* < \lambda_{ij}$. Entonces, si denominamos $\mathsf{FACTOR}_{\lambda\sigma^+} = \lambda_{ij}(1-|\xi_1|)^{-1/3}$, conocer si se produce solapamiento se limita a chequear la condición necesaria y suficiente $\lambda_{ij} < {r_{ij}}^* < \mathsf{FACTOR}_{\lambda\sigma^+}$. Podemos definir en lugar de un único $\mathsf{FACTOR}_{\lambda\sigma^+}$ un conjunto de n_k factores seleccionando $\xi_1(n_k)$ valores de escalamiento de $|\xi_1|$, para de este modo calcular realmente el límite $|\xi_1| \to 0$ en la simulación.

Pero, dado que en el código de computación se calcula el cuadrado de la distancia entre pares de partículas $rr = {r_{ij}}^{*2} = x^*_{ij}y^*_{ij} + y^*_{ij}x^*_{ij} + z^*_{ij}z^*_{ij}$ conviene definir

$$\mathsf{FACTOR2(n_k)}_{\lambda\sigma^+} = \mathsf{FACTOR}(n_k)_{\lambda\sigma^+} \times \mathsf{FACTOR}(n_k)_{\lambda\sigma^+} \tag{4.76}$$

de manera que dos moléculas, i y j, separadas una distancia al cuadrado rr (variable de código) solaparán ante un cambio $\xi_1(n_k)$ si

$${\lambda_{ij}}^2 < rr < \mathsf{FACTOR2(n_k)}_{\lambda\sigma^+} \tag{4.77}$$

Con el mismo esquema actuaríamos en la discontinuidad en $r_{ij} = {\sigma_{ij}}^+$, de manera que la contribución a la presión, que denominaremos P_{σ^+} , podemos calcularla haciendo

$$P_{\sigma^+} = \lim_{\Delta r_{ij}\to 0} \frac{K_B T}{3V} \frac{\langle n(\sigma^+)\rangle}{\frac{|\Delta r_{ij}|}{\sigma_{ij}}} = \lim_{\xi_2 \to 0} \frac{K_B T}{V} \frac{n(\xi_2)}{|\xi_2|} \tag{4.78}$$

Ahora ante un escalamiento ${r_{ij}}'^{*} = (1-|\xi_2|)^{1/3} r^*_{ij}$ existe solapamiento si ${r_{ij}}^* < 1$, y si denominamos $\mathsf{FACTOR2(n_k)}_{\sigma^+} = (1-|\xi_2(n_k)|)^{-2/3}$ computacionalmente equivale a chequear

$$rr < \mathsf{FACTOR2(n_k)}_{\sigma^+} \tag{4.79}$$

Para el caso de la discontinuidad en $r_{ij} = (\lambda_{ij}\sigma_{ij})^-$ el esquema cambia ligeramente ya que la evaluamos mediante la expansión isotrópica ${r_{ij}}'^{*} = (1+|\xi_3|)^{1/3} r^*_{ij}$, de manera que realmente la contribución de $\langle n(\lambda\sigma^-)\rangle$ a la presión, $P_{\lambda\sigma^-}$, viene a representar el número medio de moléculas que estaban solapadas y abandonan la discontinuidad. Computacionalmente equivale a chequear

$$\mathsf{FACTOR2(n_k)}_{\lambda\sigma^-} < rr < {\lambda_{ij}}^2 \tag{4.80}$$

donde $\mathsf{FACTOR2(n_k)}_{\lambda\sigma^-} = \lambda_{ij}(1+|\xi_3(n_k)|)^{-2/3}$

Por último comentar que a nivel de programación de código se puede utilizar un único conjunto de valores de ξ, ya que podemos relacionar $\xi_1(n_k)$, $\xi_2(n_k)$ y $\xi_3(n_k)$ mediante $\Delta r_{ij}/\sigma_{ij}$ de manera que

$$\xi_1(n_k) = \xi_3(n_k) = \frac{\xi_2(n_k)}{\lambda_{ij}} \tag{4.81}$$

Capítulo 5

Método para la determinación de las componentes del tensor de presiones y de la tensión superficial mediante el virial

Los métodos más usados para determinar las componentes del tensor de presiones y la tensión superficial se basan en las definiciones mecánicas y en el correspondiente uso del virial. La definición de Irving-Kirkwood (IK) [62], el método de Harasima [63], la definición de Kirkwood-Buff [64] o su versión local KBZ [65] son métodos muy extendidos cuya diferencia resulta de la concreción de la ambigüedad a la hora de definir las componentes del tensor de presiones. Esta ambigüedad ha sido ampliamente discutida en la literatura [62, 66–68] y básicamente reside en la arbitrariedad a la hora de decidir qué fuerzas intermoleculares contribuyen al tensor a través de un determinado elemento de área $d\mathcal{A}$.

Kirkwood and Buff [64] introducen en 1949 una definición mecánico-estadística de la tensión superficial donde se establece que la tensión superficial puede ser determinada por la diferencia entre la presión normal y la presión tangencial a la interfase (método KB). La definición del método KB sienta los fundamentos para la posterior y ampliamente utilizada aproximación mecánica para el cálculo de la tensión superficial. Un año después, Irving and Kirkwood [62] proponen otro método para calcular la tensión superficial, el cual está basado en el cálculo del perfil local de las componentes normal y tangencial a la interfase del tensor de presiones (método IK). La mayor ventaja del método IK es que solamente en la región interfacial la diferencia entre las componentes de la presión normal y de la presión tangencial es distinta de cero, mientras que la diferencia es cero en las zonas de bulk de líquido y de vapor. Para la definición que implica el perfil de la presión local, aparece una controversia después de que Harasima [63] introdujera una definición diferente (método H) en 1958. La mayor diferencia entre las definiciones de IK y H reside en la expresión de la componente tangencial de la presión en la interfase. Sin embargo, ambas definiciones conducen a la misma expresión para la tensión superficial cuando integramos sobre la dirección normal a la interfase. Ambos métodos IK y H han sido utilizados para calcular la tensión superficial, siendo el método IK utilizado principalmente en sistemas con interacciones descritas mediante potenciales aditivos por pares, mientras que el método H ha sido utilizado en sistemas con interacciones no aditivas por pares como por ejemplo en sumas de Ewald [69, 70].

En este capítulo se aborda la metodología seguida basada en la elección de la definición de Irving-Kirkwood (IK) para el cálculo de las componentes microscópicas del tensor de presiones para un sistema inhomogeneo de interfases planas en el ensamble NVT, aunque previamente en los apartados 5.1 y 5.2 se abordan las definiciones mecánicas y conceptos básicos relativos a las componentes del tensor de presiones y la tensión superficial. El mayor problema con la ruta mecánica se nos presenta con sistemas que interactúan a través de potenciales discontinuos de tal manera que la derivada del potencial en el punto de la discontinuidad es también discontinua y viene representada por una delta de Dirac. La estimación de estas deltas de Dirac será necesaria para evaluar las componentes microscópicas del tensor de presiones. Esto implica que tendremos que ser especialmente cuidadosos en el manejo de las relaciones mecánicas en sistemas que interactúan en condiciones de potenciales de LJ truncados o de potenciales de square-well (SW). Por tanto, dedicaremos también el capítulo a revisar los principales detalles del cálculo computacional del tensor microscópico de presiones para el potencial de SW, para el cual el problema es especialmente delicado debido a la discontinuidades presentadas en el punto de esfera dura y en el límite de la zona atractiva, y las expresiones mecánicas que están escritas en términos de derivadas de los potenciales de pares deben de reformularse para dar cabida a la presencia de fuerzas impulsivas en las zonas de discontinuidad.

5.1 Definición mecánica de las componentes del tensor de presiones

El tensor de presiones $\hat{\mathbb{P}}(\mathbf{r})$ es un objeto matemático que representa las fuerzas que el resto de un medio continuo (en nuestro caso un fluido) ejerce sobre un elemento diferencial de área dado del fluido en un punto espacial $\mathbf{r}$. En un fluido homogéneo e isótropo $\hat{\mathbb{P}}(\mathbf{r}) = P\hat{\mathbb{I}}$, donde $\hat{\mathbb{I}} = \hat{\mathbf{e}}_x \otimes \hat{\mathbf{e}}_x + \hat{\mathbf{e}}_y \otimes \hat{\mathbf{e}}_y + \hat{\mathbf{e}}_z \otimes \hat{\mathbf{e}}_z = \hat{\mathbf{e}}_x\hat{\mathbf{e}}_x + \hat{\mathbf{e}}_y\hat{\mathbf{e}}_y + \hat{\mathbf{e}}_z\hat{\mathbf{e}}_z$ es el tensor unidad [1], donde $\{\hat{\mathbf{e}}_x, \hat{\mathbf{e}}_y, \hat{\mathbf{e}}_z\}$ son un conjunto de vectores unitarios ortogonales. Es decir, el tensor de presiones es constante en todo el sistema y sus elementos iguales, $P = P_{xx} = P_{yy} = P_{zz}$. La presión escalar viene entonces dada por la traza

$$P = \frac{1}{3}Tr(\hat{\mathbb{P}}) = \frac{1}{3}(P_{xx} + P_{yy} + P_{zz}) \tag{5.1}$$

Un sistema inhomogeneo no es isótropo y en este caso el tensor de presiones es un tensor simétrico que en coordenadas cartesianas puede expresarse como

$$\hat{\mathbb{P}} = \sum_{\alpha}\sum_{\beta} P_{\alpha\beta}\hat{\mathbf{e}}_\alpha\hat{\mathbf{e}}_\beta \quad \alpha, \beta = x, y, z \tag{5.2}$$

donde $P_{\alpha\beta}$ son las componentes del tensor $\hat{\mathbb{P}}$. En el caso especial de un fluido homogéneo e isótropo $P_{\alpha\alpha} = P$ y $P_{\alpha\beta} = 0$ para $\alpha \neq \beta$. La fuerza $d\vec{F}(\mathbf{r})$ que el resto del fluido ejerce sobre la diferencial de área dS, localizada en el punto espacial $\mathbf{r}$, es

$$\vec{F}(\mathbf{r}) = -\hat{\mathbb{P}}(\mathbf{r}) \cdot \hat{n}(\mathbf{r})dS \tag{5.3}$$

donde $\hat{n}(\mathbf{r})$ es un vector unitario normal al diferencial de superficie en $\mathbf{r}$.

Imaginemos ahora una capa de líquido la cual es perpendicular al eje z en su superficie plana y en contacto con su vapor en equilibrio. En este sistema inhomogeneo el tensor de presiones depende de la posición $\hat{\mathbb{P}} = \hat{\mathbb{P}}(\mathbf{r})$. La situación de equilibrio requiere de la condición de estabilidad mecánica [5,71]

$$\nabla \cdot \hat{\mathbb{P}} = 0 \tag{5.4}$$

---

[1] El producto diádico ha sido sustituido por la notación sin punto, más simplificada, de tal manera que $\hat{A} \otimes \hat{B} = \hat{A}\hat{B}$.

en el entorno de la interfase plana. Por otro lado la simetría de la superficie requiere que $\hat{\mathbb{P}}$ sea un tensor diagonal

$$\hat{\mathbb{P}}(\mathbf{r}) = P_{xx}(\mathbf{r})\hat{\mathbf{e}}_x\hat{\mathbf{e}}_x + P_{yy}(\mathbf{r})\hat{\mathbf{e}}_y\hat{\mathbf{e}}_y + P_{zz}(\mathbf{r})\hat{\mathbf{e}}_z\hat{\mathbf{e}}_z \tag{5.5}$$

con $P_{xx}(\mathbf{r}) = P_{yy}(\mathbf{r}) \neq P_{zz}(\mathbf{r})$. Si sustituimos Eq. (5.5) en (5.4) se demuestra que P_{xx} y P_{yy} son funciones de z, y P_{zz} es constante:

$$P_{xx}(z) = P_{yy}(z) = P_T(z) \qquad P_{zz}(z) = P_N(z) = P \tag{5.6}$$

De forma que en una interfase plana distinguimos solamente dos componentes del tensor de presiones, una componente normal P_N y una componente tangencial P_T, donde P_N es constante a igual a la presión de vapor de equilibrio P del sistema, y P_T solamente puede ser una función de z. En coordenadas cartesianas el tensor de presiones puede entonces expresarse como

$$\hat{\mathbb{P}}(z) = P_T(z)(\hat{\mathbf{e}}_x\hat{\mathbf{e}}_x + \hat{\mathbf{e}}_y\hat{\mathbf{e}}_y) + P_N(z)\hat{\mathbf{e}}_z\hat{\mathbf{e}}_z \tag{5.7}$$

Puesto que $\hat{\mathbb{P}} = P\hat{\mathbb{I}}$ en las fases de bulk o cerca de la interfase, se deduce que $P_T = P_N$ cuando $z \gg d$, donde d es la anchura de la zona interfacial [71]. Por las condiciones de simetría establecidas (equilibrio hidrostático, interfase plana, simetría e isotropía transversal del tensor) uno solamente puede concluir que la presión tangencial depende únicamente de la posición con respecto a la zona interfacial [5,71].

Como hemos visto, el tensor de presiones es una función que varía de un punto a otro en un fluido. Éste puede calcularse como un promedio en el ensamble en la posición $\mathbf{r}$ [62,66]. En el tensor podemos contemplar dos contribuciones: una cinética que resulta del cambio en la cantidad de movimiento debido a las partículas que atraviesan un elemento de volumen en $\mathbf{r}$, y otra configuracional, consecuencia de la variación en la cantidad de movimiento debida a la presencia de campos externos y de la interacción entre las partículas contenidas en el volumen elemental centrado en $\mathbf{r}$ y el resto de las partículas del fluido (ver Fig. 5.1). Para el caso de un fluido homogéneo, donde las componentes del tensor no dependen de la posición, en ausencia de fuerzas externas y bajo interacciones aditivas por pares, las componentes del tensor se resumen en una presión macroscópica de bulk la cual viene dada por la expresión ya conocida para el virial en la Eq. (4.15).

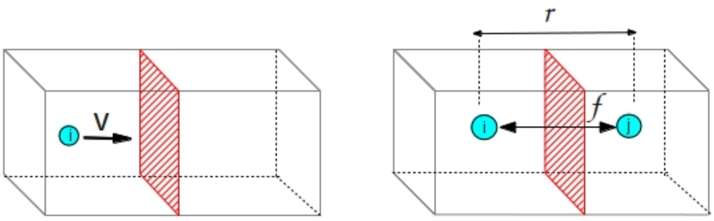

Figura 5.1: Desde un punto de vista didáctico podemos interpretar la presión como un flujo de cantidad de momimiento a través de un área $P = A^{-1}d(mv)/dt$. La cantidad de movimiento puede transferirse de dos formas: transportado a través de un área por una partícula en movimiento (izquierda) o mediante la interacción entre pares de partículas (derecha).

Para sistemas inhomogéneos, la densidad y el tensor de presiones son funciones de la posición en el fluido. Ahora bien, la definición del tensor de presiones en un sistema inhomogeneo presenta un problema, que surge del hecho de que la parte configuracional del tensor no puede definirse de una forma única [64, 66, 72]. Podemos decir que no hay una forma no ambigüa de decidir qué pares de moléculas contribuyen al tensor en un punto dado $\mathbf{r}$. Es difícil especificar dónde un virial intermolecular dado está actuando en un fluido, y cómo está distribuido en una zona del espacio. Con objeto de proponer la escritura formal del tensor, Gloor et al.(2005) [4] definen $\xi_{\alpha\beta}(\mathbf{r}, \mathbf{r}_i, \mathbf{r}_j)$ como la fracción del virial intermolecular entre un par de moléculas en $\mathbf{r}_i$ y $\mathbf{r}_j$ asignado a la posición $\mathbf{r}$ cuando se calcula la componente $\alpha - \beta$ del tensor, satisfaciendo la condición de normalización

$$\int d\mathbf{r}\ \zeta_{\alpha\beta}(\mathbf{r}, \mathbf{r}_i, \mathbf{r}_j) = 1 \tag{5.8}$$

Así que haciendo uso de la función anterior podemos definir el tensor de presiones como

$$P_{\alpha\beta}(\mathbf{r}) =< \rho(\mathbf{r}) k_B T \delta_{\alpha\beta} > + \left\langle \sum_i \sum_{j>i} r_{ij}^{\alpha}\, f_{ij}^{\beta} \zeta_{\alpha\beta}(\mathbf{r}, \mathbf{r}_i, \mathbf{r}_j) \right\rangle \tag{5.9}$$

donde $\delta_{\alpha\beta}$ es la delta de Kronecker, $\langle \cdots \rangle$ el promedio en ensamble, r_{ij}^{α} la componente α del vector intermolecular $\mathbf{r}_{ij}$, f_{ij}^{β} la componente β de la fuerza intermolecular $\mathbf{f}_{ij}$, K_B la constante de Boltzmann, y $\rho(\mathbf{r})$ la densidad numérica de moléculas. Para un sistema inhomogeneo con una interfase plana perpendicular al eje z, el tensor de presiones depende únicamente de la distancia z a la interfase. En este escenario $\zeta_{\alpha\beta}$ sería una función dependiente de la distancia z, y de las posiciones z_i y z_j de las moléculas, representando la fracción de virial entre un par de moléculas que es asignado a un slab de área $\mathcal{A}$ paralelo a la interfase y centrado en la posición z [4]

$$\zeta_{\alpha\beta}(\mathbf{r}, \mathbf{r}_i, \mathbf{r}_j) = \frac{1}{\mathcal{A}}\ \zeta_{\alpha\beta}(z, z_i, z_j) \tag{5.10}$$

sin olvidar la condición de normalización

$$\int_{-\infty}^{+\infty} dz\ \zeta_{\alpha\beta}(z, z_i, z_j) = 1 \tag{5.11}$$

Teniendo en cuenta la condición de simetría para una interfase plana dada en la Eq. (5.6) y la definición de $\zeta_{\alpha\beta}$ de la Eq.(5.10), podemos escribir las componentes de tensor de presiones de la Eq. (5.9) como

$$P_N(z) =< \rho(z) k_B T > + \frac{1}{\mathcal{A}} \left\langle \sum_i \sum_{j>i} \frac{z_{ij}^2}{r_{ij}} \left(-\frac{du(r_{ij})}{dr_{ij}} \right) \zeta_N(z, z_i, z_j) \right\rangle \tag{5.12}$$

$$P_T(z) =< \rho(z) k_B T > + \frac{1}{2\mathcal{A}} \left\langle \sum_i \sum_{j>i} \frac{x_{ij}^2 + y_{ij}^2}{r_{ij}} \left(-\frac{du(r_{ij})}{dr_{ij}} \right) \zeta_T(z, z_i, z_j) \right\rangle \tag{5.13}$$

teniendo en cuenta que $P_T(z) = [P_{xx}(z) + P_{yy}(z)]/2$. Las funciones ζ_N y ζ_T son las definición de la funcion ζ para las componentes normal y tangencial respectivamente. Precisamente la elección de ζ nos lleva a distintos métodos de calcular las componentes del tensor de presiones, como el método de Irving-Kirkwood (IK) [4,5,62,71,73] elegido en este trabajo o el de Harasima (H) [63] y que retomamos en el apartado 5.3.

5.2 Definición mecánica de la tensión superficial

Imaginemos una película de líquido como la de la Fig. 5.2. La fuerza F necesaria para mantener la tensión en equilibrio en las dos caras de la película es proporcional a la longitud L. Sea $F = 2\gamma L$, de forma que el trabajo necesario para aumentar la superficie de la película $\Delta\mathcal{A} = 2L\Delta x$ viene dado por:

$$\delta W = F\Delta x = \left(\frac{F}{2L}\right)\Delta\mathcal{A} = \gamma\Delta\mathcal{A} \tag{5.14}$$

La tensión por unidad de longitud en una superficie simple, o tensión superficial γ, es numéricamente igual a la energía de superficie por unidad de área.

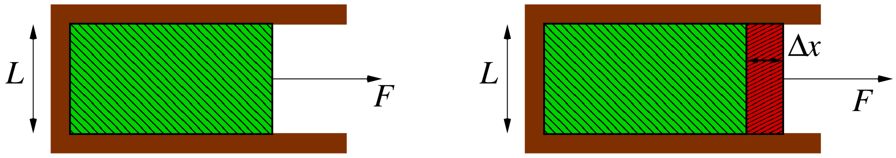

Figura 5.2: Una película de líquido está contenida en un marco de alambre con la parte derecha del contorno móvil. Supongamos que esta película está formada por dos caras cuya separación supera el rango de las fuerzas intermoleculares de forma que podemos considerar una situación de dos superficies libres. Ejemplo extraido de *Molecular Theory of Capillarity* de J.S. Rowlinson y B. Widom [5].

Cambios en el área $\mathcal{A}$, por ejemplo a temperatura y volumen constante, darán como resultado cambios en la tensión superficial. Supongamos que tenemos dos fases confinadas en un cubo de arista l, y área interfacial $\mathcal{A} = l^2$. Provoquemos una variación en el área interfacial de valor $\delta\mathcal{A}$ de forma isoterma y reversible. Para ello ejecutaremos dos pasos: una expansión isoterma de la cara $y = +l/2$ (Fig. 5.3) y una compresión isoterma de la cara $z = +l/2$ (Fig. 5.4), de forma que el volumen del sistema después de la transformación total permanezca constante.

Si la cara $y = +l/2$ se desplaza isotérmica y reversiblemente tal que el área aumenta en $\delta\mathcal{A}$, el trabajo δW_T (tangencial) realizado sobre el sistema se calcula como

$$d(\delta W_T) = -P_T(z)dV = -P_T(z)\delta\mathcal{A}dz \quad \longrightarrow \quad \delta W_T = -\delta\mathcal{A}\int_{-l/2}^{+l/2} P_T(z)dz \tag{5.15}$$

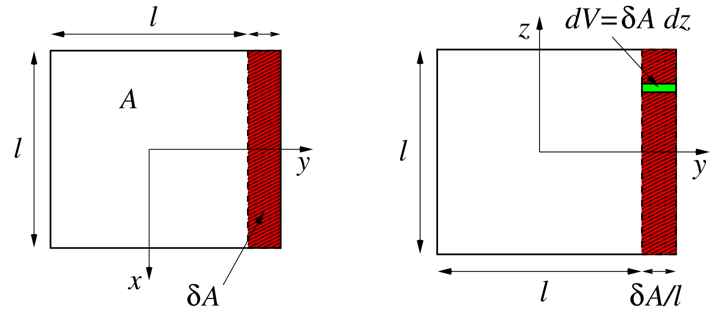

Figura 5.3: Expansión isotérmica en la cara $y = +l/2$.

Un desplazamiento similar de la cara $z = +l/2$ basado en una compresión isotérmica mediante un desplazamiento $\delta\mathcal{A}/l$ da lugar a un cambio de volumen $\Delta V = (\mathcal{A} + \delta\mathcal{A})(l - \delta/l) - (\mathcal{A} + \delta\mathcal{A})l \approx$

$-\mathcal{A}\,(\delta\mathcal{A}/l)$, de manera que teniendo en cuenta que $P_N(z) = P$ el trabajo δW_N (normal) realizado sobre el sistema se calcula como

$$d(\delta W_N) = -P_N(z)dV = -PdV \quad \longrightarrow \quad \delta W_N = -\delta\mathcal{A}\int_{-l/2}^{+l/2} Pdz \tag{5.16}$$

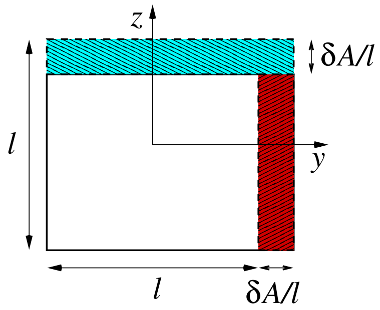

Figura 5.4: Compresión isotérmica en la cara $z = +1/2$. El desplazamiento $\delta\mathcal{A}/l$ garantiza el mantener el volumen constante.

Así pues el trabajo total realizado y por lo tanto el incremento de energía por unidad de área será

$$\delta W = \delta W_T + \delta W_N = -\delta\mathcal{A}\int_{-l/2}^{+l/2} \left[P - P_T(z)\right]\, dz \tag{5.17}$$

Los límites de integración podemos tomarlos entre $\pm\infty$ puesto que realmente $P_T(z)$ difiere de la presión P unicamente cerca de la interfase. Así que este incremento de energía por unidad de área es igual a la tensión superficial

$$\gamma = \int_{-l/2}^{+l/2} \left[P - P_T(z)\right]\, dz = \int_{-\infty}^{+\infty} \left[P - P_T(z)\right]\, dz \tag{5.18}$$

La ecuación anterior es normalmente denominada definición mecánica de la tensión superficial. Ecuación que deja clara la contribución de las componentes del tensor de presiones, no equilibradas en la zona interfacial, a la tensión superficial.

5.3 Determinación del tensor microscópico de presiones mediante el método IK para sistemas de interfases planas

Para calcular tensor microscópico de presiones o perfil de las componentes del tensor de presiones $P_N(z)$ y $P_T(z)$ necesitamos dividir la caja de simulación en slabs y calcular la presión local en cada uno de ellos. La caja de simulación es por lo tanto dividida en slabs de anchura Δz y área $\mathcal{A}$ paralela a la interfase (en el plano xy). El primer término de las componentes del tensor corresponde a la parte ideal (cinética), y su contribución al tensor microscópico de la presión se obtiene desde el valor del perfil de la densidad en una determinada posición z.

Sin embargo, como ya hemos introducido no hay una definición única sobre la forma en que la contribución de la interacción entre una molécula i y una molécula j tiene que ser distribuida en cada slab, lo que nos lleva a la famosa ambigüedad entre las definiciones de IK y H. Por lo tanto nos encontramos en la situación, tal y como comentamos en el apartado 5.1, de la elección de la función ζ para la parte configuracional de las componentes normal y tangencial. Para el caso de sistemas con interacciones aditivas por pares la elección de IK para ζ consiste en [5,35,65,74–76]

$$\zeta_N = \zeta_T = \zeta(z, z_i, z_j) = \frac{1}{|z_{ij}|}\,\Theta\left(\frac{z - z_i}{z_{ij}}\right)\Theta\left(\frac{z_j - z}{z_{ij}}\right) \tag{5.19}$$

donde $\Theta(x)$ es la función salto unidad de Heaviside definida como $\Theta(x) = 0$ cuando $x < 0$ y $\Theta(x) = 1$ cuando $x \geq 0$, y se cumple la condición de normalización dada por la Eq. (5.8) para ζ. En la elección de IK, las moléculas i y j contribuyen al tensor de presiones en un slab determinado si la línea que une los centros de masa de las moléculas atraviesa, comienza o termina en el slab. La contribución total de la interacción $i - j$, incluida la debida a las LRC, se reparte por igual en cada uno de los slabs. Si la distancia a lo largo del eje z entre pares de moléculas i y j, $|z_{ij}|$ es dividida en n_{ij} slabs de anchura ΔZ y centrados en z_k, y en la discretización que hacemos del perfil, las moléculas i y j están localizadas en los slabs k_i y k_j, respectivamente, el número de slabs entre ellas es $n_{ij} = |k_j - k_i| - 1$, donde se incluyen los slabs ocupados por las propias moléculas. La Eq. (5.19) es entonces proporcional al factor $1/(n_{ij}\Delta z)$. A la hora de incorporar este factor en el código de programación lo haremos de la siguiente forma

$$\frac{1}{n_{ij}} = \begin{cases} 1 & n_{ij} = -1 \\ 1/2 & n_{ij} = 0 \text{ or } n_{ij} = n_s - 2 \\ \dfrac{1}{(n_{ij}+2)} & n_{ij} < \dfrac{n_s}{2} \\ \dfrac{1}{(n_s - n_{ij})} & n_{ij} \geq \dfrac{n_s}{2} \end{cases} \tag{5.20}$$

donde n_s es el número de slabs en que dividimos la caja de simulación a lo largo del eje z. Puntualizar que las condiciones $n_{ij} = n_s - 2$ y $n_{ij} \geq \frac{n_s}{2}$ corresponden a la situación en que las partículas i y j interaccionan a través de la condición de mínima imagen. Cuando evaluamos la distancia entre pares de moléculas $|z_{ij}|$, para ser consistente con el cálculo de la interacción intermolecular durante la simulación, también aplicamos la condición de mínima imagen.

En la definición de Harasima la elección de la función ζ es [63,66]

$$\zeta_N(z, z_i, z_j) = \frac{1}{|z_{ij}|}\,\Theta\left(\frac{z - z_i}{z_{ij}}\right)\Theta\left(\frac{z_j - z}{z_{ij}}\right) \tag{5.21}$$

$$\zeta_T(z, z_i, z_j) = \delta(z - z_j) \tag{5.22}$$

La elección de IK y H coinciden en la componente normal, $P_N^{IK}(z) = P_N^{H}(z)$, pero difieren en la expresión de la componente tangencial, $P_T^{IK}(z) \neq P_T^{H}(z)$. En IK la presión local es independiente del número de slabs cuando el ancho de slabs es más pequeño que la distancia entre las partículas (rango de interacción), ya que el volumen del slab y la fracción de la línea (que conecta las partículas) en el slab escalan linealmente con el ancho del slab. Es decir, la presión en un slab es independiente de la anchura del slab. En la elección H, cuando se incrementa el número de slabs (se reduce por tanto el ancho del slab) causa que la presión tangencial, en los dos slabs con las partículas que interactúan, se incremente. Aunque este efecto desaparece en el caso de un sistema homogéneo, debido al movimiento de las partículas, y los perfiles obtenidos por IK y H son idénticos [66]. Por tanto las ambiguedades aparecen en el tratamiento de sistemas inhomogéneos. La invarianza de la presión local con el ancho del slab puede favorecer el uso de la expresión de IK sobre la de H, aunque esto no implica que los perfiles de IK sean más correctos tal y como indica Sonne et al.

(2005) [70]. Schofield y Henderson (1982) [66] demuestran que en un sistema de interfases planas y un potencial de corto alcance, la diferencia de las componentes transversales calculadas por IK y por H, $\Delta P_T(z) = P_T^{IK}(z) - P_T^{H}(z)$, cumple que $\int dz \Delta P_T(z) = 0$, por lo que propiedades como el valor de la tensión superficial definida por la Eq. (5.18) es independiente de la elección y no existe por tanto ambigüedad. Sin embargo, $\int dz f(z) \Delta P_T(z)$ no es independiente de la elección de $P_T(z)$ para una función $f(z)$ arbitraria [63, 66], y por ejemplo la posición de la superficie de tensión, que juega un papel fundamental en el caso de superficies esféricas, definida mecánicamente por $Z_s = \gamma^{-1} \int z[P_N - \Delta P_T(z)]dz$ [77], difiere de la elección tomada para calcular las componentes microscópicas del tensor de presiones [66] .

5.3.1 Componentes del tensor microscópico de presiones en un potencial continuo LJ

Una vez tomada la elección de IK, la contribución total de las componentes del tensor de presiones se obtendrá promediando el virial total en el ensamble NVT. Para el caso de que tengamos un potencial de LJ la expresión final de las componentes microscópicas del tensor de presiones vendrá dada por

$$P_N(z) = \langle \rho(z)\, k_B T \rangle + P_N^{\mathrm{CUT}}(z) + P_N^{\mathrm{LRC}}(z) \tag{5.23}$$

Como ya hemos visto, el primer término corresponde a la contribución ideal al tensor microscópico de presiones. Los otros dos términos, $P_N^{\mathrm{CUT}}(z)$ y $P_N^{\mathrm{LRC}}(z)$, son las contribuciones a la componente normal del tensor de presiones, $P_N(z)$, debido a la interacción directa de las interacciones para un determinado radio de corte r_c y a las LRC, respectivamente. La contribución de $P_N^{\mathrm{CUT}}(z)$ puede escribirse a partir de la Eq. (5.12) como

$$P_N^{\mathrm{CUT}}(z) = -\frac{1}{\mathcal{A}\,\Delta z} \left\langle \sum_{i=1}^{N-1} \sum_{j=i+1}^{N} \frac{z_{ij}^2}{r_{ij}} \frac{\mathrm{d}u_{LJ}(r_{ij})}{\mathrm{d}r_{ij}} \frac{1}{n_{ij}}) \right\rangle \tag{5.24}$$

La componente tangencial, $P_T^{\mathrm{CUT}}(z)$, vendrá dada por una expresión de la forma de la Eq. (5.24) sin más que cambiar z_{ij}^2 por $(x_{ij}^2 + y_{ij}^2)/2$.

Con objeto de no presentar información redundante, los detalles más importantes correspondientes a las contribuciones a las componentes del tensor de presiones correspondiente a las correcciones de largo alcance inhomogéneas, P_N^{LRC} y P_T^{LRC}, se recogen en los apartados 9.2, 9.3, y material suplementario del capítulo 9 dentro de la parte de resultados de este trabajo.

5.3.2 Componentes del tensor microscópico de presiones en un potencial discontinuo SW

A continuación se presenta la metodología utilizada en este trabajo para la determinación del perfil de las componentes de la diagonal del tensor de presiones, $P_{xx}(z)$, $P_{yy}(z)$ y $P_{zz}(z)$, para lo cual se generaliza el esquema computacional presentado en el apartado 4.2.2 para un sistema bulk a un sistema inhomogéneo de interfases planas. Al igual que con el potencial de LJ, partiremos de las definiciones generales dadas por las Eqs. (5.12) y (5.13). Con objeto de abreviar la exposición, y sin pérdida de generalidad, podemos centrarnos en la obtención del perfil de la componente $P_{xx}(z)$ del tensor de presiones, ya que el esquema que sigamos es absolutamente extrapolable al resto de las componentes. Por tanto, nos fijaremos en la Eq. (5.13) para proponer para la componente $P_{xx}(z)$ la siguiente expresión

$$P_{xx}(z) = P_{xx}^{id}(z) + P_{xx}^{conf}(z) =< \rho(z) k_B T > + \frac{1}{\mathcal{A}} \left\langle \sum_i \sum_{j>i} \frac{x_{ij}^2}{r_{ij}} \left(-\frac{du_{SW}(r_{ij})}{dr_{ij}} \right) \zeta_{xx}(z, z_i, z_j) \right\rangle \tag{5.25}$$

definiendo $\zeta_{xx} = \zeta_{xx}(z, z_i, z_j)$, para la elección de IK, de forma idéntica a como se hizo en la Eq. 5.19. Para solventar el problema de evaluar de la derivada $du_{SW}(r_{ij})/dr_{ij}$ contamos con el recurso definido por la Eq (4.61) en el apartado 4.2.1 para el potencial SW, de forma que si sustituimos en la parte configuracional de la (5.25) tendremos

$$P_{xx}^{conf}(z) = \frac{k_B T}{\mathcal{A}} \left\langle \sum_i \sum_{j>i} \frac{x_{ij}^2}{r_{ij}} \zeta_{xx}(z, z_i, z_j) e^{\beta u(r_{ij})} \left\{ e^{\beta \epsilon_{ij}} \delta(r_{ij} - \sigma_{ij}) - \left(e^{\beta \epsilon_{ij}} - 1 \right) \delta(r_{ij} - \lambda_{ij} \sigma_{ij}) \right\} \right\rangle \tag{5.26}$$

Al igual que se hizo para un sistema bulk, para evaluar la componente $P_{xx}(z)$ tendremos que evaluar las discontinuidades en $r_{ij} = {\sigma_{ij}}^+$, $r_{ij} = (\lambda_{ij}\sigma_{ij})^-$ y $r_{ij} = (\lambda_{ij}\sigma_{ij})^+$ definidas en las formas de δ-Dirac expresión formal de la Eq. (5.26). Si por ejemplo queremos evaluar la discontinuidad en $r_{ij} = (\lambda_{ij}\sigma_{ij})^+$, tendremos que evaluar el sumando implicado en esta discontinuidad igual que hicimos en el caso de un sistema bulk con la Eq. (4.69). Como nos aproximamos a la discontinuidad por la derecha tendremos que $e^{\beta u(r_{ij})} = 1$, además r_{ij} es tal que $\lambda_{ij}\sigma_{ij} < r_{ij} < \lambda_{ij}\sigma_{ij} + \Delta r_{ij}$ con $\Delta r_{ij} \to 0^+$, por lo que entonces $r_{ij} \to \lambda_{ij}\sigma_{ij}$. Con estas consideraciones y con la aproximación de la δ-Dirac podemos hacer, para el sumando del que estamos hablando de la expresión formal dada por la Eq. (4.69) , la siguiente aproximación

$$\left\langle \sum_{i=1}^{N-1} \sum_{j=i+1}^{N} \frac{x_{ij}^2}{r_{ij}} \zeta_{xx}(z, z_i, z_j) e^{\beta u(r_{ij})} \delta(r_{ij} - \lambda_{ij}\sigma_{ij}) \right\rangle \approx \left\langle \sum_{i=1}^{N-1} \sum_{j=i+1}^{N} \frac{x_{ij}^2}{\lambda_{ij}\sigma_{ij}} \zeta_{xx}(z, z_i, z_j) \frac{1}{\Delta r_{ij}} \right\rangle \tag{5.27}$$

Para calcular un promedio, como el de la aproximación que acabamos de hacer, llevaremos a cabo escalamientos del sistema a lo largo de una dirección, en esta caso la x, manteniendo todas las demás cordenadas constantes, en lugar de en lugar de llevar a cabo escalamientos virtuales e isotrópicos del sistema como se hizo en el caso de un sistema bulk. Evidentemente, al igual que el caso de bulk, tendremos que llevar a cabo tres escalamientos con objeto de evaluar las discontinuidades en $r_{ij} = {\sigma_{ij}}^+$, $r_{ij} = (\lambda_{ij}\sigma_{ij})^-$ y $r_{ij} = (\lambda_{ij}\sigma_{ij})^+$, aunque la relación entre las coordenadas r_{ij} antes del escalamiento y después del escalamiento r'_{ij} será diferente que en el caso isotrópico.

Por ejemplo, siguiendo con la ejemplificación que estábamos desarrollando en $r_{ij} = (\lambda_{ij}\sigma_{ij})^+$, para evaluar el promedio de la aproximación dada por la Eq.(5.27), hacemos una compresión virtual del sistema a lo largo de la dirección x, pero manteniendo las demás coordenadas constantes, de manera que el volumen del sistema pasa de V a $V' = V(1 - |\xi_1|)$ con $\xi_1 = -|\Delta V|/V$ con la transformación de coordenadas las moléculas: ${x_{ij}}' = x_{ij}(1 - |\xi_1|)$, ${y_{ij}}' = y_{ij}$, ${z_{ij}}' = z_{ij}$. Bajo estas consideraciones tendremos que

$${r_{ij}}'^2 = {r_{ij}}^2 + {x_{ij}}^2 \left[(1 - |\xi_1|)^2 - 1 \right] \tag{5.28}$$

Escogeremos un valor de ξ_1 de modo que si las distancias antes del escalamiento son $r_{ij} = \lambda_{ij}\sigma_{ij} + \Delta r_{ij}$, después sean $r_{ij} = \lambda_{ij}\sigma_{ij}$. Si sustituimos esta condición en la Eq. (5.28), y teniendo en cuenta que $|\xi_1| << 1$ y $\Delta r_{ij} << 1$, obtenemos la relación entre Δr_{ij} y ξ_1 siguiente

$$(\lambda_{ij}\sigma_{ij})^2 = (\lambda_{ij}\sigma_{ij} + \Delta r_{ij})^2 + {x_{ij}}^2 \left[(1 - |\xi_1|)^2 - 1 \right] \quad \Rightarrow \quad \Delta r_{ij} = \frac{{x_{ij}}^2 |\xi_1|}{\lambda_{ij}\sigma_{ij}} \tag{5.29}$$

Si sustituimos esta relación en la Eq. (5.27) tendremos

$$\left\langle \sum_{i=1}^{N-1}\sum_{j=i+1}^{N} \frac{x_{ij}^2}{\lambda_{ij}\sigma_{ij}}\zeta_{xx}(z,z_i,z_j)\frac{1}{\Delta r_{ij}}\right\rangle \approx \frac{\left\langle \sum_{i=1}^{N-1}\sum_{j=i+1}^{N}\zeta_{xx}(z,z_i,z_j)\right\rangle}{|\xi_1|} \tag{5.30}$$

El promedio obtenido, $\left\langle \sum_{i=1}^{N-1}\sum_{j=i+1}^{N} 1\times\zeta_{xx}(z,z_i,z_j)\right\rangle$, representa el promedio sobre el ensamble del número de pares de moléculas qe se encuentran separadas una distancia entre $\lambda_{ij}\sigma_{ij}$ y $\lambda_{ij}\sigma_{ij}+\Delta r_{ij}$ con $\Delta r_{ij}\to 0^+$ o número de pares de moléculas que se solapan cuando se hace la compresión virtual del sistema. Pero hay que aclarar que la expresión, dada en la Eq. (5.30), es un ejemplo de la dificultad que en ocasiones supone el verbalizar matemáticamente una solución computacional que se extiende a lo largo numerosas líneas de código, ya que la apariencia forzada de la función $\zeta_{xx}(z,z_i,z_j)$ no es más que el reparto que se va haciendo del tensor a lo largo de la coordenada z conforme a la elección de IK.

El mismo esquema será el que se siga para evaluar las discontinuidades en $r_{ij}={\sigma_{ij}}^+$, $r_{ij}=(\lambda_{ij}\sigma_{ij})^-$. Así que en resumen; para calcular las componentes del tensor de presiones ($P_{xx}(z)$, $P_{yy}(z)$, $P_{zz}(z)$), podemos utilizar expresiones formales similares a las del caso de un sistema homogeneo

$$P_{xx}(z) =< \rho(z)k_BT > + \lim_{\xi\to 0}\frac{k_BT}{\mathcal{A}}\frac{\langle n^{xx}(\xi)\zeta_{xx}(z,z_i,z_j)\rangle}{|\xi|} \tag{5.31}$$

$$P_{yy}(z) =< \rho(z)k_BT > + \lim_{\xi\to 0}\frac{k_BT}{\mathcal{A}}\frac{\langle n^{yy}(\xi)\zeta_{yy}(z,z_i,z_j)\rangle}{|\xi|} \tag{5.32}$$

$$P_{zz}(z) =< \rho(z)k_BT > + \lim_{\xi\to 0}\frac{k_BT}{\mathcal{A}}\frac{\langle n^{zz}(\xi)\zeta_{zz}(z,z_i,z_j)\rangle}{|\xi|} \tag{5.33}$$

con $\zeta_{xx}=\zeta_{yy}=\zeta_{zz}=\zeta_{(}z,z_i,z_j)$. Los términos $n^{xx}(\xi)$, $n^{yy}(\xi)$ $n^{zz}(\xi)$ representan el número de solapamientos que se producen en el sistema ante escalamientos virtuales cuando variamos una coordenada manteniendo las otras dos constantes.

Ahora, igual que se hizo en el apartado 4.2.2 , conocer el número de solapamientos se resume a chequear condiciones muy simples para los escalamientos en x, y, o z, y que se presentan a continuación trabajando en unidades reducidas:

a) Condiciones a chequear para solapamientos en $r_{ij}=(\lambda_{ij}\sigma_{ij})^+$:

$$\begin{array}{l} {\lambda_{ij}}^2 < {r^*_{ij}}^2 < {\lambda_{ij}}^2 - {x^*_{ij}}^2[(1-\lambda_{ij}|\xi_1|)^2-1] \\ {\lambda_{ij}}^2 < {r^*_{ij}}^2 < {\lambda_{ij}}^2 - {y^*_{ij}}^2[(1-\lambda_{ij}|\xi_1|)^2-1] \\ {\lambda_{ij}}^2 < {r^*_{ij}}^2 < {\lambda_{ij}}^2 - {z^*_{ij}}^2[(1-\lambda_{ij}|\xi_1|)^2-1] \end{array} \tag{5.34}$$

b) Condiciones a chequear para solapamientos en $r_{ij}={\sigma_{ij}}^+$:

$$\begin{array}{l} {r^*_{ij}}^2 < 1 - {x^*_{ij}}^2[(1-|\xi_2|)^2-1] \\ {r^*_{ij}}^2 < 1 - {y^*_{ij}}^2[(1-|\xi_2|)^2-1] \\ {r^*_{ij}}^2 < 1 - {z^*_{ij}}^2[(1-|\xi_2|)^2-1] \end{array} \tag{5.35}$$

c) Condiciones a chequear para solapamientos en $r_{ij}=(\lambda_{ij}\sigma_{ij})^-$:

$$\begin{array}{l} {\lambda_{ij}}^2 - {x^*_{ij}}^2[(1-\lambda_{ij}|\xi_3|)^2-1] < {r^*_{ij}}^2 < {\lambda_{ij}}^2 \\ {\lambda_{ij}}^2 - {y^*_{ij}}^2[(1-\lambda_{ij}|\xi_3|)^2-1] < {r^*_{ij}}^2 < {\lambda_{ij}}^2 \\ {\lambda_{ij}}^2 - {z^*_{ij}}^2[(1-\lambda_{ij}|\xi_3|)^2-1] < {r^*_{ij}}^2 < {\lambda_{ij}}^2 \end{array} \tag{5.36}$$

Por último, con objeto de realmente calcular el límite $|\xi| \to 0$ en la simulación, utilizaremos un conjunto de n_k valores de escalamiento, de manera que $\xi_1 = \xi_1(n_k)$, $\xi_2 = \xi_2(n_k)$ y $\xi_3 = \xi_3(n_k)$.

5.4 Determinación de la tensión superficial a partir del perfil de las componentes del tensor de presiones

Una vez determinado el perfil de la presión local en sus dos componentes, la presión normal $P_N = P_N(z)$ y la presión tangencial $P_T = P_T(z)$, hacemos uso del método de IK para el cálculo de la tensión superficial, donde ésta es calculada a partir de las componentes locales del tensor de presiones. Haciendo uso de la definición dada en la Eq. (5.18) podemos decir que

$$\gamma = \int_{-L_z/2}^{+L_z/2} \left[P_N(z) - P_T(z) \right] \, dz \tag{5.37}$$

donde L_z es la longitud de la caja de simulación a lo largo del eje z.

Expresando la tensión superficial como una función de las componentes microscópicas del tensor de presiones es posible definir un perfil local a lo largo del eje z de la tensión superficial como

$$\gamma(z) = \int_{-\infty}^{z} \left[P_N(z) - P_T(z) \right] \, dz \tag{5.38}$$

Para algunos autores, el uso de la función $\gamma(z)$ es una clave para chequear la estabilidad de las interfases, la independencia y la constancia de la tensión superficial en las fases de bulk. Aunque no se ha incluido en los trabajos de los resultados, si se ha utilizado, junto con la observación de los perfiles de la densidad, como un elemento más del simulador para chequear la calidad de la equilibración de las interfases líquido-vapor. Y es en este sentido donde un método local como el de IK muestra su posición de ventaja, ya que aunque KB calcula la tensión superficial a partir del tensor de presiones total, en IK no perdemos la información microscópica de forma que por ejemplo podemos estar seguros que realmente se establece un equilibrio líquido-vapor y que la fuente de la tensión superficial realmente reside en las zonas de las regiones interfaciales. Es importante también destacar que aunque los diferentes métodos IK, HA o KBZ, que provienen de diferentes definiciones a la hora de repartir el virial, proporcionan diferentes perfiles del tensor microscópico de presiones, fundamentalmente de $P_T(z)$, el valor macroscópico de γ obtenido mediante la integración de la Eq.5.37 permanece en general independiente de la definición utilizada [73,75,76].

Otra ventaja del método IK es la relativa facilidad de incluir en el cálculo de la tensión superficial las LRC de Janeček (2006) [15], y la adaptación de éstas por MacDowell y Blas (2009) [14], ya que esas correcciones realmente se llevan a cabo sobre las componentes del tensor de presiones. Para método KB, donde la tensión superficial es calculada directamente a partir del virial mediante

$$\gamma = \frac{1}{2\mathcal{A}} \left\langle \sum_{\substack{i<j \\ r<r_c}} \left(r_{ij} - \frac{3z_{ij}}{r_{ij}} \right) \frac{\partial u(r_{ij})}{\partial r_{ij}} \right\rangle \tag{5.39}$$

, el desarrollo de las LRC por parte de diferentes autores no ha sido del todo satisfactorio. Para esta expresión Chapela et al. (1977) [34] propuso una corrección de largo alcance para añadir a posteriori de la simulación, γ^{tail}. Para esta correción de truncamiento era necesario conocer ρ_L, ρ_V y la distancia interfacial d, supuesto un perfil de la densidad que ajusta a una función tangente hiperbólica.

Esta γ^{tail} es corregida debido a errores algebraicos en el trabajo de Blockhuis et al. (1995) [78] para sistemas de un único componente. Sin embargo, para mezclas este tipo de correcciones presentan el problema de que los perfiles parciales de densidad necesariamente no tienen por que ajustarse a una función tangente hiperbólica. Estaríamos obligados entonces a aplicar las correcciones sin distinguir los diferentes componentes y sus interacciones. Este escenario es inconsistente con alguno de los aspectos más elementales que debe cumplir γ^{tail} en una simulación para mezclas, como por ejemplo que la tensión superficial obtenida para un determinado r_c decrezca cuando la concentración del componente más volátil aumente. Para solucionar este problema Mecke et al. (1999) [79] extienden el algoritmo propuesto en Mecke et al. (1997) [38] para calcular γ^{tail} para mezclas binarias, desarrollándose sendos trabajos en simulaciones de MD. Con este algoritmo se pasa de una corrección a posteriori de la simulación al cálculo de una contribución γ_i^{tail} de cada partícula i en cada paso de simulación. Para determinar γ_i^{tail} se aplica la Eq. (5.39) para la interacción de una partícula i en la caja de simulación con el resto de las partículas fuera del radio de corte en un volumen infinito. Todas esas partículas son sustituidas por el perfil de la densidad. En el caso de una mezcla binaria se usan los perfiles parciales calculados en cada paso de simulación. Para cada partícula i se calculan por separado las contribuciones de ambos componentes y se suman después. Estas expresiones son solamente válidas para sistemas binarios y no pueden extenderse a sistemas con 3 componentes [75] . Por otro lado, en el análisis crítico realizado por Janeček (2006) [15], donde las correcciones de Mecke se implementan en simulación MC, se explica que las correcciones de Mecke no contemplan todas las interacciones fuera del radio de corte, proporcionando valores menores de la tensión superficial, y a temperaturas altas ofrece resultados para los perfiles de la densidad y de la tensión superficial que no son independientes del radio de corte.

5.5 Estructura general del perfil del tensor microscópico de presiones y la tensión superficial en sistemas de interfases planas

En un perfil del tensor microscópico de presiones, como el que se muestra en la Fig.5.5, la condición de estabilidad mecánica requiere que $P_N(z)$ sea constante y la diferencia $P_N(z) - P_T(z)$ fluctua alrededor de cero en las zonas de bulk de vapor y de líquido. Estas fluctuaciones son más acusadas en la fase de líquido que es la más sensible. La anisotropía en la zona interfacial, en el caso de un fluido de puro, es consecuencia directa de la variación de la densidad a lo largo de la zona. La naturaleza de la variación de la densidad a lo largo de la zona interfacial está gobernada por la parte cinética de la presión normal, $\rho(z)\, k_B T$, y está balanceada con la parte configuracional (por ejemplo en un sistema LJ: $P_N^{\mathrm{CUT}}(z) + P_N^{\mathrm{LRC}}(z)$), de tal manera que la suma permanece constante, lo cual es la condición de equilibrio hidrostático. En un fluido de varios componentes, la anisotropía del tensor de presiones no se debe únicamente a variación de la densidad sino también a la variación de las composiciones requerida para que se establezca el equilibrio hidrostático.

En lo que respecta a la componente tangencial, ésta cambia al atravesar la zona interfacial desarrollando un mínimo y un máximo [71, 80]. La componente tangencial $P_T(z)$ puede presentar valores negativos grandes en la zona interfacial, como podemos observar en la Fig.5.5, con zonas de tensión donde $P_T < P_N$, y puede tomar también valores mayores que la componente normal P_N (zonas de compresión). Aunque la estabilidad de la interfase requiere únicamente que la integral de $P_N - P_T$ a lo largo de la zona interfacial sea positiva. Este comportamiento de la componente P_T, al pasar a través de la zona interfacial, está íntimamente relacionado con el papel que juega la

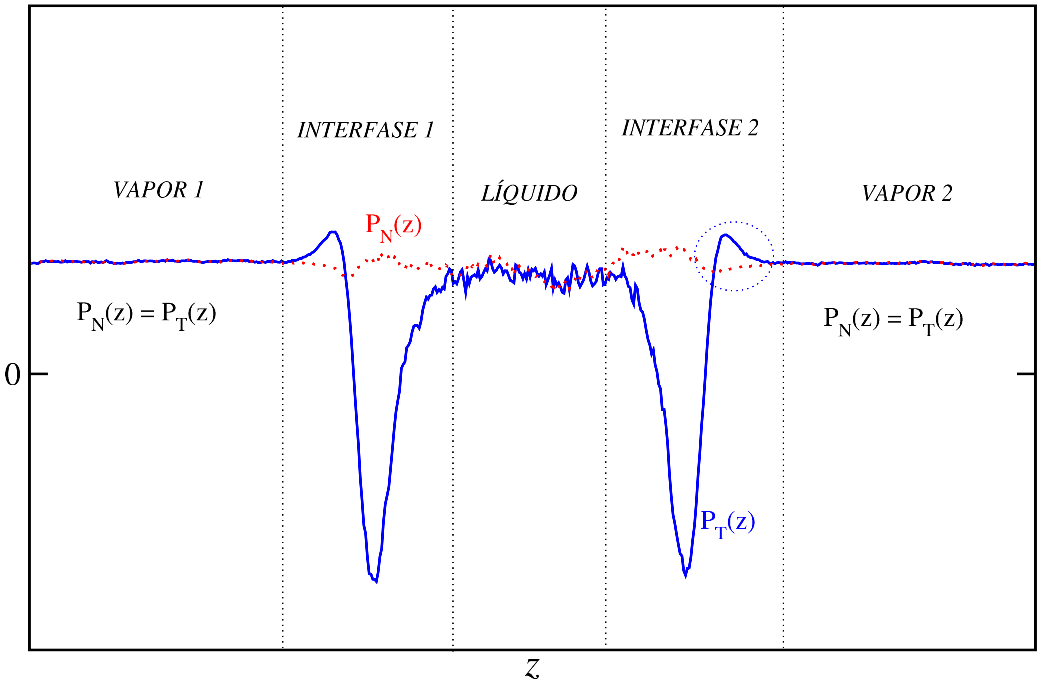

Figura 5.5: Ejemplo las componentes del $P_N(z)$ y $P_T(z)$ del tensor microscópico de presiones en un sistema de dos fases de interfases planas. Encirculado en azul tenemos una zona de compresión donde $P_T > P_N$.

región espinodal en la física de una interfase ante la necesidad de atravesar dicho dominio espinodal cuando pasamos de una densidad de bulk a otra a lo largo de la interfase [71,81]. La región entre la curva de presión de vapor que representa las condiciones de equilibrio y la curva espinodal vapor-líquido corresponde a vapor metaestable, mientras que la región entre la curva espinodal líquido-vapor y la de presión de vapor corresponde a líquido metaestable. Es interesante denotar que el mínimo que presenta la componente tangencial P_T está precisamente relacionado con el valor más bajo que puede tomar la presión espinodal en la región de líquido metaestable [81]. Si hicieramos una transformación del perfil de la componente tangencial del tensor de presiones $P_T(z)$ para llevar la dependencia con la coordenada z a una dependencia con la densidad $P_T(\rho)$, haciendo uso del perfil de la densidad $\rho(z)$, obtendríamos curvas que nos recordarían al conocido lazo de la ecuación de estado de Van der Waals. Y es que en gran medida la imagen actual de un líquido está contenida en la ecuación de estado de Van der Waals. La extensión de sus ideas al estudio de una interfase líquido-vapor, realizada por el propio Van der Waals, puede considerarse como una versión inicial de las teorías del funcional de la densidad locales aplicadas a líquidos y su teoría de la interfase como una aproximación funcional de gradiente cuadrado (aunque originalmente fue formulada desde un punto de vista más fenomenológico).

Aunque solamente sea de una forma muy elemental comentar que, en una teoría del gradiente a través de un desarrollo de segundo orden en ∇, el tensor de presiones toma la forma

$$\hat{\mathbb{P}}(\mathbf{r}) = P_0\hat{\mathbb{I}} + l_{11}\nabla^2\rho\hat{\mathbb{I}} + l_{12}\nabla\nabla\rho\hat{\mathbb{I}} + l_{21}(\nabla\rho)^2\hat{\mathbb{I}} + l_{22}\nabla\rho\nabla\rho \tag{5.40}$$

donde tanto P_0, que es la presión de un fluido homogéneo, como l_{ij} son funciones de la densidad local $\rho(\mathbf{r})$ [71]. Estas funciones deben determinarse de forma experimental o desde un modelo teórico. Una ecuación de estado para $P_0(\rho)$ utilizada por su simplicidad, y que captura la mayor parte del comportamiento cualitativo de los fluidos reales, es la ecuación de Van der Waals. La dependencia con la densidad $P_0(\rho)$ en un fluido homogéneo solamente puede ser investigada fuera del dominio spinodal. Sin embargo, en principio, las dependencias con la densidad de $P_0(\rho)$ y $l_{ij}(\rho)$ para densidades dentro del dominio espinodal pueden determinarse experimentalmente en fluidos inhomogéneos (por ejemplo en las zonas interfaciales). El tema es, que estados de densidad inestables en un fluido homogéneo pueden estabilizarse por la formación de gradientes de densidades, cuyos efectos sobre el tensor de presiones se miden mediante l_{ij}. Para un sistema de interfases planas, donde $\rho = \rho(z)$, la presión normal y tangencial pueden expresarse como

$$P_N = P_0(\rho) + (l_{11} + l_{12})\frac{d^2\rho}{dz^2} + (l_{21} + l_{22})\left(\frac{d\rho}{dz}\right)^2 \tag{5.41}$$

$$P_T = P_0(\rho) + l_{11}\frac{d^2\rho}{dz^2} + l_{21}\left(\frac{d\rho}{dz}\right)^2 \tag{5.42}$$

En los trabajos como los de Davis y Scriven (1982) [71] y Teletzke et al. (1981) podemos encontrar cómo a partir de la Eq. 5.42 es posible calcular $P_T(z)$ y cómo reproduce el comportamiento comentado dentro de la zona interfacial.

Por último, para concluir este apartado, si observamos un perfil de $P_N(z) - P_T(z)$, como el de la Fig. 5.6, podemos observar dos picos simétricos en las zonas interfaciales y la contribución en las fases de bulk muestra fluctuaciones propias de la condición de estabilidad mecánica $P_N(z) - P_T(z) = 0$. Adicionalmente, el perfil de la integral $\gamma(z)$ es plano en las fases de bulk, lo que indica que no contribuyen a la tensión superficial, es idéntica en ambas interfases, lo que nos indicará que hemos construido dos interfases independientes y que ambas están bien equilibradas [37, 65, 75, 76, 82, 83]. Cuando la temperatura aumenta, el ancho de la zona interfacial aumenta y los picos de la componente tangencial tienden a aplanarse, y por tanto la tensión superficial disminuye.

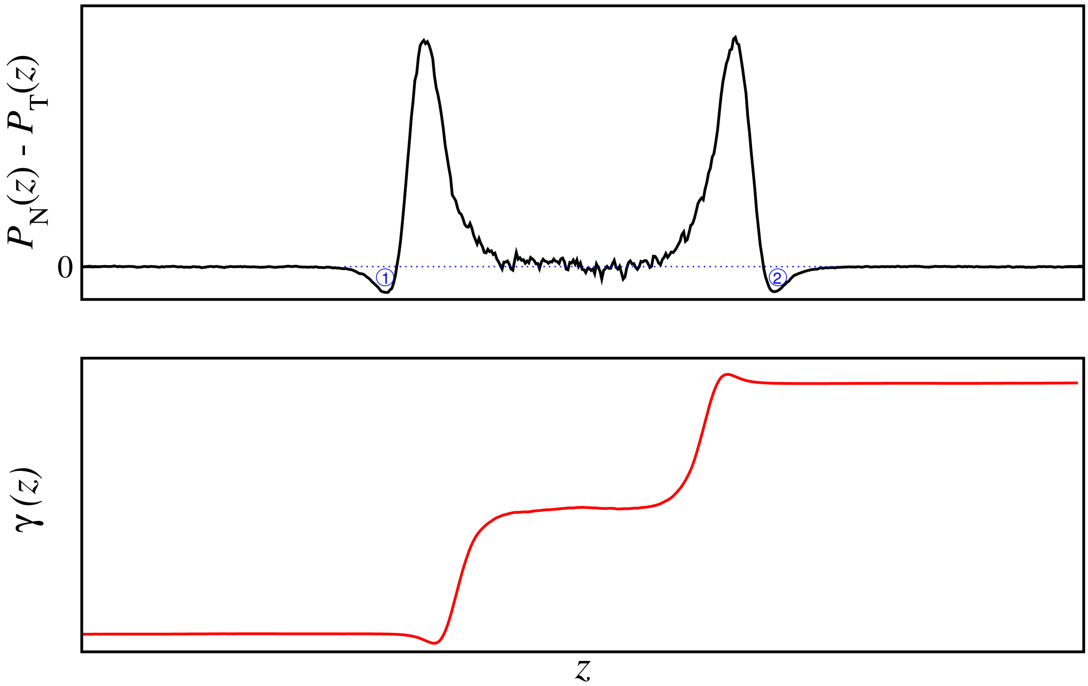

Figura 5.6: En la gráfica superior se representa un perfil típico de $P_N(z) - P_T(z)$. En las zonas señaladas como ① y ② se tiene que $P_N(z) < P_T(z)$. En la gráfica inferior se representa el perfil de la tensión superficial $\gamma(z)$.

Capítulo 6

Métodos termodinámicos perturbativos

En el capítulo anterior se presentaba una metodología basada en el concepto de tensor de presiones, una magnitud mecánica que está bien definida independientemente de la existencia de leyes termodinámicas. Es decir, no se requiere que funciones como la entropía o la energía libre existan y se obedezca la segunda ley de la termodinámica. Como hemos visto en el capítulo anterior este tipo de técnicas son implementables en simulación MC, aunque no obstante tienen el coste explicito de tener que calcular las fuerzas; aunque este cálculo no se requiere para muestrear el espacio de configuración del sistema. Para modelos de potenciales intermoleculares sencillos el virial es realmente directo, aunque no es el caso de potenciales intermoleculares complejos, potenciales discontinuos o interfases no planas, donde el cálculo de las fuerzas puede ser bastante complejo o simplemente consumir mucho tiempo de computación. La naturaleza directa de una metodología puramente mecánica suele ser atractiva por su generalidad, sin embargo debemos poner en la balanza la pérdida de la potencia que proporcionan las leyes de la termodinámica en el estudio del problema.

En este capítulo se presentan metodologías basadas en rutas termodinámicas como alternativas a esta definición mecánica. Concretamente el método VP (volumen perturbation) para el cálculo de las componentes macroscópicas del tensor de presiones [16] y el Test-Área (TA) [4] para el cálculo de la tensión superficial, ambos utilizados en este trabajo de tésis para el modelo de potencial continuo de LJ, en simulaciones de coexistencia directa de sistemas inhomogéneos de interfases planas líquido-vapor y líquido-líquido. Ambos métodos parten de las definiciones termodinámicas, en relación con la energía libre de Helmholtz F, de las propiedades a calcular, la presión y la tensión superficial respectivamente. Como veremos en las dos secciones siguientes, estos métodos se plantean como aproximaciones del cambio de energía libre ΔF asociado a pequeños cambios virtuales (perturbaciones) en el volumen (VP) o en el área interfacial (Test-Área) del sistema. La estimación numérica de estos cambios es expresada como un promedio en el ensamble correspondiente del factor de Boltzmann.

Aunque existen métodos para estimar la tensión superficial mediante diferencias de energía libre, como por ejemplo el método de Bennett [84–86] o el Expanded Ensamble [11, 12, 87], un especial interés ha cobrado en estos últimos años el método perturbativo del TA, con más de 50 citas al trabajo original de Gloor et al.(2005) [4] sobre la determinación de la tensión superficial en interfases vapor-líquido de sistemas LJ y SW. El atractivo del método TA reside en que se trata de un método elegante y sencillo, fácilmente implementable en un código MC o MD, que permite determinar la tensión superficial mediante una única simulación en interfases planas (vapor-líquido, líquido-líquido, fluido-sólido, etc) de sistemas puros y mezclas de moléculas simples y poliatómicas, y con una gran validez para el caso de potenciales continuos como el LJ. Su versatilidad ha hecho que haya sido utilizado para determinar la tensión superficial de un gran número de sistemas, como por ejemplo potenciales realistas (n-alcanos [88], agua [89], mezclas binarias de n-alcanos [90] , metano-agua [75], ...) o modelos de fluidos (cadenas de segmentos LJ [12–14, 91], Mie n-6 [92] , gotas de fluidos LJ [93],...).

El punto de partida, tanto del VP como del TA, será la variación de la energía libre de Helmholtz de un sistema en el ensemble canónico (donde el número de partículas N, el volumen V y la temperatura T permanecen constantes) debida a una perturbación desde un estado de referencia del sistema 0 a un estado 1, y puede definirse, teniendo en cuenta la Eq. (2.12), en términos de las correspondientes funciones de partición Q_0 y Q_1 como

$$\Delta F_{0\to 1} = F_1 - F_0 = -k_B T \ln\left(\frac{Q_1}{Q_0}\right) \tag{6.1}$$

Si tenemos en cuenta que la función de partición puede expresarse como el producto de una parte ideal y una parte configuracional, tal y como vimos en el apartado 2.2.1 en las Eqs. (2.14), (2.15) y (2.16), podemos expresar el cociente Q_1/Q_0 como el cociente de integrales configuracionales siguientes

$$\frac{Q_1}{Q_0} = \frac{\int d\mathbf{r}^N \exp\left[-\beta \mathcal{U}_1(\mathbf{r}^N)\right]}{\int d\mathbf{r}^N \exp\left[-\beta \mathcal{U}_0(\mathbf{r}^N)\right]} \tag{6.2}$$

La energía configuracional $\mathcal{U}_1(\mathbf{r}^N)$ consiste en una perturbación de la energía configuracional inicial (o estado de referencia) $\mathcal{U}_0(\mathbf{r}^N)$, de forma que $\mathcal{U}_1 = \mathcal{U}_0 + \Delta\mathcal{U}$, donde $\Delta\mathcal{U}$ corresponde a una perturbación de prueba desde el estado de referencia. Es importante recalcar que esta perturbación en la energía no entra dentro de la cadena de Markov, es decir, no es contabilizada para el movimiento Monte Carlo de partículas y por tanto tampoco se contabiliza en el promedio de la energía del sistema.

6.1 Método de perturbaciones de volumen (VP) para la determinación de las componentes del tensor de presiones P_N y P_T y de la tensión superficial en modelos de potencial continuos

Como ya hemos visto en el capítulo anterior, en un sistema inhomogeneo la presión es una propiedad tensorial. Para un sistema inhomogeneo, con número de partículas N, volumen V y temperatura T constantes, las componentes del tensor de presiónes $P_{\alpha\alpha}$ $(\alpha = x, y, z)$ pueden definirse termodinámicamente como

$$P_{\alpha\alpha} = -\left(\frac{\partial F}{\partial V}\right)_{N,V,L_{\beta\neq\alpha}} = -k_B T \left(\frac{\partial \ln Q_{NVT}}{\partial V}\right)_{N,V,L_{\beta\neq\alpha}} \tag{6.3}$$

donde L_α es la dimensión del sistema en la dirección α. Para evaluar la derivada de la Eq. (6.3) se ha seguido la metodología planteada por de Miguel y Jackson (2006) [16], basada en los trabajos iniciales de Eppengea y Frenkel (1984) [94] y Harismiadis et al. (1996) [95], donde se propone evaluar dicha derivada mediante al estimación numérica de la variación de la energía libre bajo una perturbación isotérmica del volumen. Si consideramos una perturbación del volumen del sistema desde V_0 a $V_1 = V_0 + \Delta V$, con $\Delta V > 0$, el cambio asociado a la energía libre viene dado por la Eq. (6.1). El cociente de las funciones de partición puede expresarse, haciendo uso de un conjunto de coordenadas escaladas ($\mathbf{s}^N; L$) con las dimensiones lineales del sistema ($\mathbf{s}^N = \mathbf{r}^N/L$), según la forma

$$\frac{Q_1}{Q_0} = \frac{\int d\mathbf{s}^N V_1^N \exp\left[-\beta \mathfrak{U}(V_1)\right]}{\int d\mathbf{s}^N V_0^N \exp\left[-\beta \mathfrak{U}(V_0)\right]} = \frac{\int d\mathbf{s}^N V_0^N \left[(V_1/V_0)^N \exp\left(-\beta \Delta \mathfrak{U}^+\right)\right] \exp\left[-\beta \mathfrak{U}(V_0)\right]}{\int d\mathbf{s}^N V_0^N \exp\left[-\beta \mathfrak{U}(V_0)\right]} \tag{6.4}$$

donde $\Delta\mathfrak{U}^+ = \mathfrak{U}(V_0 + \Delta V) - \mathfrak{U}(V_0)$ es la energía asociada con el incremento del volumen. Si ahora tenemos en cuenta la forma en que calculamos promedios en el ensemble (ver Eq. (2.17)), la Eq. (6.4) puede expresarse como el factor de Boltzmann de la variación $\Delta\mathfrak{U}$ promediada sobre el estado de referencia del sistema no perturbado de volumen V_0, de forma que

$$\frac{Q_1}{Q_0} = \left\langle \left(1 + \frac{\Delta V}{V_0}\right)^N \exp(-\beta \Delta \mathfrak{U}^+) \right\rangle \tag{6.5}$$

Si en lugar de llevar a cabo una perturbación basada en un incremento de volumen hacemos una disminución del mismo, donde $\Delta\mathfrak{U}^- = \mathfrak{U}(V_0 - |\Delta V|) - \mathfrak{U}(V_0)$ es el cambio de energía configuracional asociado a dicha pertrbación, entonces la Eq. (6.5) toma la forma

$$\frac{Q_1}{Q_0} = \left\langle \left(1 - \frac{|\Delta V|}{V_0}\right)^N \exp(-\beta \Delta \mathfrak{U}^-) \right\rangle \tag{6.6}$$

La derivada primera de la Eq. (6.3), para el caso de una perturbación basada en un incremento de volumen, podemos aproximarla por diferencias finitas según

$$\frac{\partial F}{\partial V} \approx \frac{F(V_0 + \Delta V) - F(V_0)}{\Delta V} \tag{6.7}$$

y haciendo uso de la Eq. (6.5), obtenemos la siguiente expresión para la componente del tensor de presiones

$$\beta P^+_{\alpha\alpha} = \frac{1}{\xi V_0} \ln \left\langle (1+\xi)^N \exp(-\beta \Delta \mathfrak{U}^+) \right\rangle \tag{6.8}$$

donde hemos denotado a la variación relativa de volumen como $\xi = \Delta V/V_0$, y el superíndice $+$ hace referencia a una perturbación por un incremento de volumen $\xi > 0$. Para evaluar la derivada durante la simulación diseñamos una expansión virtual (no contabilizada en la cadena de Markov) de volumen en la que la dimensión de la caja de simulación L_α aumenta a $L_\alpha + \Delta L_\alpha$ manteniendo las otras dimensiones L_β ($\beta \neq \alpha$) constantes de forma que $\xi = \Delta L_\alpha / L_\alpha > 0$. Si hacemos una compresión virtual $\xi < 0$, donde la dimensión de la caja L_α disminuye a $L_\alpha - \Delta L_\alpha$, utilizamos una expresión equivalente a la Eq. (6.8) de la componente del tensor de presiones

$$\beta P^-_{\alpha\alpha} = \frac{1}{-|\xi| V_0} \ln \left\langle (1-|\xi|)^N \exp(-\beta \Delta \mathfrak{U}^-) \right\rangle \tag{6.9}$$

La consistencia termodinámica requiere que la presión calculada mediante un incremento de volumen sea igual que la calculada mediante una disminución de volumen en el límite $\Delta V \to 0$. Esto es esperable para el caso de estar trabajando con potenciales continuos, aunque en la práctica, realmente usamos valores muy pequeños y finitos de ΔV y ambas aproximaciones no tomarán exactamente el mismo valor. Aún así la presión puede calcularse mediante una combinación de promedios del factor de Boltzmann asociado a dos perturbaciones de volumen y expresarla como

$$P_{\alpha\alpha} = \frac{P^+_{\alpha\alpha} + P^-_{\alpha\alpha}}{2} \tag{6.10}$$

En el caso de potenciales discontinuos debemos tener precaución en el uso de este tipo de metodologías ya que las Eqs. (6.8) y (6.10) carecerían de validez. Por ejemplo en el caso de un potencial SW la parte de esfera dura sería insensible a una expansión virtual del sistema [94] y solamente sería válido el cálculo de la presión mediante la expresión dada en la Eq. (6.9) [16,50].

En interfases planas como ya sabemos $P_{xx} = P_{yy} = P_T$ y $P_{zz} = P_N \equiv P$, y podemos expresar la definición termodinámica de la Eq. (6.3) como

$$P_N = -\left(\frac{\partial F}{\partial V}\right)_{TNL_xL_y} = -\frac{1}{\mathcal{A}}\left(\frac{\partial F}{\partial L_z}\right)_{TN\mathcal{A}} \tag{6.11}$$

$$P_T = -\left(\frac{\partial F}{\partial V}\right)_{TNL_z} = -\frac{1}{L_z}\left(\frac{\partial F}{\partial \mathcal{A}}\right)_{TNL_z} \tag{6.12}$$

Si la caja de simulación tiene una longitud L_z y área interfacial $\mathcal{A} = L_xL_y$ $(L_x = L_y)$, el promedio macroscópico de la componente normal P_N se calcula haciendo variaciones virtuales del vo - lumen según la dirección normal z (Fig. 6.1), para lo cual reescalamos tanto la longitud de la caja de simulación y las posiciones de los centros de masas de las partículas según $L_z = L_{z,0}(1 \pm |\xi|)$ y $z_i = z_{i,0}(1 \pm |\xi|)$ respectivamente. El promedio macroscópico de la componente tangencial P_T se calcula variando de forma isotrópica, y simultánea, las longitudes de la caja L_α $(\alpha = x, y)$ manteniendo constante L_z. Para ello reescalamos igualmente las dimensiones de la caja $L_\alpha = L_{\alpha,0}\sqrt{1 \pm |\xi|}$ y las coordenadas x, y de los centros de masas según $x_i = x_{i,0}\sqrt{1 \pm |\xi|}$ e $y_i = y_{i,0}\sqrt{1 \pm |\xi|}$. En ambos casos, $|\xi| = |\Delta V|/V_0$ define la variación relativa del cambio de volumen asociado a la perturbación.

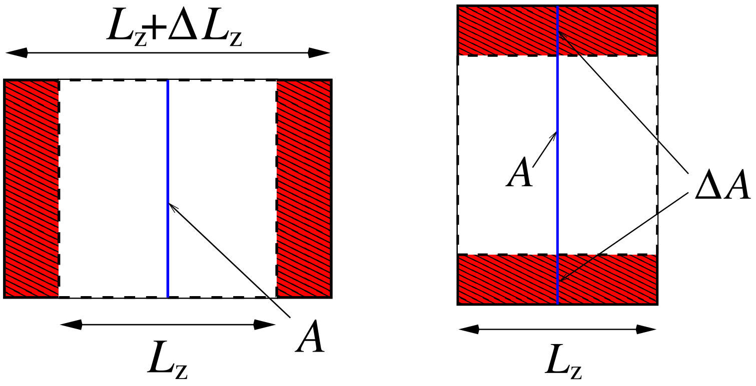

Figura 6.1: Perturbación del volumen del estado de referencia que se logra variando virtualmente la longitud Lz de la caja de simulación manteniendo el área interfacial $\mathcal{A}$ constante (fig. izquierda), o manteniendo constante Lz y variando el área interfacial (fig. derecha).

En la simulaciónes las perturbaciones se han llevado a cabo cada 5 ciclos de movimientos de partículas MC una vez que el sistema ha sido equilibrado. Evidentemente la eficiencia en la aproximación de la derivada de primer orden, mediante diferencias finitas, requiere que los cambios en las perturbaciones de volumen sean lo suficientemente pequeños, pero no tan pequeños como para no apreciar cambios en las propiedades termodinámicas del sistema. Para ello las perturbaciones han consistido en cambios relativos de volumen (expansiones y compresiones) en el rango de $2 \times 10^{-4} \leq |\xi| \leq 15 \times 10^{-4}$, dentro del cual la presión presenta un comportamiento lineal. La componentes macroscópicas del tensor de presiones P_N y P_T son obtenidas entonces mediante una extrapolación lineal (para las expansiones y compresiones) de este conjunto de datos cuando $|\xi| \to 0$ y teniendo en cuenta la Eq. (6.10).

Determinación de la tensión superficial

Una vez que las componentes macroscópicas del tensor de presiones han sido determinadas, podemos determinar la tensión superficial a partir de ellas. En el caso de interfases planas, la tensión superficial se define termodinámicamente en el ensemble canónico como

$$\gamma = \left(\frac{\partial F}{\partial \mathcal{A}}\right)_{NVT} \tag{6.13}$$

Si tenemos en cuenta que para un sistema de interfases planas es posible expresar la energía libre en función de la longitud de la caja de simulación L_z y del área de la superficie interfacial $\mathcal{A}$, es decir $F = F(N, V, T) \equiv F(N, L_z, \mathcal{A}, T)$, de forma que si calculamos la diferencial de la energía libre dF, manteniendo constante el número de partículas N y la temperatura T, tenemos

$$dF = \left(\frac{\partial F}{\partial L_z}\right)_{NT\mathcal{A}} dL_z + \left(\frac{\partial F}{\partial \mathcal{A}}\right)_{NTL_z} d\mathcal{A} \tag{6.14}$$

Como el volumen del sistema permanece constante $dV = L_z d\mathcal{A} + \mathcal{A} dL_z = 0$, las variaciones en los parámetros L_z y $\mathcal{A}$ están relacionadas según $dL_z = -L_z/\mathcal{A} d\mathcal{A}$. Haciendo uso de esta relación, y teniendo en cuenta las definiciones termodinámicas dadas en las Eqs. (6.11), (6.12) y (6.13) , podemos sutituir en la relación dada por la Eq. (6.14) de forma que para un sistema con una interfase relacionamos la tensión superficial con las componentes macroscópicas del tensor de presiones

$$dF = L_z(P_N - P_T)d\mathcal{A} \quad \to \quad \gamma = L_z(P_N - P_T) \tag{6.15}$$

6.2 Método Test Área (TA) para la determinación de la tensión superficial en modelos de potencial continuos

El método TA, propuesto por Gloor et al.(2005) [4], consiste en diseñar pequenõs cambios en el área interfacial del sistema, disminuyendo y aumentando las dimensiones de la caja de simulación en el plano de la interfase , a la vez que la longitud de la caja normal a la interfase aumenta y disminuye respectivamente para mantener el volumen total del sistema constante.

Si denominamos $\mathcal{A}_0$ al área del estado de equilibrio, que tomamos como referencia, podemos generar un estado perturbado (estado 1) aumentando el área interfacial, de modo que el nuevo área es $\mathcal{A}_1 = \mathcal{A}_0(1 + \Delta\mathcal{A}^*)$ y la variación de la energía libre es $\Delta F_{0\to 1} = F_1(A_1) - F_0(A_0)$. O podemos disminuir el área interfacial (estado -1), de modo que el nuevo área sea $\mathcal{A}_{-1} = \mathcal{A}_0(1 + \Delta\mathcal{A}^*)$ y la variación de la energía libre es $\Delta F_{0\to -1} = F_{-1}(A_{-1}) - F_0(A_0)$. La perturbación en el área interfacial se lleva a cabo de forma que las dimensiones x e y se modifiquen de igual manera, es decir, $L_{x,1} = L_{x,0}\sqrt{(1 + \Delta\mathcal{A}^*)}$ y $L_{y,1} = L_{y,0}\sqrt{(1 + \Delta\mathcal{A}^*)}$ en un aumento del área interfacial, o $L_{x,-1} = L_{x,0}\sqrt{(1 - \Delta\mathcal{A}^*)}$ y $L_{y,-1} = L_{y,0}\sqrt{(1 - \Delta\mathcal{A}^*)}$ en una disminución del área interfacial. Como queremos mantener el volumen de la caja de simulación constante, la dimensión z deberá responder disminuyendo según $L_{z,1} = L_{z,0}(1 - \Delta\mathcal{A}^*)^{-1}$ si el área interfacial aumenta, y aumentando según $L_{z,-1} = L_{z,0}(1 + \Delta\mathcal{A}^*)^{-1}$ si el área interfacial disminuye (Fig. 6.2).

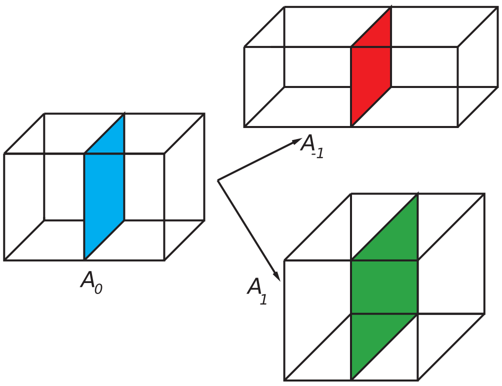

Figura 6.2: Perturbación del estado de referencia 0 mediante aumento (estado 1) o disminución (estado -1) del área interfacial. En ambos casos la dimensión z debe responder de forma que el volumen del sistema permanezca constante.

El parámetro adimensional $\Delta\mathcal{A}^*$ es fijado al inicio de la simulación y representa la pequeña variación en el área interfacial $\Delta\mathcal{A} = \mathcal{A}_0\Delta\mathcal{A}^*$ (es asumido positivo en todo este desarrollo). Las coordenadas de las partículas son igualmente transformadas de forma que mantengan sus posiciones relativas en término de los ejes de la caja de simulación. Al igual que en la metodología VP, las configuraciones de los estados perturbados, generadas en este caso mediante una variación del área, solamente se utilizan para evaluar una diferencia de energía libre pero no afectan al muestreo del sistema de referencia.

Si $\mathcal{U}_0(\mathbf{r}^N)$ representa la energía configuracional del estado 0 de referencia con área $\mathcal{A}_0$ y $\mathcal{U}_1(\mathbf{r}^N)$ la energía configuracional del estado perturbado 1 con área $\mathcal{A}_1$, la Eq. (6.2) puede expresarse como

$$\frac{Q_1}{Q_0} = \frac{\int d\mathbf{r}^N \exp\left(-\beta\mathcal{U}_0(\mathbf{r}^N)\right)\exp\left(-\beta\Delta\mathcal{U}(\mathbf{r}^N)\right)}{\int d\mathbf{r}^N \exp\left(-\beta\mathcal{U}_0(\mathbf{r}^N)\right)} \tag{6.16}$$

Si igual que en la metodología VP tenemos en cuenta la forma en que calculamos los promedios en el ensemble, la Eq. (6.16) anterior representa el factor de Boltzmann de la variación $\Delta\mathcal{U}$ promediado sobre el estado del sistema no perturbado. La variación energía libre de la Eq. (6.1) toma la forma

$$\Delta F_{0\to 1} = -k_B T \ln\left\langle \exp\left(-\frac{\Delta\mathcal{U}}{k_B T}\right)\right\rangle_0 \tag{6.17}$$

Entonces la tensión superficial puede determinarse a partir de su definición termodinámica (Eq.(6.13)) como una extrapolación de perturbaciones infitesimales del área interfacial

$$\gamma = \lim_{\Delta\mathcal{A}\to 0}\left(\frac{\Delta F_{0\to 1}}{\Delta\mathcal{A}}\right)_{NVT} = \lim_{\Delta\mathcal{A}\to 0}\frac{-k_B T}{\Delta\mathcal{A}}\ln\left\langle \exp\left(-\frac{\Delta\mathcal{U}}{k_B T}\right)\right\rangle_0 \tag{6.18}$$

En las simulaciones de este trabajo, el TA se llevado a cabo cada 10 ciclos de movimientos MC de todas las partículas. En cada TA se plantean dos perturbaciones independientes desde un mismo estado de referencia, una de aumento y otra de disminución del área interfacial, de forma que calculamos por separado los promedios de cada factor de Boltzmann correspondientes a cada cambio de la energía libre, y obtenemos dos valores de la tensión superficial, γ^+ y γ^-, según

$$\gamma^+ = \lim_{\Delta\mathcal{A}\to 0} -\frac{k_B T}{\Delta\mathcal{A}}\ln\left\langle \exp\left(-\beta\,\Delta U^+\right)\right\rangle \quad y \quad \gamma^- = \lim_{\Delta\mathcal{A}\to 0} -\frac{k_B T}{\Delta\mathcal{A}}\ln\left\langle \exp\left(-\beta\,\Delta U^-\right)\right\rangle \tag{6.19}$$

El valor de la tensión superficial vendrá dado por

$$\gamma = \frac{\gamma^+ + \gamma^-}{2} \tag{6.20}$$

Para realizar estas perturbaciones infinitesimales deberemos usar valores apropiados de $\Delta\mathcal{A}^*$, y aunque el método TA no es tan sensible al valor de $\Delta\mathcal{A}^*$ [96] como el caso de VP al valor de ξ [16]. Su valor por un lado debe ser lo suficientemente pequeño para obtener la precisión deseada en el cálculo de γ desde la Eq. (6.18), y lo suficientemente grande como para proporcionar una estadística razonable del factor de Boltzmannn. Un valor adecuado para fluidos LJ es $\Delta\mathcal{A}^* = \Delta\mathcal{A}/\mathcal{A}_0 = \pm 0.0005$ [4, 11, 13, 65, 89, 96, 97]. Éste ha sido el valor utilizado en el trabajo relativo cadenas flexibles LJ en el capítulo 12 de este trabajo. En las simulaciones de moléculas esféricas LJ (trabajos de los capítulos 9 y 10), donde el coste de tiempo de computación no ha sido un factor a tener tan en cuenta como en el trabajo de cadenas flexibles LJ, el esquema seguido ha sido similar al planteado por Sampayo et al.(2010) [91] (similar también al planteado en el método que hemos visto en el apartado anterior para VP [16]), queriendo así recoger el sentido de realmente evaluar el límite $\Delta\mathcal{A} \to 0$. Para ello se han llevado a cabo perturbaciones independendientes, positivas y negativas, del área interfacial para un conjunto de 8 valores de $\Delta\mathcal{A}^*$ en el rango de $2 \times 10^{-4} \leq |\Delta\mathcal{A}^*| \leq 15 \times 10^{-4}$, y obtenido el promedio del correspondiente factor de Boltzmannn para cada una de ellas. El valor de la tensiones superficiales, γ^+ y γ^-, se ha obtenido mediante una extrapolación de $\Delta\mathcal{A} \to 0$ mediante el ajuste lineal de los promedios obtenidos para la serie de perturbaciones, positivas y negativas, para los diferentes valores de $\Delta\mathcal{A}^*$. El valor final de la tensión superficial vendrá dado de nuevo por la Eq. (6.20).

Capítulo 7

Métodos termodinámicos no perturbativos

En este capítulo se expone la metodología seguida para la determinación de la presión de vapor de cadenas flexibles SW similar a la utilizada en el trabajo de MacDowell y Blas (2009) [14] para cadenas flexibles LJ. La metodología permite conocer la presión de vapor de forma indirecta combinando la simulación en el ensemble GCMC (apartados 2.2.3 y **??**) con la integración termodinámica. Aunque aparentemente esta combinación deriva en una metodología lenta desde el punto de vista de trabajo del simulador, es sin embargo sencilla y robusta. El objetivo de una integración termodinámica es calcular la diferencia en una propiedad termodinámica del sistema entre un estado de referencia y un estado de interés. La medida de dicha variación desde el estado inicial al final se caracteriza por una variación infinitamente lenta de los parámetros termodinámicos que caracterizan al sistema de tal manera que en cada paso a lo largo del camino el sistema se encuentra en equilibrio, asegurándonos que el proceso es reversible. A diferencia de un experimento real, donde estamos limitados por unas pocas variables termodinámicas tales como el volumen, la presión o la temperatura para controlar el camino de intergración, en un experimento de simulación molecular son posibles una gran variedad de caminos reversibles y estados de referencia. En nuestro caso la simulación previa en GCMC nos permite obtener un camino donde el potencial químico, a una temperatura dada, varía con la densidad, mediante simulaciones en fases homogeneas de vapor con una rápida convergencia para cada uno de los puntos. Este potencial químico es posteriormente integrado isotérmicamente haciendo uso de la relación de Gibbs-Duhem. La estimación de la incertidumbre asociada a la integración termodinámica ha sido estimada haciendo uso del *método sintético* propuesto por de Miguel (2008) [12].

También se exponen en este capítulo los elementos básicos de la metodoloía WIM (Wandering Interface Method) propuesta por MacDowell and Bryk (2007) [10] y utilizada en este trabajo de tésis, como herramienta para el cálculo de la tensión superficial de cadenas SW en el equilibrio líquido-vapor. Se engloba dentro de las nuevas metodologías de simulación que han sido propuestas en estos últimos años, y que nos permite determinar la tensión superficial de una forma fácil elegante de calcular la tensión superficial en una gran cantidad de sistemas complejos, como aquellos que interactúan mediante el potenciales discontinuos como el potencial intermolecular SW. El método se basa en un claro y atractivo fundamento físico: dado que una interfase tiene generalmente un coste energético extra, el sistema intentará acomodarse para minimizar el área interfacial. La característica principal del WIM es permitir que el área interfacial del sistema fluctúe libremente y determinar la energía libre de la superficie a partir de la distribución de probabilidad asociada al área de la superficie interfacial.

7.1 Integración termodinámica para el cálculo de la presión de vapor y análisis sintético para la estimación de errores

En una situación de coexistencia de fases líquido-vapor, en un sistema de un solo componente, la situación de equilibrio en términos de variables intensivas requiere que: $T_L = T_V$ (equilibrio térmico), $P_L = P_V$ (equilibrio mecánico), y $\mu_L = \mu_V$ (equilibrio con respecto al flujo de materia). Como consecuencia de que la relación fundamental $U = U(S, V, N)$ es una función de estado homogenea (de primer orden) en las variables extensivas tenemos una restricción en la variación simultanea de T, P y N en una fase. Dicha restricción viene dada por la relación de Gibbs-Duhem [98]

$$SdT - VdP + Nd\mu = 0 \tag{7.1}$$

de forma que ahora en el equilibrio de fases se cumple

$$\begin{aligned} T_L &= T_V \\ P_L &= P_V \\ \mu_L(T_L, P_L) &= \mu_V(T_V, P_V) \end{aligned} \tag{7.2}$$

La relación de Gibbs-Duhem es el punto de arranque de la metodología de integración termodinámica utilizada. Si fijamos la temperatura del sistema $dT = 0$ y la Eq. (7.1) se reduce a la ecuación diferencial

$$dP = \rho\, d\mu \tag{7.3}$$

donde $\rho = N/V$. En principio con la Eq. (7.3) podemos calcular la presión del sistema si conocemos la densidad ρ en función del potencial químico μ. Si lo hacemos a la inversa, es decir, tratando el potencial químico como una función de la densidad $\mu = \mu(\rho)$ de forma que

$$d(\rho\mu) = \rho\, d\mu + \mu\, d\rho \quad \rightarrow \quad \rho\, d\mu = d(\rho\mu) - \mu\, d\rho \tag{7.4}$$

Por tanto, la ecuación diferencial fundamental es ahora

$$dP = d(\rho\mu) - \mu\, d\rho \tag{7.5}$$

Sea un sistema arbitrario, y dos estados cualesquiera, caracterizados por densidades y potenciales químicos (ρ_0, μ_0) y (ρ, μ), de forma que podemos integrar la ecuación anterior a lo largo de una isoterma que una ambos estados del siguiente modo

$$\int_{P_0}^{P} dp = \int_{\rho_0\mu_0}^{\rho\mu} d(\rho\mu) - \int_{\rho_0}^{\rho} \mu\, d\rho \tag{7.6}$$

$$P = P_0 + \rho\,\mu - \rho_0\,\mu_0 - \int_{\rho_0}^{\rho} \mu(\rho')\, d\rho' \tag{7.7}$$

Consideremos ahora, además de nuestro sistema, un sistema ideal (no existen interacciones intermoleculares) de forma que haciendo uso de la Eq. (7.7) tenemos

$$P^{id} = P_0^{id} + \rho\,\mu^{id} - \rho_0\,\mu_0^{id} - \int_{\rho_0}^{\rho} \mu^{id}(\rho')\, d\rho' \tag{7.8}$$

Hemos considerado, para integrar y aplicar la ecuación anterior, los dos mismos estados, a densidades ρ_0 y ρ. Restando las Eqs. (7.7) y (7.8) tenemos

$$P - P^{id} = P_0 - P_0^{id} + \rho(\mu - \mu^{id}) - \rho_0(\mu_0 - \mu_0^{id}) - \int_{\rho_0}^{\rho} \Big[\mu(\rho') - \mu^{id}(\rho')\Big]\, d\rho' \tag{7.9}$$

Tomaremos como estado (0) un estado en el que $\rho_0 \to 0$. Esto significa que en dicho estado (0) el sistema real se comporta como un gas ideal

$$\lim_{\rho_0 \to 0} P_0 = P_0^{id} \qquad \lim_{\rho_0 \to 0} \mu_0 = \mu_0^{id} \tag{7.10}$$

y por tanto la Eq. (7.9) queda simplificada según

$$P = P^{id} + \rho(\mu - \mu^{id}) - \int_{0}^{\rho} \Big[\mu(\rho') - \mu^{id}(\rho')\Big]\, d\rho' \tag{7.11}$$

Teniendo en cuenta que el potencial químico residual $\mu_r(\rho) = \mu(\rho) - \mu^{id}(\rho)$ es una función de la densidad al igual que $P = P(\rho)$ y $P^{id} = P^{id}(\rho)$, la ecuación fundamental para llevar a cabo la integración termodinámica para determinar la presión de vapor del sistema, y en particular, a la densidad de coexistencia del equilibrio LV (ρ_V) vendrá dada a partir de la Eq. (7.11) por

$$P(\rho_V) = P^{id}(\rho_V) + \rho_V\, \mu_r(\rho_V) - \int_0^{\rho_V} \mu_r(\rho')d\rho' \tag{7.12}$$

Evidentemente para poder llevar a cabo esta integración necesitamos conocer el potencial químico residual en función de la densidad $\mu_r = \mu_r(\rho)$. El procedimiento para determinar la presión de vapor del equilibrio LV pasa por seleccionar la temperatura a lo largo de la cual se llevará a cabo la integración termodinámica y haciendo uso del ensemble GCMC simulamos a lo largo de la fase vapor (sistema homogeneo). Con objeto de construir un camino donde variamos el potencial químico con la densidad se realizan entre 10 y 20 simulaciones (n_{simu}) de estados termodinámicos correspondientes a diferentes valores del potencial químico, desde valores muy pequeños (que corresponden a densidades de cadena muy bajas $\cong 10^{-7} - 10^{-8}$) hasta densidades que superen claramente la ρ_V, es decir, desde el límite de gas ideal hasta un vapor supersaturado. Pero cuando muestreamos la densidad, ¿cómo sabemos que superamos el valor de la ρ_V?. La respuesta a esta cuestión parte de que el valor de ρ_V es conocido, ya que la presión puede calcularse a posteriori después de hacer simulaciones NVT en coexistencia directa donde hemos calculado el valor de dicha densidad de vapor. Pero además, debemos tener la precaución de que entre en la zona de metaestabilidad (es decir, entre la curva binodal y la curva espinodal) para lo cual exploraremos hasta densidades de aproximadamente el doble del valor de ρ_V. Este último aspecto requiere de cierta paciencia y habilidad del simulador, aunque es fácil saber cuándo (en términos del potencial químico de entrada) sobrepasamos la línea espinodal, porque entonces el sistema pasa directamente a fases líquidas, y las simulaciones son sustancialmente mucho más largas, pasando de escasos minutos de simulación de las fases de vapor a simulaciones entorno a 30 minutos.

Las simulaciones GCMC son divididas en una fase de equilibración y otra de producción. Los ciclos de producción son divididos adecuadamente en M bloques descorrelacionados, o estadísticamente independientes, de forma que la densidad correspondiente a cada potencial químico se obtiene como un promedio sobre esos M bloques. En cuanto a los tamaños de caja tenemos que tener en cuenta que estamos simulando gases muy diluidos, y se comprueba en las simulaciones la independencia de $\mu_r = \mu_r(\rho)$ con el tamaño de caja, eligiendo cajas de simulación grandes (un ejemplo típico $L_x = L_y = L_z = 90\sigma$) con objeto de tener mayor número de moléculas y mejorar la estadística.

Con objeto de obtener un camino continuo para hacer la integración termodinámica, una vez obtenido, para una temperatura dada, un conjunto de puntos del potencial químico residual μ_r para cada densidad muestreada, ajustamos el potencial químico como una función de la densidad mediante una función polinómica

$$\mu_r(\rho) = \sum_{i=1}^{n} b_i\, \rho^{i-1} \tag{7.13}$$

En principio, no son necesarias funciones más complejas, ya que el potencial químico residual μ_r es prácticamente lineal con la densidad ρ. Con esta parametrización polinómica del potencial químico podemos resolver fácilmente la contribución de la integral en la Eq. (7.12)

$$\int_0^{\rho_V} \mu_r(\rho')d\rho' = \int_0^{\rho_V} \sum_{i=1}^{n} b_i\, {\rho'}^{\,i-1} d\rho' = \sum_{i=1}^{n} b_i \int_0^{\rho_V} {\rho'}^{\,i-1} d\rho' = \sum_{i=1}^{n} \frac{b_i}{i} \rho_V^i \tag{7.14}$$

Introduciendo que $P^{id}(\rho_V) = \rho_V T$ (supondremos unidades reducidas a partir de ahora), la parametrización dada por la Eq. (7.13) y la contribución de la Eq. (7.14), en la Eq. (7.12), obtenemos la expresión general para la presión

$$P(\rho_V) = \rho_V\, T + \sum_{i=1}^{n} b_i \left(1 - \frac{1}{i}\right) \rho_V^i \tag{7.15}$$

Mencionar que con objeto de verificar la robustez de los resultados, se ha ajustado $\mu_r(\rho)$ a polinómios de grado 1 a 5 ($n = 2, 3, 4, 5$ donde n es el límite superior del sumatorio), no existiendo diferencias apreciables en ninguna propiedad (P y μ_r) cuando se usan $n = 3, 4, 5$, con lo que se puede afirmar que en las simulaciones de cadenas LJ [14] y SW el procedimiento de ajuste es en esencia independiente de grado del polinomio de ajuste.

LLegados a este punto, nos planteamos la estimación de la incertidumbre asociada a la ecuación de estado para la presión dada en la Eq. (7.15), ya que la propagación de errores através del ajuste del potencial químico (Eq. (7.13)) y posterior integración (Eq. (7.14)) no puede ser descrita de forma analítica. Para ello se ha segido el método propuesto por de Miguel (2008) [12] obteniendo una distribución gaussiana para la presión de vapor a cada temperatura a partir de la generación de una réplica potencial (datos sintéticos) del conjunto de datos de la simulación.

Para iniciar el procedimiento contamos con una serie de datos iniciales (0): para una temperatura dada contamos con el conjunto de puntos del integrando $(\rho_i^{(0)}, {\mu_r}_i^{(0)})$ $(i = 1, \ldots, n_{simu})$ correspondiente a las diferentes simulaciones para construir el camino hasta la densidad de vapor $\rho_V^{(0)}$. Tal y como hemos visto, ${\mu_r}_i^{(0)}$ es ajustado a un polinomio de orden n en ρ, por lo que P depende paramétricamente de dicha familia de parámetros ajustables. Denominaremos a esta familia de parámetros por $\{b_m^{(0)}\}$ $(m = 1, \ldots, n)$ y por $P^{(0)} \equiv P(\{b_m^{(0)}\}; \rho_V^{(0)})$ a la presión para un valor de ρ_V con estos parámetros de ajuste en particular. Para la estimación de la incertidumbre asociada a la integral dada en la Eq. (7.14) asuminos la hipótesis de que la densidad ρ se distribuye de forma gaussiana, es decir, podemos decir que $\rho_i^{(0)} \pm \sigma_{\rho_i^{(0)}}$ y $\rho_V^{(0)} \pm \sigma_{\rho_V^{(0)}}$ (asumimos que se mantiene el teorema del límite central). Ahora la implementación práctica comprende los pasos:

1. Generamos un conjunto de k datos sintéticos para la densidad $\{\rho_i^{(k)}\}$, $\rho_V^{(k)}$ (5×10^6 conjuntos). Para ello $\rho_i^{(k)} = \rho_i^{(0)} + \xi_i$, donde ξ_i es un número aleatorio sacado de una distribución gaussiana con valor medio cero y desviación estándar $\sigma_{\rho_i^{(0)}}$.
2. Encontramos los parámetros de ajuste de los datos sintéticos $\{b_m^{(k)}\}$, y el valor de la presión $P^{(k)}$ correspondiente. Ahora la distribución de datos sintéticos de la presión sigue una distribución gaussiana con valor medio $P^{(0)}$, es decir

$$\mathcal{P}(P) = \frac{1}{\sigma_P \sqrt{2\pi}} \exp\left(-\frac{(P - P^{(0)})^2}{2\sigma_P^2}\right) \tag{7.16}$$

3. Finalmente asociamos la desviación estándar de esta distribución gaussiana con la incertidumbre asociada a la presión ($P \pm \sigma_P$ o $P \pm 2\sigma_P$ para un nivel del confianza del 68% o del 95% respectivamente).

7.2 Método Wandering Interface (WIM)

La técnica WIM es una extensión del ensemble NPT en el que se permite que el área interfacial fluctúe aleatoriamente. Esto se logra introduciendo un nuevo movimiento MC, que consiste en intentos de deformar la caja de simulación mediantecambios en el área interfacial manteniendo el volumen del sistema constante. Los intentos de movimientos son aceptados de acuerdo a las reglas de esquema Metropolis, de manera que se introduce un camino aleatorio de Markov del área interfacial. La tensión superficial se calcula mediante el análisis de las distribución de probabilidad del área interfacial $P(\mathcal{A}) = \exp(-\beta\gamma\mathcal{A})$, obteniendo la pendiente mediante el ajuste de mínimos cuadrados del $\ln P(\mathcal{A})$.

El área interfacial es muestreada de forma que, después de cada ciclo MC de movimiento de moléculas, se propone un nuevo valor de prueba $\mathcal{A}_n = \mathcal{A}_0 + \Delta\mathcal{A}$. Puesto que el sistema se va amoldando de manera continua, puede darse la situación en la que la superficie interfacial desapareciera, por lo que $\Delta\mathcal{A}$ debe ser seleccionado cuidadosamente, y de manera uniforme, en el intervalo $[-\Delta\mathcal{A}_{min}, \Delta\mathcal{A}_{max}]$. Elintento de variación del área interfacial es aceptado con probabilidad

$$\min\left[1, \exp(-\beta(\mathcal{U}_n - \mathcal{U}_0 + \mathcal{W}_n - \mathcal{W}_0)\right] \tag{7.17}$$

donde $\mathcal{U}_n - \mathcal{U}_0$ es la variación en la energía configuracional del sistema asociada a la deformación del área interfacial. Como es esencial mantener las fluctuaciones del área interfacial en el intervalo adecuado, la elección de la función $\mathcal{W}$ es un punto realmente clave en el método para ayudar al sistema a conseguir el adecuado estado de equilibrio. En el trabajo original, de la metodología WIM, MacDowell y Bryk proponen, como mejor elección, la función de sesgo

$$e^{-\beta W(\mathcal{A})} = \begin{cases} 0 & \mathcal{A} < \mathcal{A}_{min} \\ 1 & \mathcal{A}_{min} < \mathcal{A} < \mathcal{A}_{max} \\ 0 & \mathcal{A} > \mathcal{A}_{max} \end{cases} \tag{7.18}$$

Obviamente, la elección adecuada del intervalo $[-\Delta\mathcal{A}_{min}, \Delta\mathcal{A}_{max}]$ no es un tema trivial y su discusión puede consultarse en el propio trabajo original [10].

Capítulo 8

Anexos

8.1 Obtención de datos a partir de perfiles de densidad

Una interfase aparece cuando dos fases coexisten en una transición de fase de primer orden, separando una fase de *bulk* de la otra. Aunque no es una superfie matemática, si tenemos una anchura interfacial t a lo largo de la cual las propiedades varían de los valores tomados en una fase de bulk a los valores tomados en la otra fase de bulk. Por ejemplo, en una interfase vapor-líquido la densidad variará de forma continua de ρ_V a ρ_L, las densidades de coexistencia de vapor y de líquido. El cuidado tratamiento del perfil de la densidad $\rho(z)$ se hace esencial por cuanto nos va a permitir la obtención de datos como: densidades de coexistencia (ρ_L y ρ_V), temperatura (T_c) y densidad ρ_c críticas, y anchura interfacial (Gibbs dividing surface).

Para obtener el perfil de la densidad, a lo largo de la dirección z de la caja de simulación, dividimos la caja en n_s capas (*slabs* o *bines*) de grosor $\Delta z = (L_z/n_s)$ paralelos al plano xy. El perfil de densidad de moléculas se obtiene promediando, una vez equilibrado el sistema, el número de moléculas $\langle N(z)\rangle$ en una capa de grosor Δz centrada en z

$$\rho(z) = \frac{\langle N(z)\rangle}{V_s} \tag{8.1}$$

donde V_s $(= L_x L_y \Delta z)$ es el volumen de un slab. Puntualizar que en el caso de cadenas moleculares los perfiles de la densidad se han calculado siempre en base a unidades monoméricas. El valor del grosor del slab Δz se escoge en el compromiso de que sea lo suficientemente pequeño para una buena discretización del sistema y lo suficientemente grande para obtener una buena precisión estadística. En este trabajo se ha elegido un número de slabs de forma que $\Delta z \approx 0.05$ ha sido el valor usual. Las fluctuaciones en el perfil de la densidad se minimizan promediando sobre un número lo sufientemente largo de ciclos. Como la determinación del perfil de la densidad es un proceso relativamente rápido, se ha calculado en cada ciclo de computación, teniendo en cuenta que en cada ciclo se intentan movimientos MC de cada una de las moléculas. Además, con objeto de mejorar la visualización y la comparación, los perfiles de densidad son desplazados de manera que el centro de masas del sistema coincida con el centro de la caja de simulación. Esta transformación se lleva en el código haciendo uso de variables locales que jamás entran dentro de la cadena de Markov, ya de que lo contrario podríamos estar introduciendo un efecto de una fuerza externa al sistema.

Las densidades de coexistencia, definidas por las zonas de bulk líquido y vapor, se obtienen promediando $\rho(z)$ sobre las correspondientes zonas lo suficientemente alejadas de la zona interfacial.

Dado que las simulaciones líquido-vapor se han preparado según una zona de bulk líquido central rodeada a izquierda y derecha por bulks de vapor (con condiciones de contorno periódicas), la densidad de coexistencia del vapor la obtenemos promediando el perfil de la densidad a ambos lados de la capa de bulk líquido. El error estadístico de ρ_V y ρ_L se estima mediante la desviación estándar de los valores medios.

A la hora de considerar un sistema inhomogeneo podemos dividirlo en tres partes: dos fases de bulk con volúmenes V_L y V_V, y la interfase σ. Aunque existen modelos, como por ejemplo el propuesto por Guggemgheim, en donde se extiende la región interfacial y se tiene en cuenta su volumen, el modelo de Gibbs es ampliamente utilizado y de fácil aplicación. En el modelo de Gibbs la interfase es infinitamente delgada ($V_\sigma = 0$) y el volumen total es $V = V_L + V_V$ (Fig. 8.1). Por supuesto es una idealización por lo que a la *Gibbs dividing surface* (así es comunmente conocida en la literatura) también se le denomina interfase ideal. El modelo se elige de forma que sus propiedades extensivas (volumen V, energía interna, entropía S, y número de partículas N) sean iguales a las del sistema real. Lógicamente las propiedades extensivas de cada una de las fases del modelo no pueden ser iguales que en el sistema real, ya que en la idealización se ha eliminado una parte del sistema (la región interfacial). En esta situación, el volumen de las fases V_L y V_V dependerá de dónde esté localizada la interfase. La clave del modelo está en asignar a la superficie divisoria valores de las propiedades extensivas para que el modelo tenga valores iguales a los del real. Estas propiedades asignadas a la *Gibbs dividing surface* se conocen como propiedades de exceso superficial (V_σ, U_σ, S_σ y N_σ)

$$V = V_L + V_V \tag{8.2}$$

$$U = U_L + U_V + U_\sigma \tag{8.3}$$

$$S = S_L + S_V + S_\sigma \tag{8.4}$$

$$N = N_L + N_V + N_\sigma \tag{8.5}$$

Por ejemplo, la cantidad de exceso superficial ni N_σ será la diferencia entre el número de partículas en el sistema real y el número de partículas que existiría si las fases fueran homogéneas hasta la superficie divisoria. Esta cantidad de exceso puede ser positiva, nula o incluso negativa.

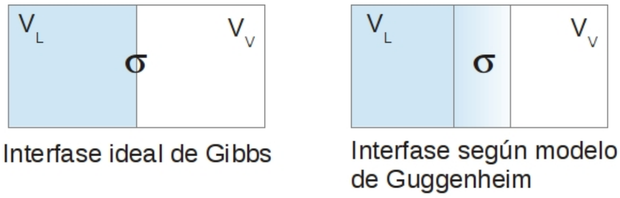

Figura 8.1: Izquierda: convenio de Gibbs donde las dos fases están separadas por una interfase σ infinitamente delgada. Derecha: Guggemheim explicita el tratamiento de la interfase como un volumen.

Pero el modelo ideal de Gibbs presenta un problema: ¿dónde está localizada la interfase ideal?. Si la interfase está dividida en dos partes separadas por un plano imaginario localizado en $z = z_0$, la fase líquida se extiende por debajo de $z = z_0$, donde $\rho(z)$ se aproxima a el valor del bulk líquido, ρ_L, mientras que para $z > z_0$, $\rho(z)$ tiende a tomar el valor de la fase de bulk vapor, ρ_V. Las adsorciones de líquido y vapor, Γ_L y Γ_V, se definen como las integrales sobre las regiones ① y ② en la Fig. 8.2:

$$\Gamma_L = \int_{-\infty}^{z_0} [\rho(z) - \rho_L] dz < 0 \tag{8.6}$$

$$\Gamma_V = \int_{z_0}^{+\infty} [\rho(z) - \rho_V] dz > 0 \tag{8.7}$$

La localización de la *Gibbs dividing surface* es arbitraria, pero comunmente es posicionada de forma que las regiones ① y ② posean igual área, en cuyo caso la adsorción total $\Gamma = \Gamma_L + \Gamma_V$ es cero (equivalente a decir $N\sigma = 0$) [1,99]. Por supuesto no deja de ser un convenio o un criterio. Para interfases planas la tensión interfacial está unívocamente definida y no depende de la posición de la superficie ideal [2,99,100].

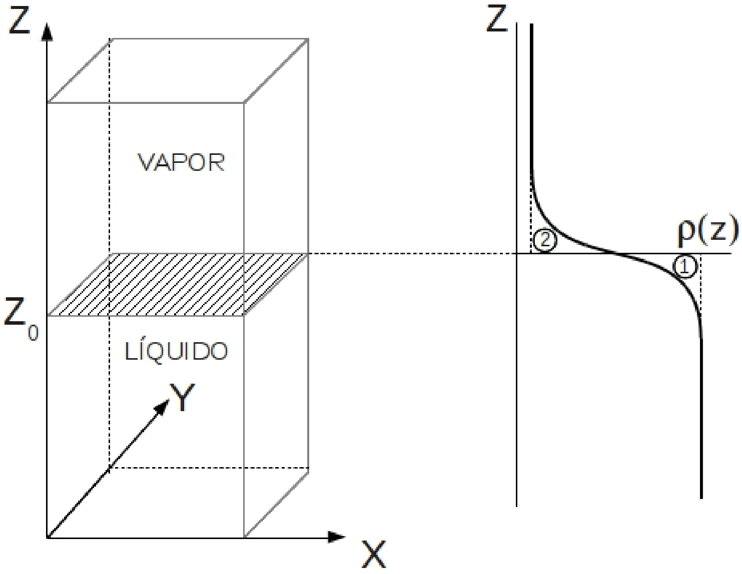

Figura 8.2: Localización de la Gibbs dividing surface para el criterio de adsorción total $\Gamma = \Gamma_L + \Gamma_V$ es cero.

El perfil $\rho(z)$, obtenido en la simulación, puede ajustarse a una forma funcional del tipo de tangente hiperbólica [2,13,34,56,101]

$$\rho(z) = \frac{1}{2}(\rho_L + \rho_V) - \frac{1}{2}(\rho_L + \rho_V) \tanh\left(\frac{z - z_0}{d}\right)$$

donde ρ_L, ρ_V, y z_0 son, en general, parámetros ajustables correspondientes a las densidades de coexistencia de líquido y vapor, y la posición de la Gibbs dividing surface. El parámetro d es una medida de la anchura interfacial la cual es sustituida por $t = 2.1972d$ o anchura interfacial "10-90". La anchura interfacial t corresponde a la distancia a lo largo de la interfase sobre la cual la densidad varía del 10% al 90% del cambio de la densidad total entre las fases de bulk, es decir, la distancia desde $[\rho_V + (0.1)(\rho_L - \rho_V)]$ hasta $[\rho_V + (0.9)(\rho_L - \rho_V)]$. La anchura interfacial así estimada resulta ser menos sensible a la forma del perfil que la anchura d [5].

Así pues, las densidades ρ_L y ρ_V son sustituidas por los valores obtenidos previamente promediando sobre las zonas de bulk, y d y z_0 serán parámetros que obtenemos del ajuste. Como se ha comentado anteriormente, el sistema se prepara con dos interfases líquido-vapor con lo cual el valor de d se obtiene como el promedio de las anchuras interfaciales de ambas interfases. La ausencia de fluctuaciones, la simetría del perfil de la densidad con respecto al punto medio del slab de líquido, o incertidumbres estadísticas de d del mismo orden, suelen ser indicadores de una buena equilibración del sistema inhomogeneo.

Por último, conocer las densidades de coexistencia también nos permite el obtener la localización del punto crítico, es decir, la temperatura crítica T_c y la densidad crítica ρ_c. Para ello tendremos en cuenta el comportamiento asintótico dado por la relación de escala para el ancho de la curva de coexistencia,

$$\rho_L - \rho_V = A(T - T_c)^{\beta} \quad (\beta = 0.325) \tag{8.8}$$

y la regla de los diámetros rectilíneos

$$\frac{\rho_L + \rho_V}{2} = B + CT \tag{8.9}$$

donde A, B, y C son constantes, y β es el correspondiente exponente crítico (ver sección siguiente).

8.2 Exponentes críticos y escalado universal

Desde un punto de vista termodinámico una transición de fase ocurre cuando hay una singularidad en la energía libre o en una de sus derivadas. Lo que es con frecuencia visible en estos fenómenos es un cambio repentino en las propiedades de la sustancia, estando definido el número máximo de fases en coexistencia por la regla de fases de Gibbs. Sobre la línea de equilibrio de fases LV (en el plano (P, T) podemos terminar en lo que se conoce como punto crítico, de manera que la distinción de fases que existe para $P < P_c$ y $T < T_c$, desaparece, y podemos decir que las dos fases son idénticas. A más altas presiones, $P > P_c$, hay una sola e indiferenciada fase fluida y no se puede evaporar por mucho que se aumente la temperatura por encima de la T_c. Cuando hay un punto crítico, se puede efectuar una transición continua entre dos estados sin que llegue a separarse en dos fases. Para lograr esto, el estado debe variarse a lo largo de una curva que pase alrededor del punto crítico y que en ningún punto intercepte a la curva de equilibrio. Es claro que el punto crítico puede existir solamente para fases cuya diferencia es puramente cuantitativa, por ejemplo un líquido y un gas que se diferencian solamente en el grado de interacción de las moléculas exhibiendo el mismo tipo de simetrías, siendo la única diferencia entre ellos en una transición su densidad.

Cerca de un punto crítico de un fluido se presentan fluctuaciones en la densidad a todas las escalas. Precisamente, en el punto crítico la escala de las más grades fluctuaciones llega a ser infinita pero las fluctuaciones más pequeñas bajo ninguna forma desaparecen. Este comportamiento crítico no se observa solamente en fluidos. En la década de los 70, Wilson [102] introducía las técnicas del grupo de renormalización que permitían cálculos sobre fases condensadas que fluctúan fuertemente, y algunos fenómenos que aparentemente parecen ser distintos, a un nivel más profundo, son idénticos y pueden describirse todos bajo una misma teoría.

A los fenómenos observados cerca del punto crítico, y referidos en la literatura como fenómenos críticos, se les suele asociar el concepto de parámetro de orden. El parámetro de orden, terminología introducida originalmente por Landau y que denominaremos genericamente $\vec{\phi}$, se identifica con una variable termodinámica extensiva, de forma que la característica fundamental del parámetro de orden es que por debajo de la temperatura crítica T_c es una función decreciente de T y se anula para T_c, por ejemplo $\phi = \rho_L - \rho_G$. Para T muy cerca de T_c, los estudios experimentales muestran un comportamiento como ley de potencia $(T_c - T)^{\beta}$, donde β es el denominado exponente crítico. Es precisamente sobre estos exponentes donde se han centrado cada vez más los estudios de fenómenos críticos. Resulta muy importante para la teoría de fenómenos críticos entender a un nivel más fundamental la forma de las divergencias y el comportamiento singular de variables termodinámicas cerca de un punto crítico. Si definimos ϵ como una variable sin dimensión para medir la desviación de la temperatura con respecto a la temperatura crítica

$$\epsilon = \frac{T - T_c}{T_c} = \frac{T}{T_c} - 1 \tag{8.10}$$

entonces el exponente crítico asociado con una función $F(\epsilon)$ es

$$\lambda = \lim_{\epsilon \to 0} \frac{\ln |F(\epsilon)|}{\ln |\epsilon|} \tag{8.11}$$

o usualmente también

$$F(\epsilon) \approx |\epsilon|^\lambda \tag{8.12}$$

donde el símbolo $\approx$ indica un comportamiento asintótico de la forma funcional $F(\epsilon)$ cuando ϵ tiende a cero. Una relación en forma de ley de potencia como la expresada en la Eq. (8.12) es un invariante de escala. La idea básica que subyace detrás de una ley de escala está relacionada con la divergencia de la longitud de correlación en el punto crítico. Asumimos que esta es la única escala espacial relevante del problema, esto es, que las propiedades que determinan la forma de las funciones termodinámicas ocurren en una escala espacial de dimensión lineal del orden de ξ. Ante esta suposición, un cambio en los parámetros termodinámicos (por ej., la temperatura) en las cercanías del punto crítico equivaldría a un cambio de escala. En otras palabras, cuando $\xi \gg 1$ podemos esperar que los detalles a pequeñas escalas se tornen irrelevantes. Un cambio en los parámetros termodinámicos que me acerque al punto crítico va a aumentar ξ; si asumimos que los detalles de pequeñas escalas son irrelevantes, al aumentar ξ esperamos ver más o menos lo mismo, pero en una escala distinta. Las leyes de potencia pertenecen a una clase más general de funciones invariantes por escala, las funciones homogéneas generalizadas. Se define una función homogénea generalizada como aquella que satisface

$$f(\lambda^{a_1} x_1, \lambda^{a_2} x_2, \ldots, \lambda^{a_n} x_n) = \lambda f(x_1, x_2, \ldots, x_n) \quad \forall \lambda, a_i \in \mathbb{R} \tag{8.13}$$

En 1965 Widom proponía la hipótesis de que en las proximidades de un punto crítico la energía libre no cambia su forma funcional sino solamente cambia su escala, de forma que si λ es un parámetro arbitrario, existen dos números, a_T y a_B, de forma que la energía libre cerca del punto crítico satisface

$$\lambda G(t, B) = G(\lambda^{a_T} t, \lambda^{a_B} B) \tag{8.14}$$

donde t es la temperatura reducida con respecto a la temperatura crítica $t = T/T_c$, y y B es la variable intensiva que resulta de derivar la energía libre respecto del parámetro de orden (por ejemplo en un fluido la presión). A partir de esta hipótesis es posible expresar los exponentes críticos en función de los parámetros de dimensionalidad [103] [1]

$$\alpha = 2 - \frac{1}{a_T} \quad \beta = \frac{1 - a_B}{a_T} \quad \gamma^\dagger = \frac{2a_B - 1}{a_T} \quad \delta = \frac{1 - a_B}{a_B} \tag{8.15}$$

Los exponentes críticos no son independientes y pueden obtenerse relaciones entre ellos también conocidas como leyes de escala (Tabla 8.2). La obtención de algunas de estas relaciones puede parecer trivial a partir de las Eq. (8.15), pero ni mucho menos aquellas que implican los exponentes ν, η y la dimensionalidad del sistema d, que nos llevaría a las ideas más fundamentales y modernas de la teoría de grupo de renormalización (RGT).

---

[1] El superíndice † se ha añadido para no confundir el exponente crítico $\gamma^\dagger$ con la simbología utilizada en este trabajo para la tensión superficial.

Tabla 8.1: Definiciones de los principales exponentes críticos en fluidos [5], [104].

Calor específico a volumen constante	$C_V \sim A^{\pm}\|1-t\|^{-\alpha}$	$T \to T_c^{\pm}$	$\alpha \simeq 0.11$
Diferencia densidades líquido-vapor	$\rho_L - \rho_V \sim B\|1-t\|^{\beta}$	$T \to T_c^{-}$	$\beta \simeq 0.325$
Compresibilidad isotérmica	$\chi \sim C^{\pm}\|1-t\|^{-\gamma^{\dagger}}$	$T \to T_c^{\pm}$	$\gamma^{\dagger} \simeq 1.24$
Isoterma crítica	$\|P-P_c\| \sim D\|\rho-\rho_c\|^{\delta}$	$T = T_c$	$\delta \simeq 4.81$
Longitud de correlación	$\xi \sim \xi_0^{\pm}\|1-t\|^{-\nu}$	$T \to T_c^{\pm}$	$\nu \simeq 0.63$
Función de correlación par	$g(r) \sim G/r^{d-2+\eta}$	$\overset{T\to T_c}{r \to \infty}$	$\eta \simeq 0.23$

Tabla 8.2: Relaciones entre exponentes críticos o leyes de escala [104], [103].

Relación de Rushbrooke	$\alpha + 2\beta + \gamma = 2$
Relación de Griffiths	$\alpha + \beta(\delta + 1) = 2$
Relación de Widom	$\gamma^{\dagger} = \beta(\delta - 1)$
Relación de Fisher	$\gamma^{\dagger} = (2-\eta)\nu$
Relación de Josephson (hiperscaling)	$d\nu = 2 - \alpha$

Los valores de los exponentes críticos han llegado a ser mucho más relevantes que la misma temperatura crítica que se asocia a un fenómeno crítico en particular. Resulta que, mientras T_c depende sensiblemente de los detalles con que ocurren las interacciones entre los constituyentes atómicos de un sistema, los exponentes críticos son en un alto grado universales puesto que dependen solamente de unos pocos parámetros universales. Estos parámetros suelen ser la dimensionalidad d del espacio donde tienen lugar las interacciones y la dimensionalidad n del parámetro de orden, que definen diferentes categorías o clases de universalidad. Por ejemplo $d = 3$ y $n = 1$ para un fluido cerca del punto crítico con parámetro de orden la diferencia de densidades [102]. Miembros de una misma clase de universalidad tendrán distinta T_c pero los mismos exponentes críticos, diferentes amplitudes críticas pero razones universales (por ejemplo $A^+/A^-, C^+/C^-, \ldots$), o mismas funciones de escala como por ejemplo la curva de coexistencia $\rho/\rho_c(T/T_c)$ [105]. Las ideas de universalidad en fenómenos críticos han arrojado mucha luz en la elaboración de las teorías que explican sus propiedades. Es usual que para modelar un sistema físico se tome la ruta de incluir todas las complicadas interacciones entre sus constituyentes atómicos. Una ruta alternativa, es escribir el modelo más simple posible que incluya la física esencial del problema y que prometa una solución analítica o numérica precisa. El proposito de este tipo de enfoque es estudiar el comportamiento universal que gobierna toda una clase dada de materiales.

Exponente crítico asociado a la tensión superficial líquido-vapor y *parachor*

Al aumentar la temperatura la energía cinética de las moléculas en un líquido y la tendencia de éstas a escapar hacia fuera aumentan, por lo tanto la tensión superficial disminuye. A medida que la temperatura se acerca a la temperatura crítica, disminuye la fuerza ejercida sobre las moléculas de la superficie y al llegar a la temperatura crítica, la tensión superficial se desvanece y la interfase desaparece. Haciendo uso del principio de los estados correspondientes Guggenheim propuso en 1945 una relación empírica entre la tensión superficial γ y la temperatura T. Esta aproximación de es capaz de correlacionar tensiones superficiales vapor-líquido de un número de sustancias con un excelente acuerdo con los datos experimentales [105],

$$\gamma = \gamma_0 \left(1 - T/T_c\right)^{11/9} \tag{8.16}$$

donde γ_0 representa la tensión superficial a "temperatura cero". Modernamente la teoría de grupo de renormalización establece que la tensión superficial vapor-líquido se desvanece cuando $T \to T_c^-$ siguiendo la relación de escala [5],

$$\gamma \sim |1 - t|^{\mu} \tag{8.17}$$

donde μ es el exponente crítico asociado a la tensión superficial vapor-líquido. Este exponente crítico está asociado con la longitud de correlación de las fluctuaciones de la densidad (ξ) mediante la relación de hiperscaling propuesta por Widom en la década de los sesenta [106], $\mu = (d-1)\nu$. Dado que para un fluido la dimensionalidad del sistema es $d = 3$ y tomando el valor del exponente crítico de la longitud de correlación $\nu = 0.629$ obtenemos un valor de $\mu = 1.258$, que es un valor muy próximo al encontrado por Guggenheim, $\mu = 11/9 \approx 1.22$, usando la relación empírica de la Eq. (8.16).

Otra aproximación empírica de interés es la relación entre la tensión superficial vapor-líquido y la diferencia entre las densidades de coexistencia, propuesta por MacLeod en 1923 [107],

$$\gamma = C(\rho_L - \rho_V)^p \tag{8.18}$$

donde C es una constante característica del líquido y $p = 4$.

La justificación que MacLeod hace del valor de p es sencilla; cuando elevamos la temperatura de un líquido sus moléculas son conducidas a separarse y la fuerza de atracción entre ellas se hace menor. La ecuación de Van der Waals se basa en la suposición de que la fuerza decae como la cuarta potencia de la distancia entre las moléculas. La tensión superficial de un líquido es una función de la distancia y por lo tanto de la densidad. La ecuación es seguida con considerable precisión por muchos líquidos sobre un amplio rango de temperaturas alrededor el punto crítico. La constancia del cociente $\gamma^{1/4}/(\rho_L - \rho_V)$ sobre un amplio rango de temperaturas hizo pensar en algo más fundamental, ese "algo" debería de estar relacionado de algún modo con la estructura química de la sustancia en particular. Sugden [108] siguiendo la aproximación de MacLeod, escribió la Eq. (8.18) como

$$\frac{M\gamma^{1/4}}{(\rho_L - \rho_V)} = [P] \tag{8.19}$$

Introducía así la masa molecular M de la sustancia y $[P]$, un nuevo componente en la ecuación, que denominó *parachor*. Al exponente $p = 4$ de la Eq. (8.18) se le suele denominar exponente de parachor. Si tenemos en cuenta que ρ_V es mucho menor que ρ_L cuando estamos lejos del punto crítico, el parachor representa el volumen molar de una sustancia cuando su temperatura es tal que la tensión superficial es la unidad.

Sugden, basándose en observaciones como por ejemplo las relativas a compuestos isoméricos de la misma familia que tenían parachors muy similares, o que la diferencia entre parachors de números sucesivos de series homólogas (por ejemplo etano-propano, propano-butano, …) es aproximadamente constante, concluyó que el parachor es una propiedad aditiva que contiene infomación estructural. Es decir, que el parachor de un determinado compuesto químico puede expresarse como la suma de un parachor atómico (que contiene la contribución de cada uno de los átomos que constituyen la molécula) y de un parachor estructural (en el cual hay contribuciones de los diversos enlaces presentes en la estructura de la molécula),

$$[P] = \sum [P_i]^{atomo} + \sum [P_i]^{enlace} \tag{8.20}$$

Correlacionando valores experimentales con estructuras moleculares, Sugden (1924) calculó parachors atómicos (C, H, O, N, Cl,...) y estructurales (enlace simple, doble, coordinado, anillo de 3 carbonos, 6 carbonos, ...). Valores que fueron posteriormente revisados y/o ampliados por Mumford and Phillips (1929) [109] y Vogel (1948) [110]. Durante las siguientes tres decadas posteriores al trabajo de Sugden los estudios basados en el parachor se convirtieron en una poderosa herramienta en algunos problemas de determinación de estructuras de compuestos químicos.

Para comprender la relación del parachor propuesta por Macleod, desde un punto de vista más fundamental, podemos escribir la relación de escala dada por la Eq. (8.17) en términos de la diferencia entre las densidades de vapor y de líquido. Para ello combinamos la Eq. (8.17) con la conocida relación de escala cerca del punto crítico para la diferencia de densidades vapor-líquido en función de la temperatura (Tabla 8.1), gobernada por el exponente crítico β, de forma que

$$\gamma \sim |1-t|^{\mu} \sim (\rho_L - \rho_V)^{\mu/\beta} \sim (\rho_L - \rho_V)^{(d-1)\nu/\beta} \tag{8.21}$$

Si comparamos la expresión anterior con la Eq. (8.18) obtenemos un valor para el exponente de parachor, obtenido mediante los exponentes críticos de la teoría de grupo de renormalización, de $p = (d-1)\nu/\beta = 3.86$. Valor que es muy similar al propuesto por Macleod ($p = 4$) pero menor que éste, situación que ya era comentada por Guggenheim [105] su trabajo sobre el principio de los estados correspondientes donde ofrecía un valor para el exponente de parachor de $p = 11/3 \approx 3.67$.

Ahora bien, ¿sería posible usar la descripción anterior para encontrar una relación universal que describa el comportamiento de la tensión superficial vapor-líquido de varias sustancias? El conocido principio de los estados correspondientes ha mostrado ser de una gran utilidad para caracterizar un comportamiento universal de fluidos simples. Si las propiedades presión, volumen y temperatura las dividimos (reducimos) por sus correspondientes valores críticos, la función de estado que relaciona la presión reducida con el volumen reducido y la temperatura reducida resulta ser la misma para todas las sustancias. En el marco de referencia del principio de los estados correspondientes Guggenheim [105] argumentaba que la tensión superficial reducida con respecto a dos propiedades críticas debe ser una función universal de t, la temperatura reducida con respecto a la temperatura crítica. Si tenemos en cuenta las tres propiedades críticas (T_c, P_c, y ρ_c), es posible definir diferentes formas de reducir la tensión superficial. La elección de Guggenheim, ampliamente utilizada en la literatura , está dada por [92,105,111,112]

$$\gamma_{r1} = \gamma \, (k_B T_c)^{-1} \, (M/\rho_c)^{-3/2} = \frac{\gamma}{k_B T_c \, (M/\rho_c)^{3/2}} \tag{8.22}$$

donde M es la masa molecular de la sustancia.

Galliero [113] también propone una forma de reducir la tensión superficial, que proporciona similares resultados a la Eq. (8.22), haciendo uso de la temperatura crítica, T_c, y la presión crítica, P_c, según

$$\gamma_{r2} = \gamma^* \, (k_B T_c)^{-1/3} \, P_c^{-3/2} = \frac{\gamma^*}{(k_B T_c)^{1/3} \, P_c^{3/2}} \tag{8.23}$$

La tensión superficial, reducida bien por la Eq. (8.22) o por la Eq. (8.23), posee un comportamiento de universalidad en función de t, como indican numerosos autores para modelos de fluidos con simetría esférica [92,105,111,112], además de para algunos fluidos reales simples [114], exceptuando sistemas con interacciones específicas como los enlaces de hidrógeno [113,115]. Independientemente de cual de las dos formas tomemos para reducir la tensión superficial, desafortunadamente, tal y como apunta Galliero [113], no es capaz de predecir un comportamiento universal para cadenas de moléculas LJ al presentar una dependencia con la longitud de la cadena. Sin embargo, como también indica Galliero, la tensión superficial reducida exhibe un comportamiento de universalidad cuando se representa como una función de $(\rho_L - \rho_V)/\rho_c$, siendo posible escribir una combinación de la relación de escala propuesta originalmente por Guggenheim y la aproximación de parachor de Macleod según

$$\gamma_{r_i} = [P_i]\left(\frac{\rho_L - \rho_V}{\rho_c}\right)^{\alpha} \tag{8.24}$$

donde en este caso α es el exponente de parachor y [P] que depende solamente de la forma en que reducimos la tensión superficial ($i = 1$ para Eq. (8.22) e $i = 2$ para la Eq. (8.23)).

Un breve epitafio histórico ...

Me permito la licencia, en parte por deformación docente ya que en mis clases suelo recordar a los olvidados de la ciencia, de aludir el trabajo de un físico experimental que en el año 1900 publicó resultados idénticos a los que en la década de los sesenta darían lugar a las ideas modernas sobre las transiciones de fase, J.E. Verschaffelt [116–118].

Este físico belga llega en 1893 a Amsterdan a estudiar con van der Waals y se traslada en el curso siguiente a Leiden a trabajar en un incipiente grupo liderado por Kammerlingh Onnes, que junto con el grupo de Ramsay constituían los dos grupos más activos en el estudio de propiedades generales de fluidos. A su llegada a Leiden estaba candente el problema de verificar el exponente crítico que van der Waals había predicho con su teoría para explicar el comportamiento de la tensión superficial de un líquido con la temperatura. En 1984 se utilizaba por primera vez una relación crítica en el estudio de la relación de la tensión superficial con la temperatura

$$\gamma \sim (T - T_c)^n \tag{8.25}$$

donde n calculado de acuerdo con su teoría debería de ser igual a $3/2$ ($n = 1.5$). K.Onnnes se echaba a cuestas la tarea de comprobar experimentalmente este valor cuando apareció un minucioso trabajo de Ramsay y Shields con datos experimentales de γ en un amplio espectro de temperaturas, obteniéndose valores de 1.23. El mismo valor era obtenido paralelamente por de Vries, estudiante de K.Onnes.

Tal era la situación cuando Verschaffelt llegó a Leiden que su primer trabajo fue repetir las mediciones de de Vries cubriendo un intervalo más amplio de temperaturas (situación con la cual se puede identificar cualquier doctorando en la actualidad). Así encontró $n = 1.311$ con el CO_2, 1.133 para el N_2O y finalmente 1.27 para el éter. Concluiría que sus resultados se aproximaban más al 1.5 calculado por de van der Waals. Además, éste último ya le había manifestado a K.Onnes que los valores de n menores que el valor teórico serían cada vez más cercanos a éste cuanto más se acercaran las mediciones experimentales a la T_c. Cabe resaltar que por aquel entonces era muy difícil acercarse a la temperatura crítica por el lado de la fase líquida. En su afán experimental obtendría nuevos puntos experimentales para el CO_2 acercándose a tan solo $0.5°C$ de T_c. A la vez comprendía que para el cálculo de la tensión superficial requería de los valores de las densidades de las fases coexistentes a esas temperaturas. Por aquellos tiempos los datos existentes todavía no habían sido analizados para ver si concordaban con la conocida curva, cuasi-parabólica, que predecía la teoría clásica para $\rho_L - \rho_G$. En un trabajo de análisis estadístico realmente brillante mostró que el exponente crítico β mantenía un valor constante y aproximadamente igual a 0.367, en total desacuerdo con la teoría de van der Waals. Además, n seguía siendo menor que 1.5.

Hasta el año 1900 seguiría trabajando con K.Onnes en otros problemas pero aparentemente la forma de la curva de coexistencia nunca dejó de inquietarle. En ese mismo año S.Young, colaborador de Ramsay, publicó datos muy precisos para las isotermas y densidades de coexistencia del isopentano. Aplicando sobre estos datos la misma técnica aplicada en años antes para el CO_2 encontró que todo el conjunto de datos ajustaba para $\beta = 0.3434$. Pero Verschaffelt no se detuvo aquí. Con gran rigor estudió la consecuencias de sustituir el valor de $3/2$ de la teoría clásica, por una fracción menos simple, y llegó a proponer una forma para las isotermas que en lugar de las ecuaciones cúbicas de van der Waals, eran ecuaciones en las cuales los exponentes de volumen eran fraccionarios, muy similar a las modernas ecuaciones de estado cerca del punto crítico. Logró incluir todos los datos de Young en una sola ecuación, la cual, para la T_c ofrecía un valor de $\delta = 4.259$, un valor muy diferente del valor 3 de van der Waals.

Hasta su muerte, en 1955, siempre volvió de una manera u otra a este problema, manteniendo la convicción de que los resultados eran correctos y que había fallos en la teoría de van der Waals. A pesar de que fueron publicados y de hecho conocidos por el propio van der Waals y por K. Onnes, nunca fueron reconocidos. Entre 1945 y 1970 se desató con verdadero furor un interés marcado por examinar de nuevo las cuestiones básicas, teóricas y experimentales, detrás de las transiciones de fase, y los resultados de Verschaffelt fueron redescubiertos en la decada de los sesenta. J.M.H Levet Senger escribió en [116] que se hizo oidos sordos del trabajo de Verschaffelt, siendo la principal causa que "sembró en una roca", ya que cada idea necesita ser madurada y demandada. Por otro lado, Senger también apunta a que casi todo su trabajo lo escribió en alemán, lo que supuso un obstáculo en la difícil tarea que suponía la comunicación científica en aquellos tiempos.

Durante años, fue secretario del Instituto Internacional de Física Solvay ...y en la famosa foto de 1927 ocupaba la tercera fila inmediatamente a la derecha de A.Einstein. En esta conferencia de Solvay, sobre "Electrones y Fotones", Einstein discutía con Niels Bohr y comentó "Usted cree en un Dios que juega a los dados", a lo que Bohr le contestó "Einstein, deje de decirle a Dios lo que debe hacer con sus dados".

Parte II

Resultados y conclusiones

Capítulo 9

Effect of dispersive long-range corrections to the pressure tensor. The vapour-liquid interfacial properties of the Lennard-Jones system revisited

The Journal of Chemical Physics 141, 184701 (2014)

F. J. Martínez-Ruiz[1,2], F. J. Blas[1,2], B. Mendiboure[3], and A. I. Moreno-Ventas Bravo[2,4]

[1]Departamento de Física Aplicada, Universidad de Huelva, 21071, Huelva, Spain

[2]Centro de Investigación de Física Teórica y Matemática, Universidad de Huelva, 21071, Huelva, Spain

[3]Laboratoire des Fluides Complexes et leurs Réservoirs, UMR5150, Université de Pau et des Pays de l'Adour, B. P. 1155, Pau Cedex 64014, France

[4]Departamento de Geología, Facultad de Ciencias Experimentales, Universidad de Huelva, 21071 Huelva, Spain

We propose an extension of the improved version of the inhomogeneous long-range corrections of Janeček [J. Janeček, *J. Phys. Chem. B* **129**, 6264 (2006)], presented recently by MacDowell and Blas [L. G. MacDowell and F. J. Blas, *J. Chem. Phys.* **131** 074705 (2009)] to account for the intermolecular potential energy of spherical, rigid, and flexible molecular systems, to deal with the contributions to the microscopic components of the pressure tensor due to the dispersive long-range corrections. We have performed Monte Carlo simulations in the canonical ensemble to obtain the interfacial properties of spherical Lennard-Jones molecules with different cutoff distances, $r_c = 2.5$, 3, 4, and 5σ. In addition, we have also considered cutoff distances $r_c = 2.5$ and 3σ in combination with the inhomogeneous long-range corrections proposed in this work. The normal and tangential microscopic components of the pressure tensor are obtained using the mechanical or virial route in combination with the recipe of Irving and Kirkwood, while the macroscopic components are calculated using the Volume Perturbation thermodynamic route proposed by de Miguel and Jackson [E. de Miguel and G. Jackson, *J. Chem. Phys.* **125** 164109 (2006)]. The vapour-liquid interfacial tension is evaluated using three different procedures, the Irving-Kirkwood method, the difference between the macroscopic components of the pressure tensor, and the Test-Area methodology. In addition to the pressure tensor and the surface tension, we also obtain density profiles, coexistence densities, vapour pressure, critical temperature and density, and interfacial thickness as functions of temperature, paying particular attention to the effect of the cutoff distance and the long-range corrections on these properties. According to our results, the main effect of increasing the cutoff distance (at fixed temperature) is to sharpen the vapour-liquid interface, to decrease the vapour pressure, and to increase the width of the

biphasic coexistence region. As a result, the interfacial thickness decreases, the width of the tangential microscopic component of the pressure tensor profile increases, and the surface tension increases as the cutoff distance is larger. We have also checked the effect of the impulsive contribution to the pressure due to the discontinuity of the intermolecular interaction potential when it is cut. If this contribution is not accounted for in the calculation of the microscopic components of the pressure tensor, incorrect values of both components as well as a wrong structure along the vapour-liquid interface are obtained.

9.1 Introduction

The phenomenology associated to fluid-fluid interfacial properties has fascinated scientifics since the time of Laplace and Young [5]. The determination of interfacial properties, and particularly surface tension, has been always an ambitious and challenging goal for many computer simulation researchers of the liquid-state community. Understanding how different microscopic mechanisms determine the thermodynamic and structural behaviour of systems that exhibit a fluid-fluid interface is essential in a large number of scientific and engineering fields, including nucleation or dynamics of phase transition, among many others. However, the fluid-fluid surface tension is probably the most challenging property to be determined and predicting using molecular-based theories and simulation techniques. Despite the number of studies carried out since computer simulation is used routinely for determining the properties of a molecular model, the calculation of surface tension is still a subtle problem. The ambiguity in the definition of the microscopic components of the pressure tensor [4,73], the finite size effects due to capillary waves [119, 120], or the difficulty for the calculation of the dispersive long-range corrections (LRC) associated to the intermolecular interactions [14, 15], make the calculation of surface tension a difficult and non-trivial problem.

The usual procedure to the evaluation of the fluid-fluid interfacial tension in a molecular simulation involves the determination of the microscopic components of the pressure tensor through the well-known mechanical or virial route. This route states that surface tension of a planar fluid-fluid interface can be readily obtained from the integration of the difference between the normal $P_N(z)$ and tangential $P_T(z)$ microscopic components of the pressure tensor profiles along the interface as,

$$\gamma = \int_0^{L_z} \left(P_N(z) - P_T(z)\right)\, dz \tag{9.1}$$

Note that here we have chosen the z-axis perpendicular to the interface and the integral is performed along the total length L_z of the simulation box. Care must be taken in cases in which there exist two vapour-liquid interfaces, which is the standard procedure for studying direct fluid-fluid coexistence in Monte Carlo (MC) and Molecular Dynamics (MD) simulation. In this case, the true value associated to a single interface is half of the value obtained from Eq. (9.1).

This method generally involves an ensemble average of the virial of Clausius according to the recipes of Irving and Kirkwood [62] or Harasima [63], among many others possible choices. Although the mechanical route is especially appropriate when molecular dynamics techniques are used to determine the interfacial tension of a system, since the evaluation of the forces is required to determine the molecular trajectories, a number of alternative methods have been proposed during the last years to calculate, not only the interfacial tension, but also for the components of the pressure tensor, without the need of evaluate the virial. The origin of these new techniques is probably due to the increasing capacity of computers for calculating larger and more complex systems and the interest of the condensed matter community for understanding from a molecular perspective the mechanisms that control the macroscopic behaviour of interfaces of fluids.

These alternative methods are especially suited in Monte Carlo simulations, in which the calculation of the forces is not required for sampling the configurational space of the system. In addition to that, although the evaluation of the virial is straightforward in systems interacting through simple intermolecular potentials, this is not the case for complex intermolecular interactions, including those governing the microscopic behaviour of chain-like molecules or system with specific interactions, and particularly models in which the intermolecular potential is discontinuous, such as the hard-sphere and square-well potentials, and in cases in which specific interactions are modeled as associating square-well sites, among others. In this situation, the evaluation of forces can be difficult and very time consuming. Exceptions to this rule in the literature are the works of Chapela, Alejandre and coworkers [121–124], and Malfreyt and coworkers [125, 126].

The new generation of alternative methods for determining the surface tension and the components of the pressure tensor constitute a collection of effective and elegant techniques based on the thermodynamic definition of these properties. Consider a system in which the number of particles, N, the volume V, and temperature T are constant. Under these conditions, the appropriate definition of surface tension γ can be written as,

$$\gamma = \left(\frac{\partial F}{\partial \mathcal{A}}\right)_{NVT} \tag{9.2}$$

The surface tension can be understood as the change in free energy F of the system for an infinitesimal change in the interfacial area, $\mathcal{A}$, while keeping N, V, and T constant. Assuming the same conditions, the diagonal components of the pressure tensor of the system, $P_{\alpha\alpha}$, with $\alpha = x, y, z$, following de Miguel and Jackson [16], can be expressed using its thermodynamic definition as,

$$P_{\alpha\alpha} = -\left(\frac{\partial F}{\partial V}\right)_{NTL_{\beta\neq\alpha}} \tag{9.3}$$

The notation $L_{\beta\neq\alpha}$ indicates that the partial derivative with respect to the volume is performed in such a way that the dimension of the system along the α-axis, L_α, is varied while keeping all other dimensions L_β ($\beta \neq \alpha$) fixed.

Eqs. (9.2) and (9.3) allow two different interpretations for calculating the surface tension and the components of the pressure tensor. In the first approach, the one we focus on exclusively in this work, equations can be written using basic Statistical Mechanics as configurational averages over the unperturbed system of surface area $\mathcal{A}$ and volume V of appropriate Boltzmann factors. These expressions (see Eq. (60) of the original work of Gloor *et al.* [4], and Eqs. (8)-(9) and (16)-(17) of the work of de Miguel and Jackson [16] for further details) suggest that both magnitudes can be calculated averaging the corresponding Boltzmann factors associated with virtual changes of surface area and volume, respectively. This approach corresponds to perturbative approaches such as the Test-Area (TA) technique [4] for the surface tension and the Volume Perturbation (VP) methods for the determination of the macroscopic components of the pressure tensor [16, 50, 51]. These methods are becoming very popular and are being used routinely to determine the vapour-liquid interfacial properties of Lennard-Jones (LJ) [13, 14, 76, 113], several models of water [89, 127], the Mie potential [92], binary mixtures [75, 128, 129], or real systems [65, 83, 96, 97, 126, 130, 131] among others.

Another interpretation for calculating the surface tension and the components of the pressure tensor using the thermodynamic definition of both magnitudes, given by Eqs. (9.2) and (9.3), is possible. In the former approach, they are evaluated averaging Boltzmann factors using virtual changes of the system, i.e., the perturbed states generated during the simulation do not correspond to real states sampled along the Markov chain generated during the simulation. Because of that most of these methods receive the generic name of perturbative methods. The second class of methods that exploit the use of Eqs. (9.2) and (9.3) are non-perturbative techniques, in which the interfacial area is sampled along the simulation, i.e., states with unperturbed and perturbed interfacial areas are explicitly considered in the Markov chain of the simulation. Representative examples of methods that follow this approach are the use of the Expanded Ensemble (EE), based on the original work of Lyuvartsev *et al.* [87], for calculating the surface tension proposed independently by Errington and Kofke [11] and de Miguel [12], and the Wandering Interface Method (WIM), introduced by MacDowell and Bryk [10]. In the first method, states of the system are sampled through a global set of sub ensembles, with different interfacial areas, allowing to calculate the difference in free energy between states (basically, the surface tension) in terms of the probability of finding the system in these states [11,12]. The second methodology, the WIM technique, can be viewed as a continuous version of the EE method in which the interfacial area is allowed to fluctuate randomly and the surface tension can be obtained from the analysis of the resulting probability distribution. The WIM approach has been successfully used for determining the fluid-fluid and solid-fluid interfacial tension of a variety of complex systems [13, 14, 132–134].

As mentioned previously, one of the major difficulties encountered in the simulation of inhomogeneous systems by molecular simulation is the truncation of the intermolecular potential. Although for homogeneous systems this issue is easily solved by including the well-known homogeneous LRC [2,3], the situation is much more complicated in the case of fluid-fluid interfaces, and in general, in inhomogeneous systems. Fortunately, this problem seems to solved satisfactorily recently in cases in which the system exhibits planar symmetry. Different authors have contributed to the establishment of appropriate and standard inhomogeneous LRC, including Blokhius [135], Mecke [38, 79], Daoulas [136], Guo and Lu [137], and finally, Janeček [15, 138], and the recent improved methods proposed by MacDowell and Blas [14] and de Gregorio *et al.* [133].

The truncation of the intermolecular potential has important effects on the calculation of any physical property. In general, all properties exhibit a dependence with the cutoff distance, but the relative effect is different depending on the specific magnitude. Though the density profiles, coexistence densities, and critical coordinates are affected by the truncation, the interfacial thickness and more particularly the surface tension show a stronger dependence on the particular choice of the cutoff distance [9, 13–15, 139]. The effect of truncation on the surface tension was already noted by the seminal work of Chapela *et al.* [34] and discussed very nicely by Trokhymchuk and Alejandre [9]. These later authors also analyzed in detail the truncation procedure and the presence of an additional force due to the discontinuity of the truncated potential at the cutoff distance. This additional force due to the discontinuity of the truncated potential at cutoff distance becomes crucial for inhomogeneous fluids and has to be included into the virial calculation in both Monte Carlo and Molecular Dynamics, as well as into the computation for interactions in Molecular Dynamics simulations.

Although different authors have recently considered the effect of truncating and applying the appropriate LRC to systems that interact through the spherical LJ intermolecular potential [4,15,139] on the surface tension, the number of studies devoted to determine the effect of using different cutoff distances for the intermolecular potential on the components of the pressure tensor is really scarce.

The main goal of this work is two fold. First, we propose an improved version of the original LRC of Janeček [15], based on a previous work of one of us to deal with the intermolecular potential energy [14], to estimate the LRC associated to the microscopic components of the pressure tensor of a spherical model in a planar fluid-fluid interface. Second, we revisit the interfacial properties of the LJ spherical model, including the density profiles, interfacial thickness, surface tension, and normal and tangential microscopic and macroscopic components of the pressure tensor. We also determine other thermodynamic properties, such as coexistence densities, vapour pressure, and critical temperature and density. In particular, we consider the spherical truncated (but not shifted) intermolecular potential with different cutoff distances, from $r_c = 2.5$ up to 5σ. We also pay special attention to the effect of neglecting the impulsive contribution to the components of the pressure tensor associated to the discontinuity of the potential at the the cutoff distance r_c. In addition to that, we also consider the full intermolecular potential, i.e., the potential truncated at $r_c = 2.5$ and 3σ with the version of inhomogeneous LRC of MacDowell and Blas [14] based on the Janeček's work [15] for the potential energy and the improved version proposed in this work for the components of the pressure tensor. In order to assess the effectiveness of the new methodology proposed, we have also determined the surface tension and the components of the pressure tensor using two different perturbative methods, the TA technique and the VP methodology. This allows to obtain independent results and compare our predictions with simulation data taken from the literature.

The rest of the paper is organized as follows. In Section 9.2 we consider an improved method for determining the contribution to the microscopic components of the pressure tensor due to the LRC of inhomogeneous spherical systems. The molecular model and the simulation details of this work are presented in Section 9.3. Results obtained are discussed in Section 9.4. Finally, in Section 9.5 we present the main conclusions.

9.2 Effective long-range pairwise corrections for the pressure tensor of spherical systems

In 2006, Janeček [15] proposed a new methodology for calculating long-range corrections (LRC) to the energy and pressure tensor in systems that interact through spherically symmetric intermolecular potentials. This procedure allows to treat in a simple way the truncation of the intermolecular energy of systems that exhibit planar interfaces. More recently, MacDowell and Blas [14] have demonstrated that the Janeček's procedure can be rewritten into an effective long-range pair potential plus a self term that allows for a fast, easy, and elegant implementation of the method. In this work we extend this improved version to deal with the long-range pair potential contributions to the components of the pressure tensor. Since the original methodology has been introduced elsewhere [15,138,140,141], the most important details corresponding to the LRC term to the components of the pressure tensor proposed by Janeček are provided in the Supplementary material [142]. Here we focus the attention to the extension of the improved version for dealing with the pressure tensor.

As mentioned previously, MacDowell and Blas [14] has proposed an improved methodology of the Janeček's method for dealing with the intermolecular interactions of an inhomogeneous system due to LRC. The method, which is simpler and more accurate, elegant, and easier to implement in a simulation code than the original one, has been applied successfully to calculate the interfacial properties of several models, including fully-flexible and rigid-linear Lennard-Jones chains [14, 143–145] and water and carbon dioxide [146]. Following the recipe of MacDowell and Blas [14, 146], Eq. (10) of the Supplemental material is written more accurately as,

$$\Pi_{\alpha\alpha}^{\mathrm{LRC}}(z_i) = \left\langle \int_{-\infty}^{+\infty} \pi_{\alpha\alpha}(|z_i - z|)\, \rho(z)\, dz \right\rangle \tag{9.4}$$

The density profile of a system formed by N particles can be written formally as a summation of δ-Dirac distributions centered at the positions z_j, with $j = 1, \ldots, N$

$$\rho(z) = \frac{1}{\mathcal{A}} \sum_{j=1}^{N} \delta(z - z_j) \tag{9.5}$$

where $\mathcal{A}$ is the interfacial area of the xy-plane of the system. Using Eq. (9.5) in Eq. (9.4), $\Pi_{\alpha\alpha}^{\mathrm{LRC}}(z_i)$ is given by

$$\Pi_{\alpha\alpha}^{\mathrm{LRC}}(z_i) = \left\langle \frac{1}{\mathcal{A}} \sum_{j=1}^{N} \pi_{\alpha\alpha}(|z_i - z_j|) \right\rangle \tag{9.6}$$

It is important to note that summation in Eq. (9.6) runs over all the values of the index j ($j = 1, \ldots, N$), and this also included the case $j = i$.

The total components of the virial tensor arising from the LRC, defined by Eq. (9) of the Supplemental material, is then expressed as

$$\Pi_{\alpha\alpha}^{\mathrm{LRC}} = \frac{1}{2} \sum_{i=1}^{N} \Pi_{\alpha\alpha}^{\mathrm{LRC}}(z_i) = \left\langle \frac{1}{2\mathcal{A}} \sum_{i=1}^{N} \sum_{j=1}^{N} \pi_{\alpha\alpha}(|z_i - z_j|) \right\rangle \tag{9.7}$$

The unrestricted summation over indexes i and j can be finally transformed into a sum of pairwise effective (integrated) intermolecular virial over all the pairs of molecules in the system and N self-energy terms as

$$\begin{aligned} \Pi_{\alpha\alpha}^{\mathrm{LRC}} &= \left\langle \frac{1}{\mathcal{A}} \sum_{i=1}^{N-1} \sum_{j=i+1}^{N} \pi_{\alpha\alpha}(|z_i - z_j|) \right\rangle + \left\langle \frac{1}{2\mathcal{A}} \sum_{i=1}^{N} \pi_{\alpha\alpha}(0) \right\rangle \\ &= \left\langle \frac{1}{\mathcal{A}} \sum_{i=1}^{N-1} \sum_{j=i+1}^{N} \pi_{\alpha\alpha}(|z_i - z_j|) \right\rangle + \left\langle \frac{N}{2\mathcal{A}} \pi_{\alpha\alpha}(0) \right\rangle \end{aligned} \tag{9.8}$$

The expressions given by Eqs. (9.6) and (9.8) are the key relationships that generalize the improved version proposed by MacDowell and Blas [14] for dealing with the components of the pressure tensor: the components of the pressure tensor due to the LRC are given by an effective pairwise components pressure tensor between all the particles forming the system.

The last term in Eq. (9.8), the self-tensor contribution, is not a truly summation of self virial tensor terms. In fact, the function $\pi_{\alpha\alpha}(z)$ is not a real contribution to the component of the virial tensor between a pair of particles but an effective (integrated) component of the virial tensor. Each contribution $\frac{1}{\mathcal{A}}\pi_{\alpha\alpha}(|z_i - z_j|)$ in Eq. (9.6) represents the contribution to the component of the virial tensor, due to the interactions between the particle i with all the particles located inside the slab centered at z_j due to the long-range interactions. Therefore, $\pi_{\alpha\alpha}(0)$ represents the contribution to the component of the virial tensor due to the interactions between a molecule and the rest of molecules located inside the same slab but beyond the cut-off radius.

This procedure provides several important advantages over the original method: (1) Eqs. (9.6) and (9.8) correspond to the exact evaluation of the components of the virial tensor due to the LRC. It is important to recall that the use of the original Janeček version of the method implies a discretization of the simulation box along the z-axis, which is in fact an approximation; (2) the improved procedure allows to evaluate $\Pi_{\alpha\alpha}^{\mathrm{LRC}}(z_i)$ and $\Pi_{\alpha\alpha}^{\mathrm{LRC}}$ without the explicit calculation of the density profile on the fly, i.e., it is not necessary to update the density profile $\rho(z)$ each Monte Carlo step, and consequently, to perform the double integral shown in the original work of Janeček (see Eq. (23) of the original paper [15]).

9.3 Model and simulation details

We consider spherical LJ molecules characterized by a diameter σ and dispersive energy ϵ. The interaction potential between two different molecules is given by,

$$u_{LJ}(r) = 4\epsilon\left[\left(\frac{\sigma}{r}\right)^{12} - \left(\frac{\sigma}{r}\right)^{6}\right] \tag{9.9}$$

where r is the distance between two molecules. During the simulation, we use a potential spherically truncated (but not shifted) at a cutoff distance r_c, defined by,

$$u(r) = u_{LJ}(r)\,\left[1 - \Theta(r - r_c)\right] = \begin{cases} u_{LJ}(r) & r \leq r_c \\ 0 & r > r_c \end{cases}, \tag{9.10}$$

where $\Theta(x)$ is the Heaviside step function.

We examine this spherically truncated potential model with several cutoff distances, $r_c = 2.5$, 3, 4, and 5σ. In addition to that, we study the interfacial and thermodynamic properties of spherically truncated LJ potential with $r_c = 2.5$ and 3σ considering inhomogeneous LRC using the MacDowell and Blas [14, 144] methodology for the intermolecular potential energy and the recipe presented in Section 9.2, based on the Janeček's method [15, 138], for the evaluation of the LRC for the components of the pressure tensor. Results obtained using these LRC are equivalent to use the full potential or a potential with infinite truncation distance.

The number of molecules, N, used in all the simulations performed in this work is constant, $N = 2048$. As in previous studies [13, 14, 133, 143–147], this choice is made so as to have systems with the same total number of molecules. Simulations are performed in the NVT ensemble. We consider a system of N molecules at a temperature T in a volume $V = L_x L_y L_z$, where L_x, L_y

and L_z are the dimensions of the rectangular simulation box. A homogeneous liquid system is first equilibrated in a rectangular simulation box of dimensions $L_x = L_y = 12\sigma$, and $L_z = 16.891\sigma$ for the lowest temperature considered ($T^* = k_B T/\epsilon = 0.70$), and $L_z = 21.153\sigma$ for the highest temperature ($T^* = 1.1$). The box is then expanded to three times its original size along the z direction, while leaving the liquid phase at the center with empty boxes of equal size at each side. The final overall dimensions of the vapour-liquid-vapour simulation box are therefore $L_x = L_y = 12\sigma$, and $L_z = 50.673\sigma$ for the lowest temperature considered ($T^* = 0.70$), and $L_z = 66.460\sigma$ for the highest temperature ($T^* = 1.1$).

The simulations are organized in cycles. A cycle is defined as N trial moves (displacement of the center of mass) and the magnitude of the appropriate displacement is adjusted so as to get an acceptance rate of $30\,\%$ approximately. We use periodic boundary conditions and minimum image convention in all three directions of the simulation box.

We have obtained the normal and tangential microscopic components of the pressure tensor from the mechanical expression or virial route. In particular, we have used the well-known Irving and Kirkwood (IK) recipe for determining the microscopic components of the pressure tensor, $P_N(z) \equiv P_{zz}(z)$ and $P_T(z) \equiv P_{xx}(z) \equiv P_{yy}(z) \equiv \frac{1}{2}(P_{xx}(z) + P_{yy}(z))$ [62]. As explained in Section 9.2, the simulation box is divided into slabs of width Δz and area $\mathcal{A}$ parallel to the interface (xy-plane). The contribution to the microscopic pressure tensor at each point of the simulation box, due to a pair of molecules i and j located at z_i and z_j, respectively, is obtained from the distribution of the pair virial among all slabs between z_i and z_j for both the normal and tangential components. Note that this also includes the contribution due to the LRC. In the improved version introduced in this work, based on the previous work of MacDowell and Blas [14,144], the contribution due to the LRC are written as an effective pairwise components of the pressure tensor between all the molecules, resulting an elegant and effective way of accounting for this contribution. In practice, to determine the contribution to the pressure due to a given pair of molecules we perform the following steps:

1. We evaluate the distance along the z-axis between the pair of molecules i and j, $|z_{ij}|$. To be consistent with the calculation of the intermolecular interactions performed during the simulation, the minimum image convention is also used when this contribution is calculated.

2. We then calculate the number of slabs between molecules i and j (after the minimum image convention is applied), including the slabs occupied by the molecules.

3. The contribution arising from the interactions between particles i and j, including the contribution due to LRC, is divided by the number of slabs obtained in point 2.

4. Finally, the pressure contribution obtained in point 3 is then assigned equally to each slab between positions z_i and z_j, including the slabs corresponding to positions z_i and z_j at which the molecules are located.

Since we are dealing with pairwise interactions, the total contribution to the components of the pressure tensor is obtained taking into account all the molecular pairs and averaging the total virial over the canonical ensemble. The final expression of the microscopic components of the pressure tensor are given by,

$$P_N(z) = \langle \rho(z)\, k_B T \rangle + P_N^{\mathrm{CUT}}(z) + P_N^{\mathrm{LRC}}(z) \tag{9.11}$$

The first term of the right-hand side of Eq. (9.11) corresponds to the ideal (kinetic) contribution to the microscopic pressure tensor. Note that this contribution is obtained from the value of the density profile at the same position z. The two other terms, $P_N^{\text{CUT}}(z)$ and $P_N^{\text{LRC}}(z)$, are the contributions to the normal microscopic component of the pressure tensor, $P_N(z)$, due to the direct interactions between molecular pairs and LRC, respectively. A similar expression is also valid for the tangential microscopic component $P_T(z)$.

The contribution to normal component of the pressure tensor due to the direct interactions between molecular pairs, $P_N^{\text{CUT}}(z)$, can be written as,

$$\begin{aligned} P_N^{\text{CUT}}(z) &= -\frac{1}{\mathcal{A}}\left\langle \sum_{i=1}^{N-1}\sum_{j=i+1}^{N} \frac{z_{ij}^2}{r_{ij}}\,\frac{\mathrm{d}u_{LJ}(r_{ij})}{\mathrm{d}r_{ij}}\,\frac{1}{|z_{ij}|}\,\Theta\left(\frac{z-z_j}{z_{ij}}\right)\Theta\left(\frac{z_j-z}{z_{ij}}\right)\right\rangle \\ &= -\frac{1}{\mathcal{A}\,\Delta z}\left\langle \sum_{i=1}^{N-1}\sum_{j=i+1}^{N} \frac{z_{ij}^2}{r_{ij}}\,\frac{\mathrm{d}u_{LJ}(r_{ij})}{\mathrm{d}r_{ij}}\,\frac{1}{n_{ij}})\right\rangle \end{aligned} \tag{9.12}$$

The corresponding contribution to the tangential component, $P_T^{\text{CUT}}(z)$, is given by an expression of the form of Eq. (9.12) but with $(x_{ij}^2+y_{ij}^2)/2$ instead of z_{ij}^2. Here the factor $1/n_{ij}\Delta z$, proportional to the product of $1/|z_{ij}|$ and the two Heaviside step functions, is used to select the position at which the interaction between particles i and j contributes to the pressure tensor. In practice, if particles i and j are located at slabs k_i and k_j, respectively, the number of the slabs located between them is $n_{ij}=|k_j-k_i|-1$.

Using Eqs. (7) and (9) of Supplemental material, Eq. (9.8), and taking into account the recipe of Irving and Kirkwood [62], the contribution to the normal component of the pressure tensor due to LRC, $P_N^{\text{LRC}}(z)$, can be written as,

$$P_N^{\text{LRC}}(z)=\frac{1}{\mathcal{A}\,\Delta z}\left\{\left\langle\frac{1}{\mathcal{A}}\sum_{i=1}^{N-1}\sum_{j=i+1}^{N}\pi_{zz}(|z_i-z_j|)\,\frac{1}{n_{ij}}\right\rangle+\left\langle\frac{1}{2\mathcal{A}}\pi_{zz}(0)\right\rangle\right\} \tag{9.13}$$

The corresponding contribution to the tangential component, $P_T^{\text{LRC}}(z)$, is given by an expression of the form of Eq. (9.13) but using $(\pi_{xx}+\pi_{yy})/2$ instead of π_{zz}. Here $\pi_{\alpha\alpha}(|z_i-z_j|)$, with $\alpha=x,y,z$, are the same functions defined previously by Eqs. (11) and (12) of Supplemental material. Note that function $w(z,z_i,z_j)$ is also used in Eq. (9.13). This means that the pressure due to the LRC associated to the virial of particles at z_i and z_j contributes to all the slabs located between them (including the slabs at positions z_i and z_j). The last term of the right-hand side of Eq. (9.13) represents the contribution to the pressure, due to the LRC, associated to the interaction between a particle and all the molecules located at the same slab. According to the meaning of this self-tensor contribution, as discussed previously in Section 9.2, and to be consistent with the Irving-Kirkwood recipe for the calculation of the microscopic components of the pressure tensor, this term contributes to the pressure at position at which each particle is located in the simulation box.

We have also determined the macroscopic components of the pressure tensor using virtual volume perturbations of magnitude $\xi=\Delta V/V$ each cycle. Here ξ defines the relative volume (compressive and expansive) change associated with the perturbation. We follow the methodology proposed by de Miguel and Jackson [16], based on the seminal works of Eppenga and Frenkel [94] and Harismiadis *et al.* [95], and rescale independently the box lengths of the simulation cell and positions of the molecular centers of mass according to linear transformations. In particular, the macroscopic average of the normal component of the pressure P_N is computed (see Eq. (60) of the original work of Gloor *et al.* [4], and Eqs. (16) and (17) of the work of de Miguel and Jackson [16]) by averaging the corresponding Boltzmann factor associated with a volume perturbation in which the normal dimension of the simulation cell is changed according to the transformation $L_z' = (1+\xi)L_z$ (including compression and expansion changes applied independently) while the transverse dimension remains unchanged. The macroscopic average of the tangential component P_T is calculated from the same equations by considering a perturbation in which the tangential dimension of the system is changed isotropically according to $L_\alpha' = (1+\xi)^{1/2}L_\alpha$, with $\alpha = x, y$ (including compression and expansion changes applied independently), keeping L_z fixed. In both cases, eight different (positive and negative) relative volume changes in the range $2\times 10^{-4} \le |\xi| \le 15\times 10^{-4}$ are used in our calculations. The final values of the macroscopic components of the pressure tensors presented in this work, P_N and P_T, correspond to the extrapolated values (as determined by a linear extrapolation to $|\xi| \to 0$ of the values obtained from increasing-volume and decreasing-volume perturbations) obtained from a combined compression-expansion perturbation.

Finally, we have also calculated the surface tension using of the TA methodology [4]. Since the method is a standard and well-known procedure for evaluating fluid-fluid interfacial tensions of molecular systems, here we only provide the most important features of the technique. For further details we recommend the original work [4] and the most important applications [13, 14, 16, 75, 89, 92, 96, 97, 127–129, 133, 143–147]. The implementation of the TA technique involves performing virtual or test area deformations of relative area changes defined as $\xi = \Delta\mathcal{A}/\mathcal{A}$ during the course of the simulation at constant N, V, and T every MC cycle. As shown by Gloor *et al.* [4], the surface tension follows from the computation of the change in Helmholtz free energy associated with the perturbation, which in turn can be expressed as an ensemble average of the corresponding Boltzmann factor. Further details can be found in Ref. [4] Note that the procedure for calculating the surface tension is similar to that used to evaluate the components of the pressure tensor, but in this case the changes in the normal and transverse dimensions are coupled to keep the overall volume constant. In particular, we use the same number and values for the relative area changes ξ, and the same procedure to obtain the extrapolated values.

As in previous studies [13, 14, 133, 143–147], for each cutoff distance (with and without LRC) we perform simulations of inhomogeneous systems at different temperatures where vapour-liquid equilibrium is expected. We typically consider seven temperatures in the range $\sim 0.5\,T_c$ up to $\sim 0.9\,T_c$, where T_c is the critical temperature of the system. Each simulation box is well equilibrated for 10^6 MC cycles, and averages are determined over a further period of 2×10^6 MC cycles. The production stage is divided into M blocks. Normally, each block is equal to 10^5 MC cycles. The ensemble average of the macroscopic components of the pressure tensor and the surface tension is given by the arithmetic mean of the block averages and the statistical precision of the sample average is estimated from the standard deviation in the ensemble average from $\overline{\sigma}/\sqrt{M}$, where $\overline{\sigma}$ is the variance of the block averages, and $M = 20$ in all cases.

All the quantities in our paper are expressed in conventional reduced units, with σ and ϵ being the length and energy scaling units, respectively. Thus, the temperature is given in units of ϵ/k_B, the densities in units of σ^{-3}, the pressure in units of the ϵ/σ^3, the surface tension in units of ϵ/σ^2, and the cutoff distance and interfacial thickness in units of σ.

9.4 Results and discussion

In this section we present the main results from simulations of the vapour-liquid interface of spherical LJ molecules using different cutoff distances, with and without LRC for the intermolecular potential energy and components of the pressure tensor. We focus mainly on the effect of using different cutoff distances on the microscopic components of the pressure tensor. To our knowledge, little work has been devoted to study the effect of cutoff distance and LRC on the microscopic components of the pressure tensor.

We have determined the components of the pressure using both the mechanical (or virial) and thermodynamic routes. Comparison between both results allows to check the validity of the method presented in Section 9.2for determining the contribution to the pressure due to the LRC. We have also examined several coexistence properties, such as coexistence densities and vapour pressures, and also other interfacial properties, such as density profiles, interfacial thickness, and surface tension. In particular, we pay special attention on the determination of the the vapour-liquid interfacial tension calculated using different routes, including the mechanical or virial route (using the traditional IK methodology) and the thermodynamic definition (using the VP and TA methods) of the surface tension.

9.4.1 Effect of cutoff distance and LRC on normal and tangential pressure

We first analyze the equilibrium normal and tangential components of the microscopic pressure tensor profiles, $P_N(z)$ and $P_T(z)$, respectively, that are computed from averages of histograms of pressures along the z direction over the production stage, according to the IK prescription explained in Section 9.3. As in the case of all properties calculated in this work, this procedure is meaningful as far as the central liquid slab is thick enough. This turns out to be the case in our simulations, including those performed at higher temperatures.

We consider the normal and tangential components of the microscopic pressure tensor profiles at a low temperature, $T = 0.72$. Fig. 9.1 shows $P_N(z)$ and $P_T(z)$ for spherical molecules with different cutoff distances for the intermolecular potential, from $r_c = 2.5$ up to 5. We have also included the results corresponding to a LJ cutoff distance $r_c = 3$ and the inhomogeneous LRC introduced in Section 9.2 (full LJ potential). Note that in all sections, except subsection B (Effect of the impulsive contribution of the intermolecular force on pressure tensor), we have taken into account the impulsive contribution to the pressure due to the discontinuity of the intermolecular force at $r = r_c$. In particular, we follow the seminal work of Trokhymchuk and Alejandre [9]. See the next subsection for further details. Tables 9.1 and 9.2 show the values for the normal and tangential macroscopic components of the pressure tensor at different temperatures and cutoff distances. As can be seen in Fig. 9.1a, the components of the microscopic pressure tensor along the two vapour-liquid interfaces exhibit the expected behaviour, i.e., the normal component of the pressure tensor profile is constant (within the statistical error) through the interface and equal to the vapour pressure of the system (according to the mechanical stability, that it requires the gradient of pressure tensor vanishes). In addition, the tangential component of the pressure tensor profile is approximately constant and equal to the normal pressure in the liquid and both vapour bulk-like regions of the simulation box. $P_T(z)$ becomes negative at the two interfacial regions of the system showing two (negative) local minima.

The values of $P_N(z)$ and $P_T(z)$ along the vapour slab are nearly independent of the cutoff dis-

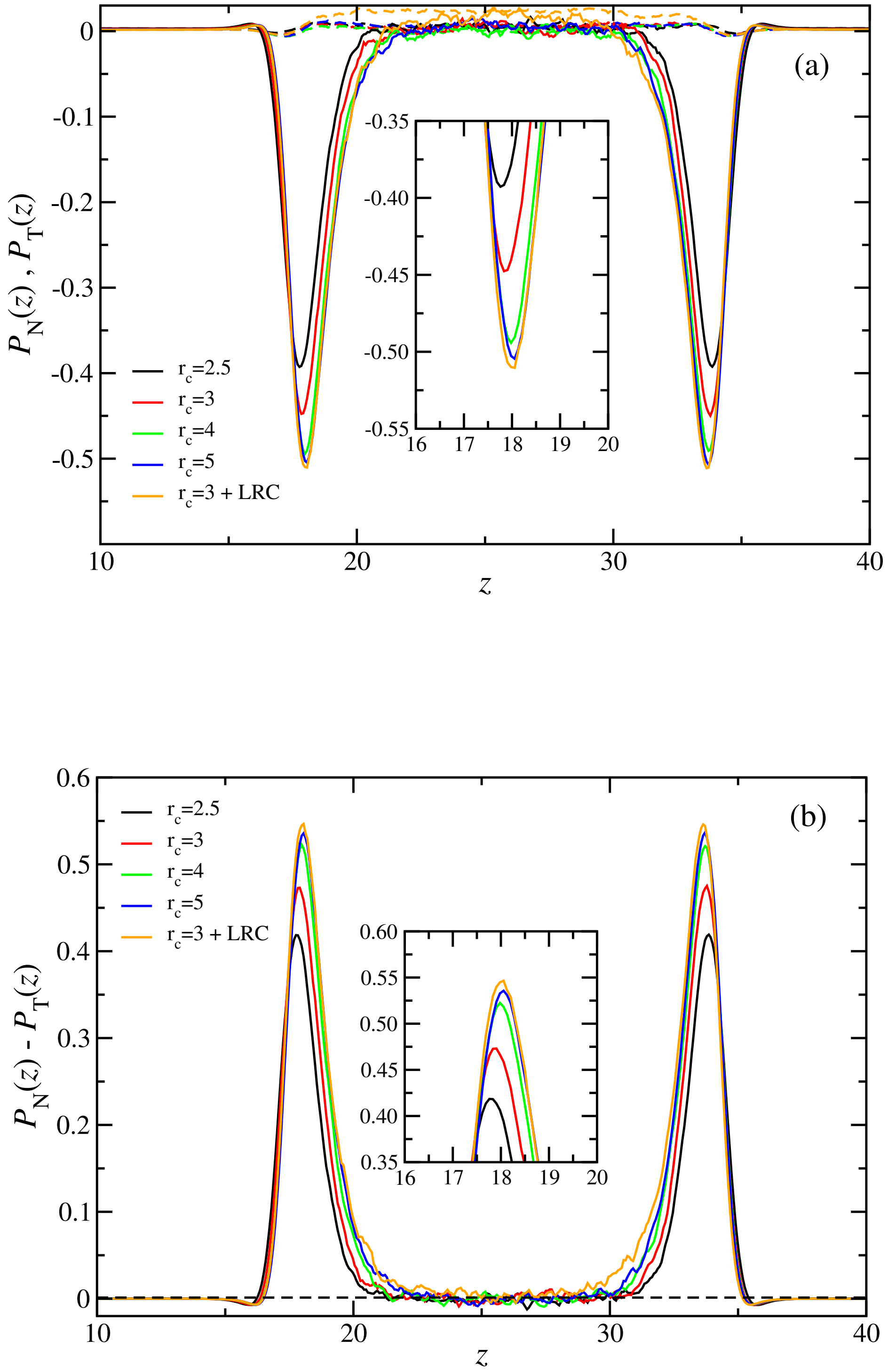

Figura 9.1: Normal $P_N(z)$ and tangential $P_T(z)$ (a), and difference between the normal and tangential microscopic components (b) of the pressure tensor profiles across the two vapour-liquid interfaces of spherical LJ molecules at $T = 0.72$ and using cutoff distances $r_c = 2.5$ (black), 3 (red), 4 (green), 5 (blue), and 3 with inhomogeneous LRC (orange). Continuous and dashed curves in part (a) correspond to the tangential and normal microscopic components of the pressure tensor, respectively. Insets correspond to the enlargement of the interfacial region for $P_T(z)$ (a) and $P_N(z) - P_T(z)$ (b).

Tabla 9.1: Liquid density, ρ_L, vapour density, ρ_V, normal macroscopic component of the pressure tensor calculated from the virial route, P_N^{vir}, normal and tangential macroscopic components of the pressure tensor calculated from VP, P_N^{VP} and P_T^{VP}, respectively, surface tension calculated from integration given by Eq. (9.1), γ^{vir}, from VP, γ^{VP}, and from TA, γ_{TA}, and $10-90$ interfacial thickness, t for a system of LJ molecules at different temperatures and cutoffs distances. All quantities are expressed in the reduced units defined in Section 9.3. The errors are estimated as explained in the text. Uncertainties of surface tension calculated from the virial route, γ^{vir}, are error estimates corresponding to the numerical calculation of the integral given by Eq. (9.1).

r_c	ρ_L	ρ_V	P_N^{vir}	P_N^{VP}	P_T^{VP}	γ^{vir}	γ^{VP}	γ_{TA}	t
					$T = 0.70$				
2.5	0.8161(13)	0.0035(3)	0.00240(3)	0.0028(7)	-0.0286(7)	0.793(6)	0.794(6)	0.795(3)	1.838(6)
3	0.8283(14)	0.00315(21)	0.002138(17)	0.0015(9)	-0.0340(9)	0.902(10)	0.901(7)	0.903(3)	1.794(2)
4	0.8367(17)	0.00246(18)	0.001677(16)	0.0023(6)	-0.0376(6)	1.017(7)	1.011(5)	1.016(3)	1.760(2)
5	0.8394(23)	0.0021(2)	0.001398(12)	0.0021(7)	-0.0403(7)	1.072(9)	1.073(6)	1.074(5)	1.7526(9)
					$T = 0.72$				
2.5	0.8066(11)	0.0048(3)	0.00330(2)	0.0031(7)	-0.0257(7)	0.744(7)	0.744(6)	0.746(2)	1.9054(18)
3	0.8195(9)	0.0038(3)	0.00264(2)	0.0032(7)	-0.0167(7)	0.866(11)	0.515(6)	0.866(4)	1.8652(4)
4	0.8279(13)	0.00305(19)	0.002130(18)	0.0018(7)	-0.0360(7)	0.975(6)	0.975(6)	0.974(3)	1.833(3)
5	0.830(2)	0.00296(19)	0.002067(18)	0.0030(10)	-0.0368(9)	1.028(6)	1.029(8)	1.030(3)	1.882(3)
					$T = 0.80$				
2.5	0.7682(12)	0.01007(23)	0.007465(22)	0.0076(7)	-0.0147(7)	0.596(5)	0.594(6)	0.595(3)	2.260(8)
3	0.7829(11)	0.0081(6)	0.00610(5)	0.0088(6)	-0.0173(6)	0.697(10)	0.696(5)	0.698(4)	2.1993(17)
4	0.7915(13)	0.00709(23)	0.00536(3)	0.0048(7)	-0.0255(8)	0.809(15)	0.809(6)	0.810(3)	2.147(7)
5	0.7949(13)	0.0070(4)	0.00527(3)	0.0045(8)	-0.0277(8)	0.859(6)	0.859(7)	0.856(3)	2.133(8)
					$T = 0.90$				
2.5	0.7152(7)	0.0265(9)	0.02013(11)	0.0198(8)	0.0054(8)	0.409(6)	0.409(7)	0.411(3)	2.865(22)
3	0.7302(11)	0.0207(6)	0.01632(7)	0.0145(7)	-0.0031(6)	0.498(10)	0.497(6)	0.497(3)	2.733(5)
4	0.7440(12)	0.01690(6)	0.01359(7)	0.0142(8)	-0.0069(8)	0.596(6)	0.597(7)	0.596(3)	2.643(6)
5	0.7470(21)	0.0168(7)	0.01308(7)	0.0118(6)	-0.0107(7)	0.635(7)	0.636(6)	0.635(2)	2.633(3)
					$T = 0.92$				
2.5	0.7041(8)	0.0302(8)	0.02311(8)	0.0233(8)	0.0100(8)	0.382(5)	0.381(7)	0.380(3)	3.014(7)
3	0.7207(11)	0.0235(7)	0.01869(7)	0.0196(7)	0.0032(8)	0.471(9)	0.470(7)	0.470(2)	2.865(20)
4	0.7325(9)	0.0198(12)	0.01603(13)	0.0144(6)	-0.0050(6)	0.558(6)	0.557(6)	0.557(2)	2.750(9)
5	0.7371(13)	0.0181(6)	0.01480(5)	0.0142(6)	-0.0070(6)	0.606(7)	0.607(6)	0.608(3)	2.730(13)
					$T = 1.00$				
2.5	0.6510(6)	0.0528(13)	0.03979(9)	0.0385(7)	0.0306(7)	0.239(5)	0.239(7)	0.240(2)	3.858(14)
3	0.6738(10)	0.0404(8)	0.03241(7)	0.0333(6)	0.0226(5)	0.327(8)	0.327(5)	0.327(2)	3.528(10)
4	0.6900(12)	0.0341(6)	0.02817(6)	0.0280(5)	0.0145(5)	0.410(7)	0.409(5)	0.409(2)	3.369(9)
5	0.6954(14)	0.0315(10)	0.02627(6)	0.0268(6)	0.0120(6)	0.449(5)	0.450(6)	0.4503(21)	3.316(10)
					$T = 1.10$				
2.5	0.5645(7)	0.0959(20)	0.06832(17)	0.0688(4)	0.0658(4)	0.099(5)	0.099(5)	0.0998(22)	5.793(14)
3	0.6015(10)	0.0759(23)	0.05825(12)	0.0588(4)	0.0538(4)	0.168(7)	0.167(4)	0.1674(19)	4.99(6)
4	0.6257(11)	0.0614(10)	0.05012(12)	0.0504(4)	0.0435(3)	0.238(5)	0.228(4)	0.237(2)	4.528(23)
5	0.6330(13)	0.0584(16)	0.04818(16)	0.0483(5)	0.0403(4)	0.268(5)	0.268(5)	0.269(2)	4.460(19)

tance used, including the values corresponding to the full potential. This is expected since vapour density is very low, especially at this temperature ($T = 0.72$), and contributions to the pressure due to particles separated beyond the lowest cutoff distance ($r_c = 2.5$) are negligible. A similar behaviour is also observed in the liquid slab, although the statistical noise is larger, as expected. However, the most interesting effect of the cutoff distance over the pressure tensor at this temperature is undeniably associated with the values of the two minima of $P_T(z)$. As can be seen, the cutoff distance has an enormous effect on this magnitude as its value is increased. In particular, the two minima values of $P_T(z)$ are a 23% higher than those corresponding to the values of the full potential for a cutoff distance of $r_c = 2.5$. Note that this difference is very important since, as it is well-known, are directly related with the value of the vapour-liquid surface tension of the system.

We have also calculated the difference of both components of the pressure tensor profile, as a function of the position along the z direction. As can be seen in Fig. 9.1b, the difference $P_N(z) - P_T(z)$

Tabla 9.2: Liquid density, ρ_L, vapour density, ρ_V, normal component of the macroscopic pressure tensor calculated from the virial route P_N^{vir}, normal and tangential components of the macroscopic pressure tensor calculated from VP, P_N^{VP} and P_T^{VP}, surface tension calculated from integration given by Eq. (9.1), γ^{vir}, from VP, γ^{VP}, and from TA, γ_{TA}, and $10-90$ interfacial thickness, t, at different temperatures for systems of LJ molecules with a cutoff distance $r_c = 3$ with inhomogeneous LRC. All quantities are expressed in the reduced units defined in Section 9.3. The errors are estimated as explained in the text. Uncertainties of surface tension calculated from the virial route, γ^{vir}, are error estimates corresponding to the numerical calculation of the integral given by Eq. (9.1).

T	ρ_L	ρ_V	P_N^{vir}	P_N^{VP}	P_T^{VP}	γ^{vir}	γ^{VP}	γ_{TA}	t
0.70	0.8421(21)	0.0020(2)	0.001353(15)	0.0002(7)	-0.0456(7)	1.158(11)	1.164(6)	1.164(4)	1.722(3)
0.72	0.8338(22)	0.00255(19)	0.001779(15)	0.0017(8)	-0.0414(8)	1.110(10)	1.114(6)	1.116(4)	1.824(3)
0.80	0.7986(16)	0.0063(2)	0.00478(3)	0.0048(7)	-0.0300(8)	0.923(10)	0.930(7)	0.927(4)	2.121(3)
0.90	0.7517(13)	0.0152(5)	0.01234(6)	0.0122(8)	-0.0130(7)	0.712(9)	0.713(7)	0.713(3)	2.601(16)
0.92	0.7414(14)	0.0172(6)	0.01415(6)	0.0139(6)	-0.0093(6)	0.667(15)	0.667(6)	0.668(3)	2.7259(11)
1.00	0.6995(10)	0.0299(3)	0.02522(7)	0.0249(4)	0.0082(4)	0.511(10)	0.510(4)	0.510(3)	3.282(12)
1.10	0.6361(8)	0.0533(8)	0.04522(12)	0.0440(5)	0.0345(5)	0.321(11)	0.316(5)	0.318(3)	4.202(6)

exhibits the expected shape, i.e., constant and equal to zero in the vapour and liquid slabs, since bulk-like regions do not contribute to the surface tension of the system, and positive peaks at both interfacial regions where the components of the pressure tensor are different due to the extra contribution of the tension to the tangential pressure at the interface. Differences between the maximum value reached by $P_N(z) - P_T(z)$ using a cutoff distance r_c (without LRC) and the full potential decrease as the cutoff is increased, as expected. We now consider the normal and tangential microscopic components of the pressure tensor, at a higher temperature, using the same cutoff distances for the LJ intermolecular potential and a cutoff distance $r_c = 3$ for the full LJ potential. The microscopic components of the pressure tensor, at $T = 1.0$, along the two vapour-liquid interfaces are shown in Fig. 9.2a. As can be seen, both components exhibit the same qualitative behaviour as at low temperature ($T = 0.72$). The separation between both interfacial regions is now smaller than in the case corresponding to low temperatures due to the growth of the interfacial regions. The normal component of the pressure (which is equal to the vapour pressure of the system) decreases as the cutoff distance is increased. This effect, that is more noticeable than in Fig. 9.1a due to the scale employed now, is in fact larger than at low temperatures. See Table 9.1 for further details.

A similar behaviour is also observed in the case of the tangential microscopic component of the pressure tensor. The two minima values of $P_T(z)$ are higher than those corresponding to the values get for the full intermolecular potential when the cutoff distance r_c is increased. These differences are systematically larger than those found at lower temperatures, as can be seen comparing Figs. 9.1a and 9.2a.

Another interesting feature exhibited by the tangential microscopic component of the pressure tensor profiles, which is more evident at high temperatures, is the increase of the region of the interface at which $P_T(z) \neq P_N$ as the cutoff distance of the intermolecular potential is increased. These regions correspond to zones of the interface at which there exist tensions and compressions, as it is explained below. This effect, that can be understood from a microscopic point of view, can be clearly seen in Fig. 9.2a. A higher value of the cutoff distance in the intermolecular potential means an increase of the range of the intermolecular forces between particles. As a consequence of this, the zones of the interface at which exist tensions and compressions spread over wider regions of the simulation box, as shown in Fig. 9.2a.

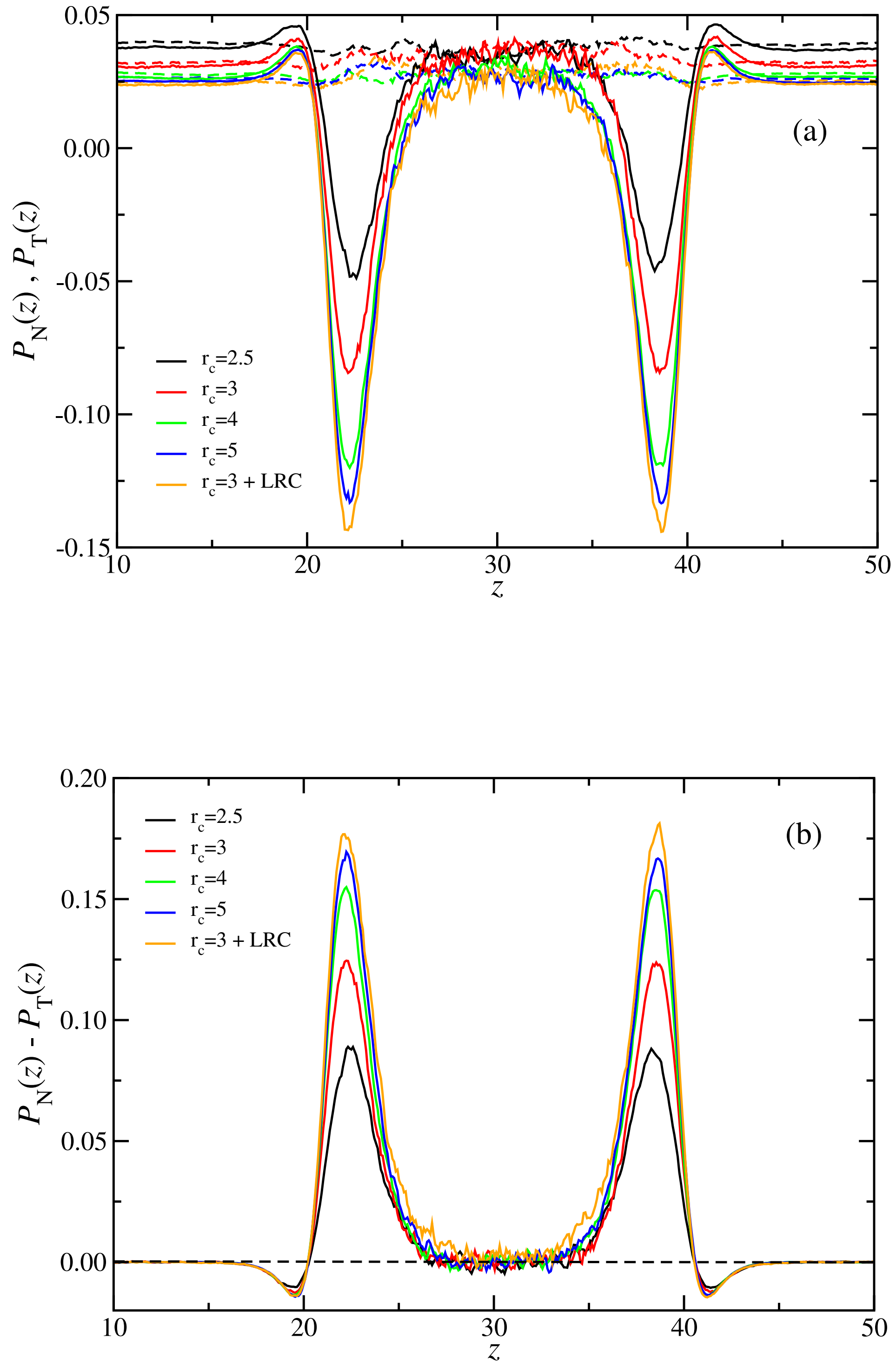

Figura 9.2: Normal $P_N(z)$ and tangential $P_T(z)$ (a), and difference between the normal and tangential microscopic components (b) of the pressure tensor profiles across the two vapour-liquid interfaces of spherical LJ molecules at $T = 1.0$. The meaning of the symbols and curves is the same as in Fig. 9.1.

As in the case of $P_N(z)$ and $P_T(z)$, the difference between both components of the pressure tensor profiles shows the same qualitative behaviour as at low temperatures. However, the effect of the cutoff distance of the intermolecular potential on $P_N(z) - P_T(z)$ is larger at high temperatures, as can be seen Figs. 9.1b and 9.2b. An interesting feature of the system, shows in Figs. 9.1 and 9.2, is that exist regions at which $P_T(z) < P_N(z)$. That regions, that correspond to most of the locations at the vapour-liquid interface, are clearly regions of tension. Contrary, small locations of the interface corresponding to zones near the vapour bulk-like regions, are regions of compression in which $P_T(z) > P_N(z)$. The reason for which the transverse pressure has values greater than P_N at the interface near the vapour phase and large negative values (and lower than P_N) at other locations of the interface is a consequence of the behaviour of the pressure in the unstable bulk phase region (spinodal region), which plays an essential role in the physics at interfaces. For further details we recommend the excellent review of Davies and Scriven [71].

From our knowledge, this is the first time the effect of the cutoff distance and the use of LRC of the dispersive interactions on the structure of $P_N(z)$, $P_T(z)$, and $P_N(z) - P_T(z)$ for the LJ system is analyzed in the same work. The only work, to our knowledge, in which related information has been shown is that of Shen *et al.* [139]. These authors show the behaviour of the difference between both components of the pressure tensor of the LJ with $r_c = 2.5$ and 4 in combination with the original method of Janeček [138] at only one temperature, 0.95 (see bottom panel of Fig. 2 of the paper of Shen *et al.* [139]). Note, however, that Janeček [140, 141] and coworkers have presented the pressure profiles, at different temperatures, for the LJ system using these LRC.

Once we have analyzed the effect of the cutoff distance on the normal and tangential microscopic components of the pressure tensor profile at two representative temperatures, 0.72 (low) and 1.0 (high), we consider the behaviour of the normal and tangential microscopic components of the pressure tensor profile in the whole range of temperatures at which the system exhibits vapour-liquid phase behaviour, from 0.70 to 1.1. We have used a cutoff distance for the LJ intermolecular potential of $r_c = 3$ with the inhomogeneous LRC described in Section 9.2. We have also obtained the normal and tangential macroscopic components of the pressure tensor, P_N and P_T, using the VP technique proposed by de Miguel and Jackson [16], which is based on a thermodynamic definition of the pressure tensor. Since this calculation is only based on energetic considerations, the results are independent of the methodology employed to estimate the contribution to the pressure due to the LRC (Section 9.2). The comparison between both results is relevant to this work since it allows to check the validity of the methodology presented in Section 9.2 to calculate the LRC to the pressure tensor.

The normal and tangential microscopic components of the pressure tensor are presented in Table 9.2. In addition to that, we have averaged the normal microscopic component of the pressure tensor along the vapour phase. As can be seen from Table 9.2, values for the normal macroscopic component of the pressure tensor calculated from the mechanical (P_N^{vir}) and thermodynamic (P_N) routes are in excellent agreement, confirming that equations proposed in Section 9.2 predict the correct behaviour of the normal pressure along the whole range of temperatures considered.

Results from the *NVT* calculations in the whole range of temperatures considered are shown in Fig. 9.3. As can be seen, the $P_N(z)$ and $P_T(z)$ profiles calculated using the IK methodology show the expected behaviour. In particular, the minimum (negative) value of the peaks associated to the tangential microscopic component of the pressure tensor profile, $P_T(z)$, becomes less negative as the temperature is increased. In addition to that, the thickness of the peaks associated to that component

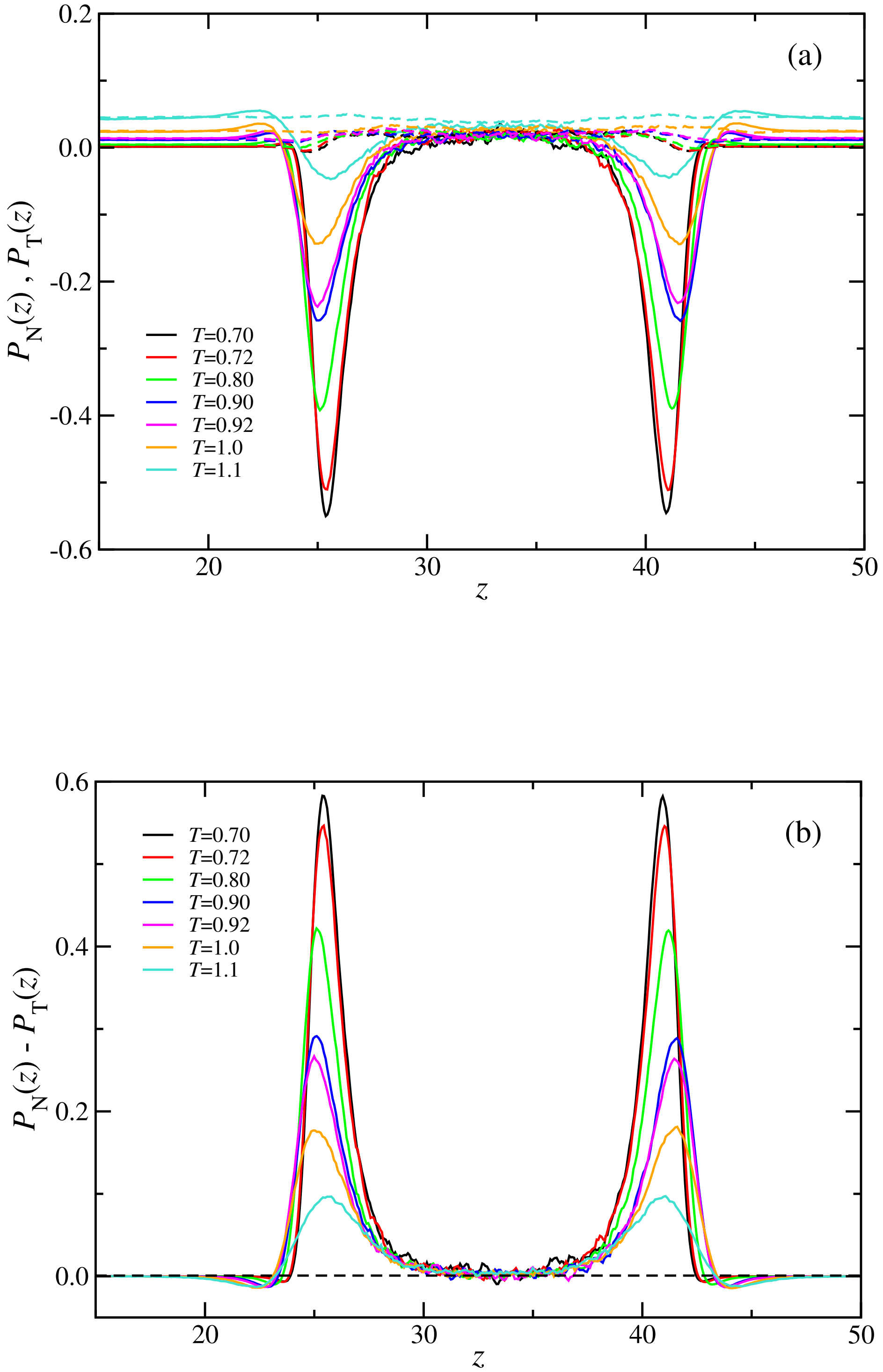

Figura 9.3: Normal $P_N(z)$ and tangential $P_T(z)$ (a), and difference between the normal and tangential microscopic components (b) of the pressure tensor profiles across the two vapour-liquid interfaces of spherical LJ molecules using a cutoff distance 3 with inhomogeneous LRC, at temperatures $T = 0.70$ (black), 0.72 (red), 0.80 (green), 0.90 (blue), 0.92 (magenta), 1.0 (orange), and 1.1 (light blue). Continuous and dashed curves in part (a) correspond to the tangential and normal microscopic components of the pressure tensor, respectively.

increases as the temperature is increased. Since the tangential component contributes positively to the surface tension (note that $P_T(z)$ is subtracted from $P_N(z)$ in the mechanical definition of surface tension given by Eq. (9.1) presented in Section 9.1), the behaviour observed in the structure of $P_T(z)$ as the temperature is varied agrees with the expected decrease of the vapour-liquid surface tension with the temperature. The behaviour of the thickness associated to the (negative) peaks exhibited by $P_T(z)$ is similar to that of the interfacial thickness of an interface, that increases with the temperature since it diverges as $T \to T_c$ [5]. As shown in Fig. 9.3a, regions at which the tangential pressure profile differs from this of the normal pressure increases as the temperature is raised. In order to give a complementary description of the structure of the microscopic components of the pressure tensor profile in the whole range of temperatures at which the system exhibits vapour-liquid phase separation, we have also considered the $P_N(z) - P_T(z)$ profiles, from 0.7 to 1.1, obtained using the full potential. As can be seen in Fig. 9.3b, $P_N(z) - P_T(z)$ shows the expected structure, which can be inferred from the results presented in Fig. 9.3a.

9.4.2 Effect of the impulsive contribution of the intermolecular force on pressure tensor

The calculation of forces in systems that interact through intermolecular potentials in which interactions are spherically truncated (but not shifted) is cumbersome. Trokhymchuk and Alejandre [9], and more recently de Miguel and Jackson [16], have clarified the importance of the additional force due to the discontinuity of the truncated potentials at cutoff distance, which is crucial for inhomogeneous fluids, as it will be shown below, and must be included into the virial if the mechanical route for calculating the pressure is used. The intermolecular force associated to the intermolecular interaction potential $u(r)$ between two LJ molecules separated a distance r is given by $\mathbf{f} = f(r)\hat{\mathbf{r}}$, with $f(r) = -(du/dr)$ and $\hat{\mathbf{r}}$ the unit vector between the interacting molecules. Since in Molecular Dynamics it is common to deal with systems in which forces are spherically truncated (but not shifted), these are usually calculated as,

$$f(r) = f_{LJ}(r)\big[1 - \Theta(r - r_c)\big] \tag{9.14}$$

where $f_{LJ}(r) = -(du_{LJ}/dr)$ is the magnitude of the force associated to the intermolecular LJ potential. As discussed by Trokhymchuk and Alejandre [9] and de Miguel and Jackson [16], $f(r)$ defined by Eq. (9.14) does not correspond to the force associated to an intermolecular potential spherically truncated (but not shifted) defined by Eq. (9.10) (see Section 9.3). The right value of the force obtained from Eq. (9.10) must be calculated as,

$$f(r) = f_{LJ}(r)\big[1 - \Theta(r - r_c)\big] + u_c\,\delta(r - r_c) \tag{9.15}$$

where $u_c = u_{LJ}(r_c)$ is the value of the LJ potential energy at $r = r_c$ and $\delta(x)$ is the δ-Dirac function. The last term on the Eq. (9.15) represents the impulsive (attractive) force, which is by no means negligible. de Miguel and Jackson [16] estimated that the impulsive force accounts for about 6% of the contributions to the total pressure in a bulk LJ liquid phase at $\rho = 0.864$ and $T = 1.5$ when a cutoff distance of $r_c = 2.5$ is used. However, as shown previously by Trokhymchuk and Alejandre [9], the effect of neglecting the impulsive force has dramatic consequences on the structure of the microscopic components of the pressure tensor profiles. Unfortunately, Trokhymchuk and Alejandre [9] only considered one value of the cutoff distance ($r_c = 2.5$) at one single temperature. Since we are studying

Tabla 9.3: Normal macroscopic component of the pressure tensor calculated from the virial route, P_N^{vir}, and surface tension calculated from integration given by Eq. (9.1), γ^{vir}, for a system of LJ molecules at different temperatures and using two different cutoff distances, $r_c = 2.5$ and 3 (without LRC). Results presented here correspond to simulation data in which forces are calculated using Eq. (9.14), i.e., the contribution to pressure due to the impulsive force at $r = r_c$ is neglected. All quantities are expressed in the reduced units defined in Section 9.3. The errors are estimated as explained in the text. Uncertainties of surface tension calculated from the virial route, γ^{vir}, are error estimates corresponding to the numerical calculation of the integral given by Eq. (9.1).

T	P_N^{vir}		γ^{vir}	
	$r_c = 2.5$	$r_c = 3.0$	$r_c = 2.5$	$r_c = 3.0$
0.70	0.00240(3)	0.00214(7)	0.679(6)	0.801(5)
0.72	0.00331(2)	0.00265(12)	0.633(7)	0.769(5)
0.80	0.00753(2)	0.00614(23)	0.503(5)	0.616(5)
0.90	0.02055(12)	0.0164(3)	0.341(13)	0.437(5)
0.92	0.02360(8)	0.0188(3)	0.319(5)	0.415(4)
1.00	0.04132(10)	0.0328(3)	0.197(5)	0.287(4)
1.10	0.07362(2)	0.0602(6)	0.081(5)	0.146(3)

the effect of cutoff distance and the use of LRC on the components of pressure tensor, we analyze in detail the structure of the pressure tensor profiles when the impulsive forces are not accounted for.

We now consider the same representative temperatures, 0.72 (low) and 1.0 (high), and study the effect of the cutoff distance on the pressure tensor profiles when the impulsive force at $r = r_c$ is neglected. Values of the normal macroscopic component of the pressure tensor and surface tension obtained from the virial route without the contribution due to the impulsive force, i.e., using Eq. (9.14), are presented in Table 9.3. Fig. 9.4a shows the $P_N(z)$ and $P_T(z)$ profiles as obtained from *NVT* Monte Carlo simulations using two different cutoff distances, $r_c = 2.5$ and 3 (without LRC and neglecting the impulsive contribution). We have also represented the results calculated including the contribution to the components of the pressure tensor due to the impulsive force at $r = r_c$. As can be seen in both cases ($r_c = 2.5$ and 3), $P_N(z)$ does not show the correct behaviour along the interface when Eq. (9.14) is used. The normal pressure profile, as obtained without the impulsive contribution, is approximately correct and constant along the vapour phase. This is expected since the impulsive contribution is negligible at very low densities. Unfortunately, the behaviour of the normal pressure is completely wrong in the liquid region. In particular, the normal pressure is not constant and its value is much higher than the true magnitude. Differences between the correct and wrong values for $P_N(z)$ (along the liquid phase) obtained using $r_c = 2.5$ are larger than those corresponding to the case $r_c = 3$. In particular, the difference between both values varies from 0.3 in the case of $r_c = 2.5$ to 0.23 for $r_c = 3$. This is also an expected result since the impulsive contribution is proportional to the value of the potential energy at $r = r_c^-$, a quantity that decreases as the cutoff distance is increased.

The use of Eq. (9.14) also introduces important nonphysical effects on the tangential pressure, as can be seen in Fig. 9.4b. The characteristic peaks at the interfacial regions are less negative and its behaviour along the liquid slab is completely wrong. Differences between calculations obtained using Eqs. (9.14) and (9.15) decrease as the cutoff distance is larger, as previously explained. In particular, the tangential pressure at the liquid phase passes from 0.3 to 0.2 when the cutoff distance increases. Note also that the impulsive contribution is negligible in the vapour phase at this temperature.

Although one of the main goals of this work is to analyze the effect of cutoff distance and LRC on the components of the pressure tensor, it is also interesting to combine the information obtained

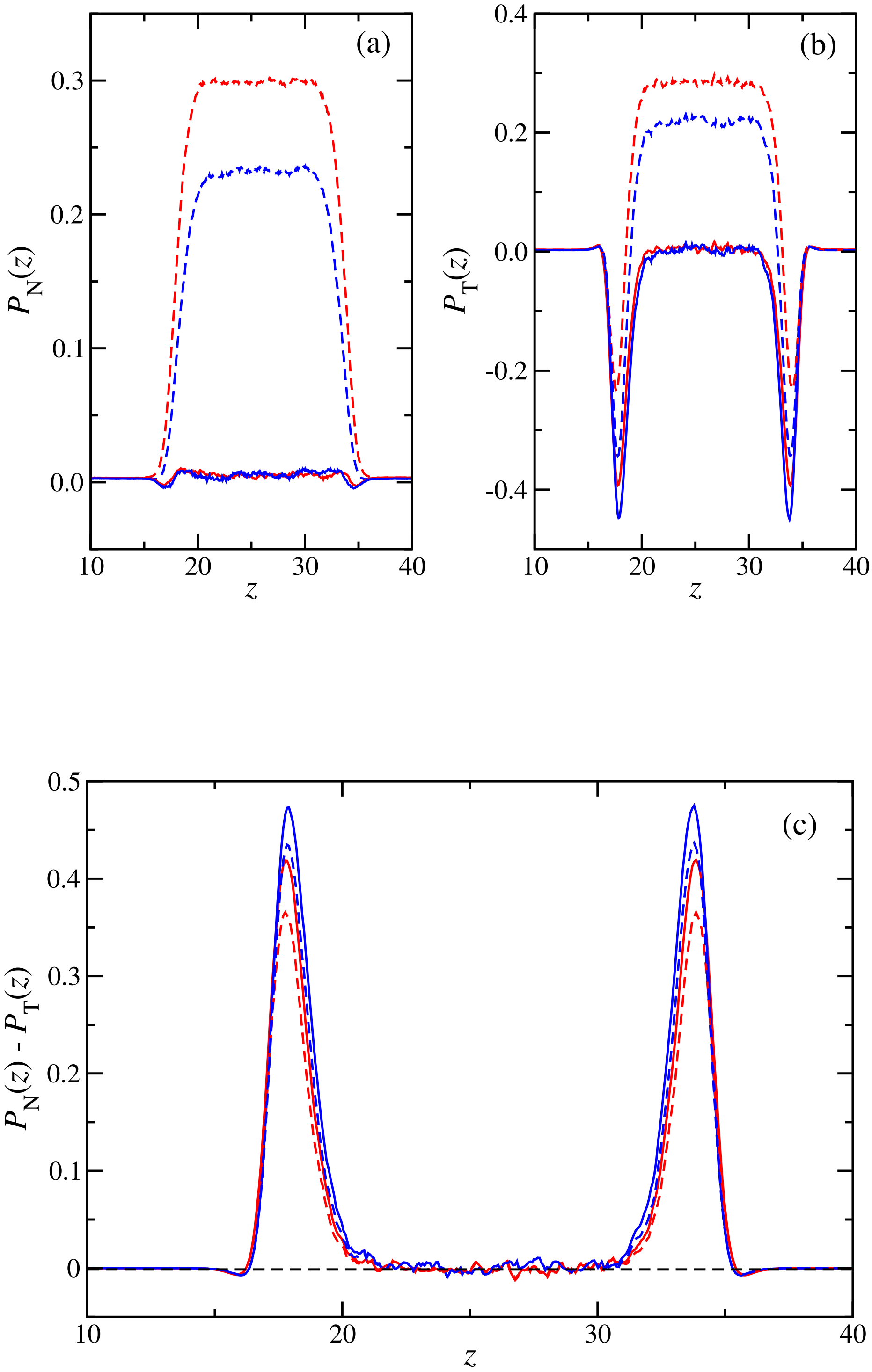

Figura 9.4: Normal $P_N(z)$ (a), tangential $P_T(z)$ (b), and difference between the normal and tangential microscopic components (c) of the pressure tensor profiles across the two vapour-liquid interfaces of spherical LJ molecules at $T = 0.72$ and using cutoff distances $r_c = 2.5$ (red) and 3 (blue) without inhomogeneous LRC. Continuous curves correspond to the results obtained using the correct expression for the intermolecular force given by Eq. (9.15) and dashed curves to the results using the incorrect expression for the intermolecular forces given by Eq. (9.14).

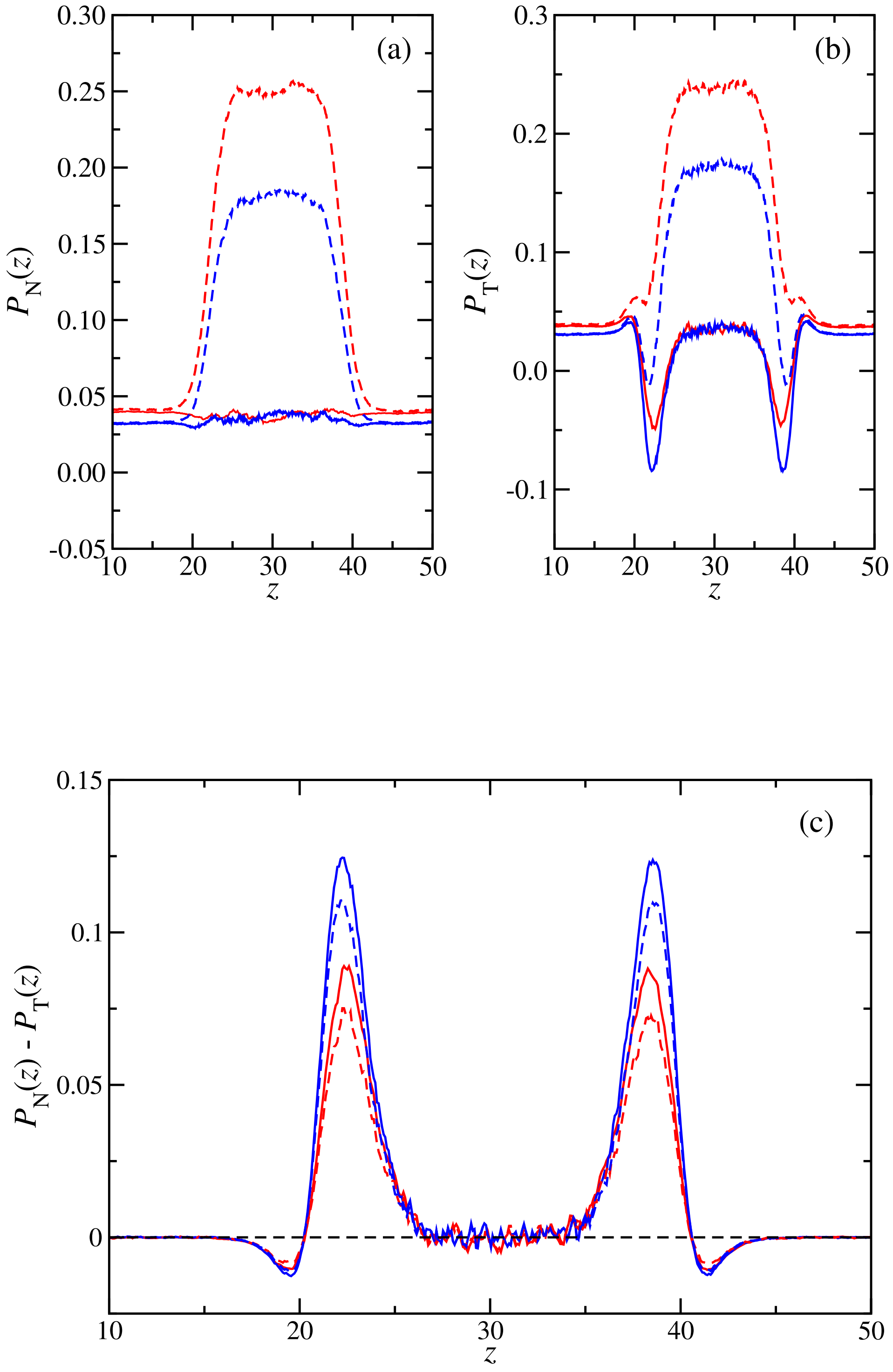

Figura 9.5: Normal $P_N(z)$ (a), tangential $P_T(z)$ (b), and difference between the normal and tangential microscopic components (c) of the pressure tensor profiles across the two vapour-liquid interfaces of spherical LJ molecules at $T = 1.00$. The meaning of the symbols and curves is the same as in Fig. 9.4.

previously to investigate from this perspective the physical consequences over the interfacial tension. Fig. 9.4c shows the difference between both components of the pressure tensor, $P_N(z) - P_T(z)$, as a function of z for the systems considered, including the use of different cutoff distances and Eqs. (9.14) and (9.15). Surprisingly, calculations obtained from Eq. (9.14) are in qualitative agreement with correct results. Why the structure of $P_N(z) - P_T(z)$ is qualitatively predicted using Eq. (9.14)? Eqs. (9.14) and (9.15) given similar results since the impulsive contribution is negligible at these densities. Although Eq. (9.14) provides completely wrong results for P_T and P_N in the liquid phase, the calculations are self-consistent, i.e., $P_N(z) = P_T(z)$ in the bulk regions, including the liquid phase, and hence $P_N(z) - P_T(z) \approx 0$ in this region, giving the correct behaviour in the liquid slab. However, $P_T(z)$ and $P_N(z)$ are not calculated correctly in the interfacial region, and surface tension values obtained using Eq. (9.14) are only qualitative. In particular, the calculations underestimate the correct width and height of the peaks centered around the two vapour-liquid interfaces.

We have also analyzed the behaviour of both microscopic components of the pressure tensor profile, as well as the difference between both components, at a higher temperature ($T = 1$) using Eqs. (9.14) and (9.15). As can be seen in Fig. 9.5a, the results at high temperature are similar than those obtained at the low temperature ($T = 0.72$). The normal pressure along the vapour phase, when Eq. (9.14) is used, is now clearly overestimated. This is a consequence of the increase of density in the vapour phase as the system approaches to the critical point. Note that the contribution to the pressure due to the impulsive force, which is negative (attractive contribution), is proportional to $u_{LJ}(r_c)$ and to the average number of molecular pairs located at distances $r \sim r_c$, or more precisely, between r_c and $r_c + \Delta r$ in the limit $\Delta r \to 0$. The absence of the impulsive contribution produces less attractions, increasing the pressure associated to the truncated force, as shown in Fig. 9.5a.

The case of $P_T(z)$ is more complicated although the behaviour is qualitatively similar to that found at $T = 0.72$. As can be seen in Fig. 9.5b, differences between $r_c = 2.5$ and 3 are larger than in the previous case (in both cases). Although the shape of P_T, as a function of z, is similar to that found at lower temperatures for the case $r_c = 3$, the shape of $P_T(z)$ for $r_c = 2.5$ is more complex, including a nonphysical structure at the interfaces due to the use of Eq. (9.14).

Finally, we have also represented the difference between the components of the pressure tensor, as a function of z (Fig. 9.5c). $P_N(z) - P_T(z)$ exhibits the same behaviour than as low temperature ($T = 0.72$), with the positive peaks lower and wider. The difference between the maximum values of the peaks using Eqs. (9.14) and (9.15) are slightly larger than in the previous case ($T = 0.72$), as expected since the temperature considered is closer to the critical temperature of the system.

9.4.3 Density profiles and phase coexistence properties

Once we have analyzed the effect of cutoff distance and LRC on the pressure tensor components, now we turn on the study of other interfacial and thermodynamic properties of the LJ system. Following the same analysis and methodology than in our previous works [13,14,143–145], we consider different cutoff distances and temperatures. The equilibrium density profiles $\rho(z)$ are computed from averages of the histogram of densities along the z direction over the production stage. The bulk vapour and liquid densities are obtained by averaging $\rho(z)$ over appropriate regions sufficiently removed from the interfacial region. As we have mentioned previously, this procedure is meaningful as far as the central liquid slab is thick enough. This turns out to be the case in our simulations, including those performed at the higher temperatures. The bulk vapour density is obtained after averaging the density profiles on both sides of the liquid film. The statistical uncertainty of these values is estimated from the standard deviation of the mean values. Following our previous works, additional interfacial properties, such as the position of the Gibbs-dividing surface, z_0, and the $10-90$ interfacial thickness, t, are obtained by fitting each of the two equilibrium density profiles to hyperbolic tangent functions [5] (see Eq. (3) of our previous work [13] for further details). We fix liquid, ρ_L, and vapour, ρ_V, densities to previously computed values and treat z_0 and t as adjustable parameters.

Our simulation results for the bulk densities, components of the pressure tensor, surface tension, and interfacial thickness for LJ molecules interacting with the full potential are collected in Tables 9.2 and 9.4, respectively. A detail account for the results obtained for the normal component of the pressure tensor, surface tension, and interfacial thickness for LJ molecules with several cutoff distances has been already presented in Table 9.1.

We show in Fig. 9.6a the density profiles $\rho(z)$ for LJ molecules using different cutoff distances at $T = 0.72$. For the sake of clarity, we only present one half of the profiles corresponding to one of the interfaces. Also for convenience, all density profiles have been shifted along z so as to place z_0 at the origin. As can be seen, the slope (in absolute value) of the density profiles in the interfacial region increases as the cutoff distance is increased, making larger the jump in densities when passing from the vapour to the liquid side of the interface. Consequently, the interfacial thickness decreases, an expected result since the cohesive energy of the system is increased, as well as the surface tension, since the cutoff distance is larger. The insets of Fig. 9.6a show the variation of the density profile close to the region of the interface at which the bulk density is reached. As can be seen, relative differences between the density profiles corresponding to a LJ system with $r_c = 2.5$ (without LRC) and $r_c = 3$ (with LRC) are larger close to the vapour phase ($\sim 46\%$) than to the liquid phase ($\sim 3\%$).

We have also analyzed the density profile of the system, using the same set of cutoff distances, but now at a higher temperature, $T = 1$. As can be seen in Fig. 9.6b, the same qualitative behaviour is observed, although the change in the slope at the interfacial region seems to be larger. The variation of the profiles close to the region of the interface at which the bulk density is reached exhibits similar increments (in absolute value) than as low temperatures.

Tabla 9.4: Liquid density, ρ_L, vapour density, ρ_V, normal macroscopic component of the pressure tensor calculated from the virial route, P_N^{vir}, normal and tangential macroscopic components of the pressure tensor calculated from VP, P_N^{VP} and P_T^{VP}, respectively, surface tension calculated from integration given by Eq. (9.1), γ^{vir}, from VP, γ^{VP}, and from TA, γ_{TA}, and $10-90$ interfacial thickness, t, at different temperatures for systems of LJ molecules with a cutoff distance $r_c = 2.5$ with inhomogeneous LRC. All quantities are expressed in the reduced units defined in Section 9.3. The errors are estimated as explained in the text. Uncertainties of surface tension calculated from the virial route, γ^{vir}, are error estimates corresponding to the numerical calculation of the integral given by Eq. (9.1).

T	ρ_L	ρ_V	P_N^{vir}	P_N^{VP}	P_T^{VP}	γ^{vir}	γ^{VP}	γ_{TA}	t
0.70	0.8408(18)	0.00190(14)	0.001301(13)	0.0013(6)	-0.0446(6)	1.174(14)	1.161(5)	1.161(4)	1.721(3)
0.72	0.8328(12)	0.00255(13)	0.001781(14)	0.0015(7)	-0.0419(7)	1.129(10)	1.121(5)	1.119(4)	1.793(5)
0.80	0.7985(12)	0.0058(5)	0.00444(5)	0.0043(7)	-0.0309(7)	0.946(12)	0.941(6)	0.940(3)	2.098(7)
0.90	0.7530(19)	0.0153(5)	0.01244(4)	0.0132(9)	-0.0124(9)	0.730(10)	0.721(8)	0.723(2)	2.576(14)
0.92	0.7434(15)	0.0162(8)	0.01328(8)	0.0142(9)	-0.0096(9)	0.689(10)	0.684(8)	0.685(2)	2.7101(23)
1.00	0.7021(12)	0.0294(9)	0.02500(10)	0.0256(5)	0.0083(5)	0.528(14)	0.524(5)	0.525(2)	3.227(16)
1.10	0.6417(15)	0.0534(20)	0.04543(10)	0.0454(5)	0.0357(5)	0.332(12)	0.324(5)	0.3244(19)	4.326(15)

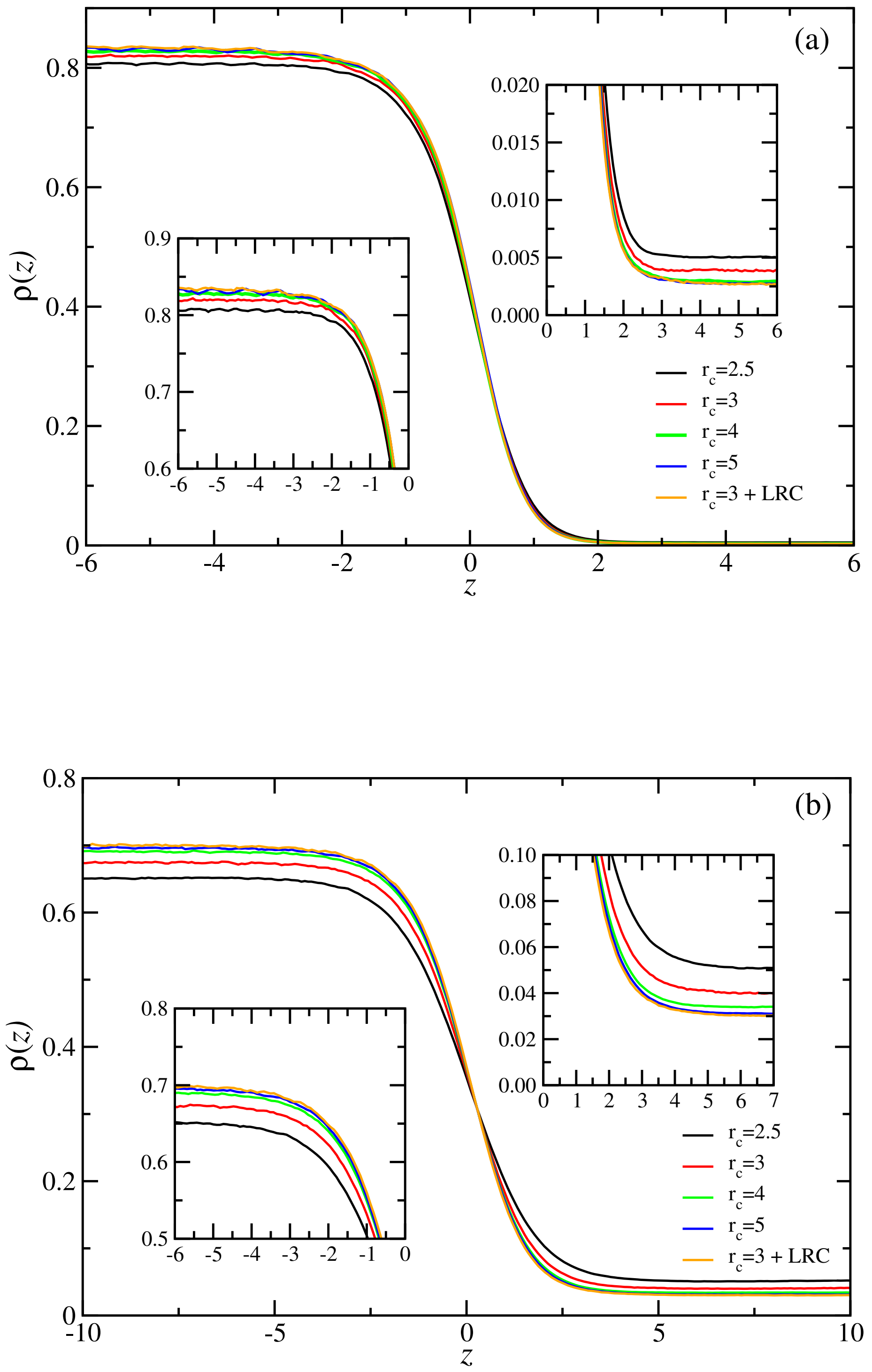

Figura 9.6: Simulated equilibrium density profiles across the vapour-liquid interface of spherical LJ molecules using cutoff distances $r_c = 2.5$ (black), 3 (red), 4 (light green), 5 (blue), 2.5 with inhomogeneous LRC (orange), and 3 with inhomogeneous LRC (dark green) at $T = 0.72$ (a) and 1.00 (b). The top and bottom insets in both parts correspond to the near-vapour and near-liquid interfacial region, respectively.

As in our previous works [13, 14, 143–145], it is also useful to estimate the location of the critical point resulting from our direct Monte Carlo simulations. The critical temperature T_c and density ρ_c are obtained using the simulation results for the vapour and liquid coexistence densities (Table 9.4) and the scaling relation for the width of the coexistence curve,

$$\rho_L - \rho_V = A(T - T_c)^\beta , \tag{9.16}$$

and the law of rectilinear diameters

$$\frac{\rho_L + \rho_V}{2} = B + CT . \tag{9.17}$$

A, B, and C are constants, and β is the corresponding critical exponent. A universal value of $\beta = 0.325$ is assumed here. [5] In Table 9.5 we report the values of the critical temperatures and densities as obtained from this procedure for all the systems studied in this work.

Tabla 9.5: †Critical temperature and density for LJ molecules with different cutoff distances r_c (and also using LRC) from the analysis of the coexistence densities using Eqs. (9.16) and (9.17), and §critical temperature obtained from the analysis of the computed surface tension data using Eq. (9.19) and fixing the critical point to $\mu = 1.258$. All quantities are expressed in the reduced units defined in Sec. III.

r_c	$\rho_c^\dagger$	$T_c^\dagger$	$T_c^\S$
2.5	0.314(9)	1.190(7)	1.194(10)
3	0.311(10)	1.234(8)	1.241(9)
4	0.310(10)	1.271(9)	1.277(9)
5	0.310(14)	1.283(13)	1.299(10)
$2.5 +$ LRC	0.310(12)	1.305(12)	1.330(9)
$3 +$ LRC	0.308(12)	1.291(11)	1.322(11)

The vapour-liquid density profiles of LJ molecules with a cutoff distance $r_c = 3$ and LRC are depicted in Fig. 9.7. We have also obtained all the profiles using a slightly lower cutoff distance, $r_c = 2.5$, in combination with the LRC presented Section 9.2. This allows to estimate the effect of the cutoff distance used in determining the interfacial properties of the full intermolecular potential. As seen in Fig. 9.7, the effect of decreasing the cutoff distance on the density profiles is really very small, especially at low temperatures. Larger differences between profiles calculated using $r_c = 3$ and 2.5 occur at the (vapour and liquid) bulk sides at the highest temperature ($T = 1.1$). Profile obtained using $r_c = 2.5$ predicts a slightly higher liquid density with respect to that obtained using $r_c = 3$ ($0.6418(15)$ and $0.6362(8)$, respectively) and a lower vapour density ($0.0534(7)$ and $0.0533(3)$, respectively). In all cases, relative differences are below 1% and within the statistical uncertainties of the simulations (see Tables 9.4 and 9.2 for further details).

The vapour-liquid phase envelopes of LJ molecules with $r_c = 2.5$, 3, 4, and 5, and using $r_c = 2.5$ and 3 with inhomogeneous LRC are depicted in Fig. 9.8. As can be seen, the phase envelope becomes wider as the cutoff distance is increased. As r_c grows, predictions are closer to the limiting case corresponding to the full potential, which corresponds to the use of a cutoff ($r_c = 2.5$ and 3) with LRC. As in the case of Fig. 9.6, although results corresponding to calculations performed using $r_c = 2.5$ and 3 with LRC are compatible, simulation data seem to indicate a small dependence of the coexistence liquid density with the cutoff distance. This result indicates that the main approximation

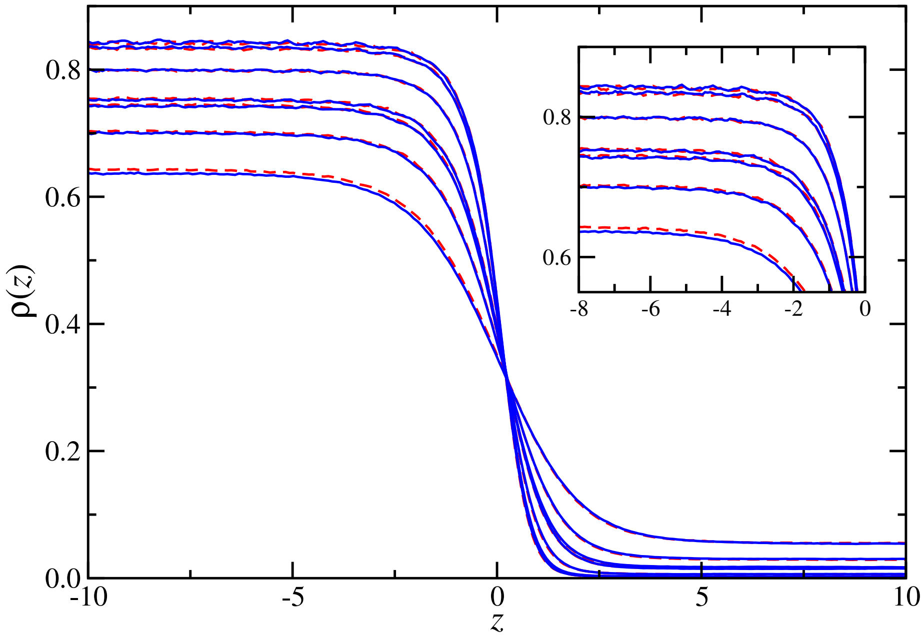

Figura 9.7: Simulated equilibrium density profiles across the vapour-liquid interface of spherical LJ molecules using cutoff distances $r_c = 2.5$ (dashed red curves) and 3 (continuous blue curves) with inhomogeneous LRC. From top to bottom (in the liquid region): $T = 0.70$, 0.72, 0.80, 0.90, 0.92, 1.0, and 1.1. Inset corresponds to the enlargement of the liquid region.

of the Janeček's methodology, i.e., the distribution of particles separated beyond r_c is uniform, works slightly better for $r_c = 3$ than $r_c = 2.5$. A possible qualitative explanation of this behaviour may be given taken into account the shape of the radial distribution function at liquid density. This function exhibits a minimum at $r_c = 2.5$ and a maximum at $r_c = 3$. Since the use of LRC implies a uniform particle distribution for $r \geq r_c$, this approximation leads to a more attractive system in the case of $r_c = 2.5$ and a more volatile for $r_c = 3$. This results in lower liquid and higher vapour coexistence densities, as it is observed in Fig. 9.7.

In order to check the consistency of our results, we have compared the predictions obtained from *NVT* MC simulations of this work with previous results obtained by several authors using different Monte Carlo and Molecular Dynamics techniques, including grand-canonical transition-matrix Monte Carlo in combination with histogram re-weighting and direct coexistence [9, 11, 15, 139]. As can be seen in Fig. 9.8, results obtained in this work are in excellent agreement with all the data taken from the literature in all cases. In addition to that, Fig. 9.8 also shows a good agreement between critical temperatures and densities obtained here and those taken from the literature. Critical data obtained from simulation in this work from vapour-liquid coexistence data and surface tension analysis are presented in Table 9.5.

Since the vapour pressure of the system is equal to the normal component of the pressure tensor, we have represented the vapour pressure, as a function of temperature, in Fig. 9.9. In particular, we have analyzed the effect of the cutoff distance on the vapour pressure. In addition to that, we have included the data corresponding to the $r_c = 2.5$ and 3 with LRC. We have also compared our

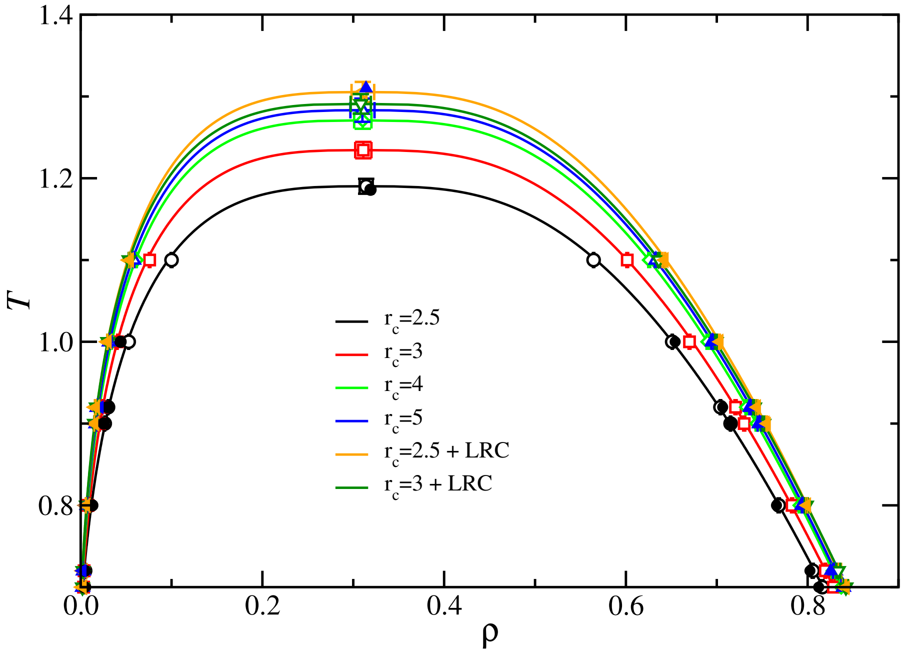

Figura 9.8: Vapour-liquid coexistence densities for spherical LJ molecules using different cutoff distances. The open black circles ($r_c = 2.5$), open red squares ($r_c = 3$), open light green diamonds ($r_c = 4$), open blue triangles up ($r_c = 5$), open orange triangles left ($r_c = 2.5$ with inhomogeneous LRC), and open dark green triangles down ($r_c = 3$ with inhomogeneous LRC) correspond to the coexistence densities obtained from MC NVT simulations for spherical molecules with different values of r_c. The filled black circles ($r_c = 2.5$) and filled blue triangles up ($r_c = 5.5$) correspond to the coexistence densities obtained by Trokhymchuk and Alejandre [9], and the filled orange triangles left to those obtained by Janeček [15]. Symbols at the highest temperatures for each of the coexistence curves represent critical points estimated from Eqs. (9.16) and (9.17) and those taken from Refs. [9, 15]. The curves represent the fits of the simulation data to the scaling relation for the width of the coexistence curve and the law of rectilinear diameters given by Eqs. (9.16) and (9.17), respectively.

results with simulation data taken from the work of Trokhymchuk and Alejandre [9] for several cutoff distances. As can be seen, the main effect of increasing the cutoff distance is to decrease the vapour pressure of the system. This is the expected behaviour since as the cutoff distance increases, more attractions are account for in the system, and the vapour pressure decreases. Agreement between results obtained in this work and simulation data taken from the literature is excellent in all cases.

9.4.4 Interfacial thickness

Another interesting property obtained from our analysis is the $10-90$ interfacial thickness (cf. Tables 9.4, 9.2, and 9.1). For a given cutoff distance, t is seen to increase with temperature, which simply reflects the fact that the interfacial region gets correspondingly wider, in agreement with our previous results, as can be observed in Fig. 9.10. At low temperatures the density profiles exhibit a sharp interface, which corresponds to a low value of the interfacial thickness. As the temperature is increased towards the critical value, the interfacial region becomes wider, and hence, the value of the interfacial thickness increases and diverges to infinity as $T \to T_c$. The variation of interfacial

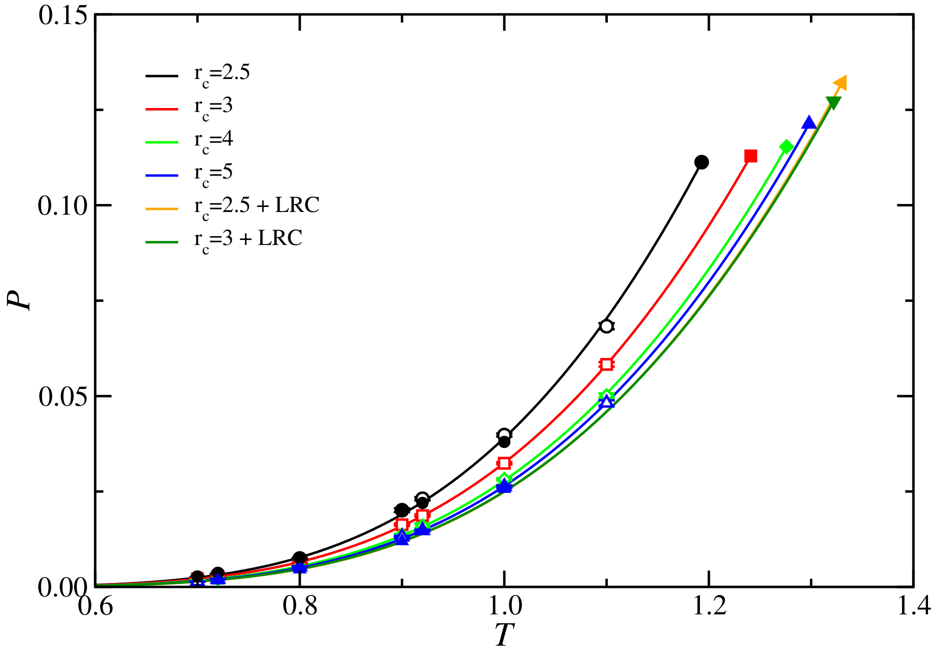

Figura 9.9: Vapour pressure, as a function of temperature, for spherical LJ molecules using different cutoff distances. The open symbols correspond to the normal microscopic component of the pressure tensor averaged along the vapour phase (taken from Tables 9.4, 9.2, and 9.1) obtained from MC NVT simulations for spherical molecules with different values of r_c. The meaning of the symbols are the same is in Fig. 9.8. The continuous curves correspond to Clausius-Clapeyron equation fitted to the vapour pressure data. Symbols at the highest temperatures for each of the vapour pressure curves represent critical points estimated from Eqs. (9.16) and (9.17) (critical temperatures) and the Clausius-Clapeyron equation (critical pressures).

thickness with temperature for different cutoff distances is illustrated in Fig. 9.10. We have also included the results corresponding to the full potential. We have compared our predictions with MC simulation results obtained by Janeček [15] using LRC. As can be seen, agreement between both results is excellent in the whole range of temperatures studied. According to the figure, increasing the cutoff distance results in a decrease of the thickness of the interface at fixed temperature, which is consistent with the fact that the systems with larger cutoff distances have a larger cohesive energy. This behaviour is consistent with that found for the shape of the vapour-liquid phase envelopes.

9.4.5 Surface tension

Finally, we have calculated the vapour-liquid surface tension of LJ molecules using several cutoff distances without LRC, as well as using the full potential. In particular, we have determined the surface tension using its mechanical definition that involves the integration of the difference between the tangential and normal microscopic components of the pressure tensor profiles, as obtained from the IK methodology, along the simulation box according to Eq. (9.1). In addition to that, we have also determined the surface tension using two perturbative approaches: the Test-Area (TA) method of Gloor *et al.* [4] and the VP technique of de Miguel and Jackson [16]. In first case, the surface tension

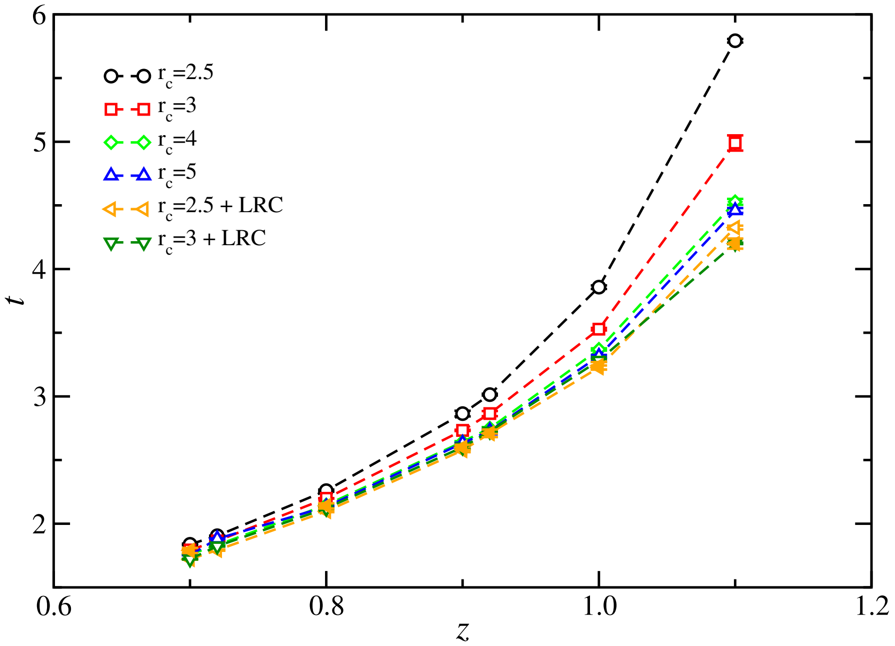

Figura 9.10: The $10-90$ interfacial thickness as a function of the temperature for spherical LJ molecules using different cutoff distances. The meaning of the open symbols are the same as in Fig. 9.8. The filled orange triangles left correspond to the interfacial thickness obtained MC NVT simulations of spherical LJ molecules with $r_c = 2.5$ with inhomogeneous LRC obtained by Janeček [15]. The curves are included as a guide to eyes.

is determined performing virtual area perturbations of a (small) magnitude during the course of the simulation at constant volume. In the second case, the surface tension is determined in two steps. In the first step, the normal and tangential macroscopic components of the pressure tensor, P_N and P_T, are calculated from their thermodynamic definitions as proposed by de Miguel and Jackson [16]. In the second step, the surface tension γ is obtained from the relationship (see Eq. (21) of the work of de Miguel and Jackson [16]),

$$\gamma = L_Z(P_N - P_T) \tag{9.18}$$

Here L_z is the simulation length along the z-axis. Note that Eq. (9.18) can be viewed as the macroscopic version of Eq. (9.1). As in the case of the microscopic definition, since there exist two vapour-liquid interfaces, the true value associated to a single interface is half of the value obtained from Eq. (9.18).

The calculation of the surface tension through three different but complementary routes allows to compare the results obtained from the mechanical and thermodynamic methods. This is another convincing test for consistency for the inhomogeneous LRC presented in Section 9.2. Note that similar consistent results have been found in previous applications of the method for calculating the total potential energy of the system [14, 143–145].

The temperature dependence of the surface tension for LJ molecules using different cutoff dis-

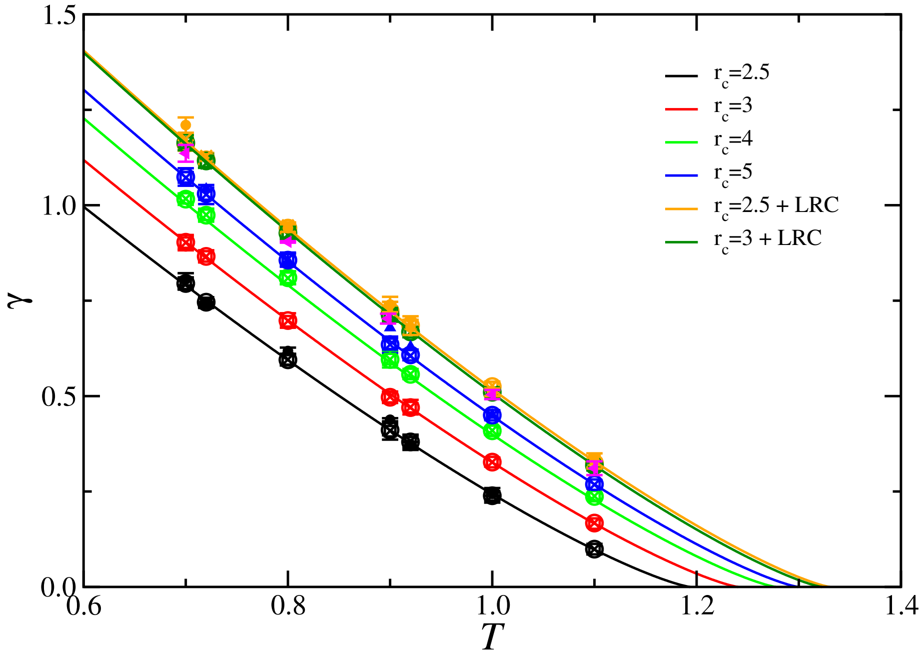

Figura 9.11: Surface tension as a function of the temperature for spherical LJ molecules using cutoff distances $r_c = 2.5$ (black), 3 (red), 4 (light green), 5 (blue), 2.5 with inhomogeneous LRC (orange), and 3 with inhomogeneous LRC (dark green). Different symbols represent the surface tension obtained from MC NVT simulations for spherical molecules using the mechanical route of Irving and Kirkwood [62] (open circles), the VP method of de Miguel and Jackson [16] (open squares), and the TA technique [4] (crosses). The filled black circles ($r_c = 2.5$) and filled blue triangles up ($r_c = 5.5$) correspond to the surface tension obtained by Trokhymchuk and Alejandre [9] using the mechanical route, the filled orange circles to the MC simulation data by Janeček [15], and the filled magenta left triangles to those obtained by Shen *et al.* [139]. The curves represent the fits of the simulation data to the scaling relationship of the surface tension near the critical point given by Eq. (9.19) with $\mu = 1.258$.

tances is shown in Fig. 9.11. We have also included the results corresponding to the full potential. The results are also compared with simulation data taken from the literature for the LJ system with different cutoff distances and using the original Janeček's methodology [9,11,15,139]. Agreement between our simulations and data taken from the literature are in excellent agreement in all cases, demonstrating that the methodology proposed in Section 9.2 is consistent with the original formulation of Janeček. As can be seen, at any given temperature, the interfacial tension is larger for molecules with larger cutoff distance. Once again, this is consistent with the larger cohesive energy in systems consisting of molecules in which attractive interactions are longer. As can be seen from Fig. 9.11, a nearly linear behaviour is found for the range of temperatures considered here, with a slight curvature close to the critical point for each system.

A comparison between the surface tension values obtained using $r_c = 2.5$ and 3 in combination with LRC reveals a tiny dependence with the value of the cutoff distance used. Although differences between both results are really small (see Tables 9.2 and 9.4 for comparison), deviations seem to be systematic and larger than the estimated errors, especially at temperatures $T \gtrsim 0.90$, indicating that the main approximation of the Janeček's method works slightly better for the case $r_c = 3$.

The computed values of the surface tension allow us to obtain an independent estimate of the critical temperature for each cutoff used from the scaling relation

$$\gamma = \gamma_0 \left(1 - T/T_c\right)^{\mu} \ , \tag{9.19}$$

where γ is the surface tension at temperature T, γ_0 is the "zero-temperature" surface tension, μ is the corresponding critical exponent, and T_c is the critical temperature. Here, we fix μ to the universal value of $\mu = 1.258$ as obtained from renormalization-group theory. [5] Our estimates for the critical temperatures are collected in Table 9.5. The overall agreement between these values and those obtained from an analysis of the coexistence densities is satisfactory.

9.5 Conclusion

We have proposed an improved version of the Janeček methodology to evaluate the contribution to the microscopic components of the pressure tensor due to the dispersive inhomogeneous LRC of spherical LJ fluid. This improved technique allows to determine the contribution as an effective pairwise virial, without need of the explicit calculation of the current density profile along the simulation. In order to assess the accuracy of the method proposed, we have determined the interfacial properties of the vapour-liquid interface of spherical LJ molecules with different spherically truncated (but not shifted) distances, $r_c = 2.5$, 3, 4, and 5σ. In addition to that, we have also obtained the same properties using cutoff distances $r_c = 2.5$ and 3σ in combination with the improved version of the inhomogeneous LRC of Janeček proposed in this work.

We use Monte Carlo *NVT* simulations of the inhomogeneous system containing two vapour-liquid interfaces. The normal and tangential microscopic components of the pressure tensor are evaluated using the mechanical or virial route in combination with the recipe of Irving and Kirkwood. We have also determined the macroscopic components of the pressure tensor using the alternative VP method of de Miguel and Jackson. In addition to that, the vapour-liquid surface tension has been evaluated using three different but equivalent procedures, the integration of the difference between the microscopic components of the pressure tensor following the mechanical route, the difference of the macroscopic components obtained from the thermodynamic perturbative method, and finally the well-known TA approach. We have examined the density profiles, interfacial thickness, and surface tension in terms of the temperature and the cutoff distance of the intermolecular potential. In addition, we have also calculated the coexistence phase envelope, including the location of the critical point from an analysis of the density profiles and the surface tension, and the vapour pressure. Results obtained in this work are in excellent agreement with simulation data taken from literature in all cases, confirming the adequacy of the methodology for calculating the inhomogeneous LRC.

The effect of the cutoff distance r_c on the microscopic and macroscopic components of the pressure tensor, surface tension, density profiles, and interfacial thickness, as well as other thermodynamic properties associated to the vapour-liquid equilibrium, such as the coexistence densities, vapour pressure, and critical temperature and density has been investigated. The normal macroscopic and microscopic components of the pressure tensor decrease and the peak of the microscopic component of the pressure tensor associated to the interface becomes more negative as the cutoff distance is increased, approaching to the full potential limit when the inhomogeneous LRC for the intermolecular potential and virial are used. The vapour-liquid interface is seen to sharpen with increasing the cutoff distance corresponding to an increase in the width of the coexistence phase envelope, and an accompanying increase in the surface tension. This is a direct consequence of the cohesive energy of the system, that increases when larger cutoff distances or inhomogeneous LRC are used.

Finally, we have also checked the effect of the impulsive contribution to the pressure due to the discontinuity of the intermolecular interaction potential when is cut (but not shifted) at r_c. If this contribution is not accounted for in the calculation of the microscopic components of the pressure tensor, incorrect values of both components as well as a wrong structure along the vapour-liquid interface are obtained. This effect is more important for short cutoff distances, an expected result since the jump at r_c is larger.

Acknowledgment

The authors would like to acknowledge helpful discussions with J. M. Míguez, L. G. MacDowell, and M. M. Piñeiro. This work was supported by Ministerio de Ciencia e Innovación (MICINN, Spain) through Grant with reference FIS2010-14866 and by Ministerio de Economía y Competitividad (MINECO) through Grant with reference FIS2013-46920-C2-1-P. Further financial support from Junta de Andalucía and Universidad de Huelva is also acknowledged.

9.6 Supplementary material of the article: long-range corrections for the pressure tensor of spherical systems

The instantaneous pressure $\mathcal{P}$ for a system of N particles in a volume V is appropriately defined as,

$$\mathcal{P} = \frac{1}{V}\left(\frac{1}{3}\sum_{i=1}^{N} m_i \mathbf{v}_i \cdot \mathbf{v}_i + \frac{1}{3}\sum_{i=1}^{N} \mathbf{r}_i \cdot \mathbf{f}_i\right) \tag{9.20}$$

where m_i is the mass, $\mathbf{r}_i$ the position, $\mathbf{v}_i$ the velocity, and $\mathbf{f}_i$ the force acting on particle i. Assuming that there are not external forces acting on the system, the only contribution to the forces arises from the intermolecular interactions.

The macroscopic pressure can be obtained from Eq. (9.20) by performing a time or statistical average over the appropriate ensemble. In the case of systems that interact through pairwise interactions, the macroscopic pressure can be written explicitly as,

$$P = \langle \rho k_B T \rangle + \left\langle \frac{1}{3V} \sum_{i=1}^{N-1} \sum_{j=i+1}^{N} \mathbf{r}_{ij} \cdot \mathbf{f} \right\rangle \tag{9.21}$$

where $\rho = N/V$ is the number density, k_B is Boltzmann constant, T is the temperature, $\mathbf{r}_{ij}$ is the intermolecular vector between a molecular pair, and $\mathbf{f}_{ij}$ is the corresponding intermolecular force.

It is possible to generalize the definitions of the instantaneous and macroscopic pressures given by Eqs. (9.20) and (9.21) for inhomogeneous systems. In this case, the pressure is no longer a scalar magnitude but a tensorial property. A suitable definition for the microscopic components of the pressure tensor $\mathcal{P}_{\alpha\beta}$ is,

$$\mathcal{P}_{\alpha\beta} = \frac{1}{V}\left(\sum_{i=1}^{N} m_i v_i^{\alpha} v_i^{\beta} + \sum_{i=1}^{N} r_i^{\alpha} f_i^{\beta}\right) \tag{9.22}$$

where v_i^{α} and v_i^{β} are the α and β components of the velocity $\mathbf{v}_i$, respectively, r_i^{α} is the α component of the position $\mathbf{r}_i$, and f_i^{β} is the β component of the force acting on particle i, $\mathbf{f}_i$. Similar to the case for the (bulk) instantaneous pressure, the components of the pressure tensor can be written in terms of the intermolecular forces between molecular pairs,

$$\begin{aligned}\mathcal{P}_{\alpha\beta} &= \frac{1}{V}\left(\sum_{i=1}^{N} m_i v_i^{\alpha} v_i^{\beta} + \sum_{i=1}^{N-1}\sum_{j=i+1}^{N} r_{ij}^{\alpha} f_{ij}^{\beta}\right) \\ &= \frac{1}{V}\left(\sum_{i=1}^{N} m_i v_i^{\alpha} v_i^{\beta} + \frac{1}{2}\sum_{i=1}^{N}\sum_{\substack{j=1\\(j\neq i)}}^{N} r_{ij}^{\alpha} f_{ij}^{\beta}\right)\end{aligned} \tag{9.23}$$

where r_{ij}^{α} is the α component of the intermolecular vector $\mathbf{r}_{ij} = \mathbf{r}_i - \mathbf{r}_j$ and f_{ij}^{β} is the β component of the intermolecular force $\mathbf{f}_{ij}$. Note that for convenience the pairwise summation over indexes i and j is expressed as a double sum using the same indexes (with the restriction $i \neq j$ to avoid nonphysical self-contributions terms to the pressure) and the factor $1/2$ to not include mutual interactions twice.

As in the case of Eq. (9.20), the first term on the right-hand side of the previous equation is the kinetic (ideal gas) contribution and the second term represents the residual contribution arising from the intermolecular interactions. This last term can be related easily with the well-known microscopic virial tensor $\mathcal{V}_{\alpha\beta}$,

$$\mathcal{V}_{\alpha\beta} = \frac{1}{2}\sum_{i=1}^{N}\sum_{\substack{j=1\\(j\neq i)}}^{N} r_{ij}^{\alpha} f_{ij}^{\beta} \tag{9.24}$$

Hence, the microscopic pressure tensor can be then written as the kinetic (ideal gas) and the virial contributions as,

$$\mathcal{P}_{\alpha\beta} = \frac{1}{V}\left(\sum_{i=1}^{N} m_i v_i^{\alpha} v_i^{\beta} + \mathcal{V}_{\alpha\beta}\right) \tag{9.25}$$

The macroscopic components of the pressure tensor can be obtained from Eq. (9.25) in a similar way as the bulk pressure, i.e., by performing a time or statistical average over the appropriate ensemble,

$$\begin{aligned}P_{\alpha\beta} &= \left\langle \frac{1}{V}\sum_{i=1}^{N} m_i v_i^{\alpha} v_i^{\beta}\right\rangle + \left\langle \frac{1}{V}\mathcal{V}_{\alpha\beta}\right\rangle \\ &= \langle \rho k_B T \delta_{\alpha\beta}\rangle + \frac{1}{V}\Pi_{\alpha\beta}\end{aligned} \tag{9.26}$$

where $\Pi_{\alpha\beta}$ are the macroscopic components of the virial tensor as obtained averaging over the appropriate ensemble the microscopic components $\mathcal{V}_{\alpha\beta}$.

The only non-zero components of the pressure tensor in a system that exhibits a planar vapor-liquid interface are the normal and tangential components of the pressure tensor. In addition to that, the normal component of the pressure tensor is constant and equal to the vapor pressure of the system, and the tangent components of the pressure tensor depend on the position along the direction perpendicular to the interface (with respect to an arbitrary origin). If we choose arbitrarily the z-axis as the direction along which the simulation box exhibits its inhomogeneity, the normal component, P_{zz}, and the tangential components, $P_{xx} \equiv P_{xx}(z)$ and $P_{yy} \equiv P_{yy}(z)$, are the relevant components, as well as the normal, Π_{zz}, and the tangential, $\Pi_{xx} \equiv \Pi_{xx}(z)$ and $\Pi_{yy} \equiv \Pi_{yy}(z)$, components of the virial tensor.

Let be $\Pi_{\alpha\alpha}$ an arbitrary diagonal component of the virial tensor, with $\alpha = x, y$ in the case of the tangential components, and $\alpha = z$ in the case of the normal component. $\Pi_{\alpha\alpha}$ may be written as

$$\Pi_{\alpha\alpha} = \left\langle \sum_{i=1}^{N} r_i^\alpha f_i^\alpha \right\rangle = \left\langle \frac{1}{2} \sum_{i=1}^{N} \sum_{\substack{j=1 \\ (j \neq i)}}^{N} r_{ji}^\alpha f_{ij}^\alpha \right\rangle \tag{9.27}$$

During a simulation, the potential energy of a particle is usually split into two contributions: one arising from the interaction of molecule i with all molecules inside a sphere of radius $r_c^{(i)}$ centered at this molecule, and a second term that corresponds to the interaction between the molecule i and the rest of molecules forming the system (i.e., all the molecules located outside the cutoff sphere). In the same way, the value of the $\alpha\alpha$ component of the virial tensor can be expressed as a part due to the direct interactions and a sum of LRC depending on the z-coordinates of molecules forming the system

$$\Pi_{\alpha\alpha} = \Pi_{\alpha\alpha}^{\text{CUT}} + \Pi_{\alpha\alpha}^{\text{LRC}} = \left\langle \frac{1}{2} \sum_{i=1}^{N} \sum_{j \in r_c^{(i)}} r_{ij}^\alpha f_{ij}^\alpha \right\rangle + \frac{1}{2} \sum_{i=1}^{N} \Pi_{\alpha\alpha}^{\text{LRC}}(z_i) \tag{9.28}$$

The first term of the right-hand side of Eq. (9.28), $\Pi_{\alpha\alpha}^{\text{CUT}}$, accounts for the components of the virial tensor due to the interactions between particles located inside the cutoff $r_c^{(i)}$, and the second term, $\Pi_{\alpha\alpha}^{\text{LRC}}$, is the contribution to the components of the virial tensor due to the long-range interactions. $r_c^{(i)}$ is the so-called cutoff distance of particle i, the notation $j \in r_c^{(i)}$ denotes all the particles j located inside the cutoff sphere centered at the position of particle i, and $\Pi_{\alpha\alpha}^{\text{LRC}}(z_i)$ represents the LRC term to the $\alpha\alpha$ component of the virial tensor due to forces acting on particle i located at position z_i. Since all molecules have the same cutoff distance, $r_c^{(i)}$ is constant, $r_c^{(i)} \equiv r_c$. Note that the second term on the right-hand side of the previous equation contains a $1/2$ factor that is not present in Eq. (19) of the original paper of Janeček [6]. This numerical factor, to not include mutual interactions twice, is implicitly taken into account by Janeček in Eqs. (21) and (22) of its original work [6].

In the original Janeček's methodology, the simulation box is divided into strips parallel to the xy-plane (and to the planar interface) of width Δz, in such a way that the number density of the system $\rho(z)$ is considered to be approximately constant inside of each of them. Here we have chosen arbitrarily the z-axis as the direction along which the simulation box exhibits its inhomogeneity. If one assumes that the pair correlation function between two particles separated beyond the cutoff distance is equal to one, i.e., the distribution of particles separated a distance $r_{ij} \geq r_c$ is uniform, the $\alpha\alpha$ component of the virial tensor at position z_i associated to the long-range forces with the rest of the system is given by [6],

$$\Pi_{\alpha\alpha}^{\mathrm{LRC}}(z_i) = \left\langle \sum_{k=1}^{n_s} \pi_{\alpha\alpha}(|z_i - z_k|)\rho(z_k)\Delta z \right\rangle \tag{9.29}$$

where $\rho(z_k)$ is the density of the system in the slab of width Δz and centered at z_k, the index k runs for all the n_s slabs in which the simulation box is divided along the z-axis, and $\pi_{\alpha\alpha}(|z_i - z_k|)$ accounts for the $\alpha\alpha$ component of the virial tensor due to the LRC interactions between the particle i at position z_i and all the particles located inside the slab centered at z_k. The particular expressions for $\pi_{\alpha\alpha}(|z_i - z_j|)$ depends on the choice of the intermolecular potential of the system. In the original Janeček's method, applicable for molecules interacting through the Lennard-Jones intermolecular potential, the functions $\pi_{\alpha\alpha}(\xi)$ are given by

$$\pi_{xx}(z) = \pi_{yy}(\xi) = \begin{cases} 4\pi\epsilon\left[\dfrac{(6r_c^2 - 5\xi^2)}{5}\left(\dfrac{\sigma}{r_c}\right)^{12} - \dfrac{(3r_c^2 - 2\xi^2)}{2}\left(\dfrac{\sigma}{r_c}\right)^{6}\right] & \xi \leq r_c \\[2ex] 4\pi\epsilon\left[\dfrac{\xi^2}{5}\left(\dfrac{\sigma}{\xi}\right)^{12} - \dfrac{\xi^2}{2}\left(\dfrac{\sigma}{\xi}\right)^{6}\right] & \xi > r_c \end{cases} \tag{9.30}$$

and

$$\pi_{zz}(\xi) = \begin{cases} 8\pi\epsilon\xi^2\left[\left(\dfrac{\sigma}{r_c}\right)^{12} - \left(\dfrac{\sigma}{r_c}\right)^{6}\right] & \xi \leq r_c \\[2ex] 8\pi\epsilon\xi^2\left[\left(\dfrac{\sigma}{\xi}\right)^{12} - \left(\dfrac{\sigma}{\xi}\right)^{6}\right] & \xi > r_c \end{cases} \tag{9.31}$$

Eqs. (9.28)–(9.31) constitute the original Janecek's method for estimating the components of the virial tensor due to LRC. Although this method allows to calculate very accurately the components of the virial tensor (and also the components of the pressure tensor), including the contributions due to the LRC of a Lennard-Jones system that exhibits a planar interface, it has several drawbacks. The most important one is the calculation of the density profile on the fly, i.e., it is necessary to have the instantaneous density profile every step for being used in Eq. (9.29) and hence, to be able to calculate the tail corrections at each Monte Carlo step. Unfortunately, this makes the procedure cumbersome, especially in the case of molecular fluids [7], and also complicates the programming since the density profile must be updated each Monte Carlo step.

Capítulo 10

Determination of interfacial tension of binary mixtures from perturbative approaches

Molecular Physics, 113, 1227 (2015)

F. J. Martínez-Ruiz[1,2] and F. J. Blas[1,2]

[1]Departamento de Física Aplicada, Universidad de Huelva, Huelva, Spain
[2]Centro de Investigación de Física Teórica y Matemática FIMAT, Universidad de Huelva, Huelva, Spain

We determine the interfacial properties of mixtures of spherical Lennard-Jones molecules from direct simulation of the vapor-liquid interface. We consider mixtures with the same molecular size but different dispersive energy parameter values. We use the extensions of the improved version of the inhomogeneous long-range corrections of Janeček [J. Janeček, *J. Phys. Chem. B* **129**, 6264 (2006)], presented recently by MacDowell and Blas [L. G. MacDowell and F. J. Blas, *J. Chem. Phys.* **131**, 074705 (2009)] and Martínez-Ruiz *et al.* [F. J. Martínez-Ruiz, F. J. Blas, B. Mendiboure, and A. I. Moreno-Ventas Bravo, *J. Chem. Phys.* **141**, 184701 (2014)], to deal with the interaction energy and microscopic components of the pressure tensor. We have performed Monte Carlo simulations in the canonical ensemble to obtain the interfacial properties of mixtures of Lennard-Jones molecules with a cutoff distances $r_c = 3\sigma$ in combination with the inhomogeneous long-range corrections. The pressure tensor is obtained using the mechanical (virial) and thermodynamic route. The vapour-liquid interfacial tension is also evaluated using three different procedures, the Irving-Kirkwood method, the difference between the macroscopic components of the pressure tensor, and the Test-Area methodology. This allows to check the validity of the recent extensions presented to deal with the contributions due to long-range corrections for intermolecular energy and pressure tensor in the case of binary mixtures. In addition to the pressure tensor and the surface tension, we also obtain density profiles, coexistence densities, and interfacial thickness as functions of pressure, at a given temperature. According to our results, the main effect of increasing the ratio between the dispersive energy parameters of the mixture, $\epsilon_{22}/\epsilon_{11}$, is to sharpen the vapour-liquid interface and to increase the width of the biphasic coexistence region. Particularly interesting is the presence of a relative maximum in the density profiles of the less volatile component at the interface. This maximum is related with adsorption or accumulation of these molecules at the interface, a direct consequence of stronger attractive interactions between these molecules in comparison with the rest of intermolecular interactions. In addition to that, the interfacial thickness decreases, the width of the tangential microscopic component of the pressure tensor profile increases, and the surface tension increases as $\epsilon_{22}/\epsilon_{11}$ is larger.

10.1 Introduction

Fluid-fluid interfaces have fascinated scientifics since the time of Laplace and Young [5]. More recently, interfacial properties, and particularly interfacial tension, have been routinely determined for many computer simulation researchers of the liquid-state community. However, the application of theories of inhomogeneous systems, and especially computer simulation, to fluids mixtures is far less common. Knowledge of interfacial properties of mixtures is essential in a large number of scientific and engineering fields, including nucleation or dynamics of phase transition, among many others. From a formal point of view, understanding how miscroscopic parameters (for instance, molecular size and dispersive energy interactions) determine the thermodynamic and structural behaviour of mixtures near interfaces is one of the classical problems in applied Statistical Mechanics and computer simulation.

Surface tension is probably the most challenging property to be determined and predicting using molecular-based theories and simulation techniques. Despite the number of studies carried out since computer simulation is used routinely for determining the properties of a molecular model, the calculation of surface tension is still a subtle problem. The ambiguity in the definition of the microscopic components of the pressure tensor [4, 73], the finite size effects due to capillary waves [119, 120], or the difficulty for the calculation of the dispersive long-range corrections (LRC) associated to the intermolecular interactions [14, 15], make the calculation of surface tension a difficult and non-trivial problem.

The usual procedure to the evaluation of the fluid-fluid interfacial tension in a molecular simulation involves the determination of the microscopic components of the pressure tensor through the well-known mechanical or virial route. This route states that surface tension of a planar fluid-fluid interface can be readily obtained from the integration of the difference between the normal and tangential microscopic components of the pressure tensor profiles along the interface. This method generally involves an ensemble average of the virial of Clausius according to the recipes of Irving and Kirkwood [62]. Although the mechanical route is an appropriate technique for determining the surface tension, a number of alternative methods have been proposed during the last years to calculate, not only the interfacial tension, but also for the components of the pressure tensor, without the need of evaluate the virial.

These new methods can be viewed as a collection of effective and elegant techniques based on the thermodynamic definition of surface tension and tensore pressure. The first one can be understood as the change in free energy when the interfacial area is changed, at constant volumen and temperature. The second one, can be expressed as the change in free energy when the volume of the system is changed along any direction, keeping constant the other two dimensions. Examples of these methods are the Test-Area (TA) technique of Gloor *et al.* [4], the Volume Perturbation (VP) method of de Miguel and Jackson [16,50,51], the Wandering Interface Method (WIM), introduced by MacDowell and Bryk [10], and the use of the Expanded Ensemble (EE), based on the original work of Lyuvartsev *et al.* [87], for calculating the surface tension proposed independently by Errington and Kofke [11] and de Miguel [12]. These methods are becoming very popular and are being used routinely to determine the vapour-liquid interfacial properties of different potential model fluids [13, 14, 65, 75, 76, 83, 89, 92, 96, 97, 113, 126–134, 142].

As mentioned previously, one of the major difficulties encountered in the simulation of inhomogeneous systems by molecular simulation is the truncation of the intermolecular potential. Although for homogeneous systems this issue is easily solved by including the well-known homogeneous LRC [2,3], the situation is much more complicated in the case of fluid-fluid interfaces, and in general, in inhomogeneous systems. Fortunately, this problem seems to solved satisfactorily recently in cases in which the system exhibits planar symmetry. Different authors have contributed to the establishment of appropriate and standard inhomogeneous LRC, including Blokhius [135], Mecke [38, 79], Daoulas [136], Guo and Lu [137], and finally, Janeček [15, 138], and the recent improved methods proposed by MacDowell and Blas [14], de Gregorio *et al.* [133], and Martínez-Ruiz *et al.* [142]

The goal of this work is to determine the vapor-liquid interfacial properties of mixtures of spherical LJ molecules with the same molecular size but different dispersive energy parameters. In particular, we focus on the effect of the dispersive energy ratio on different interfacial properties, including density profiles, normal and tangential microscopic components of the pressure tensor profiles, and surface tension. In addition to that, we also analyze the effect of the dispersive energy ratio on other thermodynamics properties, such as coexistence density and pressure-composition slices of the phase diagram. In all cases, we use the improved versions of the inhomogenenous LRC of Janeček [15] recently proposed by MacDowell and Blas [14] for the intermolecular energy and Martínez-Ruiz *et al.* [142] for the microscopic components of the pressure tensor. In order to check the effectiveness of these methods in the case of mixtures, we also determine the surface tension and the components of the pressure tensor using two different perturbative methods, the TA technique and the VP methodology. This allows to obtain independent results and compare our predictions with simulation data taken from the literature. To our knowledge, this is the first time the surface tension and components of the pressure tensor of mixtures of LJ spheres are calculated using perturbative methods in both cases and taking into account the LRC associated to the intermocular potential and components of the pressure tensor.

The rest of the paper is organized as follows. In Section 10.2 we present the model and simulation details of this work. Results obtained are discussed in Section 10.3. Finally, in Section 10.4 we present the main conclusions.

10.2 Model and simulation details

We consider binary mixtures of spherical LJ molecules characterized by diameters σ_{ii} and dispersive energies ϵ_{ii}, where index i denotes component i. The interaction potential between two different molecules of species i and j is given by,

$$u_{ij}^{LJ}(r) = 4\epsilon_{ij}\left[\left(\frac{\sigma_{ij}}{r}\right)^{12} - \left(\frac{\sigma_{ij}}{r}\right)^{6}\right] \tag{10.1}$$

where r is the distance between two molecules, and σ_{ij} and ϵ_{ij} are the intermolecular parameters (size and dispersive energy) associated to the interaction between molecules of type i and j. In this work, we use the well-known Lorentz-Berthelot combining rules for unlike dispersive interactions,

$$\sigma_{ij} = \frac{\sigma_{ii} + \sigma_{jj}}{2} \tag{10.2}$$

and

$$\epsilon_{ij} = (\epsilon_{ii}\epsilon_{jj})^{1/2} \tag{10.3}$$

During the simulation, we use a potential spherically truncated (but not shifted) at a cutoff distance r_c, defined by,

$$u_{ij}(r) = u_{ij}^{LJ}(r)\ [1 - \Theta(r - r_c)] = \begin{cases} u_{ij}^{LJ}(r) & r \leq r_c \\ 0 & r > r_c \end{cases} , \tag{10.4}$$

where $\Theta(x)$ is the Heaviside step function. Note that since we restrict our study to binary mixtures with the same size, $\sigma_{11} = \sigma_{22} = \sigma_{12}$, we also use the same cutoff distance r_c for all the interactions.

We examine mixtures interacting with this spherically truncated potential model with cutoff distance $r_c = 3\sigma$ and several interaction dispersive parameter values $\epsilon_{22}/\epsilon_{11}$. Standard homogeneous LRC to the intermolecular interaction energy and pressure [3] are used in NPT simulations of bulk phases. In addition to that, inhomogeneous LRC using the MacDowell and Blas [14, 144] methodology for the intermolecular potential energy and the recipe presented in our recent paper [142], based on the Janeček's method [15, 138], for the evaluation of the LRC for the components of the pressure tensor. Results obtained using these LRC are equivalent to use the full potential or a potential with infinite truncation distance.

The number of molecules, N, used in the simulations performed in this work for studying the vapour-liquid interface of mixtures of LJ molecules varied from $N = 2150$, for the lowest pressure considered ($P^* = P\sigma_{11}^3/\epsilon_{11} = 0.06$), to $N = 2750$, for the highest pressure analyzed ($P^* = P\sigma_{11}^3/\epsilon_{11} = 0.16$). Note that it is not possible to have systems with the same total number of molecules and with the same interfacial area since we are dealing with binary mixtures in which composition must be taken into account. Whereas the initial setup for simulations of vapour-liquid interfaces for pure systems is relatively easy, the initial configuration of a vapour-liquid interface involving binary mixtures is a delicate issue. To obtain the initial interfacial simulations boxes at different pressures, we firstly use the well-known Soft-SAFT approach, based on Wertheim's Thermodynamic Perturbation Theory [17–20], and developed by one of us [21, 22], to calculate the complete phase diagrams of the mixtures to be studied. This allows to have an initial precise picture of the coexistence envelope of the system at thermodynamic conditions at which the simulations are performed. In particular, initial densities and compositions of each component of the mixture in both, the vapour and liquid phases, are obtained using the Soft-SAFT approach for the mixtures considered in this work.

Simulations are performed in two steps. In the first step, homogeneous liquid and vapour systems, at a given temperature and pressure, are equilibrated in a rectangular simulation box of dimensions $L_x = L_y = 10\sigma$, and varying L_z. Box length measured along the z-axis is chosen in such a way that the corresponding densities match the predictions obtained from the Soft-SAFT approach at temperature and pressure selected. In addition to that, the particular number of molecules of each species, in both liquid and vapour phases, are also selected according to the SAFT predictions. Both simulation boxes (liquid and vapour phases) are equilibrated at the same temperature and pressure using an NPT ensemble in which L_x and L_y are kept constant and only L_z is varied along the simulation. NPT simulations of homogeneous phases are organized by cycles. A cycle is defiend as N trial moves (displacement of the center of mass) and an attempt to change the box length along the z-axis (L_z). The magnitude of the appropriate displacement is adjusted so as to get an acceptance rate of $30\,\%$ approximately. We use periodic boundary conditions and minimum image convention in all three directions of the simulation box. In addition to that, homogeneous LRC corrections to the intermolecular energy and pressure are also used [3].

In a second step, the interfacial simulation box is prepared leaving the previous homogeneous liquid phase at the center of the new box with the same homogeneous vapour phase boxes of equal size previously prepared at each side. Since L_x and L_y ($\mathcal{A} = L_x L_y$, i.e., the interfacial area) is the same for all homogeneous phases, it is always posible to build up the interfacial simulation box as explained here. The final overall dimensions of the vapour-liquid-vapour simulation box are therefore $L_x = L_y = 10\sigma$, and $L_z = 78.17\sigma$ for the lowest pressure considered ($P^* = k_B T/\epsilon = 0.70$), and $L_z = 99.48\sigma$ for the highest pressure ($P^* = k_B T/\epsilon = 1.1$).

The simulations for studying the vapour-liquid interface are also organized in cycles. In this case, a cycle is defined as N trial moves (displacement of the center of mass) and the magnitude of the appropriate displacement is adjusted so as to get an acceptance rate of $30\,\%$ approximately. We use periodic boundary conditions and minimum image convention in all three directions of the simulation box. To be consistent with simulations performed using the NPT ensemble for preparing the definitive simulation box, we use inhomogeneous LRC to the intermolecular energy of MacDowell and Blas [14, 144] methodology for the intermolecular potential energy and the recipe presented in our previous paper [142] for the evaluation of the LRC for the components of the pressure tensor, both of them based on the Janeček's method [15].

We have obtained the normal and tangential microscopic components of the pressure tensor from the mechanical expression or virial route,

$$P_{\alpha\beta} = \langle \rho k_B T \rangle + \left\langle \frac{1}{V} \sum_{i=1}^{N-1} \sum_{j=i+1}^{N} r_{ij}^{\alpha} f_{ij}^{\beta} \right\rangle \tag{10.5}$$

In this work, we have followed the same procedure as in our previous work [142] and used the well-known Irving and Kirkwood (IK) recipe [62, 63] for determining the microscopic components of the pressure tensor, $P_N(z) \equiv P_{zz}(z)$ and $P_T(z) \equiv P_{xx}(z) \equiv P_{yy}(z) \equiv \frac{1}{2}(P_{xx}(z) + P_{yy}(z))$. The components of the pressure tensor are calculated each cycle.

Following de Miguel and Jackson [16], we have also determined the macroscopic components of the pressure tensor using its thermodynamic defintion as,

$$P_{\alpha\alpha} = -\left(\frac{\partial F}{\partial V}\right)_{NTL_{\beta\neq\alpha}} \tag{10.6}$$

The notation $L_{\beta\neq\alpha}$ indicates that the partial derivative with respect to the volume is performed in such a way that the dimension of the system along the α-axis, L_α, is varied while keeping all other dimensions L_β ($\beta \neq \alpha$) fixed.

We follow the methodology proposed by de Miguel and Jackson [16], based on the seminal works of Eppenga and Frenkel [94] and Harismiadis *et al.* [95], an use virtual volume perturbations of magnitude $\xi = \Delta V/V$ every five MC cycles. Here ξ defines the relative volume (compressive and expansive) change associated with the perturbation, i.e., rescale independently the box lengths of the simulation cell and positions of the molecular centers of mass according to linear transformations along the appropriate directions. In all cases, eight different (positive and negative) relative volume changes in the range $2 \times 10^{-4} \leq |\xi| \leq 15 \times 10^{-4}$ are used in our calculations. The final values of the macroscopic components of the pressure tensors presented in this work, P_N and P_T, correspond to the extrapolated values (as determined by a linear extrapolation to $|\xi| \to 0$ of the values obtained from increasing-volume and decreasing-volume perturbations) obtained from a combined compression-expansion perturbation.

Surface tension is determined using three independent routes. In the first one, we used the mechanical definition that involves the integration of the difference between the tangential and normal microscopic components of the pressure tensor profiles, as obtained from the IK methodology, along the simulation box according to,

$$\gamma = \int_0^{L_z} \left(P_N(z) - P_T(z) \right) \, dz \tag{10.7}$$

Note that here we have chosen the z-axis perpendicular to the interface and the integral is performed along the total length L_z of the simulation box.

In the second route,the surface tension is calculated using the thermodynamic definitions of P_N and P_T, as proposed by de Miguel and Jackson [16]. The surface tension is obtained as,

$$\gamma = L_Z(P_N - P_T) \tag{10.8}$$

Here L_z is the simulation length along the z-axis. Note that Eq. (10.8) can be viewed as the macroscopic version of Eq. (10.7). As in the case of the microscopic definition, since there exist two vapour-liquid interfaces, the true value associated to a single interface is half of the value obtained from Eqs. (10.7) and (10.8).

Finally, in the third route we use TA methodology [4], which is based in the thermodynamic definiton of surface tension as,

$$\gamma = \left(\frac{\partial F}{\partial \mathcal{A}} \right)_{NVT} \tag{10.9}$$

Since the method is a standard and well-known procedure for evaluating fluid-fluid interfacial tensions of molecular systems, here we only provide the most important features of the technique. For further details we recommend the original work [4] and the most important applications [13, 14, 16, 75, 89, 92, 96, 97, 127–129, 133, 143–147]. The implementation of the TA technique involves performing virtual or test area deformations of relative area changes defined as $\xi = \Delta\mathcal{A}/\mathcal{A}$ during the course of the simulation at constant N, V, and T every five MC cycles. As shown by Gloor *et al.* [4], the surface tension follows from the computation of the change in Helmholtz free energy associated with the perturbation, which in turn can be expressed as an ensemble average of the corresponding Boltzmann factor. Further details can be found in Ref. [4] Note that the procedure for calculating the surface tension is similar to that used to evaluate the components of the pressure tensor, but in this case the changes in the normal and transverse dimensions are coupled to keep the overall volume constant. In particular, we use the same number and values for the relative area changes ξ, and the same procedure to obtain the extrapolated values.

We typically consider six reduced pressures in the range $P^* = P\sigma_{11}^3/\epsilon_{11} = 0.06$ up to 0.16. In the case of NPT simulations of the homogeneous liquid and vapour phases prepared in the first step, each simulation box is equilibrated for 10^6 MC cycles. In the case of the NVT simulations corresponding to the interfacial box, the system is also well equilibrated for other 10^6 equilibration MC cycles. In addition to that, averages are determined over a further period of 2×10^6 MC cycles. The production stage is divided into M blocks. Normally, each block is equal to 10^5 MC cycles. The ensemble average of the macroscopic components of the pressure tensor and the surface tension is given by the arithmetic mean of the block averages and the statistical precision of the sample average is estimated from the standard deviation in the ensemble average from $\overline{\sigma}/\sqrt{M}$, where $\overline{\sigma}$ is the variance of the block averages, and $M = 20$ in all cases.

All the quantities in our paper are expressed in conventional reduced units of component 1, with σ_{11} and ϵ_{11} being the length and energy scaling units, respectively. Thus, the temperature is given in units of ϵ_{11}/k_B, the densities of both components and the total density in units of σ_{11}^{-3}, the bulk pressure and components of the pressure tensor in units of the $\epsilon_{11}/\sigma_{11}^3$, the surface tension in units of $\epsilon_{11}/\sigma_{11}^2$, and the cutoff distance and interfacial thickness in units of σ_{11}.

10.3 Results and discussion

In this section we present the main results from simulations of the vapour-liquid interface of mixtures of spherical LJ molecules using LRC for the intermolecular potential energy and components of the pressure tensor. We focus mainly on the effect of the dispersive energy interaction between the components of the mixture on several interfacial properties. We have determined the components of the pressure using both the mechanical (or virial) and thermodynamic routes. Comparison between both results allows to check the validity of the method presented in previous works [14, 142, 144] for determining the contribution to the energy and pressure due to the LRC in mixtures of LJ systems. We have also examined several coexistence properties, such as coexistence densities, and also other interfacial properties, including density profiles, interfacial thickness, and surface tension. As in our previous work for pure systems [142], we pay special attention on the determination of the the vapour-liquid interfacial tension calculated using different routes, including the mechanical or virial route (using the traditional IK methodology) and the thermodynamic definition (using the VP and TA methods) of the surface tension.

We first analyze the effect of the dispersive energy parameter between components of the mixtures on density profiles. We follow the same analysis and methodology than in our previous works [13,14, 142–145] and consider different dispersive energy parameters and pressures. The equilibrium density profiles of each of components of the mixture, $\rho_1(z)$ and $\rho_2(z)$, as well as the total density, $\rho(z) = \rho_1(z) + \rho_2(z)$, are computed from averages of the histogram of densities along the z direction over the production stage. The bulk vapour and liquid densities of both components and the total density are obtained by averaging $\rho_1(z)$, $\rho_2(z)$, and $\rho(z)$, respectively over appropriate regions sufficiently removed from the interfacial region. This procedure is meaningful as far as the central liquid slab is thick enough. This turns out to be the case in our simulations, including those performed at the higher pressure. The bulk vapour densities are obtained after averaging the corresponding density profiles on both sides of the liquid film. The statistical uncertainty of these values is estimated from the standard deviation of the mean values. Following our previous works, additional interfacial properties, such as the position of the Gibbs-dividing surface, z_0, and the $10-90$ interfacial thickness, t, are obtained by fitting each of the equilibrium density profiles to hyperbolic tangent functions [5] (see Eq. (3) of our previous work [13] for further details). We fix liquid, ρ_L, and vapour, ρ_V, densities for each component and for the total density to previously computed values and treat z_0 and t as adjustable parameters.

Our simulation results for the bulk densities of each component, total densities, molar fractions of both component in each, components of the pressure tensor, surface tension, and interfacial thickness for mixtures of LJ molecules interacting with different dispersive energy parameters and the full potential, at different pressures, are collected in Tables 10.1 and 10.2.

Tabla 10.1: Liquid density, ρ^L, vapour density, ρ^V, liquid density of component 1, ρ_1^L, vapour density of component 1, ρ_1^V, liquid density of component 2, ρ_2^L, and vapour density of component 2, ρ_2^V at $T = 1.6$ and different pressures P_N^{vir}, for mixtures of LJ molecules with different dispersive energy parameters, $\epsilon_{22}/\epsilon_{11}$, and a cutoff distance $r_c = 3$ with inhomogeneous LRC. All quantities are expressed in the reduced units defined in Section 10.2. The errors are estimated as explained in the text.

P_N^{vir}	$\rho^{(L)}$	$\rho^{(V)}$	$\rho_1^{(L)}$	$\rho_1^{(V)}$	$\rho_2^{(L)}$	$\rho_2^{(V)}$
			$\epsilon_{22}/\epsilon_{11} = 1.5$			
0.05863(18)	0.6585(2)	0.0463(4)	0.00657(10)	0.00180(4)	0.65194(21)	0.0444(4)
0.07691(22)	0.6430(4)	0.0632(3)	0.0561(3)	0.01667(11)	0.5869(5)	0.04654(21)
0.0961(3)	0.6182(3)	0.0835(8)	0.1045(3)	0.0331(4)	0.5136(6)	0.0504(3)
0.1179(6)	0.5950(4)	0.1124(10	0.1467(2)	0.0538(5)	0.4483(5)	0.0586(5)
0.1361(4)	0.5531(6)	0.1411(17)	0.19249(12)	0.0766(7)	0.3606(5)	0.0644(9)
			$\epsilon_{22}/\epsilon_{11} = 1.75$			
0.0420(13)	0.7349(3)	0.02881(17)	0.03763(20)	0.01176(15)	0.6973(3)	0.01705(13)
0.0731(7)	0.7122(4)	0.0553(4)	0.1088(8)	0.0349(3)	0.6034(12)	0.02032(18)
0.0955(8)	0.6908(3)	0.0758(3)	0.1607(3)	0.05467(23)	0.5301(5)	0.02117(15)
0.1118(8)	0.67272(19)	0.0928(4)	0.1973(3)	0.0689(3)	0.4753(3)	0.0238(3)
0.1315(6)	0.6392(3)	0.1206(8)	0.2509(3)	0.0930(5)	0.3882(5)	0.0276(3)
0.1486(8)	0.6102(4)	0.1473(11)	0.28281(17)	0.1163(8)	0.3274(5)	0.0311(4)
			$\epsilon_{22}/\epsilon_{11} = 2.0$			
0.05126(15)	0.7822(3)	0.03595(16)	0.0679(3)	0.02838(13)	0.7144(4)	0.00757(9)
0.06980(14)	0.7749(3)	0.0491(3)	0.0935(6)	0.0405(3)	0.6814(9)	0.00858(6)
0.0868(12)	0.7638(3)	0.0646(3)	0.1285(7)	0.05562(23)	0.6353(9)	0.00898(8)
0.1069(12)	0.7485(3)	0.0829(4)	0.1733(5)	0.0728(4)	0.5751(7)	0.01011(12)
0.1235(6)	0.7352(3)	0.1040(7)	0.2041(7)	0.0911(6)	0.5311(10)	0.01296(14)
0.1464(15)	0.7083(3)	0.1262(4)	0.2628(10)	0.1121(4)	0.4455(13)	0.01416(13)

Tabla 10.2: Normal component of the macroscopic pressure tensor calculated from the virial route P_N^{vir}, normal and tangential components of the macroscopic pressure tensor calculated from VP, P_N and P_T, surface tension calculated from integration given by Eq. (10.7), γ^{vir}, from VP, γ, and from TA, γ_{TA}, and $10-90$ interfacial thickness, t, at $T = 1.6$ and different pressure for mixtures of LJ molecules with different dispersive energy parameters, $\epsilon_{22}/\epsilon_{11}$, and a cutoff distance $r_c = 3$ with inhomogeneous LRC. All quantities are expressed in the reduced units defined in Section 10.2. The errors are estimated as explained in the text. Uncertainties of surface tension calculated from the virial route, γ^{vir}, are error estimates corresponding to the numerical calculation of the integral given by Eq. (10.7).

P_N^{vir}	P_N^*	P_T^*	γ^{vir}	$\gamma*$	γ_{TA}	t
			$\epsilon_{22}/\epsilon_{11} = 1.5$			
0.05863(18)	0.0586(7)	0.0473(6)	0.565(5)	0.56(4)	0.559(5)	4.090(5)
0.07691(22)	0.0801(6)	0.0701(6)	0.438(3)	0.44(3)	0.438(4)	4.63(4)
0.0961(3)	0.0947(7)	0.0869(6)	0.333(3)	0.32(3)	0.320(4)	5.49(6)
0.1179(6)	0.1148(4)	0.1093(4)	0.258(3)	0.24(2)	0.251(3)	6.46(15)
0.1361(4)	0.1316(5)	0.1283(5)	0.166(2)	0.15(3)	0.153(4)	7.97(17)
			$\epsilon_{22}/\epsilon_{11} = 1.75$			
0.0420(13)	0.0423(10)	0.0178(10)	1.025(4)	1.03(6)	1.027(6)	3.069(10)
0.0731(7)	0.0735(7)	0.0572(7)	0.730(4)	0.73(4)	0.742(6)	3.91(11)
0.0955(8)	0.0944(8)	0.0803(7)	0.554(3)	0.55(4)	0.552(6)	4.49(7)
0.1118(8)	0.1097(8)	0.0998(7)	0.431(3)	0.42(4)	0.424(4)	5.234(5)
0.1315(6)	0.1308(8)	0.1242(8)	0.294(3)	0.28(4)	0.280(3)	6.455(11)
0.1486(8)	0.1478(8)	0.1432(8)	0.204(2)	0.19(5)	0.190(4)	8.111(19)
			$\epsilon_{22}/\epsilon_{11} = 2.0$			
0.05126(15)	0.0506(7)	0.0209(6)	1.312(5)	1.32(4)	1.321(9)	2.99(8)
0.06980(14)	0.0666(7)	0.0418(7)	1.085(4)	1.09(4)	1.095(6)	3.46(8)
0.0868(12)	0.0838(7)	0.0618(7)	0.959(4)	0.96(4)	0.967(6)	3.761(18)
0.1069(12)	0.1048(8)	0.0865(7)	0.753(3)	0.75(4)	0.748(8)	4.323(5)
0.1235(6)	0.1200(7)	0.1070(7)	0.605(3)	0.60(4)	0.594(9)	5.181(16)
0.1464(15)	0.1465(9)	0.1365(9)	0.422(2)	0.41(5)	0.415(7)	6.362(4)

We show in Fig. 10.1 the density profiles $\rho_1(z)$, $\rho_2(z)$, and $\rho(z)$ for three mixtures of LJ molecules with the same size, $\sigma_{22} = \sigma_{11}$ and different dispersive energy parameters of the component 2, $\epsilon_{22}/\epsilon_{11} = 1.50$, 1.75, and 2.00, at $T = 1.6$ and several pressures. For the sake of clarity, we only present one half of the profiles corresponding to one of the interfaces. Also for convenience, all density profiles have been shifted along z so as to place z_0 at the origin. As can be seen, for a given mixture (or value of the dispersive energy parameter $\epsilon_{22}/\epsilon_{11}$), the slope (in absolute value) of the density profiles corresponding to component 1 and total density in the interfacial region decreases as the pressure is increased, making smaller the jump in densities when passing from the vapour to the liquid side of the interface. Consequently, the interfacial thickness increases, an expected behaviour that indicates the phase envelope is becoming thicker as the system approaches to the critical point of the mixture.

Fig. 10.1 also shows the effect of increasing the dispersive energy parameter $\epsilon_{22}/\epsilon_{11}$ on the density profiles, i.e., when the mixture becomes more asymmetric. As can be seen comparing parts (a), (b), and (c) of the figure, an increase of $\epsilon_{22}/\epsilon_{11}$ results in steeper density profiles of component 1 and total density along the interfacial region. This effect, which also produces narrower interfacial regions, is related with the increasing of the asymmetry of the mixture. As $\epsilon_{22}/\epsilon_{11}$ becomes larger, the mixture is more asymmetric and the phase envelope (see Fig. 10.2) becomes wider in terms of densities (and also in molar fractions), or in other words, jumps in density from the vapour to the liquid side of the interface increases.

Special attention deserves the behaviour of the density profiles corresponding to the component 2 of the system, the less volatile substance of the mixture. As can be seen inf Fig. 10.1, $\rho_2(z)$ exhibits a nearly monotonic increasing behaviour when passing from the vapour to the liquid size of the interface when $\epsilon_{22}/\epsilon_{11} = 1.50$. However, as the difference in dispersive energies between both components increases, $\epsilon_{22}/\epsilon_{11} = 1.75$ and 2.00, $\rho_2(z)$ exhibits a relative maximum at the interface. This maximum is related with adsorption of component 2 at the interface. These molecules tend to accumulate at the interface on increasing the dispersive energy parameter of component 2 and decreasing of the pressure. This type of enhanced adsorption of one component relative to the other is usually seen in binary mixtures of spherical molecules when there are significant differences in the values of the unlike dispersion interactions [148].

The vapour-liquid phase envelopes of mixtures of LJ molecules with different dispersion interaction values $\epsilon_{22}/\epsilon_{11}$, as calculated from the analysis of the density profiles obtained from our Monte Carlo simulations, are depicted in Fig. 10.2. The Soft-SAFT theoretical approach has been also used to obtain the complete phase diagram of mixtures of LJ molecules with different dispersive interation parameter values. Although, as we have mentioned in the Introduction and Model and simulation details sections, we have used the information from the theory for obtaining initial guesses of the liquid and vapour densities and compositions of mixtures to be studied by simulation at particular thermodynamic conditions, this theoretical predictions can also be used as results to compare our simulation results and check the ability of SAFT in predicting the phase behaviour of these mixtures. As can be seen in part (a) of the figure, the pressure-density or $P\rho$ slice of the phase diagram of mixture indicates that the phase envelope of the system, at $T = 1.60$, becomes wider as the dispersive energy parameter $\epsilon_{22}/\epsilon_{11}$ is increased. The enlargement of the width associated to the phase envelope is essentially due to the increase of the liquid density as the dispersive energy is higher. As can be seen, agreement between Monte Carlo simulation results and prediction from SAFT is excellent in all cases. It is important to recall here that results from the theory are predictions obtained using the Lorentz-Berthelot combining rules without any further fitting procedure. We have also obtained the pressure-composition or Px slice of the mixture at the same thermodynamic conditions and using the same dispersive energy parameters. As can be seen in part (b) of the figure, we have presented the molar fractions of the three mixtures from the analysis of the density profiles, as well as the predictions obtained from the Soft-SAFT. The phase diagrams show the expected behaviour, in agreement with part (a) of the figure: as the asymmetry of the system is increased (higher values of $\epsilon_{22}/\epsilon_{11}$), the phase envelope of the mixture also increases. As can be seen, the region at which the system exhibits vapour-liquid phase separation increases in compositions and pressures, an expected behaviour of mixtures that exhibit type I phase behaviour according to the classification of Scott and Konynenburg [149,150]. Agreemenet between Monte Carlo simulation and theoretical predictions is excellent in all cases. In summary, increasing the dispersive energy parameter $\epsilon_{22}/\epsilon_{11}$ results in larger cohesive energy in the system, which manifiests as wider phase envelopes and larger critical pressures.

Once we have studied the phase equilibria properties of the mixtures studied form the analysis of the density profiles, we now turn on the study of other interfacial properties of mixtures of LJ systems with different dispersion interactions. We analyze the equilibrium normal and tangential components of the microscopic pressure tensor profiles, $P_N(z)$ and $P_T(z)$, respectively, of mixtures of LJ molecules with different dispersive energy parameters. The profiles are computed from averages of histograms of pressures along the z direction over the production stage, according to the IK prescription explained in Section 10.2. As we have mentioned previously, this procedure is meaningful as far as the central liquid slab is thick enough. In addition to the methododology of IK, based on the mechanical route, we have also determined the macroscopic components of the pressure tensor. In particular, we have averaged the normal microscopic component of the pressure tensor obtained from the IK along the vapour phase (P_N^{vir}). We have also calculated the normal and tangential components of the pressure tensor from the thermodynamic route (P_N and P_T). It is important to recall here that all calculations presented in this work are obtained using LRC for the intermolecular energy and pressure following the improved method proposed previously by MacDowell and Blas and Martínez-Ruiz *et al.*, based on the Janeček's methodology [15], as explained in Section 10.2. This means that both routes, mechanical and thermodynamic, take into account explicitly the LRC. Results from the different routes are presented in Table 10.2. As can seen, agreement between all results is excellent in all cases.

We consider the normal and tangential components of the microscopic pressure tensor profiles at $T = 1.6$ and several pressures. As can be seen in Fig. 10.3, the components of the microscopic pressure tensor along the two vapour-liquid interfaces exhibit the expected behaviour, i.e., the normal component of the pressure tensor profile is constant (within the expected statistical error) through the interface and equal to the vapour pressure of the system (according to the mechanical stability, that it requires the gradient of pressure tensor vanishes). In addition, the tangential component of the pressure tensor profile is approximately constant and equal to the normal pressure in the liquid and both vapour bulk-like regions of the simulation box. $P_T(z)$ becomes negative at the two interfacial regions of the system showing two (negative) local minima. As can be seen, negative contributions to the tangential pressure became more negative as the dispersive energy parameter $\epsilon_{22}/\epsilon_{11}$ is increased. This produces more tension along the interface, decreasing the interfacial thickness of the system (as previously shown in the density profiles of Fig. 10.1). As we will see later, this produces higher interfacial tension, in agreement with the results already presented. An interesting feature observed in the pressure profiles, also seen in pure systems [142], is that there are regions at which $P_T(z) < P_N(z)$, located at the vapour-liquid interface, corresponding to zones of tension. Contrary, small locations at the interface corresponding to zones near the vapour bulk-like regions, are regions of

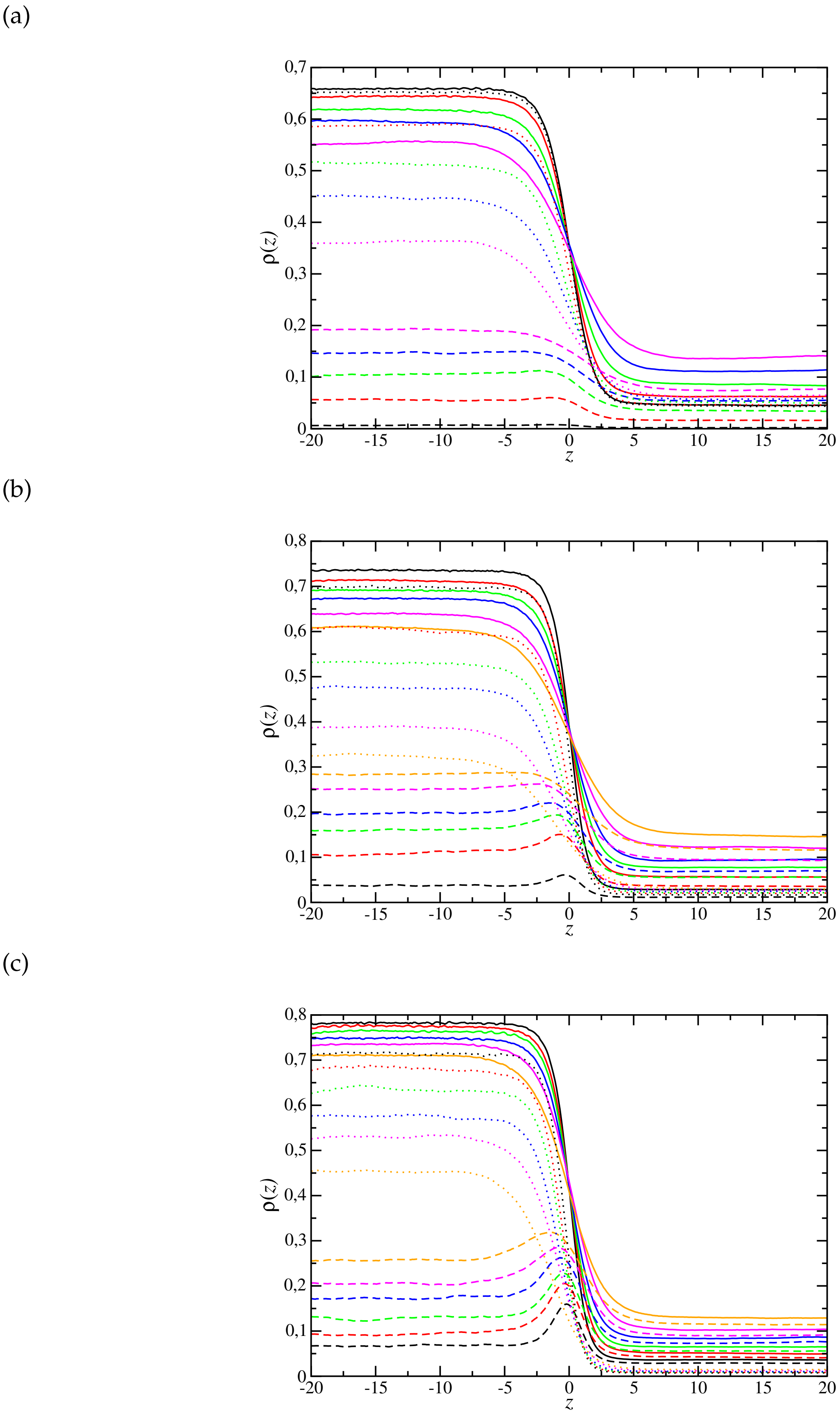

Figura 10.1: Simulated equilibrium total density profiles (continuous curve), density profiles of component 1 (dotted curve) and density profiles of component 2 (dashed curve) across the vapour-liquid interface of mixtures of spherical LJ molecules with the same molecular size and dispersive energy ratio $\epsilon_{22}/\epsilon_{11} = 1.50$ (a), 1.75 (b), and 2.0 (c). Pressure of system is equal to, from top to bottom in the liquid phase, $P^* = 0.06$ (black), 0.08 (red), 0.10 (green), 0.12 (blue), 0.14 (magenta), and 0.16 (orange).

compression in which $P_T(z) > P_N(z)$. The reason for which the transverse pressure has values greater than P_N at the interface near the vapour phase and large negative values (and lower than P_N) at other locations of the interface is a consequence of the behaviour of the pressure in the unstable bulk phase region (spinodal region), which plays an essential role in the physics at interfaces. For further details we recommend the excellent review of Davies and Scriven [71].

(a)

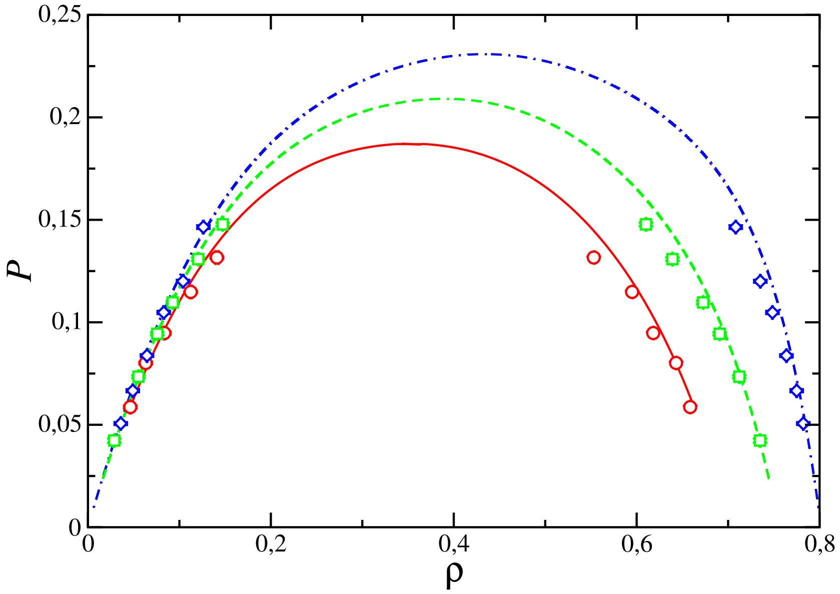

(b)

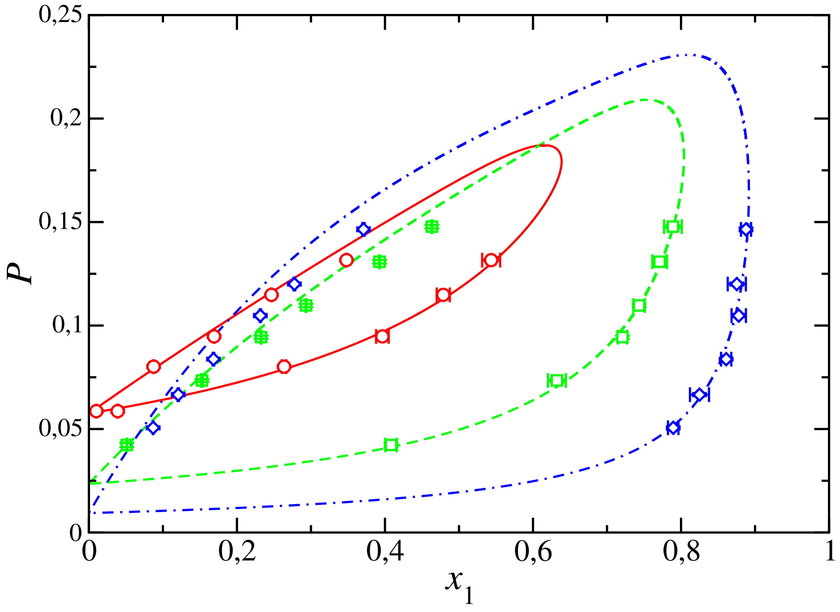

Figura 10.2: Pressure-density (a) and pressure-composition (b) slices of the phase diagram of mixtures of spherical LJ molecules with the same molecular size and dispersive energy ratio $\epsilon_{22}/\epsilon_{11} = 1.5$ (red circles and continuous curves), 1.75 (green squares and dashed curves), and 2.0 (blue diamonds and dash-dotted curves). Symbols correspond to simulation data obtained in this work and curves are the predictions obtained from the Soft-SAFT equation of state.

(a)

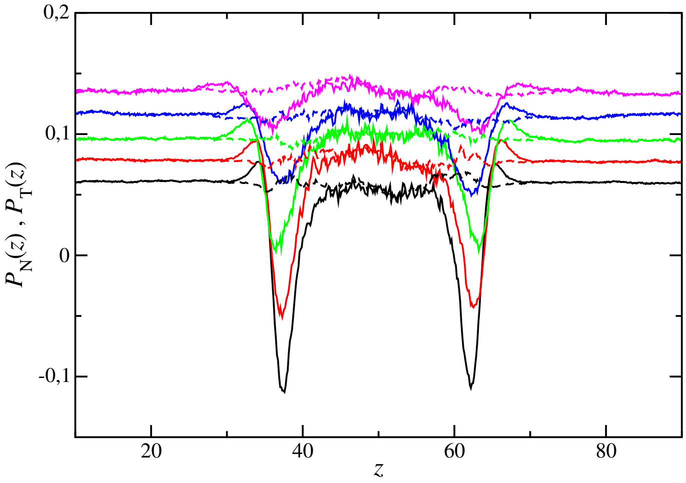

(b)

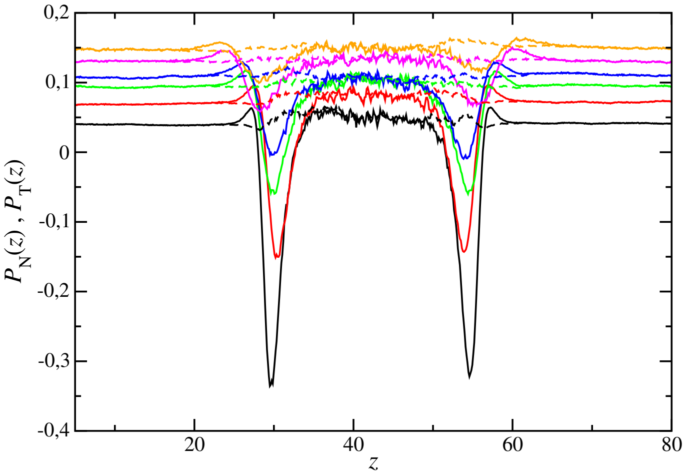

(c)

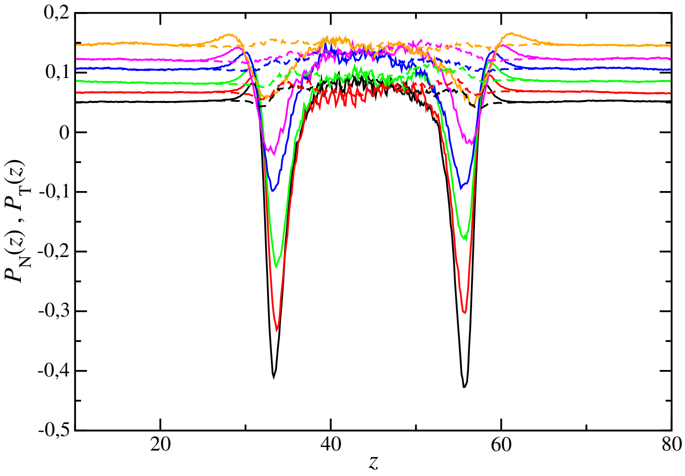

Figura 10.3: Normal $P_N(z)$ and tangential $P_T(z)$ microscopic components of pressure tensor profiles across the two vapor-liquid interface at $T = 1.6$ and $P = 0.06$ (black curves), 0.08 (red curves), 0.10 (green curves), 0.12 (blue curves), 0.14 (magenta curves), and 0.16 (orange curves) of binary mixtures of spherical LJ molecules with the same molecular size and different dispersive energy ratios $\epsilon_{22}/\epsilon_{11} = 1.5$ (a), 1.75 (b), and 2.0 (c). Continuous and dashed curves correspond to tangential and normal microscopic components of the pressure tensor, respectively.

Another interesting property obtained from our analysis is the $10-90$ interfacial thickness (cf. Table 10.2). For a given cutoff distance, t is seen to increase with pressure, which simply reflects the fact that the interfacial region gets correspondingly thinner, in agreement with our previous results. This behaviour may be clearly seen in Fig. 10.4. At low pressure the density profiles exhibit a sharp interface, which corresponds to a low value of the interfacial thickness. As the pressure is increased towards the critical value, the interfacial region becomes wider, and hence, the value of the interfacial thickness increases. The variation of interfacial thickness with the dispersive energy parameter $\epsilon_{22}/\epsilon_{11}$ can be seen in the same figure. As can be seen, an increase of $\epsilon_{22}/\epsilon_{11}$, at constant pressure, results in a decreased of the interfacial thickness, which is consistent with the fact that the systems with larger dispersive energies have a larger cohesive energy. This behaviour is also consistent with that found for the shape of the vapour-liquid phase envelopes.

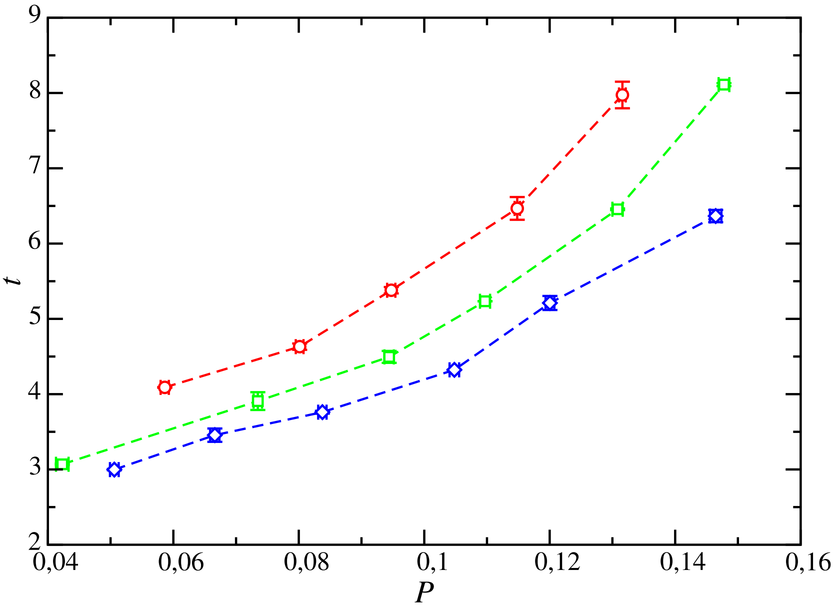

Figura 10.4: The $10-90$ interfacial thickness as a function of the pressure for mixtures of spherical LJ molecules with the same molecular size and dispersive energy ratio $\epsilon_{22}/\epsilon_{11} = 1.5$ (red circles), 1.75 (green squares), and 2.0 (blue diamonds). Symbols correspond to simulation data obtained in this work and curves are included as a guide to eyes.

Finally, we have calculated the vapour-liquid interfacial tension of mixtures of LJ molecules using several dispersive energy parameters $\epsilon_{22}/\epsilon_{11}$. In particular, we have determined the surface tension using its mechanical definition that involves the integration of the difference between the tangential and normal microscopic components of the pressure tensor profiles, as obtained from the IK methodology, along the simulation box according to Eq. (10.7). In addition to that, we have also determined the surface tension using two perturbative approaches: the Test-Area (TA) method of Gloor *et al.* [4] and the VP technique of de Miguel and Jackson [16]. In first case, the surface tension is determined performing virtual area perturbations of a (small) magnitude during the course of the simulation at constant volume. In the second case, the surface tension is determined in two steps. In the first step, the normal and tangential macroscopic components of the pressure tensor, P_N and P_T, are calculated from their thermodynamic definitions as proposed by de Miguel and Jackson [16]. In the second step, the surface tension γ is obtained from Eq. (10.8) (see Eq. (21) of the work of de Miguel and Jackson [16]).

The calculation of the surface tension through three different but complementary routes allows to compare the results obtained from the mechanical and thermodynamic methods. This is another convincing test for consistency for the inhomogeneous LRC presented in our previous works for mixtures. Note that similar consistent results have been found in previous applications of the method for calculating the total potential energy of the system [14, 143–145].

The pressure dependence of the interfacial tension for mixtures of LJ molecules interacting with different dispersive energy parameters $\epsilon_{22}/\epsilon_{11}$ is shown in Fig. 10.5. Agreement between our independent simulations demonstrates that both methodologies are fully equivalent for all the systems and conditions studied. As can be seen, at any given pressure, the interfacial tension is larger for molecules with larger values of $\epsilon_{22}/\epsilon_{11}$. Once again, this is consistent with the larger cohesive energy in systems consisting of molecules in which attractive interactions are longer.

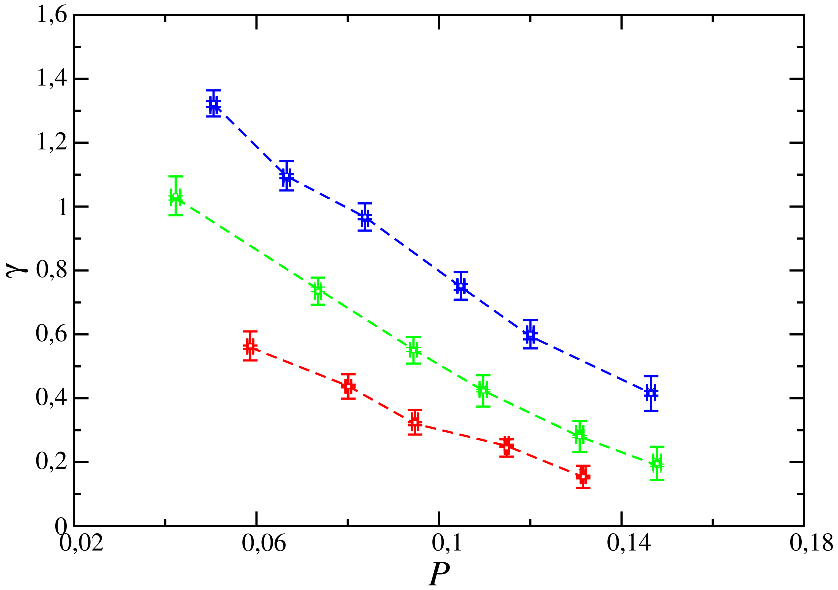

Figura 10.5: Surface tension as a function of pressure for mixtures of spherical LJ molecules with the same molecular size and dispersive energy ratio $\epsilon_{22}/\epsilon_{11} = 1.5$ (red), 1.75 (green), and 2.0 (blue). Different symbols represent the surface tension obtained from MC NVT simulations for spherical molecules using the mechanical route of Irving and Kirkwood [62] (open circles), the VP method of de Miguel and Jackson [16] (open squares), and the TA technique [4] (crosses). The curves are included as a guide to eyes.

10.4 Conclusions

We have simulated the interfacial properties of the vapor-liquid interface of mixtures of spherical LJ molecules. Three mixtures of molecules with the same molecular size but different dispersive energy parameters are considered. The intermolecular interactions are truncated at a cutoff distance of 3σ, σ being the diameter of the molecules, and inhomogeneous long-range corrections for dispersive interactions and pressure tensor are used. The microscopic and macroscopic components of normal and tangential pressure are determined using two different routes, their mechanical (virial route) and thermodynamic (virtual pressure route) definitions. The interfacial tension is also evaluated using three different procedures, the Irving-Kirkwood method, the difference between the macroscopic components of the pressure tensor, and the Test-Area methodology. We have examined the density profiles, interacial thickness, and surface tension in terms of the pressure and the dispersive energy paremeter ratio $\epsilon_{22}/\epsilon_{11}$. In addition, we have also calculated the coexistence diagram (pressure *versus* density) and the pressure-composition slice of the phase diagram at a constant temperature from an analysis of the density profiles.

The effect of the dispersive energy parameters of the mixture, $\epsilon_{22}/\epsilon_{11}$, on density profiles, microscopic components of the normal and tangential pressure tensor profiles, coexistence densities, interfacial thickness, and interfacial tension has been investigated. The vapor-liquid interface is seen to sharpen with increasing dispersive energy ratio corresponding to an increase in the width of the coexistence phase envelope and the pressure-composition slice of the phase diagram and an accompanying increase in the surface tension.

Acknowledgments

The authors would like to acknowledge helpful discussions with A. I. Moreno-Ventas Bravo. This work was supported by Ministerio de Ciencia e Innovación through Grant with reference FIS2010-14866 and Ministerio de Economía y Competitividad through Grant with reference FIS2013-46920-C2-1-P. Further financial support from Junta de Andalucía and Universidad de Huelva is also acknowledged.

Capítulo 11

Liquid-liquid interfacial properties of a symmetrical Lennard-Jones binary mixture

The Journal of Chemical Physics 143, 104706 (2015)

F. J. Martínez-Ruiz[1], , A. I. Moreno-Ventas Bravo[2] and F. J. Blas[1,a)]

[1]Laboratorio de Simulación Molecular y Química Computacional, CIQSO-Centro de Investigación en Química Sostenible and Departamento de Física Aplicada, Universidad de Huelva, 21007, Huelva, Spain
[2]Laboratorio de Simulación Molecular y Química Computacional, CIQSO-Centro de Investigación en Química Sostenible and Departamento de Geología, Universidad de Huelva, 21007, Huelva, Spain

We determine the interfacial properties of a symmetrical binary mixture of equal-sized spherical Lennard-Jones molecules, $\sigma_{11} = \sigma_{22}$, with the same dispersive energy between like species, $\epsilon_{11} = \epsilon_{22}$, but different dispersive energy between unlike species low enough to induce phase separation. We use the extensions of the improved version of the inhomogeneous long-range corrections of Janeček [J. Janeček, *J. Phys. Chem. B* **129**, 6264 (2006)], presented recently by MacDowell and Blas [L. G. MacDowell and F. J. Blas, *J. Chem. Phys.* **131**, 074705 (2009)] and Martínez-Ruiz *et al.* [F. J. Martínez-Ruiz, F. J. Blas, B. Mendiboure, and A. I. Moreno-Ventas Bravo, *J. Chem. Phys.* **141**, 184701 (2014)], to deal with the interaction energy and microscopic components of the pressure tensor. We perform Monte Carlo simulations in the canonical ensemble to obtain the interfacial properties of the symmetrical mixture with different cutoff distances r_c and in combination with the inhomogeneous long-range corrections. The pressure tensor is obtained using the mechanical (virial) and thermodynamic route. The liquid-liquid interfacial tension is also evaluated using three different procedures, the Irving-Kirkwood method, the difference between the macroscopic components of the pressure tensor, and the Test-Area methodology. This allows to check the validity of the recent extensions presented to deal with the contributions due to long-range corrections for intermolecular energy and pressure tensor in the case of binary mixtures that exhibit liquid-liquid immiscibility. In addition to the pressure tensor and the surface tension, we also obtain density profiles and coexistence densities and compositions as functions of pressure, at a given temperature. According to our results, the main effect of increasing the cutoff distance r_c, is to sharpen the liquid-liquid interface and to increase the width of the biphasic coexistence region. Particularly interesting is the presence of a relative minimum in the total density profiles of the symmetrical mixture. This minimum is related with a desorption of the molecules at the interface, a direct consequence of a combination of the weak dispersive interactions between unlike species of the symmetrical binary mixture and the presence of an interfacial region separating the two immiscibile liquid phases in coexistence.

11.1 Introduction

Interfacial tension is probably the most challenging property to be determined and predicted using computer simulation techniques [5]. Despite the number of studies carried out since computer simulation is used routinely for determining the properties of a molecular model, the calculation of interfacial tension is still a subtle problem. The ambiguity in the definition of the microscopic components of the pressure tensor [4, 73], the finite size effects due to capillary waves [119, 120], or the difficulty for the calculation of the dispersive long-range corrections (LRC) associated to the intermolecular interactions [14, 15], make the calculation of interfacial tension a difficult and non-trivial problem.

The standard methodology used to determine the fluid-fluid interfacial tension in a molecular simulation involves the determination of the microscopic components of the pressure tensor, i.e., the normal and tangential pressure, $P_N(z)$ and $P_T(z)$, respectively, through the well-known mechanical or virial route. Once both components are determined, the interfacial tension of a planar fluid-fluid interface can be readily obtained from the integration of the difference between the normal and tangential microscopic components of the pressure tensor profiles along the interface:

$$\gamma = \int_0^{L_z} \left(P_N(z) - P_T(z)\right) dz \tag{11.1}$$

Note that the z-axis is chosen perpendicular to the interface and the integral is performed along the total length L_z of the simulation box. Care must be taken in cases in which there exist two fluid-fluid interfaces, which is the standard procedure for studying direct fluid-fluid coexistence in Monte Carlo (MC) and Molecular Dynamics (MD) simulation. In this case, the true value associated to a single interface is half of the value obtained from Eq. (11.1). This method generally involves an ensemble average of the virial of Clausius according to the recipes of Irving and Kirkwood [62].

Although the mechanical route is an appropriate technique for determining the interfacial tension, a number of alternative methods have been proposed during the last years to calculate, not only the interfacial tension, but also for the components of the pressure tensor, without the need of evaluate the virial. These new effective and elegant methods are based on the thermodynamic definition of surface tension and pressure tensor. The first one can be understood as the change in free energy when the interfacial area is changed, at constant volume and temperature. The second one, can be expressed as the change in free energy when the volume of the system is changed along any direction, keeping constant the other two dimensions. Examples of these methods are the Test-Area (TA) technique of Gloor *et al.* [4], the Volume Perturbation (VP) method of de Miguel and Jackson [16, 50,51], the Wandering Interface Method (WIM), introduced by MacDowell and Bryk [10], and the use of the Expanded Ensemble (EE), based on the original work of Lyuvartsev *et al.* [87], for calculating the surface tension proposed independently by Errington and Kofke [11] and de Miguel [12]. These methods are becoming very popular and are being used routinely to determine the vapour-liquid interfacial properties of different potential model fluids [13,14,65,75,76,83,89,92,96,97,113,126–133, 142,151].

As mentioned previously, one of the major difficulties encountered in the simulation of inhomogeneous systems by molecular simulation is the truncation of the intermolecular potential. Although for homogeneous systems this issue is easily solved by including the well-known homogeneous LRC [2,3], the situation is much more complicated in the case of fluid-fluid interfaces, and in general, in inhomogeneous systems. Fortunately, this problem seems to solved satisfactorily recently in cases in which the system exhibits planar symmetry. Different authors have contributed to the establishment of appropriate and standard inhomogeneous LRC, including Blokhius [135], Mecke [38, 79], Daoulas [136], Guo and Lu [137], and finally, Janeček [15, 138], and the recent improved methods proposed by MacDowell and Blas [14], de Gregorio *et al.* [133], and Martínez-Ruiz *et al.* [142, 151]

Despite the great number of studies carried out during the last ten years for determining the interfacial tension and pressure tensor from Monte Carlo and Molecular Dynamics methodologies, most of them have focused on using the mechanical or virial route for determining these properties. Little work, however, has been developed to determine the interfacial properties, and particularly the surface tension and pressure tensor, from perturbative and thermodynamic methods for binary mixtures involving liquid-liquid separation. An important exception is the work of Neyt *et al.* [131], in which oil-water liquid-liquid interfaces are investigated using atomistic and coarse grained force fields.

The goal of this work is two-fold. The first objective is to determine the liquid-liquid interfacial properties of a symmetrical binary mixture of equal-sized LJ spheres, $\sigma_{11} = \sigma_{22}$, with dispersive energies of equal strengths between like species, $\epsilon_{11} = \epsilon_{22}$, but with the dispersive energy between unlike species low enough to induce phase separation, $\epsilon_{12} = 0.5\epsilon_{11}$. The phase behavior of the system is dominated by large regions of liquid-liquid coexistence brought about by the small value of unlike dispersive interaction in comparison with the strengths between like species ($\epsilon_{11} = \epsilon_{22}$). In particular, we focus on the effect of the cutoff distance of the intermolecular potential energy, r_c, on different interfacial properties, including density profiles, normal and tangential microscopic components of the pressure tensor profiles, and interfacial tension. In addition to that, we also analyze the effect of the cutoff distance on other thermodynamics properties, such as coexistence density and pressure-composition projection of the phase diagram. The second objective is to check the accuracy of the improved versions of the inhomogeneous LRC of Janeček [15] recently proposed by MacDowell and Blas [14] for the intermolecular energy and Martínez-Ruiz *et al.* [142, 151] for the microscopic components of the pressure tensor. In order to check the effectiveness of these methods in the case of a mixture that exhibits liquid-liquid phase separation, we also determine the interfacial tension and the components of the pressure tensor using two different perturbative methods, the TA technique and the VP methodology. This allows to obtain independent results and compare our predictions with simulation data taken from the literature. To our knowledge, this is the first time the interfacial tension and components of the pressure tensor of a symmetrical mixture of LJ spheres are calculated using perturbative methods in both cases and taking into account the LRC associated to the intermolecular potential and components of the pressure tensor.

The rest of the paper is organized as follows. In Section 11.2 we present the model and simulation details of this work. Results obtained are discussed in Section 11.3. Finally, in Section 11.4 we present the main conclusions.

11.2 Model and simulation details

As we have mentioned in the Introduction, the simplest model mixture incorporating both attractive and repulsive dispersive interactions which displays liquid-liquid immiscibility is a binary mixture of equal-sized LJ spheres, $\sigma_{11} = \sigma_{22} \equiv \sigma$, with dispersive energies of equal strengths between like species, $\epsilon_{11} = \epsilon_{22} \equiv \epsilon$, but with the dispersive energy between unlike species low enough to induce phase separation. In this work, we consider this simple symmetrical binary mixture.

The interaction potential between any pair of molecules of species i and j is given by,

$$u_{ij}^{LJ}(r) = 4\epsilon_{ij}\left[\left(\frac{\sigma_{ij}}{r}\right)^{12} - \left(\frac{\sigma_{ij}}{r}\right)^{6}\right] \tag{11.2}$$

where r is the distance between two molecules, and σ_{ij} and ϵ_{ij} are the intermolecular parameters (size and dispersive energy) associated to the interaction between molecules of type i and j. Since all the molecules considered are of equal-sized LJ spheres, we use the well-known Lorentz combining rule for unlike molecular size,

$$\sigma_{ij} = \frac{\sigma_{ii} + \sigma_{jj}}{2} \tag{11.3}$$

Note that $\sigma_{11} = \sigma_{22} = \sigma_{12} \equiv \sigma$. In addition to that, we also fix the unlike dispersive energy $\epsilon_{12} = 0.5\epsilon$.

During the simulation, we use a potential spherically truncated (but not shifted) at a cutoff distance r_c, defined by,

$$u_{ij}(r) = u_{ij}^{LJ}(r)\ [1 - \Theta(r - r_c)] = \begin{cases} u_{ij}^{LJ}(r) & r \leq r_c \\ 0 & r > r_c \end{cases}, \tag{11.4}$$

where $\Theta(x)$ is the Heaviside step function. Note that since we restrict our study to binary mixtures with the same size, σ, we also use the same cutoff distance r_c for all the interactions.

We examine the symmetrical mixture interacting with this spherically truncated potential model with two different cutoff distances, $r_c = 3$ and 4σ. In addition to that, we also consider a cutoff distance $r_c = 3\sigma$ with LRC for the interaction energy and pressure. Standard homogeneous LRC to both magnitudes [3] are used in NPT simulations of bulk phases. In addition to that, inhomogeneous LRC using the MacDowell and Blas [14, 144] methodology for the intermolecular potential energy and the recipe presented in our recent paper [142], based on the Janeček's method [15, 138] for the evaluation of the LRC for the components of the pressure tensor, are used. Results obtained using these LRC are equivalent to use the full potential or a potential with infinite truncation distance.

The number of molecules, N, used in the simulations performed in this work for studying the liquid-liquid interface of the symmetrical mixture varied from $N = 2688$, for the lowest pressure considered ($P^* = P\sigma^3/\epsilon \approx 1.5$), to $N = 3216$, for the highest pressure analyzed ($P^* = P\sigma^3/\epsilon \approx 3.5$). Note that it is not possible to have systems with the same total number of molecules and with the same interfacial area since we are dealing with binary mixtures in which composition must be taken into account. Whereas the initial setup for simulations of vapour-liquid interfaces for pure systems is relatively easy, the initial configuration of a vapour-liquid or liquid-liquid interface involving a binary mixture is a delicate issue. To obtain the initial interfacial simulations boxes at different pressures, we follow the approach used in our previous paper [151] and use firstly the well-known Soft-SAFT approach, based on Wertheim's Thermodynamic Perturbation Theory [17–20], and developed by Blas and Vega [21, 22], to calculate the complete phase diagram of this symmetrical mixture. The Soft-SAFT approach, as the different versions of this successful theoretical framework for predicting the phase behavior of complex mixtures, are well-know equations of state based on a molecular theory, and have been explained and applied extensively during last twenty-five years. If the reader is interested on the details and foundations of the approach we recommend the excellent reviews existing in the literature [152–156].

The Soft-SAFT approach, in the case of mixtures of spherical LJ molecules, reduces to the well-know Johnson *et al.* equation of state [33]. This equation is an extended Benedict-Webb-Rubin equation of state that was fitted to simulation data for the Lennard-Jones fluid. The use of this theory allows to have an initial precise picture of the coexistence envelope of the system at thermodynamic conditions at which the simulations are performed. In particular, initial densities and compositions of each component of the mixture in both liquid phases are obtained using the Soft-SAFT approach for the mixtures considered in this work. We account for a detailed picture of the phase behavior of the symmetrical mixture in Section 11.3.

Simulations are performed in two steps. In the first step, both homogeneous liquid phases, at a given temperature, $T^* = k_B T/\epsilon = 1.5$, and several pressures, are equilibrated in a rectangular simulation box of dimensions $L_x = L_y = 10\sigma$, and varying L_z. Box length measured along the z-axis is chosen in such a way that the corresponding densities match the predictions obtained from the Soft-SAFT approach at temperature and pressure selected. In addition to that, the particular number of molecules of each species, in both liquid phases, are also selected according to the SAFT predictions. Both simulation boxes are equilibrated at the same temperature and pressure using an $NP_z\mathcal{A}T$ ensemble in which L_x and L_y or the interfacial area, $\mathcal{A} = L_x L_y$ are kept constant and only L_z is varied along the simulation. $NP_z\mathcal{A}T$ simulations of homogeneous phases are organized by cycles. A cycle is defined as N trial moves (displacement of the particle position) and an attempt to change the box length along the z-axis (L_z). The magnitude of the appropriate displacement is adjusted so as to get an acceptance rate of $30\,\%$ approximately. We use periodic boundary conditions and minimum image convention in all three directions of the simulation box. In addition to that, homogeneous LRC corrections to the intermolecular energy and pressure are also used [3].

In a second step, the interfacial simulation box is prepared leaving one of the previous homogeneous liquid phases (i.e., liquid 2 or L_2) at the center of the new box with the same homogeneous liquid phase boxes (i.e., liquid 1 or L_1) of half size along the z-axis previously prepared at each side. Since L_x and L_y is the same for all homogeneous phases, it is always possible to build up the interfacial simulation box as explained here. The final overall dimensions of the L_1–L_2–L_1 simulation box are therefore $L_x = L_y = 10\sigma$, and $L_z \approx 40\sigma$ for all the pressures considered. It is worthy to note that liquid-liquid interfaces are usually thinner than vapour-liquid interfaces, and consequently, shorter interfacial simulation box along the z-axis are necessary to simulation such an interface.

The simulations for studying the liquid-liquid interface are also organized in cycles. Note that the simulations of the liquid-liquid interface are performed in the NVT or canonical ensemble. We use periodic boundary conditions and minimum image convention in all three directions of the simulation box. To be consistent with simulations performed using the $NP_z\mathcal{A}T$ ensemble for preparing the definitive simulation box, we use inhomogeneous LRC to the intermolecular energy of MacDowell and Blas [14, 144] methodology for the intermolecular potential energy and the recipe presented in our previous paper [142] for the evaluation of the LRC for the components of the pressure tensor, both of them based on the Janeček's method [15].

We have obtained the normal and tangential microscopic components of the pressure tensor from the mechanical expression or virial route following the same procedure as in our previous works [142, 151] and used the well-known Irving and Kirkwood (IK) recipe [62, 63] for determining the microscopic components of the pressure tensor, $P_N(z) \equiv P_{zz}(z)$ and $P_T(z) \equiv P_{xx}(z) \equiv P_{yy}(z) \equiv \dfrac{1}{2}(P_{xx}(z) + P_{yy}(z))$. The components of the pressure tensor are calculated each cycle.

Following de Miguel and Jackson [16], we have also determined the macroscopic components of the pressure tensor using its thermodynamic definition. As in our previous work for determining the vapour-liquid interfacial properties of binary mixtures of LJ molecules, we have also determined the components of the pressure tensor of the symmetrical LJ mixture using an alternative approach. We follow the methodology proposed by de Miguel and Jackson [16], based on the seminal works of Eppenga and Frenkel [94] and Harismiadis *et al.* [95], and use virtual volume perturbations of magnitude $\xi = \Delta V/V$ every five MC cycles. Here ξ defines the relative volume (compressive and expansive) change associated with the perturbation, i.e., rescale independently the box lengths of the simulation cell and positions of the molecular centers of mass according to linear transformations along the appropriate directions. In all cases, eight different (positive and negative) relative volume changes in the range $2 \times 10^{-4} \leq |\xi| \leq 15 \times 10^{-4}$ are used in our calculations. The final values of the macroscopic components of the pressure tensors presented in this work, P_N and P_T, correspond to the extrapolated values (as determined by a linear extrapolation to $|\xi| \to 0$ of the values obtained from increasing-volume and decreasing-volume perturbations) obtained from a combined compression-expansion perturbation.

Similarly, surface tension is determined using three independent routes. In the first one, we use the mechanical definition that involves the integration of the difference between the tangential and normal microscopic components of the pressure tensor profiles, as obtained from the IK methodology. In the second route, the surface tension is calculated using the thermodynamic definitions of P_N and P_T, as proposed by de Miguel and Jackson [16]. Finally, in the third route we use TA methodology [4]. Since the method is a standard and well-known procedure for evaluating fluid-fluid interfacial tensions of molecular systems, here we only provide the most important features of the technique. For further details we recommend the original work [4] and the most important applications [13,14,16,75,89,92,96,97,127–129,133,142–144,146,147]. The implementation of the TA technique involves performing virtual or test area deformations of relative area changes defined as $\xi = \Delta\mathcal{A}/\mathcal{A}$ during the course of the simulation at constant N, V, and T every five MC cycles. Note that the procedure for calculating the surface tension is similar to that used to evaluate the components of the pressure tensor, but in this case the changes in the normal and transverse dimensions are coupled to keep the overall volume constant. In particular, we use the same number and values for the relative area changes ξ, and the same procedure to obtain the extrapolated values.

In this work, we consider six reduced pressures in the range $P^* = P\sigma^3/\epsilon \approx 1.5$ up to 3.5 for each cutoff distance used. In the case of $NP_z\mathcal{A}T$ simulations of the homogeneous liquid phases prepared in the first step, each simulation box is equilibrated for 10^6 MC cycles. In the case of the NVT simulations corresponding to the interfacial box, the system is also well equilibrated for other 10^6 equilibration MC cycles. In addition to that, averages are determined over a further period of 2×10^6 MC cycles. The production stage is divided into M blocks. Normally, each block is equal to 10^5 MC cycles. The ensemble average of the macroscopic components of the pressure tensor and the surface tension is given by the arithmetic mean of the block averages and the statistical precision of the sample average is estimated from the standard deviation in the ensemble average from $\overline{\sigma}/\sqrt{M}$, where $\overline{\sigma}$ is the variance of the block averages, and $M = 20$ in all cases.

From this point, all the quantities in our paper are expressed in conventional reduced units of component 1, with σ and ϵ being the length and energy scaling units, respectively. Thus, the temperature is given in units of ϵ/k_B, the densities of both components and the total density in units of σ^{-3}, the bulk pressure and components of the pressure tensor in units of the ϵ/σ^3, the surface tension in units of ϵ/σ^2, and the distances, including the cutoff radius, in units of σ.

11.3 Results and discussion

In this section we present the main results from simulations of the liquid-liquid interface of a symmetrical mixture of spherical LJ molecules using different cutoff distances and LRC for the intermolecular potential energy and components of the pressure tensor. We focus mainly on the effect of the cutoff distance of the intermolecular potential on several interfacial properties. As in our previous works [142, 151], we have determined the components of the pressure using both the mechanical (or virial) and thermodynamic routes. Comparison between both results allows to check the validity of the method presented in previous works [14, 142, 144, 151] for determining the contribution to the energy and pressure due to the LRC in mixtures of LJ systems. We now extend the methodology to deal with liquid-liquid interfaces. We also examine the phase equilibria of the mixture, including pressure-density or $P\rho$, and pressure-composition or Px, projections of the phase diagram at a given temperature. In addition to that, we also analyze the most important interfacial properties, such as density profiles and interfacial tension. As in our previous works for pure and binary mixtures [142, 151], in which we concentrate on vapour-liquid interfaces, we now pay special attention on the determination of the liquid-liquid interfacial tension calculated using different routes, including the mechanical or virial route (using the traditional IK methodology) and the thermodynamic definition (using the VP and TA methods) of the surface tension.

It is important to recall here that, although the major difference between liquid and vapour phases from a macroscopic point of view is density, from a microscopic view both phases are radically different. Whereas in a vapour phase correlations between molecules separated distances beyond 2σ approximately, being σ the molecular diameter of the molecular specie, liquids, especially at high densities, exhibit large correlations that strongly affect macroscopic properties. Many of those properties, with particular emphasis on interfacial properties such as interfacial tension, are extremely sensible to such molecular details. As we have mentioned explicitly in the Introduction, one of the main goals of the present work is to establish clearly if inhomogeneous LRC to the potential energy and pressure and perturbative methods based on a thermodynamic perspective are suitable for predicting interfacial properties of this kind of mixtures.

We apply the methodology explained in Section 11.2 to the model previously presented. As we have mentioned, the system is a limiting case of a mixture in which both components are identical, i.e., the molecules of both components have the same molecular sizes and dispersive energy interactions. However, the unlike dispersive energy between unlike components is half of the pure components. In order to clarify the nature of the phase behavior exhibited by the system under study, we present the phase diagram of the mixture as obtained from the well-known Soft-SAFT approach.

The pressure-temperature PT projection of the PTx surface corresponding to the phase diagram of the symmetrical mixture of LJ spheres is shown in Fig. 11.1. It is interesting to mention here that Jackson [157], in early 1990s, studied a binary mixture of equal-sized hard spheres with mean-field attractive forces between like species and not between unlike species using the SAFT equation of state. The phase diagram of that mixture is similar to that obtained here from the Soft-SAFT approach. The continuous black curves are the vapour pressure curves of pure components 1 and 2, which are coincident for the mixture due to its symmetry. As can be seen, the system exhibits a liquid-liquid-vapour (LLV) three-phase line (green dashed curve), located at pressures above the vapour pressure curves of pure components. In addition to that, the mixture has two critical lines with different characters. The first one is a gas-liquid critical line (dot-dashed red curve), running

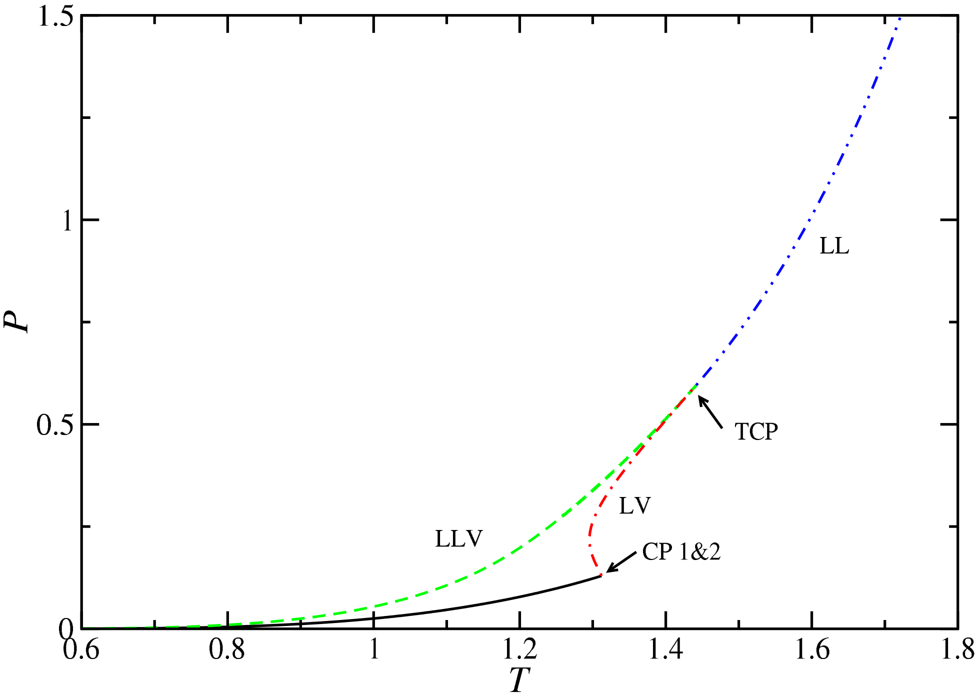

Figura 11.1: PT projection of the phase diagram for the symmetrical mixture of LJ molecules with different dispersive energy between unlike species, $\epsilon_{12} = 0.5\epsilon$, as obtained from the Soft-SAFT theoretical formalism. Continuous black curves represent the vapour pressure of the pure components (1&2), the dashed green curve represents the LLV three-phase line, the dot-dashed red curve is the vapour-liquid critical (VL) critical line, and the dot-dot-dashed curve is the liquid-liquid (LL) critical line. TCP denotes the tricritical point of the mixture.

from the critical point of pure components 1 and 2 to a tricritical point (TCP). The second one is a liquid-liquid critical line (dot-dot-dashed blue curve), running from the TCP of the mixture toward high pressures and temperatures. The PT projection of the phase diagram is characterized by two salient features. Firstly, the phase behavior of the mixture is dominated by a large liquid-liquid immiscibility region extending left of the liquid-liquid critical line and three-phase line. Secondly, there is the unusual occurrence of a TCP in a binary mixture, at $T \approx 1.442$ and $P \approx 0.596$. A TCP is a thermodynamic state at which three coexisting phases become identical. Note that the existence of this critical state is a consequence of the symmetrical nature of the interactions, since the rule phase forbids unsymmetrical TCPs in systems with less than three components. In fact, TCPs appear in either ternary mixtures at an unique temperature and pressure or in quaternary mixtures at fixed pressure and unique temperature. For details about TCPs we recommend the work of Vega and Blas [158] and references therein. According to the classification of Scott and Konynenburg [149,150], the phase diagram corresponding to the mixture is just the symmetrical limit of type III phase behavior with heteroazeotropy or simple type III-HA.

To better understand the phase behavior exhibited by the mixture it is also useful to examine the pressure-composition Px or temperature-composition Tx projections of the PTx surface of the phase diagram. Fig. 11.2 shows the Px constant-temperature projection at different temperatures. Part (a)

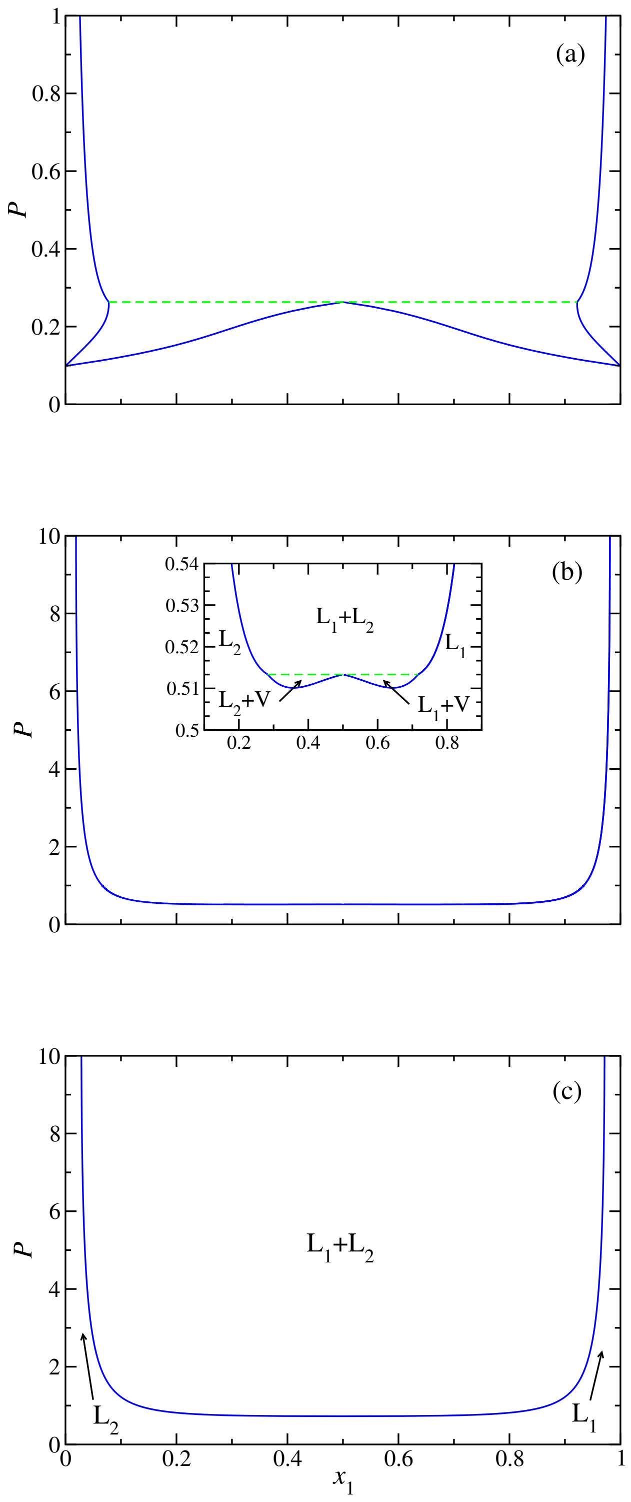

Figura 11.2: Px projection of the phase diagram for the symmetrical mixture of LJ molecules with different dispersive energy between unlike species, $\epsilon_{12} = 0.5\epsilon$, as obtained from the Soft-SAFT theoretical formalism at reduced temperatures (a) $T = 1.25$, (b) $T = 1.4$, and (c) $T = 1.5$. Continuous green curves represent the vapour-liquid (VL) and liquid-liquid (LL) phase envelopes and the dashed green curves correspond to the LLV three-phase line at the corresponding pressure.

of the Figure shows the Px projection at $T = 1.25$, below the critical point of pure components. As can be seen, the system exhibits two equivalent vapour-liquid coexistence regions (due to the symmetry of the mixture) at low pressures, below the three-phase coexistence at $P \approx 0.263$, and liquid-liquid immiscibility at high pressures. We have also studied the Px projection of the phase diagram at $T = 1.4$, a temperature above the critical temperature of pure components, but below the tricritical temperature of the mixture, $T_{\text{TCP}} \approx 1.442$, as shown in part (b) of the figure. The system also exhibits two equivalent vapour-liquid envelopes, since the temperature is above the critical point of pure components, and liquid-liquid phase separation at high pressures. Finally, at $T = 1.5$, above the tricritical point of the mixture, the vapour-liquid coexistence has merged into the liquid-liquid coexistence and only liquid-liquid immiscibility is stable at these conditions, as it is shown in part (c) of the Figure.

Once we have obtained a general picture of the complete phase diagram of the mixture, we consider the most important interfacial properties of the system. We first analyze the effect of the cutoff distance of the intermolecular potential energy on density profiles. We follow a similar analysis and methodology than in our previous works [13,14,142–144,151] and consider different cutoff distances and pressures. The equilibrium density profiles of each of components of the mixture, $\rho_1(z)$ and $\rho_2(z)$, as well as the total density, $\rho(z) = \rho_1(z) + \rho_2(z)$, are computed from averages of the histogram of densities along the z direction over the production stage. The bulk vapour and liquid densities of both components and the total density are obtained by averaging $\rho_1(z)$, $\rho_2(z)$, and $\rho(z)$, respectively over appropriate regions sufficiently removed from the interfacial region. The densities obtained are meaningful since the central liquid slab is thick enough at all pressures. The bulk vapour densities are obtained after averaging the corresponding density profiles on both sides of the liquid film. The statistical uncertainty of these values is estimated from the standard deviation of the mean values.

Our simulation results for the bulk densities of each component, total densities, molar fractions of both components in each phase, components of the pressure tensor, and surface tension for symmetrical mixtures of LJ molecules interacting with the Lennard-Jones intermolecular potential using different cutoff distances, at different pressures, are collected in Tables 11.1 and 11.2.

We show in Fig. 11.3 the density profiles $\rho_1(z)$, $\rho_2(z)$, and $\rho(z)$ for the mixture of LJ molecules using cutoff distances $r_c = 3$ and 4, and $r_c = 3$ with inhomogeneous LRC, at several pressures. For the sake of clarity, we only present one half of the profiles corresponding to one of the interfaces. Also for convenience, all density profiles have been shifted along z so as to place z_0, the position of the Gibbs-dividing surface, approximately at the origin. As can be seen, the density profiles of both components along the interface are perfectly symmetric. The bulk density of one of the components in one of the liquid phases is identical to the other in the second phase liquid, and hence, the compositions of both components are also symmetric (see the details in Table 11.1). This is a consequence of the symmetrical nature of the interactions of the system. As can be seen, for a given value of the cutoff distance of the intermolecular potential, the slope of the density profiles corresponding to both components in the interfacial region increases as the pressure is increased, making larger the jump in densities when passing from one liquid phase to the other liquid phase of the interface. Consequently, the interfacial thickness increases, an expected behavior that indicates the phase envelope is becoming thinner as the pressure increases with respect to the critical pressure of the mixture. It is important to recall that the critical pressure of the mixture, at $T = 1.5$, is $P \sim 0.727$ as predicted by the Soft-SAFT approach, well below the pressures considered here.

Special attention deserves the behavior of the total density profile. As we have mentioned before,

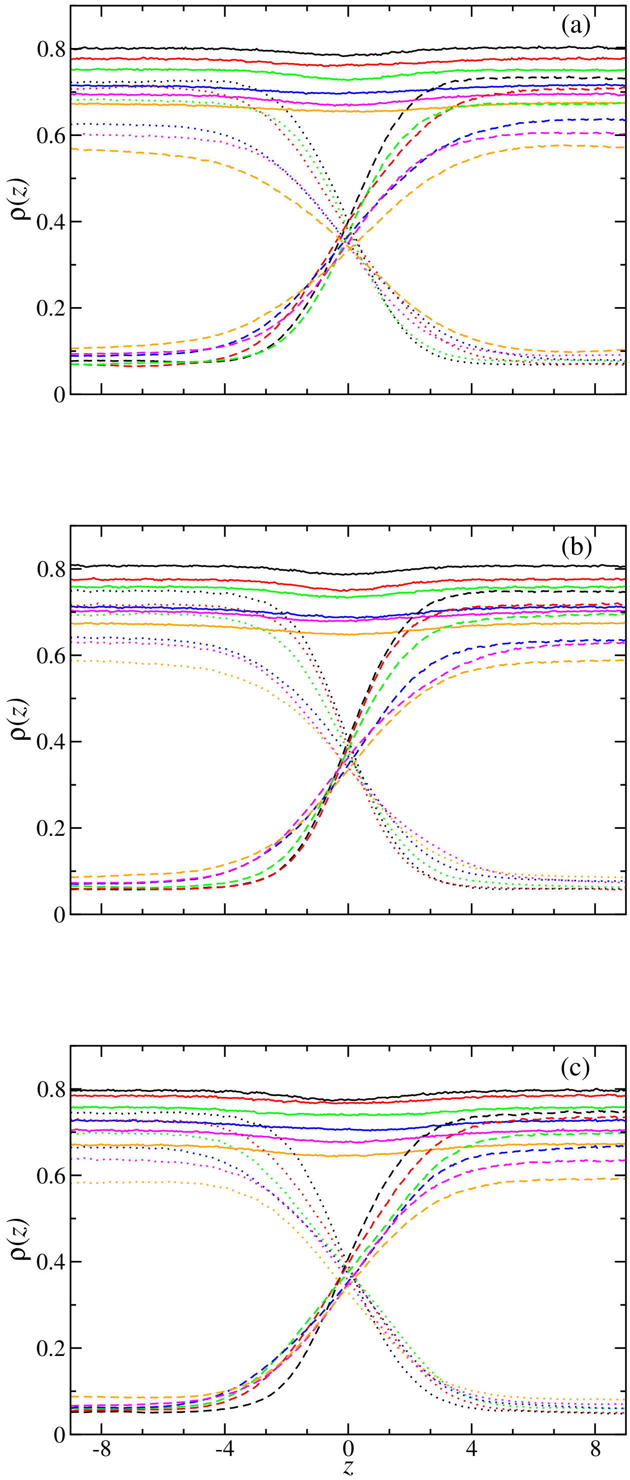

Figura 11.3: Simulated equilibrium total density profiles (continuous curves), density profiles of component 1 (dotted curves), and density profiles of component 2 (dashed curves) across the liquid-liquid interface of the symmetrical mixture of LJ molecules with different dispersive energy between unlike species, $\epsilon_{12} = 0.5\epsilon$, at $T = 1.5$ and using a cutoff distance for the intermolecular potential (a) $r_c = 3$, (b) $r_c = 4$, and (c) $r_c = 3$ with inhomogeneous LRC. Pressure of the system increases from bottom to top in the total density profile (orange, magenta, blue, green, red, and black). Note that curves with the same colour correspond to the same pressure value.

Tabla 11.1: Total liquid density at liquid phases L_1 and L_2, ρ, density of component 1 at liquid L_1, $\rho_1^{L_1}$, density of component 1 at liquid L_2, $\rho_1^{L_2}$, molar composition of component 1 at liquid L_1, $x_1^{L_1}$, molar composition of component 1 at liquid L_2, $x_1^{L_2}$, density of component 2 at liquid L_1, $\rho_2^{L_1}$, density of component 2 at liquid L_2, $\rho_2^{L_2}$, at $T = 1.5$ and different pressure P_N^{vir} for the symmetrical mixture of LJ molecules with different dispersive energy between unlike species, $\epsilon_{12} = 0.5\epsilon$, at $T = 1.5$ and using a cutoff distance for the intermolecular potential (a) $r_c = 3$, (b) $r_c = 4$, and (c) $r_c = 3$ with inhomogeneous long-range corrections. All quantities are expressed in the reduced units defined in Section 11.2. The errors are estimated as explained in the text.

P_N^{vir}	ρ	$\rho_1^{L_1}$	$\rho_1^{L_2}$	$x_1^{L_1}$	$x_1^{L_2}$	$\rho_2^{L_1}$	$\rho_2^{L_2}$
			$r_c = 3.0$				
1.7349(14)	0.6730(5)	0.5644(18)	0.1059(4)	0.838(5)	0.1573(7)	0.1086(15)	0.5673(6)
1.9405(18)	0.6946(21)	0.6034(17)	0.0989(9)	0.868(4)	0.1427(14)	0.0917(6)	0.5946(11)
2.1724(20)	0.7149(20)	0.6330(18)	0.0876(6)	0.885(4)	0.1226(8)	0.0820(8)	0.6272(7)
2.6921(21)	0.7511(22)	0.6745(19)	0.0717(3)	0.898(5)	0.0954(4)	0.0762(5)	0.6800(4)
3.1403(16)	0.7774(12)	0.7114(12)	0.0693(5)	0.915(3)	0.0893(7)	0.0663(8)	0.7074(6)
3.6735(24)	0.802(3)	0.7312(20)	0.07681(22)	0.911(5)	0.0958(5)	0.0710(4)	0.7245(3)
			$r_c = 4.0$				
1.6251(13)	0.6736(19)	0.5889(17)	0.0880(5)	0.874(4)	0.1307(8)	0.0847(6)	0.5853(7)
1.9053(12)	0.7025(7)	0.6302(14)	0.0743(4)	0.897(3)	0.1059(6)	0.0725(11)	0.6276(8)
2.0229(19)	0.7112(21)	0.6330(18)	0.0733(6)	0.890(5)	0.1031(9)	0.0782(4)	0.6377(7)
2.6818(19)	0.7577(22)	0.6935(21)	0.0656(4)	0.915(5)	0.0866(6)	0.0641(6)	0.6921(5)
2.9951(18)	0.775(3)	0.7159(21)	0.0613(5)	0.923(5)	0.0790(7)	0.0598(4)	0.7138(7)
3.6535(19)	0.807(3)	0.7472(20)	0.0561(6)	0.926(5)	0.0695(8)	0.0593(3)	0.7510(7)
			$r_c = 3.0 + LRC$				
1.5510(13)	0.6713(7)	0.5912(6)	0.08659(15)	0.8797(16)	0.1293(3)	0.0805(3)	0.58321(23)
1.8634(14)	0.7039(21)	0.6346(19)	0.0681(3)	0.902(5)	0.0968(5)	0.0692(5)	0.6359(5)
2.1423(14)	0.7265(23)	0.6626(24)	0.0633(5)	0.912(5)	0.0871(7)	0.0640(8)	0.6629(7)
2.6045(16)	0.7569(22)	0.6955(20)	0.05989(22)	0.919(5)	0.0791(3)	0.0611(4)	0.6975(3)
3.0826(20)	0.7842(8)	0.7327(10)	0.0556(3)	0.9342(20)	0.0709(4)	0.0516(7)	0.7282(4)
3.3374(16)	0.7964(24)	0.7455(23)	0.0513(3)	0.936(5)	0.0644(3)	0.0508(7)	0.7452(3)

the bulk liquid total densities associated to both liquid phases are identical, as can be also seen in Table 11.1. However, the total density profile, $\rho(z) = \rho_1(z) + \rho_2(z)$, which in nearly constant in the bulk region of the liquid phases, exhibits a local minimum at the interface, when passing from one liquid phase to the other. This minimum is obviously related with a desorption of both components at the interface. We think this phenomena is a combination of the weak dispersive interactions between unlike species of the mixture and the presence of an interfacial region, that separates the two immiscible liquid phases in coexistence, in which molecules of both components must accommodate in order to minimize the free energy of the system. A similar behavior has been previously observed for liquid-liquid interfaces in partially miscible mixtures of LJ-like systems from MD simulation [159–161] and Density Functional Theory [161, 162].

From a phase equilibria perspective, preferential adsorption or desorption of one of the components of a heterogeneous mixture can also be understood in terms of molar barotropy phenomena and the existence of isopycnic states. Molar density inversion, a phenomena also known as molar barotropy, corresponds to a singular behavior that occurs when molar densities of two immiscible liquid phases in equilibrium change their relative position of phases in the heterogeneous mixture. The points of the diagram at which both liquid phases exhibit equal molar densities of volume are called isopycnic states [163–165]. Experimentally, this phenomena may be observed when varying the equilibrium conditions of temperature or pressure. From an experimental point of view, molar

Tabla 11.2: Normal component of the macroscopic pressure tensor calculated from the virial route P_N^{vir}, normal and tangential components of the macroscopic pressure tensor calculated from VP, P_N and P_T, interfacial tension calculated from integration given by Eq. (11.1), γ^{vir}, from VP, γ_{VP}, and from TA, γ_{TA}, at $T = 1.5$ and different pressures for the symmetrical mixture of LJ spherical molecules with different dispersive energy between unlike species, $\epsilon_{12} = 0.5\epsilon$, at $T = 1.5$ and using a cutoff distance for the intermolecular potential (a) $r_c = 3$, (b) $r_c = 4$, and (c) $r_c = 3$ with inhomogeneous long-range corrections. All quantities are expressed in the reduced units defined in Section 11.2. The errors are estimated as explained in the text. Uncertainties of interfacial tension calculated from the virial route, γ^{vir}, are error estimates corresponding to the numerical calculation of the integral given by Eq. (11.1).

P_N^{vir}	P_N^*	P_T^*	γ^{vir}	γ_{VP}	γ_{TA}
		$r_c = 3.0$			
1.7349(14)	1.7344(16)	1.7288(17)	0.116(6)	0.11(4)	0.118(3)
1.9405(18)	1.9408(11)	1.9329(11)	0.159(6)	0.16(3)	0.159(4)
2.1724(20)	2.1727(12)	2.1625(13)	0.197(5)	0.20(3)	0.199(5)
2.6921(21)	2.6924(7)	2.6783(8)	0.282(8)	0.285(22)	0.284(9)
3.1403(16)	3.1407(7)	3.1251(7)	0.310(8)	0.315(20)	0.313(6)
3.6735(24)	3.6736(13)	3.6539(13)	0.395(6)	0.39(3)	0.397(8)
		$r_c = 4.0$			
1.6251(13)	1.6253(13)	1.6157(14)	0.187(6)	0.19(4)	0.189(5)
1.9053(12)	1.9054(9)	1.8933(9)	0.244(6)	0.24(2)	0.245(4)
2.0229(19)	2.0228(11)	2.0094(12)	0.272(6)	0.27(3)	0.274(6)
2.6818(19)	2.6821(13)	2.6632(14)	0.374(6)	0.37(3)	0.376(5)
2.9951(18)	2.9951(9)	2.9747(10)	0.411(7)	0.41(3)	0.414(6)
3.6535(19)	3.6537(5)	3.6301(6)	0.466(8)	0.472(17)	0.469(9)
		$r_c = 3.0 + LRC$			
1.5510(13)	1.5431(12)	1.5317(12)	0.236(6)	0.23(3)	0.229(6)
1.8634(14)	1.8537(13)	1.8381(14)	0.311(6)	0.31(3)	0.313(5)
2.1423(14)	2.1317(11)	2.1122(11)	0.390(5)	0.39(3)	0.390(5)
2.6045(16)	2.5958(8)	2.5725(9)	0.468(7)	0.47(3)	0.461(8)
3.0826(20)	3.0761(7)	3.0495(8)	0.550(11)	0.535(22)	0.535(7)
3.3374(16)	3.3251(6)	3.2954(5)	0.580(7)	0.601(17)	0.596(8)

density inversions are likely to occur in partially miscible mixtures that exhibit type III or type V phase behavior according to the Scott and Konynenburg classification [149,150]. In particular, isopycnic curves, along which the phase density inversions take place, are clearly observed to occur in an equilibrium range that goes from the LLV three-phase line up to the vapour-liquid critical line of the mixture [166]. In this work, due to the symmetrical nature of the interactions, molar density of both phases liquids at the LLV coexistence line are identical, and hence, all the states along the three-phase line are isopycnic states.

Tardón *et al.* [166] have demonstrated recently from computer simulation and the use of the density gradient theory that this particular phase behavior of mixtures that exhibit liquid-liquid immiscibility produces a drastic distorsion of the total density profile of the system along the liquid-liquid interface. We think the desorption phenomena observed in the total density profile of the mixture shown in Fig. 11.3 should be related to the existence of isopycnic states at which two liquids coexist with the same molar density. Since the goal of this work is not to investigate this delicate and interesting phenomena, we plan to carry out a detailed study of the effect of isopycnity of symmetrical binary mixtures of equal-sized LJ spheres from a computer simulation approach in a future work.

Comparison of Figs. 11.3a, 11.3b, and 11.3c also shows the effect of increasing the cutoff distance of the intermolecular potential energy, $r_c = 3$ and 4, and the use of inhomogeneous LRC with $r_c = 3$ (full intermolecular potential). As can be seen, an increase of cutoff distance results in steeper density profiles of both components along the interfacial region. This effect, which also produces narrower interfacial regions, is related with the increasing of the interfacial tension of the mixture, as it will be shown later. As more interactions are taken into account, the unlike intermolecular interactions are larger, and the Px pressure-composition phase envelope (see Fig. 11.2) becomes wider in terms of molar fractions, or in other words, the jump in composition increases when going from one liquid phase to the the other one.

Note that this behavior is not easy to identify from Fig. 11.3 since, although simulated pressures are approximately equal, they are in fact not identical since we have simulated the interface using the NVT or canonical ensemble. Under these conditions, pressure is not specified *a priori* but it is calculated along the simulation. Although initial simulation boxes are prepared carefully trying to ensure the same final values of the pressure, small differences are nearly impossible to avoid (see Tables 11.1 and 11.2 for further details). Obviously, since we are dealing with a binary mixture, the use of the $NP_z\mathcal{A}T$ or isothermal-isobaric ensemble in which the normal pressure (perpendicular to the liquid-liquid interface) is kept constant, seems to be more appropriate ensemble than the standard NVT ensemble. We have not used the $NP_z\mathcal{A}T$ ensemble because the precise composition between different density profiles at exactly the same pressure was not the primary goal of this work. However, we plan to use this ensemble in future works.

The liquid-liquid phase envelopes of the mixture of LJ molecules using different cutoff distances for the intermolecular potential, r_c, including the full potential as calculated from the analysis of the density profiles obtained from our Monte Carlo simulations, are depicted in Fig. 11.4. The Soft-SAFT theoretical approach has been also used to obtain the complete phase diagram of the symmetrical mixture for the full potential case. Although, as we have mentioned in the Introduction and Model and simulation details sections, we have used the information from the theory for obtaining initial guesses of the liquid and vapour densities and compositions of mixtures to be studied by simulation at particular thermodynamic conditions, this theoretical predictions can also be used as results to compare our simulation results and check the ability of SAFT in predicting the phase behavior of these mixtures. As can be seen in part (a) of the figure, the pressure-density or $P\rho$ projection of the phase diagram of mixture, at $T = 1.5$, only exhibits one branch of the liquid-liquid coexistence diagram. As it has been explained previously in the case of the PT projection of the phase diagram, this is a direct consequence of the symmetrical nature of the interactions of the system. In other words, both curves collapse in a unique coexistence curve since the densities of each of the liquid phases are identical.

The coexistence densities of both phases increase as the pressure of the system is increased, an expected behavior due to the compression effect. In addition to that, at each pressure considered, the coexistence densities increase as the intermolecular potential cutoff distance r_c is increased. This enlargement of the liquid coexistence density associated to the phase envelope is essentially due to the increase of the attractions in the system (r_c is increased) as more interactions are taken into account. This increasing behavior has an asymptotic limiting behavior associated to the case in which all attractive interactions are taken into account, i.e., when considering the full intermolecular potential. As can be seen, agreement between Monte Carlo simulation results obtained using the inhomogeneous LRC (full potential) and predictions from SAFT is excellent in all cases. It is important to recall here that results from the theory are predictions without any further fitting procedure.

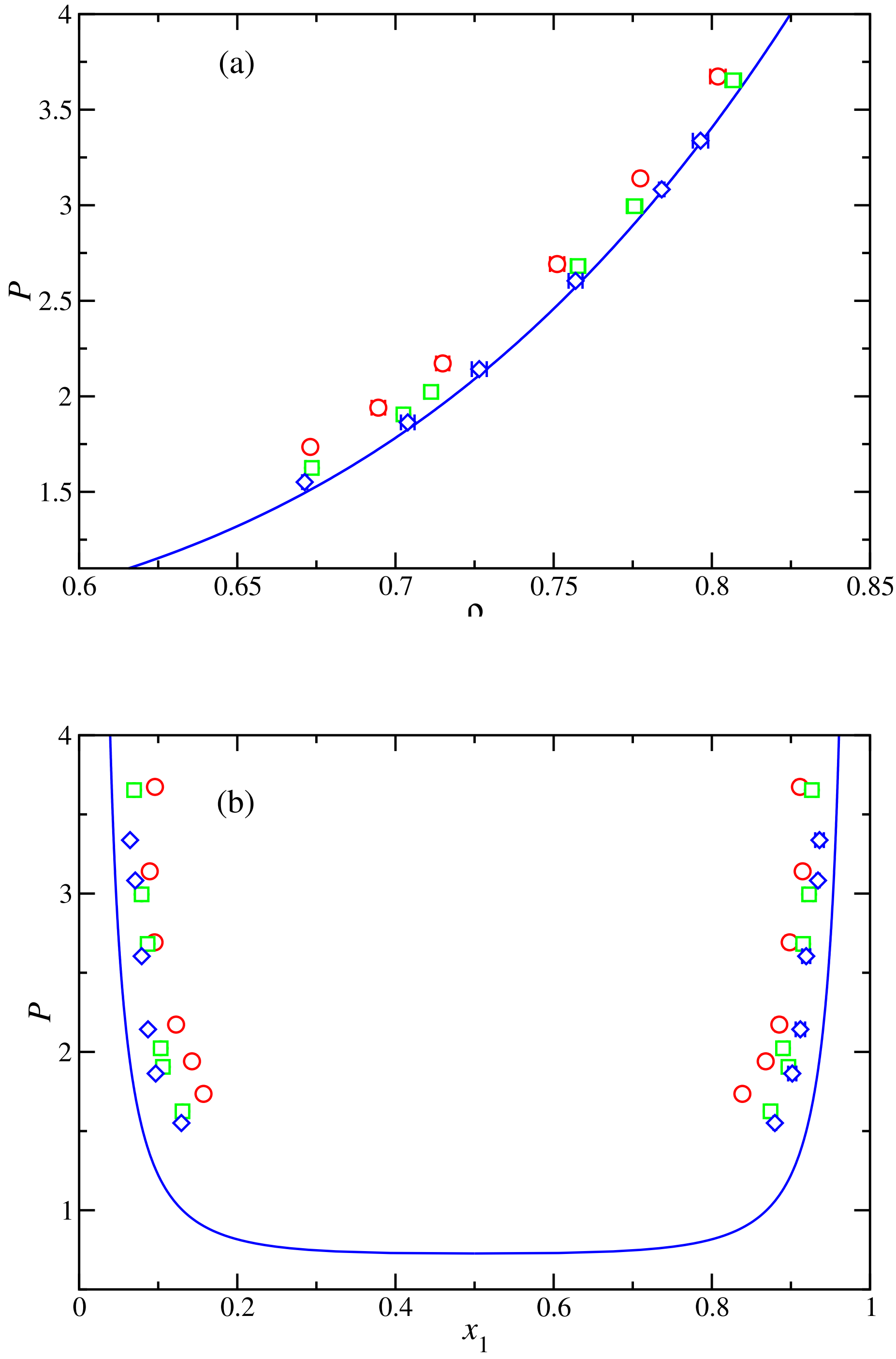

Figura 11.4: Pressure-density or $P\rho$ (a) and pressure-composition or Px projections projection of the phase diagram of the symmetrical mixture of LJ molecules with different dispersive energy between unlike species, $\epsilon_{12} = 0.5\epsilon$, at $T = 1.5$ and using a cutoff distance for the intermolecular potential $r_c = 3$ (red circles), $r_c = 4$ (green triangles), and $r_c = 3$ with inhomogeneous long-range corrections (blue squares). Symbols correspond to simulation data obtained in this work and curves are the predictions obtained from the Soft-SAFT theoretical formalism.

We have also obtained the pressure-composition or Px projection of the mixture at the same thermodynamic conditions and using the same cutoff distances for the intermolecular potential energy, including the case in which the inhomogeneous LRC are used. As can be seen in part (b) of the figure, we have presented the molar fractions of the mixture from the analysis of the density profiles, as well as the predictions obtained from the Soft-SAFT. The phase diagrams for cases in which different cutoff distances are used show the expected behavior, in agreement with part (a) of the figure. In particular, the phase separation of the mixture increases as the pressure is increased. In addition to that, the coexistence compositions in both liquid phases, at a given pressure, increase as the cutoff distance of the intermolecular potential energy is increased (higher values of r_c). As can be seen, the liquid-liquid immiscibility region of the phase diagram of the symmetrical mixture increases in compositions as pressure is increased, an expected behavior of mixtures that exhibit type III phase behavior according to the classification of Scott and Konynenburg [149, 150]. Agreement between Monte Carlo simulation and theoretical predictions is good when the full intermolecular potential is taken into account through the inhomogeneous LRC. Again, it is important to recall here that no single adjustable parameter has been used to obtain the prediction from the Soft-SAFT theoretical formalism.

Once we have studied the phase equilibria properties of the mixture from the analysis of the density profiles, we now turn on the study of the liquid-liquid interfacial tension of the mixture using different values of the cutoff distance for the intermolecular potential energy and the inhomogeneous LRC of MacDowell and Blas [14] and Blas and Martínez-Ruiz [142,151]. In particular, we have determined the liquid-liquid interfacial tension using its mechanical definition that involves the integration of the difference between the tangential and normal microscopic components of the pressure tensor profiles, as obtained from the IK methodology, along the simulation box (Eq. (11.1)). In addition to that, we have also determined the interfacial tension using two perturbative approaches: the Test-Area (TA) method of Gloor *et al.* [4] and the VP technique of de Miguel and Jackson [16]. In first case, the surface tension is determined performing virtual area perturbations of a small magnitude during the course of the simulation at constant volume. In the second case, the surface tension is determined in two steps. In the first step, the normal and tangential macroscopic components of the pressure tensor, P_N and P_T, are calculated from their thermodynamic definitions as proposed by de Miguel and Jackson [16]. In the second step, the surface tension γ is obtained from Eq. (21) of the work of de Miguel and Jackson [16].

The calculation of the surface tension through three different but complementary routes allows to compare the results obtained from the mechanical and thermodynamic methods. This is another convincing test for consistency for the inhomogeneous LRC presented in our previous works for mixtures. Note that similar consistent results have been found in previous applications of the method for calculating the total potential energy of the system [14,142–144]. This is the first time the inhomogeneous LRC for both, the intermolecular energy and pressure tensor, is used to predict the liquid-liquid interfacial properties of mixtures, and to our knowledge, this is also the first time the Volume Perturbation methodology proposed by de Miguel and Jackson [16] for determining the components of the pressure tensor is used to deal with liquid-liquid interfaces.

The pressure dependence of the interfacial tension for the mixture interacting with different cutoff distances for the intermolecular potential is shown in Fig. 11.5. Agreement between our independent simulations demonstrates that both methodologies are fully equivalent for all the systems and conditions studied. As can be seen, at any given pressure, the interfacial tension is larger for simulations in which the cutoff distance is larger, and particular, for the simulations at which the inhomogeneous

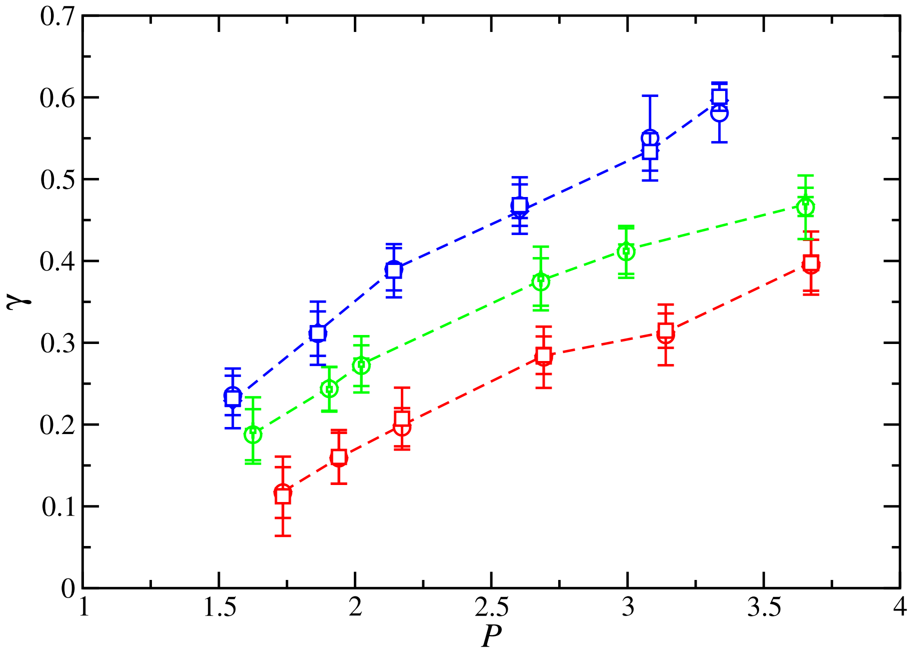

Figura 11.5: Liquid-liquid interfacial tension as a function of pressure of the symmetrical mixture of LJ molecules with different dispersive energy between unlike species, $\epsilon_{12} = 0.5\epsilon$, at $T = 1.5$ and using a cutoff distance for the intermolecular potential $r_c = 3$ (red symbols), $r_c = 4$ (green symbols), and $r_c = 3$ with inhomogeneous long-range corrections (blue symbols). Different symbols represent the interfacial tension obtained from MC NVT simulations using the mechanical route of Irving and Kirkwood [62] (open circles), the VP method of de Miguel and Jackson [16](open squares), and the TA technique [4] (open diamonds). The curves are included as guide to eyes.

LRC are used. This later case correspond, as previously mentioned, to the case in which the full intermolecular potential is used. This behavior of the liquid-liquid interfacial tension is consistent with the larger cohesive energy in systems in which longer range of interactions are considered.

11.4 Conclusions

We have simulated the interfacial properties of the liquid-liquid interface of a symmetrical mixture of equal-sized spherical LJ molecules, with the same dispersive energy between like species, but with different dispersive energy between unlike species low enough to induce phase separation. The intermolecular interactions are truncated at two different cutoff distances for the intermolecular potential, $r_c = 3$ and 4σ, σ being the diameter of the molecules. In addition to that, inhomogeneous long-range corrections for dispersive interactions and pressure tensor are also used. The microscopic and macroscopic components of normal and tangential pressure are determined using two different routes, their mechanical (virial route) and thermodynamic (virtual pressure route) definitions. The interfacial tension is also evaluated using three different procedures, the Irving-Kirkwood method, the difference between the macroscopic components of the pressure tensor, and the Test-Area methodology. We have examined the density profiles and surface tension in terms of the pressure and the cutoff distance for the intermolecular potential energy, r_c. In addition, we have also calculated the coexistence diagram (pressure *versus* density) and the pressure-composition projection of the phase diagram at a constant temperature from an analysis of the density profiles.

The effect of the cutoff distance for the intermolecular potential energy of the symmetrical mixture on density profiles, microscopic components of the normal and tangential pressure tensor profiles, coexistence densities, and interfacial tension has been investigated. The liquid-liquid interface is seen to sharpen with increasing cutoff distance corresponding to an increase in the width of the coexistence phase envelope and the pressure-composition projection of the phase diagram and an accompanying increase in the surface tension.

Acknowledgments

The authors would like to acknowledge helpful discussions with J. M. Garrido, J. M. Míguez, M. M. Piñeiro, and E. de Miguel. This work was supported by Ministerio de Economía y Competitividad through Grant with reference FIS2013-46920-C2-1-P (confinanced with EU Feder funds). Further financial support from Junta de Andalucía and Universidad de Huelva is also acknowledged.

Capítulo 12

Effect of molecular flexibility of Lennard-Jones chains on vapor-liquid interfacial properties

The Journal of Chemical Physics 141, 184701 (2014)

F. J. Blas[1,2], A. I. Moreno-Ventas Bravo[3,2], J. Algaba[1,2], Francisco José Martínez-Ruiz[1,2] and L. G. MacDowell [4]

[1]Departamento de Física Aplicada, Universidad de Huelva,21071, Huelva, Spain
[2]Centro de Investigación de Física Teórica y Matemática FIMAT, Universidad de Huelva, Huelva, Spain
[3]Departamento de Geología, Facultad de Ciencias Experimentales, Universidad de Huelva, Huelva, Spain
[4]Departamento de Química Física, Facultad de Ciencias Químicas, Universidad Complutense, Madrid, Spain

---

We have determined the interfacial properties of short fully-flexible chains formed from tangentially bonded Lennard-Jones monomeric units from direct simulation of the vapor-liquid interface. The results obtained are compared with those corresponding to rigid-linear chains formed from the same chain length, previously determined in the literature [F. J. Blas, A. I: Moreno-Ventas Bravo, J. M. Míguez, M. M. Piñeiro, and L. G. MacDowell, *J. Chem. Phys.* **137** 084706 (2012)]. The full long-range tails of the potential are accounted for by means of an improved version of the inhomogeneous long-range corrections of Janeček [J. Janeček, *J. Phys. Chem. B* **129**, 6264 (2006)] proposed recently by MacDowell and Blas [L. G. MacDowell and F. J. Blas, *J. Chem. Phys.* **131** 074705 (2008)] valid for spherical as well as for rigid and flexible molecular systems. Three different model systems comprising of 3, 5, and 6 monomers per molecule are considered. The simulations are performed in the canonical ensemble, and the vapor-liquid interfacial tension is evaluated using the test-area method (TA). In addition to the surface tension, we also obtained density profiles, coexistence densities, critical temperature and density, and interfacial thickness as functions of temperature, paying particular attention to the effect of the chain length and rigidity on these properties. According to our results, the main effect of increasing the chain length (at fixed temperature) is to sharpen the vapor-liquid interface and to increase the width of the biphasic coexistence region. As a result, the interfacial thickness decreases and the surface tension increases as the molecular chains get longer. Comparison between predictions for fully-flexible and rigid-linear chains, formed by the same number of monomeric units, indicate that the main effects of increasing the flexibility, i.e., passing from a rigid-linear to a fully-flexible chain, are: (a) to decrease the difference between the liquid and vapor densities; (b), to decrease the critical temperature and to increase the critical density; (c) to smooth the density profiles along the interfacial region; (d) to increase the interfacial thickness; and (e) to decrease the vapor-liquid surface tension.

12.1 Introduction

Interfacial properties play a key role in many different fields, including nucleation or dynamics of phase transitions, and their knowledge is essential in a great number of practical and industrial applications. This has attracted the attention from simulators of the liquid community over the last years. Among all the interfacial properties, surface tension is obviously the most important and challenging property to be determined and predicted in the context of inhomogeneous systems [5,8,167]. Despite the great number of studies, especially in the area of computer simulation, the calculation of surface tension remains a subtle problem due to different reasons, being the most important the ambiguity in the definition of the pressure tensor [5], the finite-size effects due to capillary waves [39,168,169], or the difficulty for the calculation of the long-range corrections (LRCs) associated to intermolecular interactions [14,15,38,79,133,135–138], among many others.

The traditional method for determining the fluid-fluid interfacial tension involves the mechanical route through the determination of the normal and tangential pressure tensor profiles using the virial according to different recipes, including those of Irving and Kirkwood [62] and Harasima [63], among others. See the works of Varnik *et al.* [73] and Ghoufi and Malfreyt [76] for a useful and recent revision of the theoretical background of these methods.

During the last ten years, there has been an intensive and fruitful development of new, elegant, and more effective methodologies for calculating the fluid-fluid interfacial tension. The common point of these methods, different from the standard technique based on the mechanical route, is thermodynamic definition of surface tension. From this point of view, different authors have proposed a new generation of methods and techniques for calculating the surface tension of simple and complex systems, including the Test-Area (TA) method of Gloor *et al.* [4], the Wandering Interface Method (WIM) of MacDowell and Bryk [10], the Expanded Ensemble technique, originally developed by Lyuvartsev *et al.* [87] and applied by Errington and Kofke [11] and de Miguel [12], and the Volume Perturbation (VP) methods of de Miguel and Jackson [16,170], who led to the more general formalism of Brumby *et al.* [51], recently implemented by Jiménez-Serratos *et al.* [61], among others.

As new methodologies and techniques were being developed, initially for simple spherical-like models such as systems interacting through the hard-sphere or Lennard-Jones intermolecular potentials, researchers were using and extending these methods for dealing with more complex systems, including chain-like models. In particular, the development of these methods has allowed to study systematically the effect of non-sphericity, and particularly chain length, on different interfacial properties, including vapour-liquid density profiles, interfacial thickness, and surface tension. Special attention has been paid to hydrocarbons, and particular to linear, cyclic, and aromatic alkanes [74,88,96,130,171,172], for which very accurate and refined realistic models, under the useful united-atom approximation, were proposed in the middle and late 90s [173–181]. The existing studies in the literature have provided an in-deep understanding on how the microscopic molecular parameters, mainly the molecular weight or chain length, affect the interfacial behaviour of these systems. However, since the intermolecular potentials are optimized for predicting a given thermodynamic property (normally the vapor-liquid phase behaviour), there has not been any real possibility of studying the effect of flexibility on interfacial properties, specially in simple chain-like models. For instance, the degree of flexibility in alkane models, which is determined by the bending and torsional potentials between chemical groups, is fixed since inter- and intramolecular potentials are optimized to provide the best description of the (vapor-liquid) phase equilibria.

Chain-like molecules are substances formed from monomeric units with a certain degree of flexibility, and n-alkanes molecules and their isomers lie in this general set of molecules. All of them exhibit intramolecular flexibility governed by bending and torsional potentials, that determine the molecular configurations the chains can adopt without overlaps. From a formal point of view, n-alkanes exhibit an intermediate behavior between those shown by two well-known model systems, i.e., the fully-flexible (FF) [13,14,182–185] and rigid-linear (RL) Lennard-Jones (LJ) chain models [186]. The FF chain-like system has neither bending nor torsional potentials between the monomers in a chain. Therefore there is no energetic penalty when the monomers of the chains adopt a close packed structure at high densities. On the contrary, in the RL chain model the bond length, bond angles, and internal degrees of freedom are fixed. As a consequence of this, both models exhibit completely different phase diagrams, as demonstrated several years ago by Galindo *et al.* [186] A related topic which we do not address here is the influence of bond length flexibility in the phase diagram and interfacial properties, which has been recently studied by Chapela et al. [122, 123]

During last five years, we have studied the interfacial properties of different simple chain-like molecular models using perturbative methods, such as the WIM and TA methodologies [13, 14, 143, 144]. Very recently [144], we have determined the interfacial properties of short RLLJ chains from direct simulation of the vapor-liquid interface, including the surface tension using the TA method. In most cases, we have used an improved version [14, 144] of the Janeček's method [15] for calculating long-range corrections (LRCs) to the energy in systems that interact through spherically symmetric intermolecular potentials. The main goal of this work is to study the vapor-liquid interfacial properties of short FFLJ chains and compare the results with previous simulation data corresponding to RLLJ obtained by us [144] to determine the effect of molecular flexibility on interfacial properties, with particular emphasis on surface tension. To account for the full intermolecular interactions, we also use the improved method of Janeček [14, 15, 144] to account for LRCs. To our knowledge, this is the first time the effect of flexibility of Lennard-Jones chains on vapor-liquid interfacial properties is studied from Monte Carlo simulation.

The rest of the paper is organized as follows. In next section we summarize the improved method of Janeček for determining the LRCs of inhomogeneous chain-like systems. The molecular model and the simulation details of this work are presented in Section 12.3. Results obtained are discussed in Section 12.4. Finally, in Section 12.5 we present the main conclusions.

12.2 Effective long-range pairwise potential for molecular systems

In 2006, Janeček [15] proposed a new methodology for calculating long-range corrections (LRC) to the energy in systems that interact through spherically symmetric intermolecular potentials. This procedure allows to treat in a simple way the truncation of the intermolecular energy of systems that exhibit planar interfaces. Three years later, MacDowell and Blas [14] have demonstrated that the Janeček's procedure can be rewritten into an effective long-range pair potential plus a self term that allows for a fast, easy, and elegant implementation of the method. More recently, Blas *et al.* [144] have formally extended the methodology to deal with both FF and RL chain-like molecules. Since the original and improved methodologies have been introduced elsewhere [14, 15, 138], we only account here for the most important details of the current version for FFLJ chains.

Consider a system of N chain-like molecules formed from m monomers contained in a volume V that interact through a pairwise intermolecular potential. The total intermolecular potential energy can be written as

$$U = \frac{1}{2}\sum_{i=1}^{N}\sum_{j=1}^{N}\sum_{k=1}^{m}\sum_{k'=1}^{m} u(r_{i,k;j,k'}) = \frac{1}{2}\sum_{i=1}^{N}\sum_{k=1}^{m} U_{i,k} \tag{12.1}$$

where $u(r_{i,k;j,k'})$ is the intermolecular potential between monomer k of molecule i and monomer k' of molecule j, that depends on the distance between the centres of monomers $r_{i,k;j,k'} \equiv |\mathbf{r}_{i,k} - \mathbf{r}_{j,k'}|$. $U_{i,k}$ is the potential energy of a monomer k of the molecule i, which is defined below. During a simulation, the potential energy of a monomer is usually split into two contributions: one arising from the interaction of monomer k in molecule i with all monomer inside a sphere of radius $r_c^{(i,k)}$ centered at this monomer, and a second term that corresponds to the interaction between the monomer k of molecule i and the rest of monomers forming the system (i.e., all the molecules located outside the cutoff sphere). The potential energy of a monomer k of the molecule i can be then written as

$$U_{i,k} = \sum_{j,k' \in r_c^{(i,k)}} u(r_{i,k;j,k'}) + U_{i,k}^{\mathrm{LRC}} \tag{12.2}$$

where the notation $j, k' \in r_c^{(i,k)}$ denotes all the monomers k' of molecules j located inside the cutoff sphere centered at the position of monomer k of molecule i, and $U_{i,k}^{\mathrm{LRC}}$ represents the intermolecular interactions between monomer k of molecule i and the rest of the system due to LRC. Note that $r_c^{(i,k)} \equiv r_c$ since all molecules have the same cutoff distance.

In the improved methodology proposed recently by MacDowell and Blas [14] and Blas *et al.* [144], the total energy felt by the whole molecule i, due to the long-range interactions with all the molecules that form the system, can be written as

$$U_i^{\mathrm{LRC}} = \sum_{k=1}^{m} U_{i,k} \tag{12.3}$$

where $U_{i,k}$ have been previously defined in Eq. (12.2). U_i^{LRC} can be splited in different contributions, i.e., intermolecular, intramolecular, and the self energy contribution,

$$U_i^{\mathrm{LRC}} = U_{i,inter}^{\mathrm{LRC}} + U_{i,intra}^{\mathrm{LRC}} + U_{i,self}^{\mathrm{LRC}} \tag{12.4}$$

The intermolecular potential energy between molecule i and the rest of molecules forming the system, due to the LRCs, can be written as

$$U_{i,inter}^{\mathrm{LRC}} = \frac{1}{\mathcal{A}} \sum_{\substack{j=1 \\ (j \neq i)}}^{N} \sum_{k=1}^{m} \sum_{k'=1}^{m} w(|z_{i,k} - z_{j,k'}|) \tag{12.5}$$

The energy corresponding to the intramolecular interactions associated to segments of molecule i is given by

$$U_{i,intra}^{\mathrm{LRC}} = \frac{1}{\mathcal{A}} \sum_{k=1}^{m-1} \sum_{k'=k+1}^{m} w(|z_{i,k} - z_{i,k'}|) \tag{12.6}$$

Note that Eq. (12.6) only takes into account the intramolecular interactions, associated to the LRC, i.e., all possible interactions between segments of molecule i. A long-range contribution from sites in the same molecules is perhaps unexpected, but follows naturally from the fact that long range corrections are implemented here on the basis of segment densities.

And finally, the self-energy contribution to the potential energy of molecule i can be simply written as

$$U_{i,self}^{\text{LRC}} = \frac{1}{\mathcal{A}}\sum_{k=1}^{m} w(0) \equiv \frac{1}{\mathcal{A}} m w(0) \tag{12.7}$$

The self-energy contribution associated to the long-range interactions given by Eq. (12.7) is only due to segments belonging to molecule i.

$w(|z_{i,k} - z_{j,k'}|)$ accounts for the intermolecular interactions due to the LRC between a monomer k of molecule i at $z_{i,k}$ and all the monomers k' of all molecules j located inside the slab centered at $z_{j,k'}$. The particular expression for $w(|z_{i,k} - z_{j,k'}|)$ depends on the election of the intermolecular potential of the system. In the original Janeček's method, applicable for molecules interacting through the Lennard-Jones intermolecular potential, the function $w(z)$ is given by

$$w(z) = \begin{cases} 4\pi\epsilon\sigma^2 \left[\dfrac{1}{5}\left(\dfrac{\sigma}{r_c}\right)^{10} - \dfrac{1}{2}\left(\dfrac{\sigma}{r_c}\right)^{4} \right] & z < r_c \\[2ex] 4\pi\epsilon\sigma^2 \left[\dfrac{1}{5}\left(\dfrac{\sigma}{z}\right)^{10} - \dfrac{1}{2}\left(\dfrac{\sigma}{z}\right)^{4} \right] & z > r_c \end{cases} \tag{12.8}$$

The total potential energy of a system of N molecules formed by m segments, due to the long-range interactions, is then calculated as

$$U^{\text{LRC}} = U_{inter}^{\text{LRC}} + U_{intra}^{\text{LRC}} + U_{self}^{\text{LRC}} \tag{12.9}$$

The total intermolecular potential energy, due to the long-range interactions, is given by

$$\begin{aligned} U_{inter}^{\text{LRC}} &= \frac{1}{2}\sum_{i=1}^{N} U_{i,inter}^{\text{LRC}} = \frac{1}{2\mathcal{A}} \sum_{i=1}^{N} \sum_{\substack{j=1 \\ (j\neq i)}}^{N} \sum_{k=1}^{m} \sum_{k'=1}^{m} w(|z_{i,k} - z_{j,k}|) \\ &= \frac{1}{\mathcal{A}} \sum_{i=1}^{N-1} \sum_{j=i+1}^{N} \sum_{k=1}^{m} \sum_{k'=1}^{m} w(|z_{i,k} - z_{j,k'}|) \end{aligned} \tag{12.10}$$

where we have transformed the unrestricted summation over indexes i and j (with the exception of the case $i = j$ corresponding to intramolecular interactions) into a sum of pairwise effective (integrated) intermolecular potential over all the pair of molecules in the system.

The total intramolecular potential energy due to the long-range interactions is given by

$$U_{intra}^{\mathrm{LRC}} = \sum_{i=1}^{N} U_{i,intra}^{\mathrm{LRC}} = \frac{1}{\mathcal{A}} \sum_{i=1}^{N} \sum_{k=1}^{m-1} \sum_{k'=k+1}^{m} w(|z_{i,k} - z_{i,k'}|) \tag{12.11}$$

Finally, the total self-energy potential energy due to the long-range interactions is written as

$$U_{self}^{\mathrm{LRC}} = \sum_{i=1}^{N} U_{i,self}^{\mathrm{LRC}} = \frac{1}{\mathcal{A}} \sum_{i=1}^{N} \sum_{k=1}^{m} w(0) \equiv \frac{1}{\mathcal{A}} \sum_{i=1}^{N} m w(0) \equiv \frac{1}{\mathcal{A}} N m w(0) \tag{12.12}$$

Equations (12.9)-(12.12) represent the generalization of the improved version of MacDowell and Blas [14], based on Janeček's method, for the inhomogeneous LRC of chain like systems, including flexible and rigid molecules. [144]

This procedure provides several important advantages over the original method [144]: (1) Eqs. (12.4)–(12.7) and (12.9)–(12.12) for molecular systems, correspond to the exact evaluation of the intermolecular interactions due to the LRCs, without a discretization of the simulation box along the z-axis; (2) the improved procedure allows to evaluate U_i^{LRC} and U^{LRC} without the explicit calculation of the density profile on the fly, i.e., it is not necessary to update the density profile $\rho(z)$ each Monte Carlo step; (3) finally, the implementation of the method is straightforward.

12.3 Model and simulation details

We consider chain molecules formed by m identical LJ sites (monomer segments) characterized by a diameter σ and dispersive energy ϵ. The molecules are modeled as FF with monomer-monomer bond length $L = \sigma$, which means that chains are formed by tangent monomers or segments. The interaction potential between two different molecules is given by,

$$u^{LJ}(1,2) = \sum_{i=1}^{m} \sum_{j=1}^{m} 4\epsilon \left[\left(\frac{\sigma}{r_{ij}} \right)^{12} - \left(\frac{\sigma}{r_{ij}} \right)^{6} \right] \tag{12.13}$$

where r_{ij} is the distance between monomer i of molecule 1 and monomer j of molecule 2. Since we are considering a FF model sites i and j can be in different or in the same molecule, so we are explicitly considering both intermolecular and intramolecular interactions. As previously discussed in the Introduction, we have recently studied a similar model, the RL model. It is important for the discussion of the results in the next section to give here a brief account of the most important features of the model. In this latter system, the molecules are strictly linear and rigid; all intramolecular degrees of freedom are frozen and both the bond distances and bond angles remain fixed. As mentioned previously, in the first model the interactions between segments are identical to those in the RL model, but as the chains are flexible, both intermolecular and in particular intramolecular interactions are now relevant since both contributions are present in the Hamiltonian of the system, as noted before.

We examine a spherically truncated potential model with a cutoff distance of $r_c = 3\sigma$. We consider inhomogeneous LRCs using the MacDowell and Blas [14] recipe (presented in the previous section), based on the Janeček's method [15, 138], obtaining results for the full LJ potential, i.e., corresponding to infinite truncation distance. According to the discussion of the previous paragraph, since intramolecular interactions are also relevant for this model, we use the full expressions for the inhomogeneous LRC corresponding to U_i^{LRC} and U^{LRC}.

The number of molecules, N, used in each simulation depends on the number of monomers per molecule. We consider $N = 672$, 403, and 336 for systems formed from 3, 5, and 6 monomers, respectively. As in previous studies [13, 14, 143, 144], this choice is made so as to have systems with the same total number of monomers irrespective of the monomers per molecule. We also compare the results obtained here with those published previously by us [14] corresponding to FF chains formed from 4 monomers (see the next section for further details).

Simulations are performed in the NVT ensemble. We consider a system of N molecules at a temperature T in a volume $V = L_x\,L_y\,L_z$, where L_x, L_y and L_z are the dimensions of the rectangular simulation box. A homogeneous liquid system is first equilibrated in a rectangular simulation box of dimensions $L_x = L_y = 11\sigma$, and $L_z = 24$ for FFLJ chains formed by 3 and 5 monomers, and $L_z = 26$ for chains with 5 monomers. The box is then expanded to three times its original size along the z direction, while leaving the liquid phase at the center. As a result, we obtain a centered liquid slab with those chain bits spanning across the boundary conditions of the original liquid configuration protruding into empty boxes of equal size at each side. The final overall dimensions of the vapor-liquid-vapor simulation box are therefore $L_x = L_y = 11\sigma$, and $L_z = 72$ and 78σ for the corresponding chain lengths.

The simulations are organized in cycles. A cycle is defined as N trial Monte Carlo moves. Our MC procedure comprises three types of configurational updates: one involving a trial displacement of the molecular center of mass, and the other two, a partial and complete molecular regrowth of the molecular chains. For the latter case, we consider a configuration bias scheme [3, 187]. Each type of move is chosen with a probability of 20%, 40%, and 40%, respectively. The magnitudes of the appropriate displacements are adjusted so as to get an acceptance rate of $30\,\%$ approximately. We use periodic boundary conditions in all three directions of the simulation box.

The calculation of the surface tension is performed using of the Test-Area (TA) methodology [4]. Since the TA method is a standard and well-known procedure for evaluating the fluid-fluid interfacial tension of liquid, we only provide the most important features of the technique. For further details we recommend the original work [4] and the most important applications [13, 14, 16, 75, 89, 92, 96, 97, 127–129, 170]. The implementation of the TA technique involves performing test-area deformations of magnitude ΔA during the course of the simulation at constant N, V, and T every MC cycle. As shown by Gloor *et al.* [4], the surface tension follows from the computation of the change in Helmholtz free energy associated with the perturbation, which in turn can be expressed as an ensemble average of the corresponding Boltzmann factor. Further details can be found in Ref. [4, 13, 14, 93, 143, 144, 146, 147, 188] We consider in all cases two perturbations of size $\Delta A^* = \Delta A/A_0 = \pm 0.0005$, where $A_0 = L_x L_y = 121\sigma^2$ is the interfacial area of the unperturbed state.

As in previous studies [13,14], for each length we perform simulations of inhomogeneous systems at different temperatures where vapor-liquid equilibrium is expected. We typically consider either eight or nine temperatures in the range $\sim 0.5\,T_c$ up to $\sim 0.9\,T_c$, where T_c is the critical temperature of the system. Each series is started at an intermediate temperature. This system is well equilibrated for 10^6 MC cycles, and averages are determined over a further period of 4×10^6 MC cycles. The systems at other temperatures of each series are equilibrated for 5×10^5 MC cycles and averages are determined over the same number of cycles (4×10^6). The production stage is divided into M blocks. Normally, each block is equal to 10^5 MC cycles. The ensemble average of the surface tension is given by the arithmetic mean of the block averages and the statistical precision of the sample average is estimated from the standard deviation in the ensemble average from $\overline{\sigma}/\sqrt{M}$, where $\overline{\sigma}$ is the variance of the block averages and M has been fixed in this work to $M = 40$.

All the quantities in our paper are expressed in conventional reduced units, with σ and ϵ being the length and energy scaling units, respectively. Thus, the temperature is given in units of ϵ/k_B, the densities in units of σ^{-3}, the surface tension in units of ϵ/σ^2, and the interfacial thickness in units of σ.

12.4 Results and discussion

In this section we present the main results from the simulations of FFLJ chains with varying chain length. We focus on the interfacial properties, such as density profiles, interfacial thickness, and surface tension of chains considering a cutoff distance of $r_c = 3\sigma$ and the effective LRCs presented in Section 12.2. We also examine the temperature and chain length dependence of these properties. In addition to that, we compare our results obtained for FFLJ chains with those corresponding to RL chain like molecules interacting through the same monomer-monomer intermolecular potential. In particular, we compare the results corresponding to chains form from 3, 4 (results taken from the work of MacDowell and Blas [14]), and 5 with those obtained recently by Blas *et al.* [144]. Results for FF chains with 6 LJ monomers, obtained in the present work, are also presented here for comparison.

We follow the same analysis and methodology than in our previous works [13, 14, 91, 144], and consider different chain lengths and temperatures. The equilibrium density profiles $\rho(z)$ are computed from averages of the histogram of densities along the z direction over the production stage. Density profiles are given in terms of the monomeric units. The bulk vapor and liquid densities are obtained by averaging $\rho(z)$ over appropriate regions sufficiently removed from the interfacial region. In addition to that, the final bulk vapor density value, at each temperature and chain length, is obtained after averaging the density profiles on both sides of the liquid film. The statistical uncertainty of these values is estimated from the standard deviation of the mean values. Following our previous works, additional interfacial properties, such as the position of the Gibbs-dividing surface, z_0, and the $10-90$ interfacial thickness, t, are obtained by fitting each of the two equilibrium density profiles to hyperbolic tangent functions [5] (see Eq. (3) of our previous work [13] for further details). We fix the liquid, ρ_L, and vapor, ρ_V, densities to previously computed values and treat z_0 and t as adjustable parameters. Our simulation results for the bulk densities and interfacial thickness for FFLJ chains formed by 3, 5, and 6 monomers are collected in Table 12.1. The interfacial thickness values summarized here correspond to the average of the values for the two interfaces appearing in the system.

Is is important, however, to mention that at high temperature, the density profiles are nearly symmetrical and may be described using a hyperbolic tangent function, as expected in the neighborhood of the critical point [5]. As the temperature is decreased, however, the profiles develop a very strong asymmetry, and the distance from the liquid and vapor densities to the density at the equimolar point is no longer equal [189]. Such asymmetry in the density profile results from the fact that the correlation lengths on the vapor and liquid side are no longer equal far from the critical point, an effect which increases with increasing chain size. As a result, these density profiles may be possible better described using another kind of function, as indicated already by Palanco. [189]

Tabla 12.1: Liquid density ρ_L, vapor density ρ_V, 10-90 interfacial thickness t, and surface tension γ at different temperatures for systems of RLLJ chains formed from m monomers with a monomer-monomer LJ cutoff distance $r_c = 3\sigma$ and inhomogeneous LRCs. All quantities are expressed in the reduced units defined in Section 12.3. The errors are estimated as explained in the text.

m	T	ρ_L	ρ_V	t	γ
3	1.20	0.787(2)	0.00093(3)	1.015(2)	0.92(5)
3	1.40	0.724(1)	0.00492(4)	1.3056(9)	0.66(2)
3	1.60	0.6554(3)	0.01674(9)	1.7484(9)	0.429(9)
3	1.80	0.5709(7)	0.0458(1)	2.599(2)	0.224(4)
3	1.85	0.5450(7)	0.0582(2)	2.973(1)	0.171(4)
3	1.90	0.515(1)	0.0744(3)	3.5032(8)	0.131(4)
5	1.00	0.869(3)	0.0000005(3)	0.722(2)	1.28(3)
5	1.20	0.817(2)	0.000024(3)	0.8804(6)	1.04(2)
5	1.40	0.766(1)	0.00031(1)	1.072(1)	0.852(9)
5	1.60	0.7115(8)	0.00193(3)	1.325(2)	0.637(9)
5	1.80	0.6525(6)	0.00737(4)	1.678(2)	0.444(8)
5	2.00	0.5856(6)	0.02138(8)	2.254(3)	0.269(6)
5	2.10	0.5460(7)	0.0346(2)	2.7244(2)	0.205(5)
5	2.20	0.4988(9)	0.0555(4)	3.488(3)	0.140(3)
6	1.00	0.874(5)	0.0000003(9)	0.705(1)	1.40(5)
6	1.20	0.825(3)	0.000004(3)	0.8564(9)	1.12(3)
6	1.40	0.775(2)	0.000087(6)	1.0302(9)	0.89(1)
6	1.60	0.723(1)	0.00072(2)	1.245(2)	0.73(1)
6	1.80	0.6690(7)	0.00337(4)	1.5382(4)	0.501(9)
6	2.00	0.6088(9)	0.01111(6)	1.982(2)	0.351(6)
6	2.20	0.5378(9)	0.0301(1)	2.2772(3)	0.204(6)
6	2.30	0.4938(7)	0.0484(2)	3.523(3)	0.141(4)
6	2.35	0.466(1)	0.0618(5)	4.14(1)	0.114(4)

We show in Fig. 12.1 the segment density profiles $\rho(z)$ for FFLJ chains formed by three ($m = 3$), five ($m = 5$), and six ($m = 6$) monomers at several temperatures in the vapor-liquid coexistence region. For the sake of clarity, we only present one half of the profiles corresponding to one of the interfaces. Also for convenience, all density profiles have been shifted along z so as to place z_0 at the origin. Since density profiles are expressed in terms of monomeric units in all cases, liquid density increases and vapor density decreases, at fixed temperature, as the chain length is increased as expected. In addition to that, the absolute value of the slope of the density profiles in the interfacial region decreases as the temperature is increased. This is an expected behavior as temperature approaches to the critical temperature of the system. This is also in agreement with the divergence, as it is shown later, of the interfacial thickness as $T \to T_c$. Another intuitive but less obvious behavior is related with the effect of chain length, at constant temperature, on the slope of the density profile going from the vapor to the liquid phase. As can be seen (it is more obvious at high densities, i.e., $T \sim 1.8$), the slopes of the profiles increase as the chain length is increased from $m = 3$ (Fig. 12.1a) through $m = 4$ (Fig. 12.1b) and $m = 5$ (Fig. 12.1c), and finally up to $m = 6$ (Fig. 12.1d).

Although the behavior of the density profiles of FF chains at different conditions is interesting, it is important to keep in mind that one of the goals of this work is to determine the effect of molecular

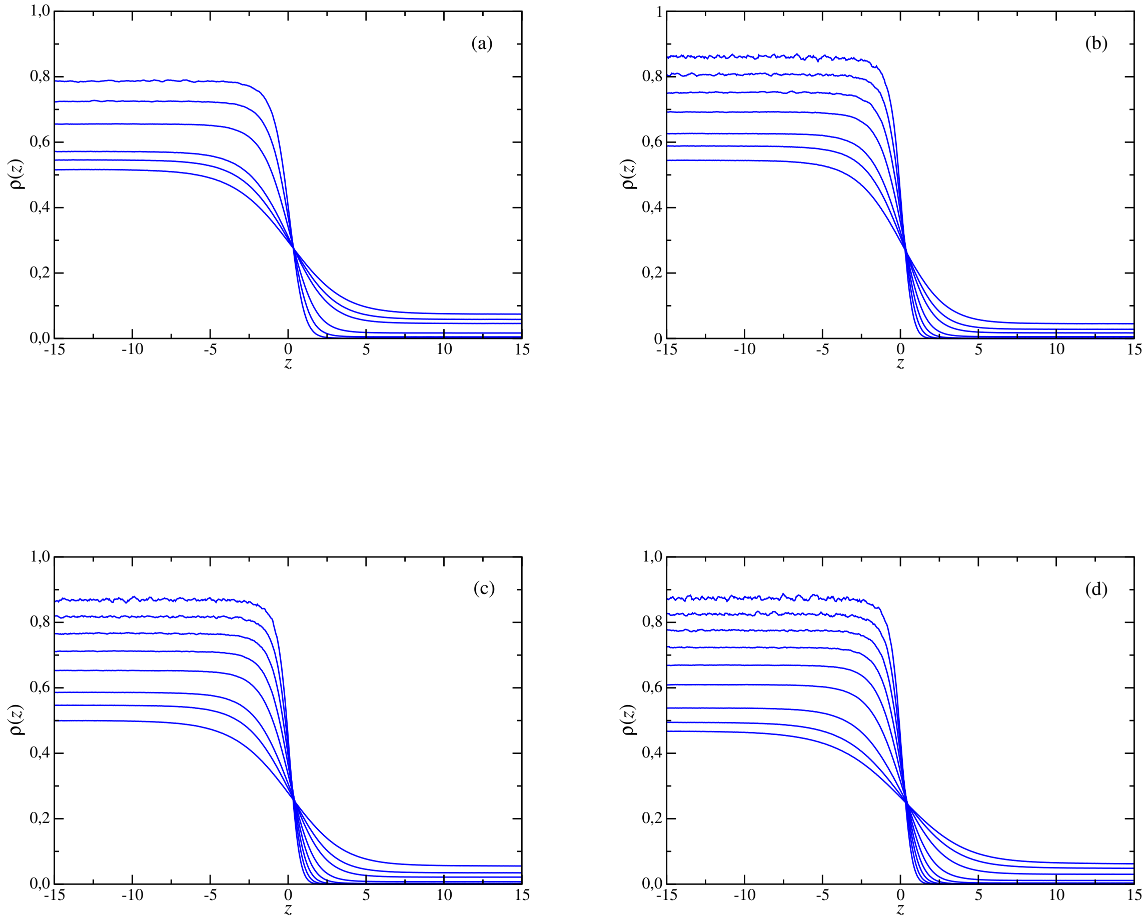

Figura 12.1: Simulated equilibrium density profiles across the vapor-liquid interface of FFLJ chains formed from three ($m = 3$) (a), four ($m = 4$) (b), five ($m = 5$) (c), and six ($m = 6$) (d) monomers with a monomer-monomer LJ cutoff of $r_c = 3\sigma$ and inhomogeneous LRCs at several temperatures. From top to bottom (in the liquid region): (a) $T = 1.20, 1.40, 1.60, 1.80.1.85$, and 1.90; (b) $T = 1.00, 1.20, 1.40, 1.60, 1.80, 1.90$, and 2.00; (c) $T = 1.00, 1.20, 1.40, 1.60, 1.80, 2.00, 2.10$, and 2.20; (d) $T = 1.00, 1.20, 1.40, 1.60, 1.80, 2.00, 2.20, 2.30$, and 2.35.

flexibility on different interfacial properties. A detailed comparison between the density profiles of FF and RLLJ chains with different chain lengths and temperatures is shown in Figure 2. As can been seen in Figure 12.2(a), the main effect of flexibility (when comparing density profiles of FF and RLLJ chains formed from four LJ monomers) is to decrease the liquid density, increase the vapor density, and decrease the absolute value of the slope of the density profile along the interfacial region. As can be seen, the change in density is larger in the case of the liquid side than in the vapor side. In addition to that, the changes in density profiles seem to be similar at the two temperatures considered, $T = 1.6$ and 1.9, although the increasing of the vapor density when passing from a RL to a FF change is enhanced as the temperature is increased. This is probably due to the proximity of the critical point of the system ($T_c \sim 2.25$), since the relative changes in vapor and liquid densities as temperature approaches to the critical state are larger in the case of vapor density.

We also consider the effect of flexibility for longer chains ($m = 5$). As can be seen, the same qualitative behavior is observed for the liquid and vapor densities, as well as for the absolute value of the slope of the density profile along the interfacial region. The effect of flexibility is more important

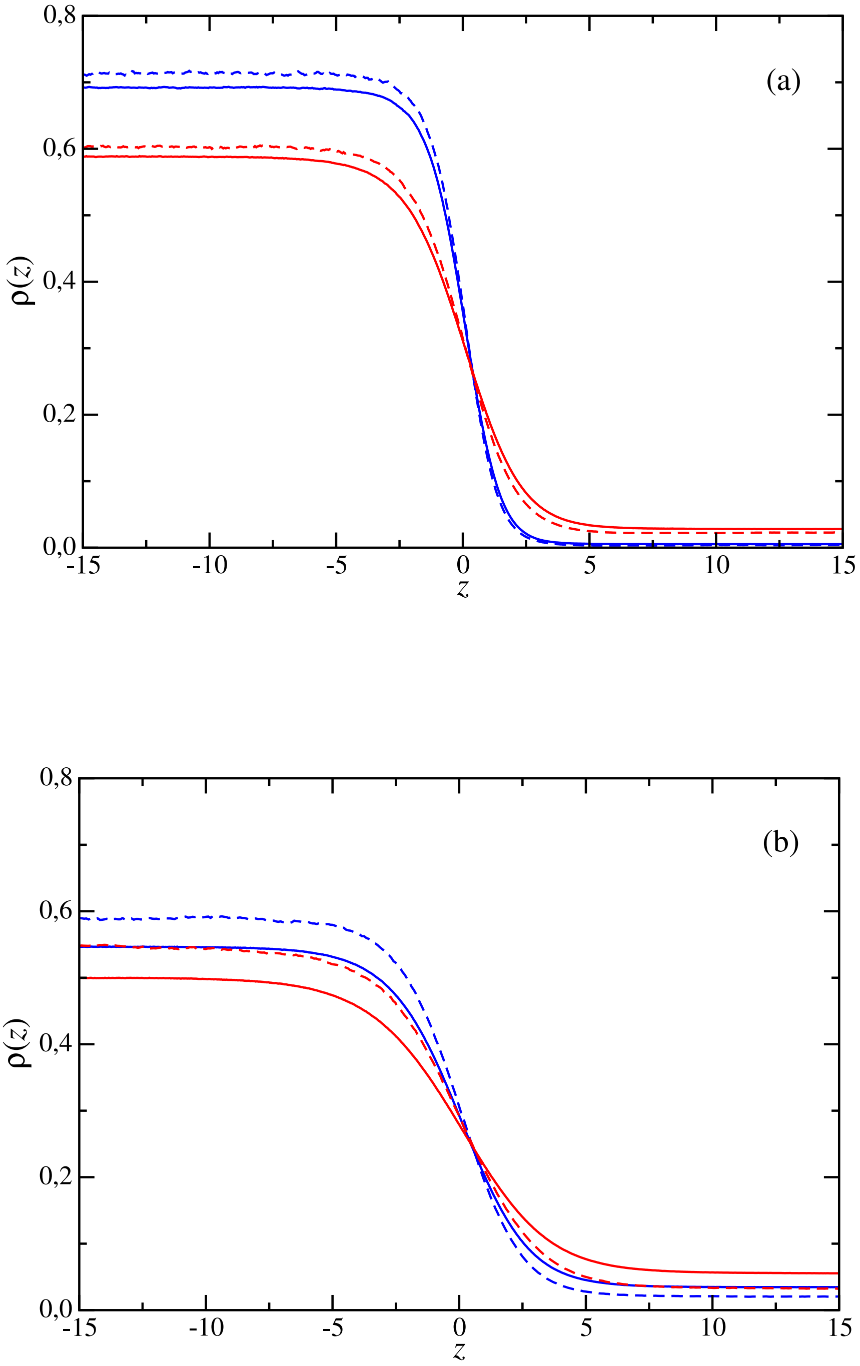

Figura 12.2: Simulated equilibrium density profiles across the vapor-liquid interface of FF (continuous curves) and RL (dashed curves) LJ chains formed from: (a) four ($m = 4$) monomers at $T = 1.6$ (blue curves) and $T = 1.9$ (red curves); (b) five ($m = 5$) monomers at $T = 1.9$ (blue curves) and $T = 2.1$ (red curves).

and noticeable in this case than in that corresponding to $m = 4$. As can be seen, the change in densities, and especially in the slope (absolute value) of the density profile along the interface is enhanced with respect to that observed for shorter chains ($m = 3$ and 4). Vapor-liquid envelopes of FF and RLLJ chains with $m = 5$ monomers are really different. As demonstrated several years ago by Galindo *et al.* [186], RLLJ chains exhibit a shrinkage of the liquid range, and that of FFLJ chains present a huge liquid range ($T_t/T_c \sim 0.14$).

We have also estimated the location of the critical point resulting from our direct Monte Carlo simulations. The critical coordinates (temperature, T_c, and density, ρ_c) are obtained following the usual procedure, i.e., using the simulation results for the vapor and liquid coexistence densities (Table 12.1) and the scaling relation for the width of the coexistence curve [5],

$$\rho_L - \rho_V = A(T - T_c)^\beta \; , \qquad (12.14)$$

and the law of rectilinear diameters

$$\frac{\rho_L + \rho_V}{2} = B + CT \; . \qquad (12.15)$$

A, B, and C are constants, and β is the corresponding critical exponent. A universal value of $\beta = 0.325$ is assumed here. [5] In Table 12.2 we report the values of the critical temperatures and densities as obtained from this procedure for all the systems studied in this work. In addition to that, we have also included the critical conditions (temperature and density) for RLLJ chains formed from 3, 4, and 5 monomers obtained by Blas *et al.* [144].

As a word of caution, we note that the error bars of critical parameters given in Table 12.2 are to be considered as the statistical uncertainty resulting from our simulations. In fact, true critical behavior is not seen in finite size simulations, since criticality is governed by a diverging correlation length which in the simulations is limited to the smallest dimension, $L = 11\sigma$. Accordingly, our error bars do not include systematic errors due to finite system size effects [190]. Such errors would need to be studied systematically by means of finite size scaling techniques, as in the works of Wilding and coworkers [191, 192]. For the purpose of our work, where we are mainly concerned with the difference between flexible and rigid systems, our results are of sufficient accuracy, however.

The vapor-liquid phase envelopes of FFLJ chains with $r_c = 3\sigma$ and inhomogeneous LRCs are depicted in Fig. 12.3. We have also included the simulation results corresponding to the coexistence curves of RLLJ chains form from three ($m = 3$), four ($m = 4$), and five ($m = 5$) monomeric units

Tabla 12.2: Critical densities of FFLJ (ρ_c^{FF}) and RLLJ (ρ_c^{RL}) chains with different chain lengths as obtained from the analysis of the coexistence densities using Eqs. (12.14) and (12.15); critical temperatures of FFLJ ($T_c^{\mathrm{FF}(a)}$) and RLLJ ($T_c^{\mathrm{RL}(a)}$) chains as obtained from the analysis of the coexistence densities using Eqs. (12.14) and (12.15); and critical temperatures of FFLJ ($T_c^{\mathrm{FF}(b)}$) and RLLJ ($T_c^{\mathrm{RL}(b)}$) chains as obtained from the analysis of the computed tension data using Eq. (12.16) and fixing the critical point to $\mu = 1.258$. All quantities are expressed in the reduced units defined in Sec. III. Results corresponding to RLLJ chains from by 3, 5, and 6 monomeric units are taken from the work of Blas *et al.* [144] Results corresponding to FFLJ chains from by four monomeric units ($m = 4$) are taken form the work of MacDowell and Blas [14]

.

m	ρ_c^{FF}	ρ_c^{RL}	$T_c^{\mathrm{FF}(a)}$	$T_c^{\mathrm{RL}(a)}$	$T_c^{\mathrm{FF}(b)}$	$T_c^{\mathrm{RL}(b)}$
3	0.274(8)	0.27(1)	2.041(9)	2.05(2)	2.09(5)	2.1(2)
4	0.264(7)	0.26(1)	2.26(1)	2.25(3)	2.29(2)	2.3(3)
5	0.253(7)	0.24(2)	2.38(1)	2.50(4)	2.44(2)	2.6(2)
6	0.245(8)	–	2.5(1)	–	2.57(2)	–

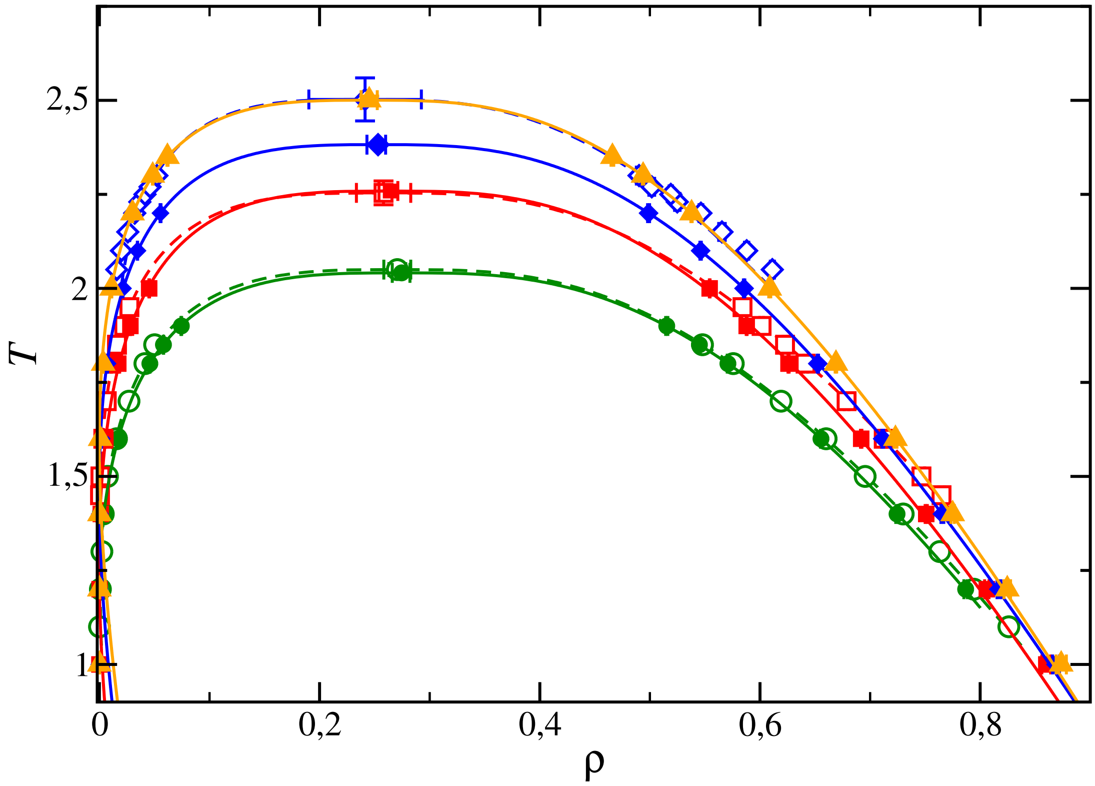

Figura 12.3: Vapour-liquid coexistence densities for FF (continuous curves and filled symbols) and RL (dashed curves and open symbols) LJ chains. The open green, red, blue, and orange curves and symbols correspond to the coexistence densities obtained from the MC NVT simulations for chains lengths of $m = 3$, $m = 4$, $m = 5$, and $m = 6$, respectively. The filled red symbols correspond to the existence densities obtained by MacDowell and Blas [14]. Symbols at the highest temperatures for each of the coexistence curve represent the critical points estimated from Eqs. (12.14) and (12.15).

from our previous work [144]. As previously mentioned, all densities are presented in terms of the monomeric densities since the coexistence curves fall in the same scale when plotted in this way.

We first analyze the phase behavior of FFLJ chains. As can be seen, the phase envelope becomes wider as the chain length is increased from three ($m = 3$) up to six ($m = 6$) segments, as one would expect. Note that we have also included the Monte Carlo simulation results corresponding to the case $m = 4$ (chains form from four LJ segments) from a previous work [14]. Obviously, the phase envelopes obtained in this work ($m = 3$, 5, and 6) follow the expected intermediate behavior than those corresponding to dimers and chains form from eight ($m = 8$) segments. The critical coordinates of chains, for different chain lengths, also follow the expected behavior, i.e., higher critical temperature and lower critical density as the chain length is increased.

Comparison between coexistence curves of FF and RLLJ chains provides interesting conclusions of the effect of molecular flexibility on the phase behavior of chain like systems. As can be seen, the coexistence curves of RLLJ chains exhibit the same qualitative behavior previously explained when the chain length is varied. However, the most interesting conclusions from Fig. 12.3 arise when comparing the coexistence envelopes of FF and RLLJ chains formed by the same number of monomeric units. As can be seen, the coexistence envelope of RLLJ chains is wider than that corresponding to FF chains, i.e., liquid and vapor densities of RL chains are higher and lower than those of FF, respectively. In addition to that, differences between both phase envelopes increase as the chain length is increased. For instance, for the case of chains formed from three segments ($m = 3$), the phase envelope of both models is nearly equal. However, for chain lengths of $m = 4$, differences are noticeable in both sides of the phase envelope, especially in the liquid side. But the case in which the differences between densities of both models are larger corresponds to $m = 5$, especially at the liquid side of the phase envelope. In summary, the key issue in order to rationalize the different properties between FF and LR chains is that the LR has a higher critical temperature at the same chain length, hence, at a fixed chosen temperature it will be relatively further away from the critical point than the corresponding FF chain. This explains why LR chains have greater segregation, greater surface tension and smaller interfacial width at a given temperature.

An important difference between the phase envelopes of the two models studied here is the range of temperatures at which vapor-liquid phase equilibria is stable in both models. As the chain length increase, from three ($m = 3$) to five ($m = 5$), the vapor-liquid coexistence range corresponding to the RL chain model is more limited. Contrary, the FFLJ model exhibits a huge liquid range in which vapor and liquid phases coexist, due to the reason previously explained in the Introduction (see also our previous works for further details [144, 186].

This effect can be understood observing the phase behavior of FFLJ chains form from six ($m = 6$) monomeric units. As can be seen, the range of temperatures at which the system exhibits vapor-liquid separation is huge, from $T \sim 1.0$ up to $T \sim T_c \sim 2.5$. No simulation data for the homologous RL model is available in the literature. We think this model exhibits liquid-crystalline phases for chain lengths equal or larger than six segments, including isotropic, nematic, and smetic phases. Due to this, the determination of the vapor-liquid coexistence properties, and particularly interfacial properties such as surface tension, is a difficult task taking into account that the solid phase would be more stable than the liquid at these conditions [144, 186].

Before presenting the results for other properties it is important mention the general influence of long-range corrections on the estimation of the critical point. The standard long range corrections to the energy introduce an effective mean field van der Waals like contribution to the Hamiltonian $a\rho^2$. Such behavior is only exact for infinitely long-range pair potentials and produces mean field like criticality [193]. The inhomogeneous long–range corrections introduced here are somewhat more subtle. Indeed, they correspond to an effective infinite long range potential for all pairs of molecules with perpendicular distance $|z_j - z_i| > r_c$, but a finite range potential for pairs of molecules $|z_j - z_i| < r_c$. This most likely also produces mean field critical behavior. However, we use a long range cutoff R_c sufficiently large that the Ising like behavior will dominate the system's behavior except in the close neighborhood of T_c [194]. In practice, this is most likely not an important issue, since we expect that for our limited system sizes finite size effects become relevant before the crossover from Ising like to mean field behavior. As a matter of fact, most estimates for long range r^{-6} potentials that are available in the literature introduce a mean field like character to the simulations by virtue of the homogeneous long range correction to the dispersive energy. In practice, the artifacts that could result are most likely not as important as the suppression of diverging correlation lengths that result from the finite system size.

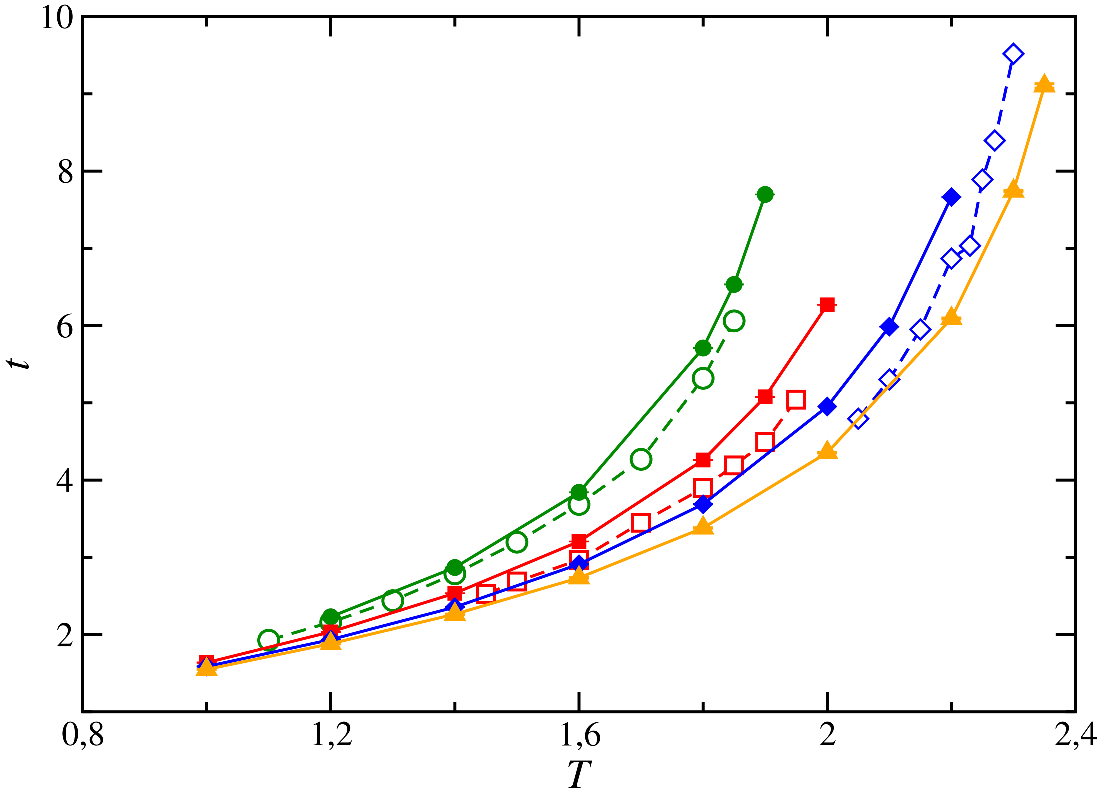

Figura 12.4: The 10-90 interfacial thickness t as a function of the temperature for FF (continuous curves and filled symbols) and RL (dashed curves and open symbols) LJ chains. The green, red, blue, and orange colors correspond to the interfacial thickness obtained from the MC NVT simulations for chains lengths of $m = 3$, $m = 4$, $m = 5$, and $m = 6$, respectively. The open symbols correspond to the interfacial thickness obtained by Blas and *et al.* [144]. The curves are included as a guide to the eyes.

Another interesting property obtained from our analysis is the $10 - 90$ interfacial thickness, t, of FFLJ chains (cf. Table 12.1). Notice the intrinsic width is not strictly an intrinsic property of the fluid, but rather, increases logarithmically with system size due to the presence of capillary waves [119]. However, our results are performed in all cases for the same lateral size, so that the comparison is meaningfull. Furthermore, the lateral system size in our simulations are only a few times as large as the fluid's correlation length so that we do not expect for such sizes a large effect of capillary wave broadening. We have also included the results obtained by Blas *et al.* [144] for RLLJ chains form from three ($m = 3$), four ($m = 4$), and five ($m = 5$) monomeric units. Fig. 12.4 shows the behavior of the $10 - 90$ interfacial tension, as a function of temperature, for different chain lengths and the models considered. As can be seen, for a given chain length, t is seen to increase with temperature, which simply reflects the fact that the interfacial region gets correspondingly wider, as can be also observed in Fig. 12.2. At low temperatures the density profiles exhibit a sharp interface which corresponds to a low value of the interfacial thickness. As the temperature is increased towards the critical value the interfacial region becomes wider, and hence, the value of the interfacial thickness increases and diverges to infinity as $T \to T_c$. Also note that at low temperatures both surface tension and interfacial widths become very similar for all chain lengths. In this regime of low temperature, the properties of the liquid phase are essentially dictated by packing effects on the scale of segment diameter, which is the same for all chains. It is in this region where Wertheim's thermodynamic perturbation theory and the related SAFT equation becomes most accurate, [21, 195, 196] as a reference monomer system provides an accurate description of the chain fluid. As the temperature increases, both interfacial width and surface tension are rather dominated by the relative distance from the critical point (c.f. Eq. 15), which is different for each chain, and the properties become very different.

We first concentrate on the behavior of the interfacial tension of FFLJ chains. According to the figure, an increase of the chain length results in a decrease of the thickness of the interface at fixed temperature. The variation of the interfacial thickness, as a function of chain length, is smaller as the chain length increases. In particular, the smallest variation in the interfacial thickness, at a given temperature, occurs when the chain length changes from $m = 5$ to $m = 6$. Note that for intermediate temperatures, $T \sim 1.6$, the interfacial thickness of chains form from five and six monomeric units is nearly identical. This is a consequence of the scaling behavior observed for FFLJ chains previously shown by different authors [13, 13, 14, 143, 144, 197, 198]. This behavior is consistent with the shape exhibited by the density profiles associated to the vapor-liquid phase envelopes, which is a consequence of the larger cohesive energy that longer chain like molecules have (in comparison with short chains).

We now consider the difference between the interfacial thickness of FF and RLLJ chains. As can be seen in Fig. 12.4, the interfacial thickness of flexible chains, at the same temperature and chain length, is larger than that of rigid molecules. The difference between the thickness of flexible and rigid chains, for a fixed chain length, increases as the temperature approaches to the critical temperature of the system. In fact, the difference between both values increases as the chain length is larger. This behavior is consistent with the results shown previous here (see Figs. 12.1-12.3).

Finally, it is also important to emphasize one important issue. The range of temperatures at which vapor-liquid phase equilibria is stable in both models is very different. In the case of the flexible model, the system exhibits a huge range in which liquid and vapor coexist. However, the vapor-liquid coexistence range corresponding to the RL chain model is much more limited, as we have explained previously in the Introduction. To recap, the main effect of rigidity on the interfacial thickness of the vapor-liquid coexistence of LJ chains models is to decrease it, especially at temperatures near the critical point and for long-chain systems.

We finally consider the behavior of the vapor-liquid surface tension of the LJ molecular chains with different sizes. In particular, we compare the results obtained in this work for the FF model with those for RL chains obtained previously [144]. This allows to understand the effect of flexibility of the molecular models on the surface tension of the systems studied. The temperature dependence of the surface tension for flexible and rigid LJ chains is shown in Fig. 12.5. As can be seen, at any given temperature, the interfacial tension is larger for longer chains. Obviously, this conclusion is valid not only for FF but also for RL chain molecules. Once again, this is consistent with the larger cohesive energy in systems formed by long chains. As can be seen from Fig. 12.5, an essentially linear behavior is found for the range of temperatures considered here, with a slight curvature close to the critical point for each system. The effect of chain length on the slope of the surface tension curves is remarkable. At a given temperature, this slope becomes less negative as m is increased, a trend which is also exhibited by FFLJ chains [13, 14], as well as by the first members of the n-alkane series. [199] The same qualitative behavior has been previously found by Bryk and collaborators [200] and a previous work [144].

But probably the most important conclusion of Fig. 12.5 is the effect of flexibility of similar molecular models, i.e., LJ chains formed from the same number of monomeric units, on the vapor-liquid surface tension. As can be seen clearly, the surface tension increases as the flexibility decreases. In other words, the surface tension of RL molecules is larger than that of FF chains. This is especially noticeable as the chain length increases (particularly for molecules formed from four and five segments). Unfortunately, as we have explained several times along the manuscript, no computer simulation data is available in the literature for RLLJ chains formed by six or more LJ spherical units.

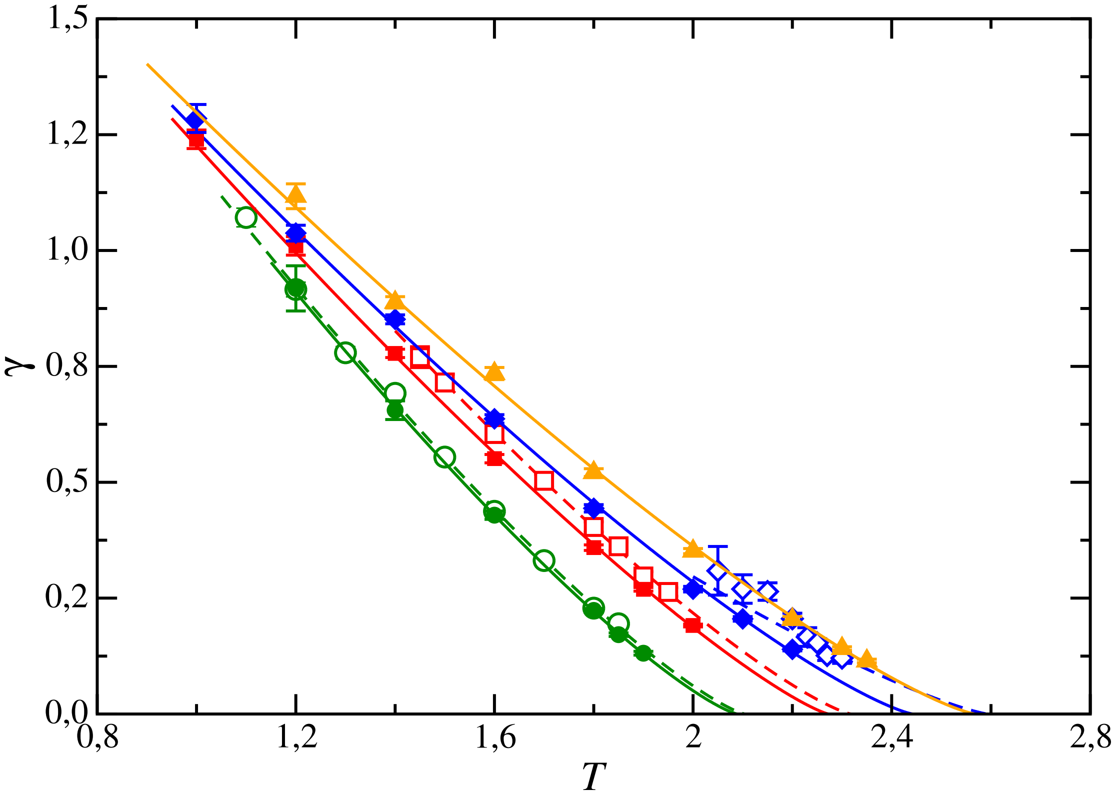

Figura 12.5: Surface tension as a function of the temperature for FF (continuous and filled symbols) and RL (dashed curves and open symbols) LJ chains. The green, red, blue and orange colors correspond to the surface tension obtained from the MC NVT simulations for chains lengths of $m = 3$, $m = 4$, $m = 5$, and $m = 6$, respectively. The open symbols correspond to the surface tension obtained by Blas and *et al.* [144]. The curves represent the fits of the simulation data to the scaling relationship of the surface tension near the critical point given by Eq. (12.16) with $\mu = 1.258$.

Similar to the case of long FF [13, 14] and short RL [144] LJ chains, the computed values of the surface tension allow us to obtain an independent estimate of the critical temperature for each chain length from the scaling relation

$$\gamma = \gamma_0 \left(1 - T/T_c\right)^{\mu} \ , \tag{12.16}$$

where γ is the surface tension at temperature T, γ_0 is the "zero-temperature" surface tension, μ is the corresponding critical exponent, and T_c is the critical temperature. Here, we fix μ to the universal value of $\mu = 1.258$ as obtained from renormalization-group theory. [5] Our estimates for the critical temperatures are collected in Table 12.2. The overall agreement between these values and those obtained from an analysis of the coexistence densities is satisfactory. It is also possible to compare these results with predictions obtained previously by Blas *et al.* [144] corresponding to the RLLJ molecular chain model. As can be seen in Table 12.2, the same conclusion obtained previously form the analysis of the coexistence densities is also observed here: the main effect of flexibility on the critical point is to decrease the critical temperature of the chain model, with the same number of monomeric units, with respect to that of the rigid one.

It is interesting to mention here that, although the surface tension values of FF and RL chains are different, at the same temperature and for molecules formed from the same number of monomeric units, we have recently found [143] that it is possible to find a universal scaling relationship to correlate short- and long-chains molecules with different degrees of flexibility and interacting through different intermolecular potentials (Lennard-Jones and square-well potentials).

Before presenting the conclusions of this work, it is interesting to comment some issues about the scaling properties we have investigated. In particular, we have considered scaling relationships for the vapor-liquid and interfacial tension but no for the interfacial width. As it is well-known, in the van der Waals theory of interfaces, the interfacial width is readily identified with the bulk correlation length. Accordingly, we could try to test the expected scaling law for the correlation length $\xi \propto t^{-\nu}$, where $t = 1 - T/T_c$, using our data for the interfacial width. However, the van der Waals theory, as other mean field theories, miss the role of capillary waves. Such waves result in an interfacial broadening which is larger than the bulk correlation length and depends on the system size. Indeed, it is expected that the interfacial width obeys $\xi^2 = \xi_0^2 + \xi_{\rm cw}^2$, where ξ_0 is the bulk correlation length, which scales as $t^{-\nu}$, while an additional interfacial broadening stemming from capillary waves is $\xi_{\rm cw}^2 = k_B T/2\pi\gamma_{\rm lv} \ln Lq_{\rm max}$, where $q_{\rm max}$ is an upper wave–vector cutoff. Accordingly, the scaling form of the interfacial width is governed by both ν and $\mu \approx 2\nu$. Far away from the critical point, clearly terms of order $t^{-\nu}$, will be important, but close to the critical point a divergence of order $t^{-\mu}$ should occur. Unfortunately, the analysis of the data obtained from simulations does not give conclusive results.

12.5 Conclusion

We have determined the interfacial properties of the vapor-liquid interface of short FFLJ chains formed from tangentially bonded monomers. Chains formed by three, five, and six monomers are considered. The intermolecular monomer-monomer interactions are truncated at a cutoff distance of three times the segment size of the monomers forming the chains. We use an improved version of the Janeček methodology proposed recently by MacDowell and Blas that allows to evaluate the long-range corrections to the potential energy as an effective pairwise intermolecular potential, without need of the explicit calculation of the current density profile along the simulation. We use Monte Carlo *NVT* simulations of the inhomogeneous system containing two vapor-liquid interfaces. The surface tension is evaluated using the Test-Area (TA) approach. We have examined the density profiles, interfacial thickness, and surface tension in terms of the temperature and the number of monomers forming the chains. In addition, we have also calculated the coexistence phase envelope, including the location of the critical point from an analysis of the density profiles and the surface tension. In addition to that, we have compared the results obtained with those corresponding to RLLJ chains formed from the same number of monomeric segments previously determined in the literature.

The effect of the chain length on the density profiles, coexistence densities, critical temperature and density, interfacial thickness, and surface tension has been investigated. The vapor-liquid interface is seen to sharpen with increasing chain length corresponding to an increase in the width of the coexistence phase envelope, and an accompanying increase in the surface tension. The vapor-liquid surface tension of RLLJ chains is seen to exhibit a universal scaling behavior when is appropriately reduced with respect to the chain length and critical density and temperature, and represented as a function of the difference between the vapor and liquid coexistence densities (relative to the critical point) [143].

Comparison between predictions for FFLJ and RLLJ with the same number of monomeric segments indicates that the flexibility of the chains affect both vapor-liquid coexistence and interfacial properties. In particular, from the thermodynamic point of view, the difference between the liquid and vapor coexistence densities decreases when passing from a RL to FF chain, with a decrease of the critical temperature and a decrease of the critical density. From the point of view of the interfacial properties, the density profiles become smoother along the interfacial region as the flexibility is increased, with the corresponding enlargement of the region in which the liquid changes continuously to vapor. This increasing of interfacial thickness produces a small decrease of the vapor-liquid surface tension for short chains, which becomes larger as the chain length is increased.

ACKNOWLEDGMENT

The authors would like to acknowledge helpful discussions with C. Vega, A. Galindo, J. M. Míguez, and M. M. Piñeiro. This work was supported by Ministerio de Ciencia e Innovación (MICINN, Spain) through Grants Nos. FIS2011-13119-E, FIS2010-14866 (FJB and FJMR), and FIS2010-22047-C05-05 (LGMD). Further financial support from Proyecto de Excelencia from Junta de Andalucía (Grant No. P07-FQM02884), Comunidad Autónoma de Madrid (Grant No. MODELICO-P2009/EPS-1691), and Universidad de Huelva are also acknowledged.

Capítulo 13

Interfacial properties of binary mixtures of square-well molecules from Monte Carlo simulation

The Journal of Chemical Physics (Submitted-2015)

F. J. Martínez-Ruiz[1] and F. J. Blas[1]

[1]Laboratorio de Simulacón Molecular y Química Computacional, CIQSO-Centro de Investigación en Química Sostenible and Departamento de Física Aplicada, Universidad de Huelva, 21071 Huelva, Spain

We determine the interfacial properties of mixtures of spherical square-well molecules from direct simulation of the vapor-liquid interface. We consider mixtures with the same molecular size and intermolecular potential range but different dispersive energy parameter values. We perform Monte Carlo simulations in the canonical ensemble to obtain the interfacial properties of mixtures of SW. In particular, we determine the pressure tensor using the mechanical (virial) route and the vapor-liquid interfacial tension evaluated using the Irving-Kirkwood method. In addition to the pressure tensor and the surface tension, we also obtain density profiles, coexistence densities, and interfacial thickness as functions of pressure, at a given temperature. According to our results, the main effect of increasing the ratio between the dispersive energy parameters of the mixture, $\epsilon_{22}/\epsilon_{11}$, is to sharpen the vapor-liquid interface and to increase the width of the biphasic coexistence region. Particularly interesting is the presence of a relative maximum in the density profiles of the less volatile component at the interface. This maximum is related with adsorption or accumulation of these molecules at the interface, since there are stronger attractive interactions between these molecules in comparison with the rest of intermolecular interactions. In addition to that, the interfacial thickness decreases and the surface tension increases as $\epsilon_{22}/\epsilon_{11}$ is larger, a direct consequence of the increasing of the cohesive energy of the system.

13.1 Introduction

Knowledge of interfacial properties of mixtures is essential in a large number of scientific and engineering fields, including nucleation or dynamics of phase transition, among many others [5]. From a formal point of view, understanding how microscopic parameters (for instance, molecular size and dispersive energy interactions) determine the thermodynamic and structural behavior of mixtures near interfaces is one of the classical problems in applied Statistical Mechanics and computer simulation. Recently, researchers of the liquid-state community have applied theories of inhomogeneous systems, with particular emphasis on computer simulation, to determine the interfacial properties of many different systems. Unfortunately, studies involving fluid mixtures is far less common.

Surface tension is probably the most challenging property to be determined and predicting using molecular-based theories and simulation techniques. Despite the number of studies carried out since computer simulation is used routinely for determining the properties of a molecular model, the calculation of surface tension is still a subtle problem. The ambiguity in the definition of the microscopic components of the pressure tensor [4, 73], the finite size effects due to capillary waves [119, 120], or the difficulty for the calculation of the dispersive long-range corrections (LRC) associated to the intermolecular interactions [14, 15], make the calculation of surface tension a difficult and non-trivial problem.

The usual procedure to the evaluation of the planar fluid-fluid interfacial tension in a molecular simulation involves the determination of the microscopic components of the pressure tensor through the well-known mechanical or virial route. This route states that surface tension of a planar fluid-fluid interface can be readily obtained from the integration of the difference between the normal and tangential microscopic components of the pressure tensor profiles along the interface. This method generally involves an ensemble average of the virial of Clausius according to the recipes of Irving and Kirkwood [62]. Although the mechanical route is an appropriate technique for determining the surface tension, the application of this methodology presents some technical problems when dealing with systems that interact through discontinuous intermolecular potentials.

The simplest system that exhibits vapor-liquid coexistence is probably that formed from molecules that interact through the well-known square-well (SW) intermolecular potential. This intermolecular potential is characterized by two length scales, the hard-sphere diameter, σ, and the potential range, λ. This potential is discontinuous at $r = \sigma$, the contact length between two SW molecules, and at $r = \lambda\sigma$, the distance at which the potential vanishes. It is certainly possible to evaluate the pressure (in bulk systems) and the components of the pressure tensor at the vapor-liquid interface, using the standard mechanical or virial route. The Irving and Kirkwood technique involves the evaluation of the virial, and hence, the intermolecular forces between the molecules. The contribution to the virial in systems interacting through discontinuous potentials could be dominated by the impulsive forces that appear at these discontinuities. In the particular case of systems interacting through the SW intermolecular potential, the contribution to the pressure arise, apart from the ideal part, from the impulsive forces between molecules separated at the distances $r = \sigma$ and $\lambda\sigma$. The pressure can be determined evaluating these discontinuities directly, as Orea *et al.* [49] demonstrated several years ago, but also using a simple extension of the elegant and standard approach of counting overlaps produced by an isotropic volume scaling [50, 94, 201–203].

The goal of this work is to determine the vapor-liquid interfacial properties of mixtures of spherical SW molecules with the same molecular size and intermolecular potential range but different dispersive energy parameters. In particular, we focus on the effect of the dispersive energy ratio on different interfacial properties, including density profiles, normal and tangential microscopic components of the pressure tensor profiles, and surface tension. In addition to that, we also analyze the effect of the dispersive energy ratio on other thermodynamics properties, such as coexistence density and pressure-composition slices of the phase diagram. To our knowledge, this is the first time the surface tension and components of the pressure tensor of mixtures of SW spheres are calculated using the mechanical route of Irving and Kirkwood.

The rest of the paper is organized as follows. In Section 13.2 we present the model and simulation details of this work. Results obtained are discussed in Section13.3. Finally, in Section 13.4 we present the main conclusions.

13.2 Model and simulation details

We consider binary mixtures of spherical SW molecules characterized by diameters σ_{ii}, dispersive energies ϵ_{ii}, and intermolecular potential ranges λ_{ii}, where index i denotes component i. The interaction potential between two different molecules of species i and j is given by,

$$u_{ij}^{SW}(r) = \begin{cases} +\infty & r < \sigma_{ij} \\ -\epsilon_{ij} & \sigma_{ij} \leq r \leq \sigma_{ij} \\ 0 & r > \sigma ij \end{cases} \tag{13.1}$$

where r is the distance between two molecules, and σ_{ij}, ϵ_{ij}, and λ_{ij} are the intermolecular parameters (size, dispersive energy, and intermolecular potential range, respectively) associated to the interaction between molecules of type i and j. In this work, we use the well-known Lorentz-Berthelot combining rules for unlike dispersive interactions,

$$\sigma_{ij} = \frac{\sigma_{ii} + \sigma_{jj}}{2} \tag{13.2}$$

and

$$\epsilon_{ij} = (\epsilon_{ii}\epsilon_{jj})^{1/2} \tag{13.3}$$

In addition to that, λ_{ij} follows the combining rule given by,

$$\lambda_{ij} = \frac{\sigma_{ii}\lambda_{ii} + \sigma_{jj}\lambda_{jj}}{\sigma_{ii} + \sigma_{jj}} \tag{13.4}$$

We examine mixtures interacting with several interaction dispersive parameter values $\epsilon_{22}/\epsilon_{11}$, and with the same size $\sigma_{11} = \sigma_{22} = \sigma_{12} \equiv \sigma$ and intermolecular potential range $\lambda_{11} = \lambda_{22} = \lambda_{12} \equiv \lambda$. The number of molecules, N, used in the simulations performed in this work for studying the vapor-liquid interface of mixtures of SW molecules varied from $N = 2248$, for the lowest pressure considered ($P^* = P\sigma_{11}^3/\epsilon_{11} \approx 0.015$), to $N = 2748$, for the highest pressure analyzed ($P^* = P\sigma_{11}^3/\epsilon_{11} \approx 0.057$).

As we have discussed previously in our previous works [151,204], it is not possible to have systems with the same total number of molecules and with the same interfacial area since we are dealing with binary mixtures in which composition must be taken into account. Following our previous works, we use the original SAFT-VR approach, based on Wertheim's Thermodynamic Perturbation Theory [17–20], and developed by Jackson and coworkers [205,206], to calculate the complete phase diagrams of the mixtures to be studied. This allows to have an initial picture of the initial densities and compositions of each component of the mixture in both phases (vapor and liquid), as predicted from the SAFT-VR approach for the mixtures considered in this work.

Similarly as we have done in our recent works, simulations are performed in two steps. In the first step, homogeneous liquid and vapor systems, at a given temperature and density, are equilibrated in a rectangular simulation box of dimensions $L_x = L_y = 12\sigma$, and varying L_z. Box length measured along the z-axis is chosen in such a way that the corresponding densities match the predictions obtained from the SAFT-VR approach at temperature and approximated pressure selected. In addition to that, the particular number of molecules of each species, in both liquid and vapor phases, are also selected according to the SAFT predictions. Both simulation boxes (liquid and vapor) are equilibrated at the same temperature and with the corresponding liquid and vapor densities using an NVT ensemble in which L_x and L_y have the same values for all the simulation boxes considered, and L_z has the appropriate values according to the state to be simulated. NVT simulations of homogeneous phases are organized by cycles. A cycle is defined as N trial moves (displacement of the center of mass). The magnitude of the appropriate displacement is adjusted so as to get an acceptance rate of $30\,\%$ approximately. We use periodic boundary conditions and minimum image convention in all three directions of the simulation box.

In a second step, the interfacial simulation box is prepared leaving the previous homogeneous liquid phase at the center of the new box with the same homogeneous vapor phase boxes of equal size previously prepared at each side. Since L_x and L_y ($\mathcal{A} = L_x L_y$, i.e., the interfacial area) are the same for all homogeneous phases, it is always possible to build up the interfacial simulation box as explained here. The final overall dimensions of the vapor-liquid-vapor simulation box are therefore $L_x = L_y = 12\sigma$, and $L_z = 97.1\sigma$ for the lowest pressure considered ($P^* = k_B T/\epsilon_{11} \approx 0.015$), and $L_z = 101.8\sigma$ for the highest pressure ($P^* = k_B T/\epsilon_{11} \approx 0.057$).

The simulations for studying the vapor-liquid interface are also organized in cycles. In this case, a cycle is defined as N trial moves (displacement of the center of mass) and the magnitude of the appropriate displacement is adjusted so as to get an acceptance rate of $30\,\%$ approximately. We use periodic boundary conditions and minimum image convention in all three directions of the simulation box.

We have obtained the normal and tangential components of the pressure tensor from the mechanical expression or virial route,

$$P_{\alpha\beta} = \left\langle \rho k_B T \right\rangle + \left\langle \frac{1}{V} \sum_{i=1}^{N-1} \sum_{j=i+1}^{N} r_{ij}^{\alpha} f_{ij}^{\beta} \right\rangle \tag{13.5}$$

In this work, we have followed the same procedure as in our previous work [142] and used the well-known Irving and Kirkwood (IK) recipe [62, 63] for determining the microscopic components of the pressure tensor, $P_N(z) \equiv P_{zz}(z)$ and $P_T(z) \equiv P_{xx}(z) \equiv P_{yy}(z) \equiv \frac{1}{2}(P_{xx}(z) + P_{yy}(z))$. Since the SW potential is discontinuous, we have followed the extension of the methodology proposed by Allen and de Miguel and Jackson [50, 201] for determining the components of the pressure tensor, based on the seminal work of Eppenga and Frenkel [94] for calculating the pressure in bulk system. In particular, we consider 200 slabs perpendicular to the simulation box (z-axis) at which we evaluate the microscopic components of the pressure tensor using the extension of the approach of counting overlaps produced by independent volume scaling along the three directions of the simulation box. We use ten different values of the virtual scaling magnitude $\xi = \Delta V/V$, in the range $0.005 \leq |\xi| \leq$

0.030. The final values of the microscopic components of the pressure tensor presented in this paper correspond to the extrapolated values, at every slab of the simulation box, as determined by a linear extrapolation to $|\xi| \to 0$ of the values obtained from the corresponding independent volume scaling along the three directions of the space.

Surface tension is determined using the mechanical definition that involves the integration of the difference between the tangential and normal microscopic components of the pressure tensor profiles, as obtained from the IK methodology, along the simulation box according to,

$$\gamma = \int_0^{L_z} \left(P_N(z) - P_T(z) \right) \, dz \tag{13.6}$$

Note that here we have chosen the z-axis perpendicular to the interface and the integral is performed along the total length L_z of the simulation box.

We typically consider nine reduced pressures in the range $P^* = P\sigma_{11}^3/\epsilon_{11} \approx 0.015$ up to 0.057, approximately. In the case of NVT simulations of the homogeneous liquid and vapor phases prepared in the first step, each simulation box is equilibrated for 20×10^6 MC cycles. In the case of the NVT simulations corresponding to the interfacial box, the system is also well equilibrated for other 10×10^6 equilibration MC cycles. In addition to that, averages are determined over a further period of 40×10^6 MC cycles. The production stage is divided into M blocks. Normally, each block is equal to 10^6 MC cycles. The ensemble average of the macroscopic components of the pressure tensor and the surface tension is given by the arithmetic mean of the block averages and the statistical precision of the sample average is estimated from the standard deviation in the ensemble average from $\overline{\sigma}/\sqrt{M}$, where $\overline{\sigma}$ is the variance of the block averages, and $M = 40$ in all cases.

All the quantities in our paper are expressed in conventional reduced units of component 1, with σ_{11} and ϵ_{11} being the length and energy scaling units, respectively. Thus, the temperature is given in units of ϵ_{11}/k_B, the densities of both components and the total density in units of σ_{11}^{-3}, the bulk pressure and components of the pressure tensor in units of the $\epsilon_{11}/\sigma_{11}^3$, the surface tension in units of $\epsilon_{11}/\sigma_{11}^2$, and the cutoff distance and interfacial thickness in units of σ_{11}.

13.3 Results and discussion

In this section we present the main results from simulations of the vapor-liquid interface of mixtures of spherical SW molecules. We focus mainly on the effect of the dispersive energy interaction between the components of the mixture on several interfacial properties. We have determined the components of the pressure using the mechanical (or virial) route. As in our recent papers [142,151,204], we have also examined several coexistence properties, such as coexistence densities, and also other interfacial properties, including density profiles, interfacial thickness, and surface tension.

We first analyze the effect of the dispersive energy parameter between components of the mixtures on density profiles. We follow the same analysis and methodology than in our previous works [13,14, 142–145] and consider different dispersive energy parameters and pressures. The equilibrium density profiles of each of components of the mixture, $\rho_1(z)$ and $\rho_2(z)$, as well as the total density, $\rho(z) = \rho_1(z) + \rho_2(z)$, are computed from averages of the histogram of densities along the z direction over the production stage. The bulk vapor and liquid densities of both components and the total density are obtained by averaging $\rho_1(z)$, $\rho_2(z)$, and $\rho(z)$, respectively over appropriate regions sufficiently

Tabla 13.1: Liquid density, $\rho^{(L)}$, vapor density, $\rho^{(V)}$, liquid density of component 1, $\rho_1^{(L)}$, vapor density of component 1, $\rho_1^{(V)}$, molar fraction of component 1 in the liquid phase $x_1^{(L)}$, molar fraction of component 1 in the vapor phase $x_1^{(V)}$, liquid density of component 2, $\rho_2^{(L)}$, and vapor density of component 2, $\rho_2^{(V)}$ at $T = 1.2$ and different pressures P_{zz}, for mixtures of SW molecules with the same molecular size, potential interaction range, but different dispersive energy parameters, $\epsilon_{22}/\epsilon_{11}$. All quantities are expressed in the reduced units defined in Section 13.2. The errors are estimated as explained in the text.

P_{zz}	$\rho^{(L)}$	$\rho^{(V)}$	$\rho_1^{(L)}$	$\rho_1^{(V)}$	$x_1^{(L)}$	$x_1^{(V)}$	$\rho_2^{(L)}$	$\rho_2^{(V)}$
				$\epsilon_{22}/\epsilon_{11} = 1.5$				
0.01721(22)	0.71702(3)	0.01548(3)	0.09078(10)	0.00967(3)	0.12661(15)	0.624(3)	0.62624(12)	0.005818(21)
0.0219(3)	0.70957(9)	0.02036(7)	0.13147(14)	0.01452(4)	0.18528(23)	0.712(3)	0.57811(21)	0.005849(20)
0.0261(3)	0.70079(4)	0.02517(8)	0.17623(7)	0.01936(6)	0.25147(11)	0.769(5)	0.52456(10)	0.00581(3)
0.0313(3)	0.69082(3)	0.03072(8)	0.22220(5)	0.02477(6)	0.32165(9)	0.806(4)	0.46861(6)	0.00595(3)
0.0363(3)	0.67984(4)	0.03716(13)	0.26643(11)	0.03115(11)	0.39190(18)	0.838(6)	0.41341(14)	0.00602(4)
0.04116(20)	0.66637(4)	0.04321(5)	0.31271(13)	0.03720(7)	0.46927(22)	0.861(3)	0.35366(16)	0.006012(23)
0.0466(3)	0.65212(4)	0.05084(9)	0.35513(9)	0.04496(7)	0.54458(18)	0.884(3)	0.29698(13)	0.00588(3)
0.0516(3)	0.63506(17)	0.05865(9)	0.39514(14)	0.05295(9)	0.6222(4)	0.903(3)	0.2399(3)	0.00570(21)
0.0566(3)	0.61609(6)	0.06767(20)	0.42869(4)	0.06237(18)	0.69581(13)	0.922(5)	0.18741(8)	0.00530(3)
				$\epsilon_{22}/\epsilon_{11} = 1.75$				
0.0160(3)	0.75618(5)	0.01435(3)	0.09173(11)	0.01277(3)	0.12131(15)	0.890(4)	0.66445(14)	0.001570(22)
0.0205(3)	0.75007(5)	0.01866(4)	0.12641(11)	0.01688(4)	0.16853(16)	0.905(5)	0.62365(13)	0.001777(12)
0.0258(3)	0.74322(4)	0.02381(5)	0.16243(10)	0.02196(5)	0.21855(15)	0.922(4)	0.58079(13)	0.001854(11)
0.0302(3)	0.73419(4)	0.02912(7)	0.20496(14)	0.02711(6)	0.27916(21)	0.931(4)	0.52923(17)	0.002004(16)
0.0355(3)	0.72410(6)	0.03498(7)	0.24779(21)	0.03302(7)	0.3422(3)	0.944(4)	0.4763(3)	0.001960(14)
0.0405(3)	0.70984(20)	0.04130(8)	0.3007(6)	0.03929(9)	0.4236(10)	0.951(4)	0.4091(8)	0.002007(11)
0.0460(3)	0.6913(8)	0.04868(13)	0.3525(5)	0.04662(12)	0.5098(14)	0.958(5)	0.3388(14)	0.002055(17)
0.0514(3)	0.67341(12)	0.05615(23)	0.40128(11)	0.05409(22)	0.5959(3)	0.963(8)	0.27213(22)	0.002061(23)
0.0572(3)	0.65035(13)	0.06646(19)	0.44382(14)	0.06432(17)	0.6824(3)	0.968(5)	0.2065(3)	0.002139(19)
				$\epsilon_{22}/\epsilon_{11} = 2.0$				
0.0150(3)	0.79107(7)	0.01294(6)	0.05593(18)	0.01240(6)	0.07070(24)	0.958(10)	0.73514(24)	0.000536(8)
0.0188(3)	0.78748(4)	0.01661(3)	0.07748(11)	0.01612(3)	0.09839(15)	0.970(4)	0.70999(14)	0.000496(8)
0.0232(3)	0.78364(5)	0.02109(6)	0.09928(12)	0.02055(6)	0.12670(16)	0.974(5)	0.68436(15)	0.000537(10)
0.02748(18)	0.77811(4)	0.02501(7)	0.13033(22)	0.02448(6)	0.1675(3)	0.978(5)	0.6478(3)	0.000528(9)
0.0324(3)	0.77210(17)	0.03100(14)	0.1594(4)	0.03032(14)	0.2065(6)	0.978(9)	0.6126(6)	0.000687(11)
0.0384(3)	0.76547(9)	0.03763(16)	0.1934(3)	0.03697(15)	0.2526(4)	0.982(8)	0.5721(4)	0.000665(11)
0.0435(3)	0.75244(10)	0.04493(5)	0.2480(4)	0.04421(5)	0.3296(5)	0.9840(24)	0.5044(4)	0.000719(8)
0.0500(3)	0.73252(19)	0.05421(14)	0.3192(5)	0.05333(14)	0.4358(8)	0.984(5)	0.4133(6)	0.000883(12)
0.0561(3)	0.6999(3)	0.06312(15)	0.4053(4)	0.06225(14)	0.5790(10)	0.986(4)	0.2947(8)	0.000876(17)

removed from the interfacial region. This procedure is meaningful as far as the central liquid slab is thick enough. The bulk vapor densities are obtained after averaging the corresponding density profiles on both sides of the liquid film. The statistical uncertainty of these values is estimated from the standard deviation of the mean values. Following our previous works [142, 151, 204], additional interfacial properties, such as the position of the Gibbs-dividing surface, z_0, and the $10-90$ interfacial thickness, t, are obtained by fitting each of the equilibrium density profiles to hyperbolic tangent functions [5] (see Eq. (3) of our previous work [13] for further details). We fix liquid, ρ_L, and vapor, ρ_V, densities for each component and for the total density to previously computed values and treat z_0 and t as adjustable parameters. Our simulation results for the bulk densities of each component, total densities, molar fractions of both component in each, components of the pressure tensor, surface tension, and interfacial thickness for mixtures of SW molecules interacting with different dispersive energy parameters and the full potential, at different pressures, are collected in Table 13.1.

We show in Fig. 13.1 the density profiles $\rho_1(z)$, $\rho_2(z)$, and $\rho(z)$ for three mixtures of SW molecules with different dispersive energy parameters of the component 2, $\epsilon_{22}/\epsilon_{11} = 1.50$, 1.75, and 2.00, at $T = 1.2$ and several pressures. For the sake of clarity, we only present one half of the profiles corresponding to one of the interfaces. Also for convenience, all density profiles have been shifted along

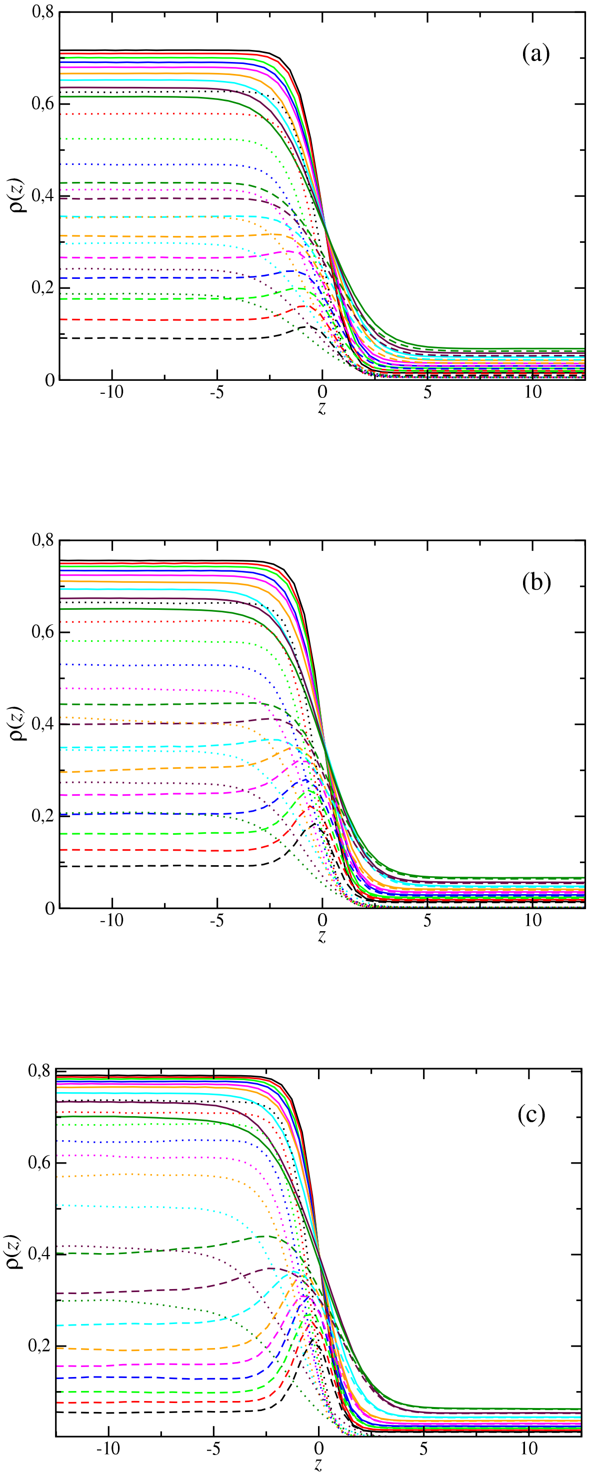

Figura 13.1: Simulated equilibrium total density profiles (continuous curves), density profiles of component 1 (dotted curves), and density profiles of component 2 (dashed curves) across the vapor-liquid interface of mixtures of spherical SW molecular with the same molecular size and dispersive energy ratio $\epsilon_{22}/\epsilon_{11} = 1.5$ (a), 1.75 (b), and 2.0 (c). $T = 1.2$ and pressures of systems in (a), (b), and (c) are equal to, from top to bottom in the liquid phases, to those presented in Table 13.1 for each value of the dispersive energy ratio $\epsilon_{22}/\epsilon_{11}$, respectively.

Tabla 13.2: Tangential components of the macroscopic pressure tensor, P_{xx} and P_{yy}, normal component of the macroscopic pressure tensor, P_{zz} calculated from the virial route, and surface tension calculated from the mechanical route, at $T = 1.2$ and different pressures for mixtures of SW molecules with the same molecular size, potential interaction range, but different dispersive energy parameters, $\epsilon_{22}/\epsilon_{11}$. All quantities are expressed in the reduced units defined in Section 13.2. The errors are estimated as explained in the text.

P_{xx}	P_{yy}	P_{zz}	γ
$\epsilon_{22}/\epsilon_{11} = 1.5$			
0.00326(23)	0.00331(22)	0.01721(22)	0.679(5)
0.01012(22)	0.01027(23)	0.0219(3)	0.585(6)
0.0154(3)	0.0155(3)	0.0261(3)	0.524(6)
0.0222(3)	0.0225(3)	0.0313(3)	0.449(6)
0.0285(3)	0.0284(3)	0.0363(3)	0.394(6)
0.03432(23)	0.03441(23)	0.04116(20)	0.339(5)
0.0411(3)	0.04111(21)	0.0466(3)	0.283(4)
0.0473(3)	0.0473(3)	0.0516(3)	0.218(5)
0.05300(22)	0.05302(22)	0.0566(3)	0.181(5)
$\epsilon_{22}/\epsilon_{11} = 1.75$			
-0.00307(24)	-0.0030(3)	0.0160(3)	0.931(8)
0.0038(3)	0.0040(3)	0.0205(3)	0.825(5)
0.0112(3)	0.0112(3)	0.0258(3)	0.715(6)
0.0178(3)	0.01776(23)	0.0302(3)	0.623(6)
0.0249(3)	0.0250(3)	0.0355(3)	0.528(5)
0.0315(3)	0.0316(3)	0.0405(3)	0.442(6)
0.0388(3)	0.03883(23)	0.0460(3)	0.366(6)
0.0457(3)	0.0456(3)	0.0514(3)	0.296(5)
0.0526(3)	0.0526(3)	0.0572(3)	0.229(5)
$\epsilon_{22}/\epsilon_{11} = 2.0$			
-0.0112(3)	-0.0110(3)	0.0150(3)	1.270(7)
-0.0043(4)	-0.0043(3)	0.0188(3)	1.144(7)
0.0021(3)	0.00220(25)	0.0232(3)	1.021(7)
0.0094(3)	0.00932(22)	0.02748(18)	0.903(6)
0.0162(3)	0.0163(3)	0.0324(3)	0.800(7)
0.0250(3)	0.0249(3)	0.0384(3)	0.662(7)
0.0325(3)	0.0325(3)	0.0435(3)	0.549(7)
0.0415(3)	0.0415(3)	0.0500(3)	0.427(6)
0.0501(3)	0.0500(3)	0.0561(3)	0.294(5)

z so as to place z_0 at the origin. As can be seen, for a given mixture (or value of the dispersive energy parameter $\epsilon_{22}/\epsilon_{11}$), the slope (in absolute value) of the density profiles corresponding to component 1 and total density in the interfacial region decreases as the pressure is increased, making smaller the jump in densities when passing from the vapor to the liquid side of the interface. Consequently, the interfacial thickness increases, an expected behavior that indicates the phase envelope is becoming thicker as the system approaches to the critical point of the mixture.

Fig. 13.1 also shows the effect of increasing the dispersive energy parameter $\epsilon_{22}/\epsilon_{11}$ on the density profiles, i.e., when the mixture becomes more asymmetric. As can be seen comparing parts (a), (b), and (c) of the figure, an increase of $\epsilon_{22}/\epsilon_{11}$ results in steeper density profiles of component 1 and total density along the interfacial region. This effect, which also produces narrower interfacial regions, is related with the increasing of the asymmetry of the mixture. As $\epsilon_{22}/\epsilon_{11}$ becomes larger, the mixture is more asymmetric and the phase envelope (see Fig. 13.2) becomes wider in terms of densities (and also in molar fractions), or in other words, jumps in density and composition from the vapor to the liquid side of the interface increases.

It is important to put special attention on the behavior of the density profiles corresponding to the component 2 of the system, the less volatile substance of the mixture. As can be seen in Fig. 13.1a, $\rho_2(z)$ exhibits a nearly monotonic increasing behavior when passing from the vapor to the liquid size of the interface at high pressures. However, for pressures equal or lower that 0.0313 approximately, the density profile of the less volatile component exhibits a relative maximum at the interface. This relative maximum becomes more pronounced as the pressure of the system is decreased, as can been clearly seen in Fig. 13.1a. This effect is even magnified as the difference in dispersive energies between both components increases, $\epsilon_{22}/\epsilon_{11} = 1.75$ and 2.00. In these cases, at any pressure (even high pressures), $\rho_2(z)$ exhibits a relative maximum at the interface. This maximum is related with adsorption of component 2 at the interface. These molecules tend to accumulate at the interface on increasing the dispersive energy parameter of component 2 and decreasing of the pressure. This type of enhanced adsorption of one component relative to the other is usually seen in binary mixtures of spherical molecules when there are significant differences in the values of the unlike dispersion interactions [148].

We have also analyzed the equilibrium normal and tangential components of the microscopic pressure tensor profiles, $P_N(z)$ and $P_T(z)$, respectively, of the three SW mixtures. The profiles are computed from averages of histograms of pressures along the z direction over the production stage, according to the IK prescription explained in Section 13.2. As we have mentioned previously, this procedure is meaningful as far as the central liquid slab is thick enough. In addition to the methodology of IK, based on the mechanical route, we have also determined the macroscopic components of the pressure tensor. In particular, we have averaged the three components of the microscopic components of the pressure tensor, P_{xx} and P_{yy} (tangential components), and P_{zz} (normal component) obtained from the IK along the z-axis of the simulation box. Results are presented in Table 13.2.

We consider the normal and tangential components of the microscopic pressure tensor profiles at $T = 1.2$ and several pressures. As can be seen in Fig. 13.2-13.4, the components of the microscopic pressure tensor along the two vapor-liquid interfaces exhibit the expected behavior, i.e., the normal component of the pressure tensor profile is constant (within the expected statistical error) through the interface and equal to the vapor pressure of the system (according to the mechanical stability, that it requires the gradient of pressure tensor vanishes). The tangential component of the pressure tensor profile is approximately constant and equal to the normal pressure in the liquid and both vapor bulk-like regions of the simulation box, according to the behavior observed in parts (b) of Figs. 13.2-13.4. $P_T(z)$ becomes negative at the two interfacial regions of the system showing two (negative) local minima. As can be seen, negative contributions to the tangential pressure became more negative as the dispersive energy parameter $\epsilon_{22}/\epsilon_{11}$ is increased. This produces more tension along the interface, decreasing the interfacial thickness of the system (as previously shown in the density profiles of Fig. 13.1). As we will see later, this produces higher interfacial tension, in agreement with the results already presented. Finally, it is also interesting to analyze the difference between both components of the pressure, $P_N(z) - P_T(z)$: it is equal to zero in the bulk regions of the simulation box (the two vapor phases and the central liquid), away from the interfacial region, and it also shows two positive peaks centered around the two vapor-liquid interfaces at which $P_N(z) \neq P_T(z)$.

An interesting feature observed in the pressure profiles, also seen in other systems interacting with different intermolecular potentials, such as the pure Lennard-Jones (LJ) fluid and binary mix-

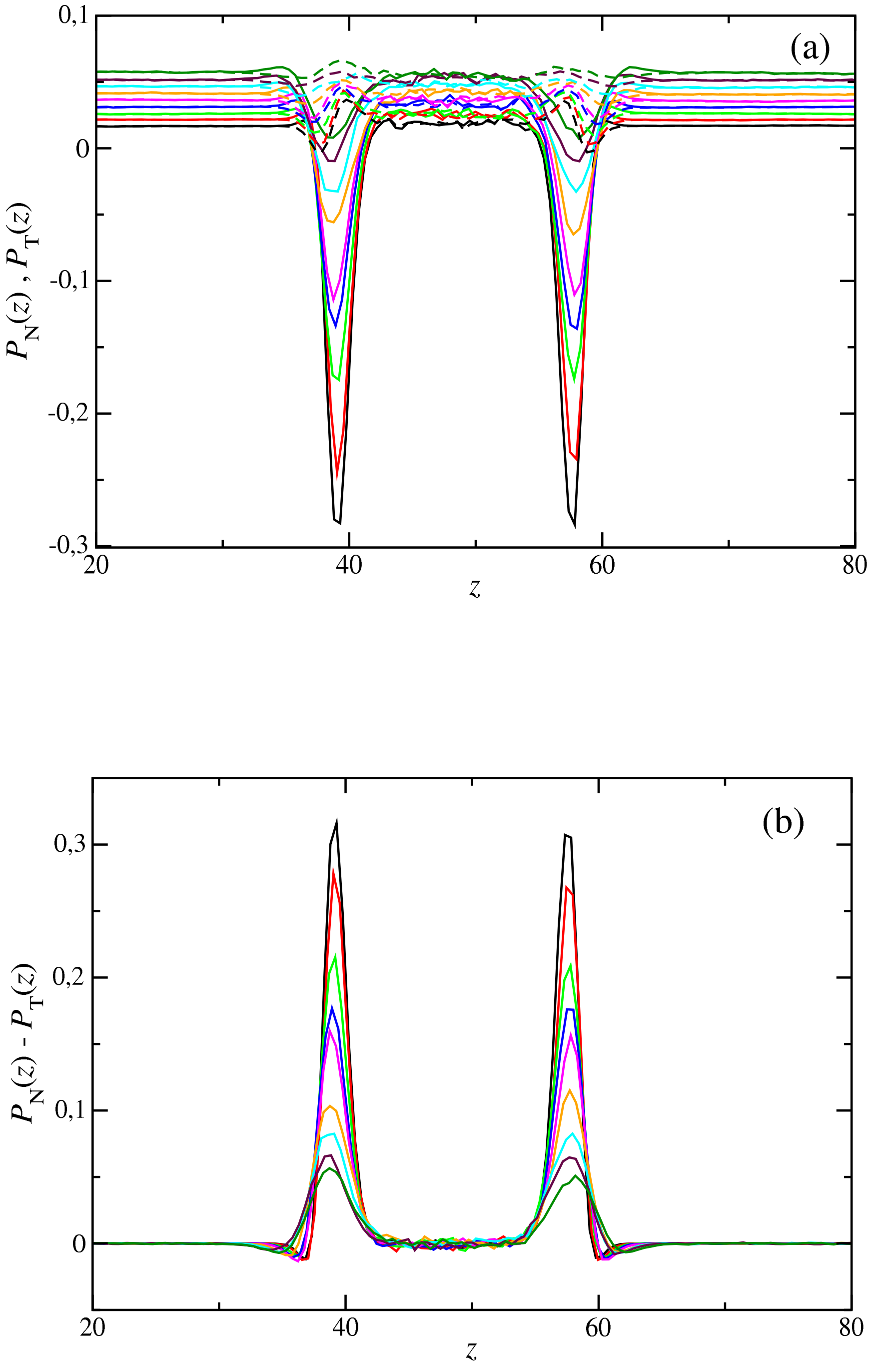

Figura 13.2: Normal $P_N(z)$ and tangential $P_T(z)$ (a), and difference between the normal and tangential microscopic components (b) of the pressure tensor profiles across the two vapor-liquid interfaces, from bottom to top in the vapor phase, at $T = 1.2$ and pressures $P = 0.01721$, 0.0219, 0.0261, 0.0313, 0.0363, 0.04116, 0.0466, 0.0516, and 0.0566, of a binary mixture of spherical SW molecules with the same molecular size and dispersive energy ratio $\epsilon_{22}/\epsilon_{11} = 1.5$. Continuous and dashed curves in part (a) correspond to the tangential and normal microscopic components of the pressure tensor, respectively.

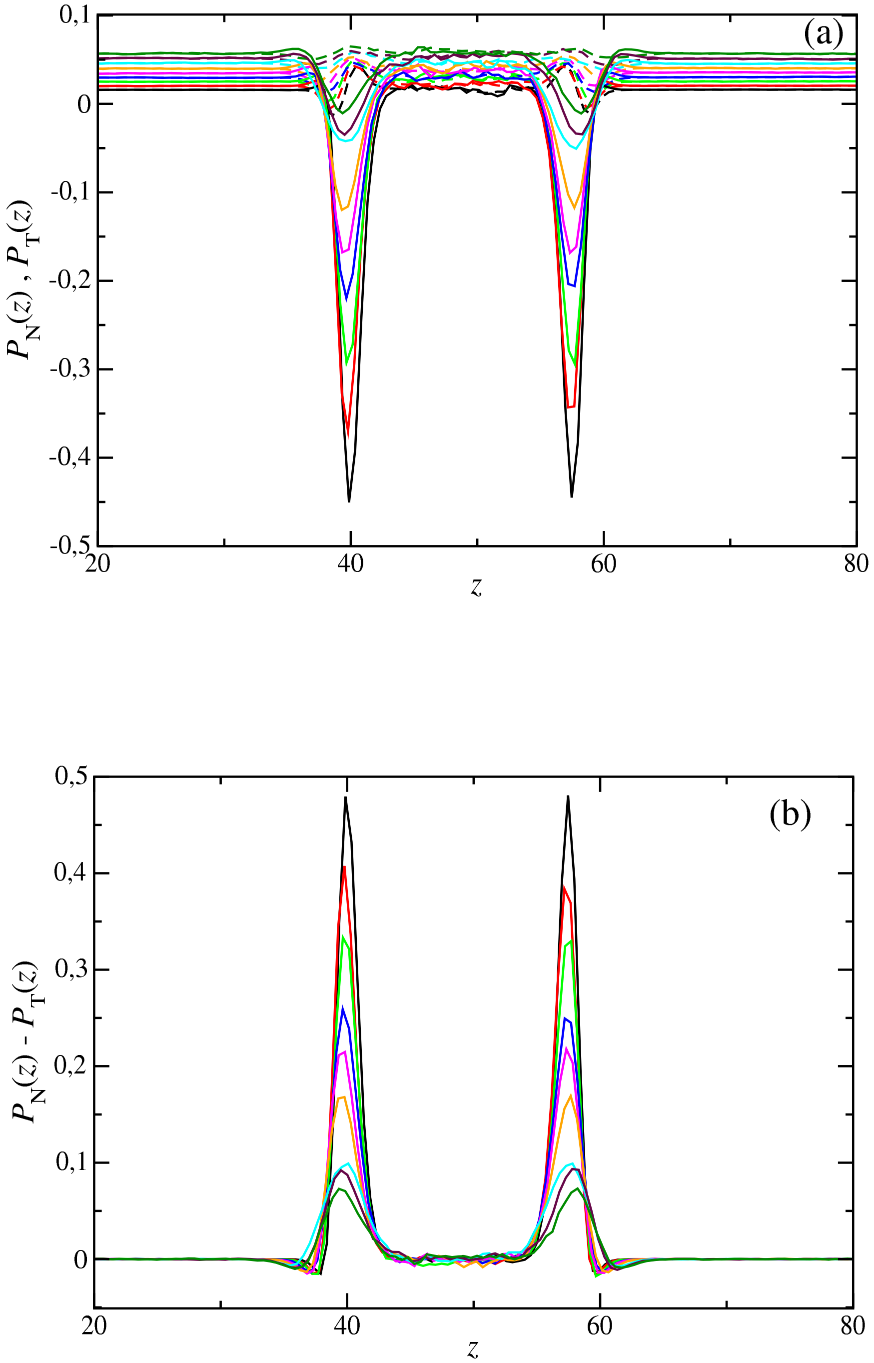

Figura 13.3: Normal $P_N(z)$ and tangential $P_T(z)$ (a), and difference between the normal and tangential microscopic components (b) of the pressure tensor profiles across the two vapor-liquid interfaces, from bottom to top in the vapor phase, at $T = 1.2$ and pressures $P = 0.0160$, 0.0205, 0.0258, 0.0302, 0.0355, 0.0405, 0.0460, 0.0514, and 0.0572, of a binary mixture of spherical SW molecules with the same molecular size and dispersive energy ratio $\epsilon_{22}/\epsilon_{11} = 1.75$. Continuous and dashed curves in part (a) correspond to the tangential and normal microscopic components of the pressure tensor, respectively.

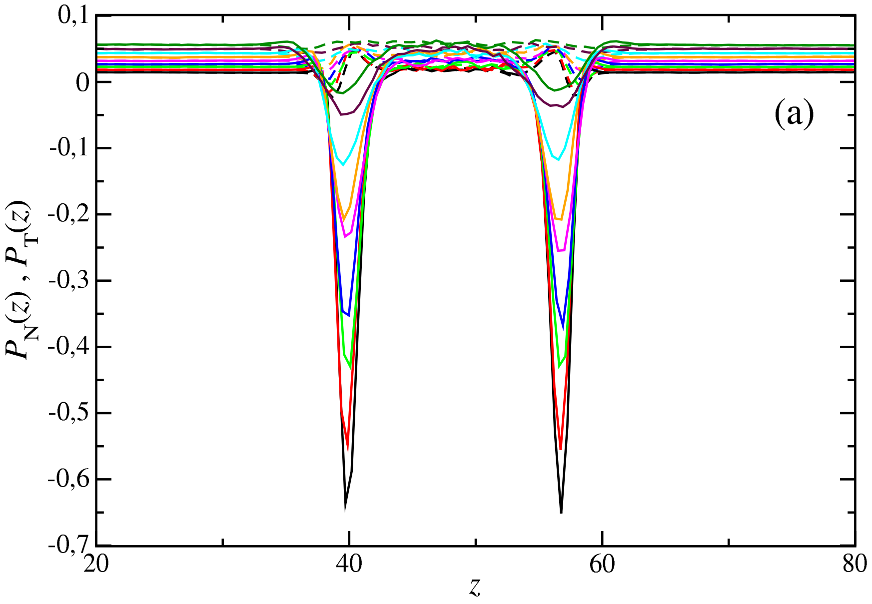

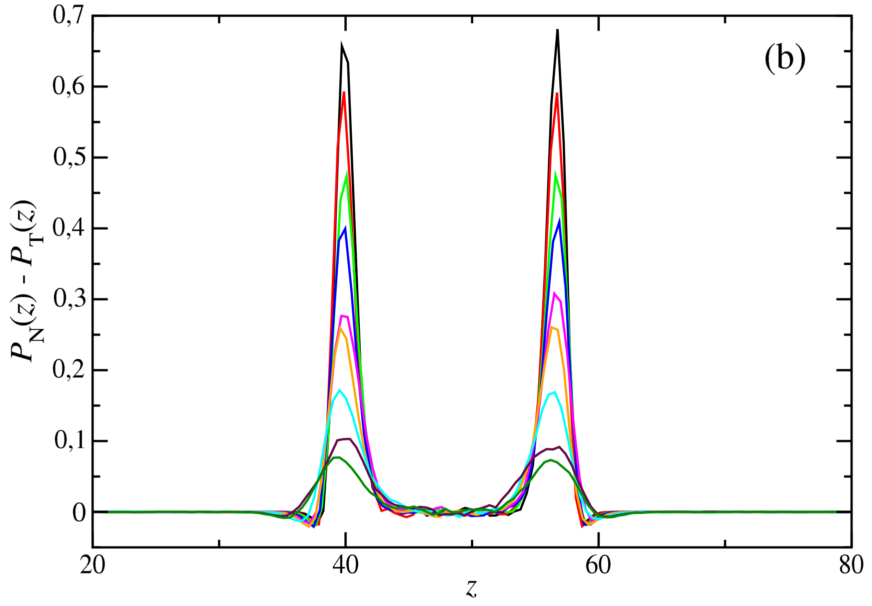

Figura 13.4: Normal $P_N(z)$ and tangential $P_T(z)$ (a), and difference between the normal and tangential microscopic components (b) of the pressure tensor profiles across the two vapor-liquid interfaces, from bottom to top in the vapor phase, at $T = 1.2$ and pressures $P = 0.0150$, 0.0188, 0.0232, 0.02748, 0.0324, 0.0384, 0.0435, 0.0500, and 0.0561, of a binary mixture of spherical SW molecules with the same molecular size and dispersive energy ratio $\epsilon_{22}/\epsilon_{11} = 2.0$. Continuous and dashed curves in part (a) correspond to the tangential and normal microscopic components of the pressure tensor, respectively.

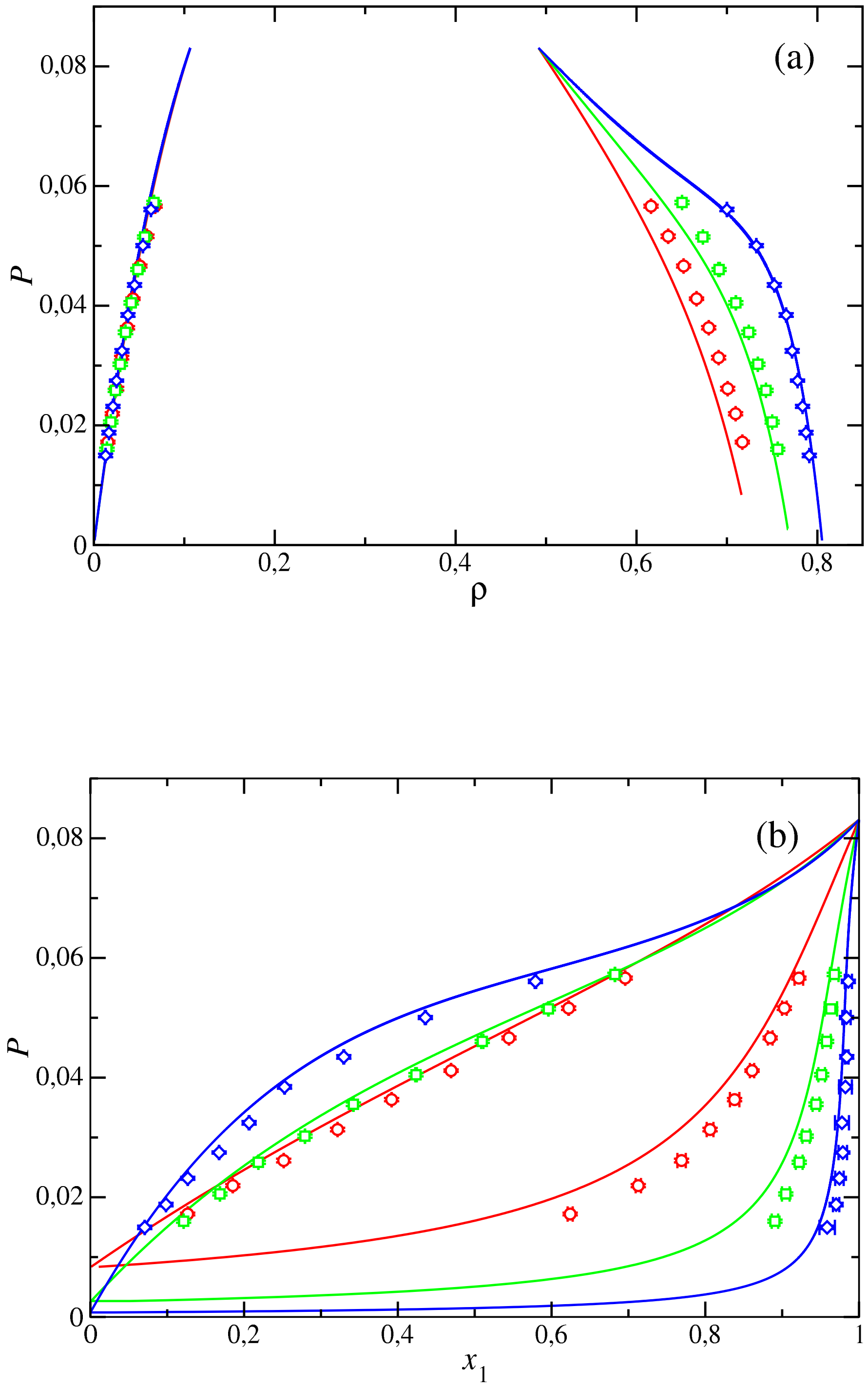

Figura 13.5: Pressure-density (a) and pressure-composition (b) slices, at $T = 1.2$, of the phase diagram of mixtures of spherical SW molecules with the same molecular size, the same potential interaction range, and dispersive energy ratio $\epsilon_{22}/\epsilon_{11} = 1.5$ (red circles and red curves), 1.75 (green squares and green curves), and 2.0 (blue diamonds and blue curves). Symbols correspond to simulation data obtained in this work and curves are the predictions obtained from the SAFT-VR equation of state.

tures of LJ spheres with different intermolecular parameters [142, 151], is that there are regions at which $P_T(z) < P_N(z)$. These regions are located at the vapor-liquid interface and correspond to zones of tension in the simulation box. Contrary, small locations at the interface corresponding to zones near the vapor bulk-like regions, are regions of compression in which $P_T(z) > P_N(z)$. Within this region of the interface, the local contribution to the surface tension is negative, as can been seen in parts (b) of Figs. 13.2-13.4 for the three different SW mixtures studied in this work. As in the case of systems interacting through the continuous LJ intermolecular potential, the reason for which the transverse pressure has values greater than P_N at the interface near the vapor phase and large negative values (and lower than P_N) at other locations of the interface is a consequence of the behavior of the pressure in the unstable bulk phase region (spinodal region), which plays an essential role in the physics at interfaces. This phenomena is nicely explained in the excellent review of Davies and Scriven [71].

Once we have analyzed the most important structural properties of the planar interface, i.e., the density and pressure profiles, we now turn to the study of the vapor-liquid phase envelopes of the SW mixtures, as calculated from the analysis of the density profiles obtained from our Monte Carlo simulations. Fig. 13.5 shows the pressure-density or $P\rho$ and pressure-composition or Px slices of the phase diagram of the three mixtures for different interaction values $\epsilon_{22}/\epsilon_{11}$. The SAFT-VR theoretical approach has been also used to obtain the complete phase diagram of the mixtures. Although, as we have mentioned in the Introduction and Model and simulation details sections, we have used the information from the theory for obtaining initial guesses of the liquid and vapor densities and compositions of mixtures to be studied by simulation at particular thermodynamic conditions, this theoretical predictions can also be used as results to compare our simulation results and check the ability of SAFT in predicting the phase behavior of these mixtures. As can be seen in part (a) of the figure, the pressure-density or $P\rho$ slice of the phase diagram of mixture indicates that the phase envelope of the system becomes wider as the dispersive energy parameter $\epsilon_{22}/\epsilon_{11}$ is increased. The enlargement of the width associated to the phase envelope is essentially due to the increase of the liquid density as the dispersive energy is higher, or in other words, due to a larger cohesive energy in the system. As can be seen, agreement between Monte Carlo simulation results and prediction from SAFT is excellent in all cases. It is important to recall here that results from the theory are predictions obtained using the Lorentz-Berthelot combining rules for the size and dispersive energy and the combining rule for the intermolecular potential range given by Eq. (13.4) without any further fitting procedure.

We have also obtained the pressure-composition or Px slice of the mixture at the same thermodynamic conditions and using the same dispersive energy parameters. As can be seen in part (b) of the figure, we have presented the molar fractions of the three mixtures from the analysis of the density profiles, as well as the predictions obtained from SAFT-VR. The phase diagrams show the expected behavior, in agreement with part (a) of the figure: as the asymmetry of the system is increased (higher values of $\epsilon_{22}/\epsilon_{11}$), the phase envelope of the mixture also increases. As can be seen, the region at which the system exhibits vapor-liquid phase separation increases in compositions and pressures, an expected behavior of mixtures that exhibit type I phase behavior according to the classification of van Konynenburg and Scott [149, 150]. Agreement between Monte Carlo simulation and theoretical predictions is excellent in all cases.

Another interesting property obtained from our analysis is the $10-90$ interfacial thickness (see Table 13.2). For a given cutoff distance, t is seen to increase with pressure, which simply reflects the fact that the interfacial region gets correspondingly thinner, in agreement with our previous results.

This behavior may be clearly seen in Fig. 13.6. At low pressure the density profiles exhibit a sharp interface, which corresponds to a low value of the interfacial thickness. As the pressure is increased towards the critical value, the interfacial region becomes wider, and hence, the value of the interfacial thickness increases. The variation of interfacial thickness with the dispersive energy parameter $\epsilon_{22}/\epsilon_{11}$ can be seen in the same figure. As can be seen, an increase of $\epsilon_{22}/\epsilon_{11}$, at constant pressure, results in a decreased of the interfacial thickness, which is consistent with the fact that the systems with larger dispersive energies have a larger cohesive energy. This behavior is also consistent with that found for the shape of the vapor-liquid phase envelopes. Finally, we have calculated the vapor-liquid interfacial tension of the mixtures. In particular, we have determined the surface tension using its mechanical definition that involves the integration of the difference between the tangential and normal microscopic components of the pressure tensor profiles, as obtained from the IK methodology, along the simulation box according to Eq. (13.6). The pressure dependence of the interfacial tension of the system is shown in Fig. 13.7. As can be seen, at any given pressure, the interfacial tension is larger for molecules with larger values of $\epsilon_{22}/\epsilon_{11}$. Once again, this is consistent with the larger cohesive energy in systems consisting of molecules in which attractive interactions are longer.

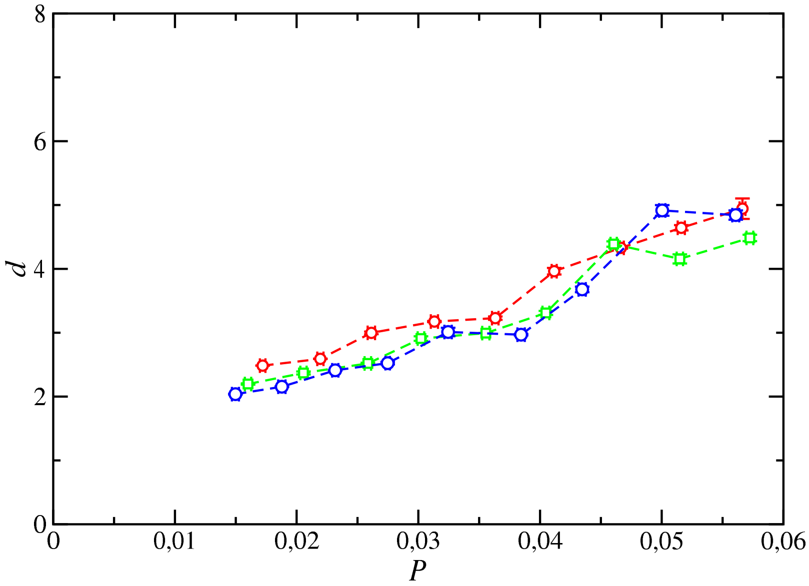

Figura 13.6: The $10-90$ interfacial thickness, at $T = 1.2$, as a function of the pressure for mixtures of spherical SW molecules with the same molecular size, the same potential interaction range, and dispersive energy ratio $\epsilon_{22}/\epsilon_{11} = 1.5$ (red circles), 1.75 (green squares), and 2.0 (blue diamonds). Symbols correspond to simulation data obtained in this work and curves are included as a guide to eyes.

13.4 Conclusion

We have simulated the interfacial properties of the vapor-liquid interface of mixtures of spherical SW molecules. Three mixtures of molecules with the same molecular size and intermolecular potential range but different dispersive energy parameters are considered. The microscopic and macro-

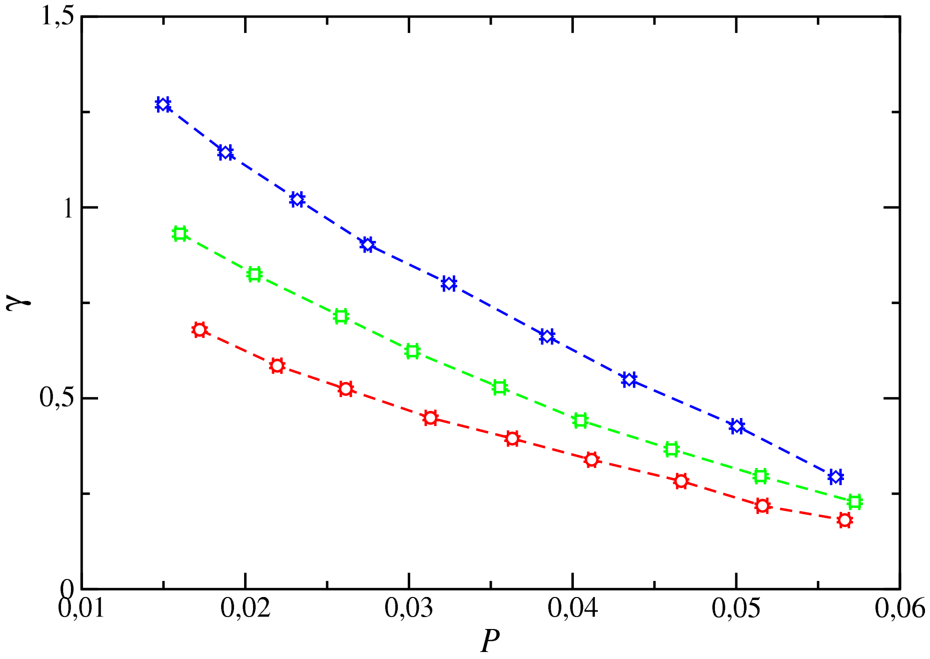

Figura 13.7: Surface tension, at $T = 1.2$, as a function of pressure for mixtures of spherical SW molecules with the same molecular size, the same potential interaction range, and dispersive energy ratio $\epsilon_{22}/\epsilon_{11} = 1.5$ (red circles), 1.75 (green squares), and 2.0 (blue diamonds). Symbols correspond to simulation data obtained in this work using the mechanical route of Irving and Kirkwood [62] and the curves are included as a guide to eyes.

scopic components of normal and tangential pressure are determined using the mechanical (virial route) definition. The interfacial tension is also evaluated using the Irving-Kirkwood method. We have examined the density profiles, interfacial thickness, and surface tension in terms of the pressure and the dispersive energy parameter ratio $\epsilon_{22}/\epsilon_{11}$. In addition, we have also calculated the coexistence diagram (pressure *versus* density) and the pressure-composition slice of the phase diagram at a constant temperature from an analysis of the density profiles.

The effect of the dispersive energy parameters of the mixture, $\epsilon_{22}/\epsilon_{11}$, on density profiles, microscopic components of the normal and tangential pressure tensor profiles, coexistence densities, interfacial thickness, and interfacial tension has been investigated. The vapor-liquid interface is seen to sharpen with increasing dispersive energy ratio corresponding to an increase in the width of the coexistence phase envelope and the pressure-composition slice of the phase diagram and an accompanying increase in the surface tension.

Acknowledgements

We thank A. Ignacio Moreno-Ventas Bravo and Jesús Algaba for helpful discussions. We also acknowledge Ministerio de Economía y Competitividad of Spain for financial support from project FIS2013-46920-C2-1-P, cofinanced with EU Feder funds. Further financial support from Universidad de Huelva and Junta de Andalucía is also acknowledged.

Capítulo 14

Vapor-liquid interfacial properties of square-well chains

Molecular Physics, (Submitted-2015)

F. J. Martínez-Ruiz[1], F. J. Blas[1], A.I. Moreno-Ventas [2] and L.G. MacDowell [3]

[1]Laboratorio de Simulación Molecular y Química Computacional, CIQSO-Centro de Investigación en Química Sostenible and Departamento de Física Aplicada, Universidad de Huelva, 21071 Huelva, Spain
[2]Laboratorio de Simulación Molecular y Química Computacional, CIQSO-Centro de Investigación en Química Sostenible and Departamento de Geología, Universidad de Huelva, 21071 Huelva, Spain
[3]Departamento de Química Física, Facultad de Ciencias Químicas, Universidad Complutense, Madrid, Spain

We consider the computation of a number of interfacial properties of molecular chains from direct simulation of the vapor-liquid interface. The molecules are modeled as fully-flexible square-well chains formed from tangentially-bonded monomers of diameter σ and potential range $\lambda = 1.5\sigma$. Four different model systems, comprising 4, 8, 12, and 16 monomers per molecule, are considered. The simulations are performed in the canonical ensemble, and the vapor-liquid interfacial tension is evaluated using the wandering interface (WIM) method. In addition to the surface tension, we also obtain density profiles, coexistence densities, vapor pressures, critical temperature and density, and interfacial thickness as functions of temperature, paying particular attention to the effect of the chain length on these properties. According to our results, the main effect of increasing the chain length (at fixed temperature) is to sharpen the vapor-liquid interface and to increase the width of the biphasic coexistence region. As a result, the interfacial thickness decreases and the surface tension increases as the molecular chains get longer. The interfacial thickness and surface tension appear to exhibit an asymptotic limiting behavior for long chains. A similar behavior is also observed for the coexistence densities and critical properties. Our results are compared with simulation data taken from the literature for the same properties, including the vapor-liquid coexistence densities, vapor pressures, interfacial thickness, and surface tension, of similar square-well molecular chains models.

14.1 Introduction

Interfacial phenomena play a key role not only in many scientific fields, such as nucleation, nanotechnology or the dynamics of phase transitions, but also in a great number of practical applications. Solubilization of immiscible fluids, detergency, lubricants, and the design of lyotropic liquid-crystalline amphiphiles for use as soaps, cosmetics and foodstuffs are some common applications where an understanding of the interfacial properties is essential.

From a microscopic point of view, interfacial problems can be studied using well-established statistical mechanics tools, either molecular theories appropriate for inhomogeneous systems [5,8,167] or molecular simulation techniques, [2,3] which are also routinely used to examine inhomogeneous systems. In this work we focus on this second approach and use Monte Carlo simulation to determine the interfacial properties of the planar vapor-liquid interface of molecular chain models.

A number of thermodynamic and structural properties play an essential role in the description of the interface in inhomogeneous systems, including density profiles, bulk coexistence densities, the interfacial thickness, surface tension, and orientational and position order along the interface. Although all these properties are relevant for the characterization of the interfacial behavior, the surface tension is arguably the most important and interesting interfacial property.

There are basically three different routes to the calculation of the surface tension from simulation. We describe these briefly here and refer the reader to recent comprehensive reviews . [4,11,207] The first class of techniques involves the calculation of the pressure tensor of the inhomogeneous system. For systems with planar vapor-liquid interfaces, the surface tension can be readily expressed in terms of the difference between the normal and tangential tensorial components of the pressure, these components being defined with respect to a frame where one of the axis is perpendicular to the interface. The most widespread method for the calculation of the components of the pressure tensor invokes the virial relation of Kirkwood and Buff. [62,64] This requires an explicit calculation of the intermolecular forces, so that the virial route is particularly appealing when molecular dynamics is the simulation technique of choice. Alternatively, the components of the pressure tensor can also be obtained directly from the formal thermodynamic expression that relates the pressure (in this case the components of the pressure tensor) with the first-order derivative of the Helmholtz free energy with respect to the volume . [94,95,170,208] The corresponding derivatives can be accurately computed from an evaluation of the change in free energy associated with appropriate small volume perturbations.

The second route to the calculation of the surface tension is based on the concepts of finite-size scaling. [209] One of the most widely used techniques is due to Binder. It relies on an estimation of the Landau free-energy barrier between the two coexisting phases, which is ultimately related to the interfacial tension. One typically considers a series of different system sizes, and a finite-size scaling analysis is then used to extract the value of the interfacial tension in the limit of an infinite system size. This methodology is adequate at high temperatures close to the critical region, where the large density fluctuations allow one to sample the two (liquid and vapor) coexisting phases. However, as the temperature is lowered from the critical temperature, sampling density fluctuations becomes increasingly difficult and the method is more inefficient. A number of variations of the method have been devised in order to enhance the efficiency of the sampling in the low-temperature regime; further details can be found in Ref. [4,207,210]

Finally, the third route to the calculation of the surface tension is based on its thermodynamic definition. The main strategy here is the computation of the free energy difference between two (or more) systems with different interfacial areas. This approach can be traced back to the work of Bennett, [84] Miyazaki *et al.*, [85] and Salomons and Mareschal. [86] Variants of this type of technique have been recently introduced. One is the so-called test-area (TA) technique proposed by Gloor *et al.* [4] This method allows one to calculate the surface tension from an evaluation of the change in free energy associated with a small, virtual change of the interfacial area at constant number of particles, volume and temperature. MacDowell and Bryk [10] developed an alternative methodology based on the probability distribution of a wandering interface, in which the interfacial area is allowed to randomly probe the available configurational space. The surface tension follows from the analysis of the corresponding interfacial area histogram. The last methodology is based on the expanded ensemble proposed by Lyuvartsev *et al.*, [87] which is designed to efficiently calculate the free energy difference between two systems. Very recently, this technique was used independently by de Miguel [12] and Errington and Kofke [11] for the calculation of the free-energy difference between two inhomogeneous systems with the same number of particles, volume and temperature, but a different interfacial area. This technique has been used to calculate the interfacial tension of the planar vapor-liquid interface of a number of molecular models (see the recent work of de Miguel [12] for further details).

Applications of these methods based on the thermodynamic definition of the surface tension have been reported for a wide range of intermolecular model potentials, including the Lennard-Jones, [4, 10] square-well, [4, 10, 12] Gay-Berne, [4, 12] several models of water, [89] the Widom-Rowlinson model [128] as well as hard sphere and bead–spring Lennard–Jones chains. [10] The TA method, in combination with the standard mechanical (virial) route, has recently been used to calculate the surface tension of several alkanes, [88] and acid gases. [83]

Whereas the computation of interfacial properties of polymer models have been the subject of a number of recent papers, [73, 207, 211–213] results for the well known fully-flexible square-well (SW) model, in which square-well segments (monomers) of diameter σ and potential range λ are tangentially bonded to form molecular chains are scarce. In particular, the knowledge of interfacial properties of this model is very limited. To the best of our knowledge, Escobedo and de Pablo performed Gibbs Ensemble Monte Carlo simulation to determine the phase equilibria of SW chains form from 4, 8, 12, and 16 segments. More recently, Chapela and Alejandre have determined the interfacial properties of vibrating fully-flexible SW chains form from the same number of segments. However, both models are different since in the first case the authors used a bead spring model to mimic the intramolecular interaction between consecutive SW segments, and in the second case the intramolecular distance between segments is not strickly σ but 0.97σ.

The goal of the present work is to study the vapor-liquid interfacial properties of fully-flexible tangent SW chains formed from 4, 8, 12, and 16 monomers with potential range $\lambda = 1.5\sigma$ using NVT Monte Carlo simulation of inhomogeneous systems. In this case, the intramolecular distance between consecutive SW segments is kept strictly fixed and equal to σ. From the corresponding density profiles, we determine properties such as the interfacial thickness and bulk coexistence densities; the latter also allows us to determine the critical properties (temperature and density) of the models and the vapor pressure using a thermodynamic integration technique. We also estimate the dependence of all the interfacial properties with the chain length and temperature, placing a special emphasis on the surface tension. We examine a spherically truncated (ST) potential model, with a cutoff distance $r_c = 4\sigma$ and without long-range corrections in most of the simulations performed, and carry out an analysis of the effect of the cutoff distance of the interactions on the interfacial properties. We study the effect of varying the ST LJ cutoff distance on different interfacial properties, including the equilibrium density profiles, coexistence densities, interfacial thickness, and surface tension.

The rest of the paper is organized as follows: In Section 14.2 we briefly consider the molecular model and the simulation details used in this work. The results obtained in this work are described in Section 14.3. Finally, in Section 14.4 we present the main conclusions.

14.2 Model and simulation details

The molecular chains considered in this work are formed from m spherical segments (monomers) that interact through the SW intermolecular potential, which in chracterized by a diameter σ, a dispersive energy ϵ, and a potential range λ. The chains are fuly flexible, i.e., the model does not consider neither bending nor torsional potentials between the segments that form the chains. However, we account for intramolecular interactions between monomer of the same chain separated by more than one bond. The SW potential between two segments, in the same of in the other molecules, is given by:

$$\phi_{ij}(r_{ij}) = \begin{cases} \infty & r_{ij} \leq \sigma \\ -\epsilon & \sigma < r_{ij} \leq \lambda\sigma \\ 0 & r > \lambda\sigma \end{cases} , \tag{14.1}$$

where r_{ij} denotes the distance between the centres of the two segments.

The number of molecules, N, used in each simulation depends on the chain length. We consider $N = 504, 252, 168$, and 126 for systems formed by 4, 8, 12, and 16 monomers, respectively. This choice is made so as to have systems with the same total number of monomers irrespective of the particular chain length.

Code for the simulation of LJ dumbbells [214] is extended for the simulation of either rigid or chain molecules in the NVT, NPT or grand canonical ensemble in either bulk or a slit-pore geometry. Translational and rotational movements are supplemented with configurational bias displacements [187,215,216] and deletion/insertion attempts. [217] The energy is evaluated efficiently with the help of a link cell list. Further details on the specific implementation of configurational bias displacements and the cell list may be found elsewhere. [218]

Simulations are performed in the NVT ensemble. We consider a system of N molecules at a temperature T in a volume $V = L_x L_y L_z$, where L_x, L_y and L_z are the dimensions of the rectangular simulation box. A homogeneous liquid system is first equilibrated in a rectangular simulation box of dimensions $L_x = L_y = 11\sigma$, and $L_z = 24$, 26, 28, and 30σ for systems with LJ chains formed by 4, 8, 12, and 16 monomers, respectively. In the case of fully-flexible chains the end-to-end dimension of the chains is of the order of $\sim m^{1/2}$, which for the longest chains of $m = 16$ studied corresponds to 4σ. The box is then expanded to three times its original size along the z direction, while leaving the liquid phase at the center. On performing this expansion, care must be taken not to break chains spanning the periodic boundary conditions of the initial configuration. As a result, we obtain a centered liquid slab with those chain bits spanning across the boundary conditions of the original liquid configuration protruding into empty boxes of equal size at each side. The final overall dimensions of the vapor-liquid-vapor simulation box are therefore $L_x = L_y = 11\sigma$, and $L_z = 72$, 78, 84, and 90σ for the corresponding chain lengths.

All simulations are organized in cycles, where each cycle corresponds to N trial MC moves. Our MC procedure comprises three types of configurational updates: one involving a trial displacement of the molecular center of mass, and the other two, a partial and complete molecular regrowth of the molecular chains. For the latter type of moves, we consider a configurational bias scheme. Each type of move is chosen with a probability of 20, 40, and 40%, respectively. The magnitudes of the appropriate displacements are adjusted so as to get an acceptance rate of $\sim 30\,\%$ to $50\,\%$. We use periodic boundary conditions in all three directions of the simulation box.

The computation of the surface tension is accomplished with the use of the WIM method. The WIM technique is an extension of the NpT ensemble in which the interfacial area is allowed to fluctuate at random. This is achieved by introducing a new MC move, which consists of an attempt to deform the box by changing the interfacial area of the system at constant volume. The attempted moves are accepted according to the usual canonical rules, and the surface tension may be extracted from the resulting surface area probability distribution. Further details can be found in Ref. [10] The WIM approach can also be implemented in the grand canonical ensemble (suitable for confined fluids against a wall) or in the canonical ensemble; the latter is a better option for the description of vapor-liquid or liquid-liquid interfaces. For the special case of discrete sampling of the surface area, the WIM technique becomes equivalent to the recent expanded ensemble methodology. [11,12]

For each chain length, we perform simulations of inhomogeneous systems at different temperatures where vapor-liquid equilibrium is expected. We typically consider either six or seven temperatures in the range $\sim 0.5\,T_c$ up to $\sim 0.9\,T_c$, where T_c is the critical temperature of the system. Each series is started at an intermediate temperature. This system is well equilibrated for 10^6 MC cycles, and averages are determined over a further period of 2×10^6 MC cycles. The systems at other temperatures of each series are equilibrated for 5×10^5 MC cycles and averages are determined over the same number of cycles (2×10^6). The production stage is divided into M blocks. The ensemble average of the surface tension is given by the arithmetic mean of the block averages and the statistical precision of the sample average is estimated from the standard deviation in the ensemble average from $\overline{\sigma}/\sqrt{M}$, where $\overline{\sigma}$ is the variance of the block averages. We consider $M = 20$, but in some cases averages are taken over more blocks.

All the quantities in our paper are expressed in conventional reduced units, with σ and ϵ being the length and energy units, respectively. Thus, the temperature is given in units of ϵ/k_B, the densities in units of σ^{-3}, pressure in units of ϵ/σ^3, the surface tension in units of ϵ/σ^2, and the interfacial thickness and potential range in units of σ.

14.3 Results and discussion

In this section we present the main results from the simulations of fully-flexible SW chains with potential range $\lambda = 1.5$ and varying chain length. We first focus on the interfacial properties, such as density profiles, interfacial thickness, and surface tension of chains. In particular, we examine the temperature and chain length dependence of these properties.

We follow the same procedure for all chain lengths and temperatures. The equilibrium density profiles $\rho(z)$ are computed from averages of the histogram of densities along the z direction over the production stage. For convenience, density profiles are presented in terms of the monomeric units. As a consequence of our initial setup, the system stabilizes two planar vapor-liquid interfaces parallel (on average) to the $x-y$ plane. The bulk vapor and liquid densities are obtained by averaging $\rho(z)$ over appropriate regions sufficiently removed from the interfacial region. This procedure is meaningful as far as the central liquid slab is thick enough. This turns out to be the case in our simulations, including those performed at the higher temperatures. The bulk vapor density is obtained after averaging the density profiles on both sides of the liquid film. The statistical uncertainty of these values is estimated from the standard deviation of the mean values. Additional interfacial properties can be determined by fitting each of the two equilibrium density profiles to hyperbolic tangent functions of the form:

$$\rho(z) = \frac{1}{2}(\rho_L + \rho_V) - \frac{1}{2}(\rho_L - \rho_V)\tanh\left(\frac{z - z_0}{d}\right) \tag{14.2}$$

where ρ_L, ρ_V, and z_0 are, in general, adjustable parameters corresponding to the liquid and vapor densities at coexistence, and the position of the Gibbs-dividing surface. d is a measure of the thickness of the interface and it is related to the '10-90 thickness' (t) by $t = 2.1972\,d$. Here we fix ρ_L and ρ_V to previously computed values and treat z_0 and d as adjustable parameters. As for the calculation of the bulk vapor density, our reported values of d correspond to the average of the values for the two interfaces appearing in the system. Values determined in this way are always found to be the same within statitistical uncertainties; this suggests that the inhomogeneous systems are properly equilibrated at all temperatures.

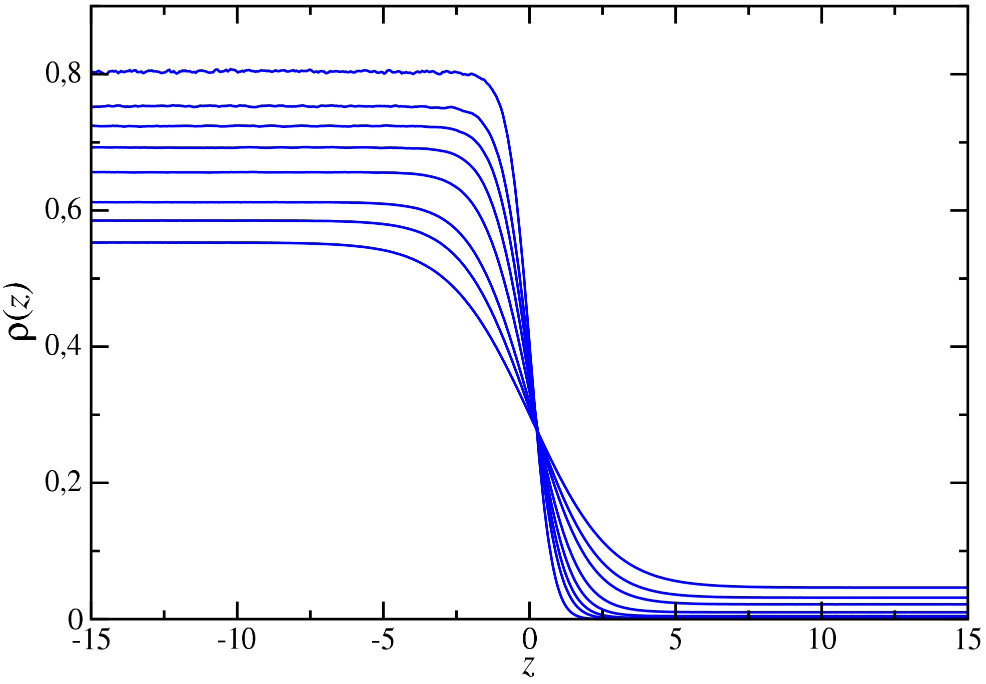

Figura 14.1: Simulated equilibrium density profiles across the vapor-liquid interface of fully-flexible SW chains formed from four monomers ($m = 4$) with potential range $\lambda = 1.5$ at temperatures, from top to bottom (in the liquid region): $T = 1.0$, 1.2, 1.3, 1.4, 1.5, 1.6, 1.65, and 1.7.

We show in Fig. 14.1 the segment density profiles $\rho(z)$ for SW chains formed by four monomers ($m = 4$) at several temperatures in the vapor-liquid coexistence region. For the sake of clarity, we only present one half of the corresponding profiles corresponding to one of the interfaces (the full profiles are displayed as an inset in the figure). Also for convenience, all density profiles have been shifted along z so as to place z_0 at the origin. Our simulation results for the bulk densities and interfacial thickness for SW chains formed by 4 monomers are collected in Table 14.1.

Tabla 14.1: Liquid density ρ_L, vapor density ρ_V, vapor pressure P, 10-90 interfacial thickness t, and surface tension γ at different temperatures for systems of fully-flexible SW chains formed from m monomers with potential range $\lambda = 1.5$. All quantities are expressed in the reduced units defined in Section 14.2. The errors are estimated as explained in the text.

T	ρ_V	ρ_L	P	t	γ
			$m = 4$		
1.0	0.000023(1)	0.8037(14)	0.00000569(24)	0.7373(3)	1.53(8)
1.2	0.000519(5)	0.7530(6)	0.0001276(12)	0.9510(6)	1.00(7)
1.3	0.001636(7)	0.7240(4)	0.0005140(21)	1.091422(24)	0.69(6)
1.4	0.004308(13)	0.6924(3)	0.001407(4)	1.2743(10)	0.49(5)
1.5	0.010027(19)	0.65613(15)	0.003305(6)	1.52862(14)	0.35(3)
1.6	0.02168(4)	0.6120(1)	0.0066(9)	1.9259(6)	0.21(3)
1.65	0.03148(15)	0.58509(19)	0.00965(4)	2.22947(4)	0.19(3)
1.7	0.04619(24)	0.55289(9)	0.01326(8)	2.6934(22)	0.131(22)
			$m = 8$		
1.2	0.000004(4)	0.7804(23)	0.0000005(6)	0.8414(15)	1.10(6)
1.4	0.00013(3)	0.7312(9)	0.000022(5)	1.0536(6)	0.81(5)
1.5	0.00049(3)	0.7039(6)	0.000090(5)	1.1935(3)	0.53(3)
1.6	0.001547(21)	0.6734(4)	0.000298(4)	1.3687(11)	0.52(3)
1.7	0.00419(7)	0.6384(4)	0.000826(13)	1.60476(17)	0.31(3)
1.8	0.0103(1)	0.59758(24)	0.001995(16)	1.9643(8)	0.24(3)
1.9	0.02372(10)	0.54580(20)	0.004308(16)	2.5796(15)	0.108(24)
1.95	0.0365(3)	0.51197(13)	0.00615(4)	3.141(4)	0.069(18)
			$m = 12$		
1.5	0.000039(25)	0.7175(17)	0.000005(3)	1.1073(3)	0.77(5)
1.6	0.00018(3)	0.6910(10)	0.000024(4)	1.2496(10)	0.49(4)
1.7	0.000677(24)	0.6600(5)	0.000094(3)	1.4218(15)	0.38(3)
1.8	0.00211(6)	0.6258(3)	0.000302(8)	1.653(3)	0.29(4)
1.9	0.00576(14)	0.5859(2)	0.000821(18)	1.9890(6)	0.16(3)
1.95	0.00924(14)	0.56273(16)	0.001297(17)	2.2263(5)	0.15(3)
2.0	0.01468(9)	0.53639(23)	0.001996(10)	2.548(3)	0.094(22)
2.05	0.02348(21)	0.50569(19)	0.003005(20)	3.0292(3)	0.084(21)
			$m = 16$		
1.5	0.000003(1)	0.723(3)	0.00000030(9)	1.070(5)	0.80(9)
1.6	0.000023(2)	0.698(3)	0.0000023(2)	1.189(4)	0.52(6)
1.7	0.000129(10)	0.6701(15)	0.0000136(10)	1.340(3)	0.42(4)
1.8	0.000526(9)	0.6380(9)	0.0000581(10)	1.530(3)	0.33(4)
1.9	0.001791(16)	0.6024(5)	0.0002034(17)	1.7872(6)	0.24(4)
2.0	0.00525(6)	0.5602(3)	0.000595(6)	2.16855(4)	0.18(3)
2.1	0.01428(13)	0.50872(17)	0.001519(11)	2.8536(4)	0.12(3)
2.15	0.0242(3)	0.47288(17)	0.002375(20)	3.5094(4)	0.034(24)

A similar analysis is used for the other chain lengths considered in this work. Bulk coexistence densities and interfacial thickness for chains formed from 8, 12, and 16 monomer segments are also gathered in Table14.1. The vapor densities and the interfacial thickness associated with both interfaces are nearly identical in all the systems and at all temperatures, as found for the shortest chains with $m = 4$. From the simulation data presented in Table 14.1 one can compare the vapor-liquid phase envelope for SW chains of different chain lengths. It is also useful to estimate the location of the critical point resulting from our direct Monte Carlo simulations. The critical temperature T_c and density ρ_c are obtained using the simulation results for the vapor and liquid coexistence densities

(Table 14.1) and the scaling relation for the width of the coexistence curve,

$$\rho_L - \rho_V = A(T - T_c)^{\beta} \ , \tag{14.3}$$

and the law of rectilinear diameters

$$\frac{\rho_L + \rho_V}{2} = B + CT \ . \tag{14.4}$$

A, B, and C are constants, and β is the corresponding critical exponent. A universal value of $\beta = 0.325$ is assumed here. [5] In Table 14.2 we report the values of the critical temperatures and densities as obtained from this procedure for all the systems studied in this work.

The vapor-liquid phase envelopes of fully-flexible SW chains are depicted in Fig. 14.2a. Note that densities are again presented in terms of the monomeric segments. The coexistence envelopes exhibit a definite trend with chain length when represented in terms of the monomeric density. As can be seen in Fig. 14.2a, the phase envelope becomes wider as the chain length is increased, as one would expect. The increase is more significant when the number of monomers is increased from 4 to 8 than when the chain length is further increased. A similar behavior is also observed for the critical properties. This is consistent with the well-known asymptotic behavior of the vapor-liquid phase envelope of SW chains expected as $m \to \infty$ [158]. We have also included the results obtained by Escobedo and de Pablo [184] from previous Gibbs ensemble simulations. The comparison between the results presented in this work and those obtained by Escobedo and de Pablo are in excellent in all cases, although the comparison at high temperatures, especially in the case of the longest chains is somewhat less good. We attribute the difference to the use of a bead spring model in the work of Escobedo and de Pablo. Apparently the bond flexibility starts having a small but noticeable effect above $T = 2.5$. Despite the small differences mentioned, we believe this comparion to be a convincing test of consistence for the simulations we have performed.

More recently, Chapela and Alejandre have determined the vapor-liquid interfacial properties of vibrating square well chains, including surface tension, orthobaric densities, and vapor pressures. In particular, they have studied linear chains form from 2, 4, and 8 spheres for intramolecular distances of 0.97, 0.6, and 0.4. In addition to that, the complete series of fully flexible *"near"* tangent square well chains is also studied for chains of 2, 4, 8, 12, and 16 particles with interamolecular distances of 0.97. We compare the results obtained in this work those presented by Chapela and Alejandre in Fig. 14.2b. As can be seen, as in the case of the simulation results obtained by Escobedo and de Pablo in 1996, agreement between both results is excellenet in all cases. Small differences between our results and those of Chapela and Alejandre, especially at temperatures close to the critical temperature of each chain lenght considered, due to the small difference between both models. It is important to emphasis that, strickly spekaing, in the simulation study of this work fully flexible tangent square well chains are considered, whereas Chapela and Alejandre use a model each with intramolecular distance is not equal to unity, in reduced units, but 0.97.

Calculation of the coexistence pressures poses some difficulties. For a model of fixed bond lengths as the one studied here, the expression for the virial is awkward, particularly for long chains whose end to end distance may be larger than half the simulation box [219]. This problem notwithstanding, acquisition of meaningful averages for such low pressures as are typical well below the critical point

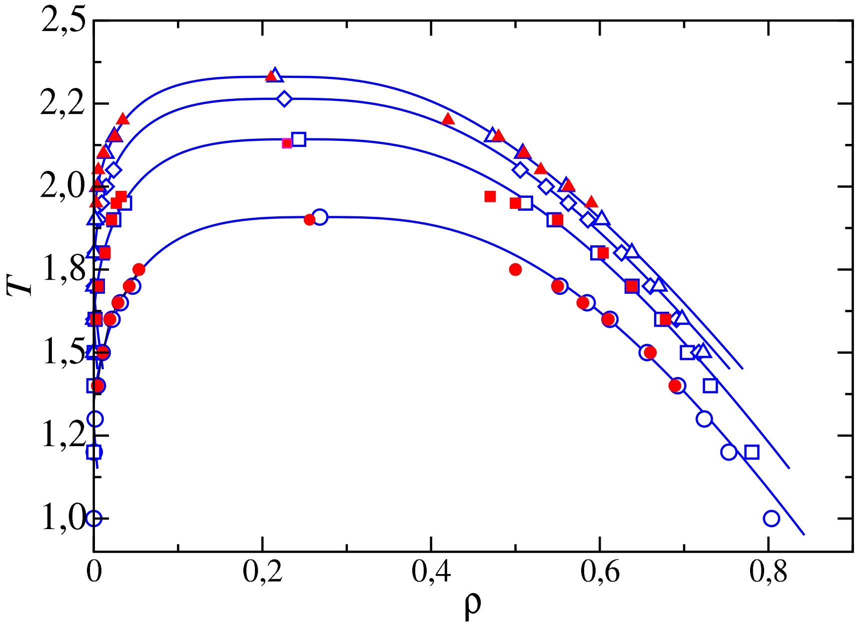

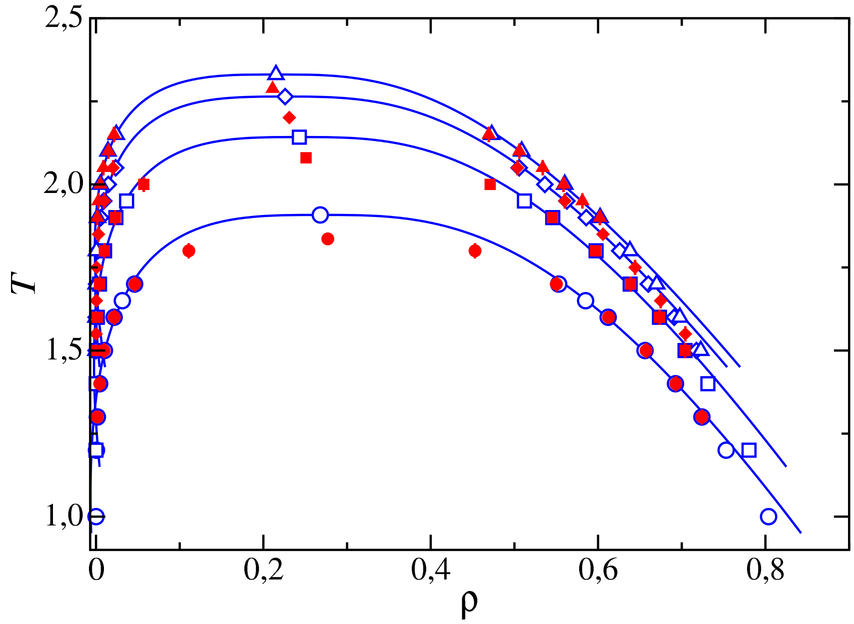

Figura 14.2: Vapor-liquid coexistence densities for fully-flexible SW chains with potenial range $\lambda = 1.5$. The open black circles, red squares, green diamonds, and blue triangles correspond to the coexistence densities obtained from the analysis of the equilibrium density profiles obtained from Monte Carlo NVT simulations, for chain lengths of $m = 4, 8, 12,$ and 16, respectively. Filled symbols in (a) are the results obtained by Escodebo and de Pablo [184] and in (b) those obtained by Chapela and Alejandre [122]. Each of the symbols at the highest temperatures correspond to the critical potins estimated from The filled symbols are the corresponding critical points estimated from Eqs. (14.3) and (14.4). The curves represent the fits of the simulation data of this work to Eq. (14.3).

Tabla 14.2: †Critical density and temperature from the analysis of the coexistence densities using Eqs. (14.3) and (14.4) and §critical temperature obtained from the analysis of the computed tension data using Eq. (14.6) and fixing the critical point to $\mu = 1.258$ for systems of fully-flexible SW chains formed from m monomers with potential range $\lambda = 1.5$. All quantities are expressed in the reduced units defined in Sec. 14.2.

m	$\rho_c^{\dagger}$	$T_c^{\dagger}$	$T_c^{\S}$
4	0.268(3)	1.908(3)	1.80(13)
8	0.243(5)	2.142(5)	2.03(8)
12	0.226(6)	2.264(6)	2.20(15)
16	0.215(10)	2.33(1)	2.30(14)

requires very lengthy simulations. For that reason, we calculated the pressure by means of a thermodynamic integration hinted at previously. [220] In this procedure we exploit the Gibbs–Duhem equation, $\mathrm{d}p = \rho \mathrm{d}\mu$, at constant temperature. By splitting the chemical potential into ideal gas and residual contributions, and integrating by parts, we obtain:

$$\beta p(\rho) = \rho - \int_0^{\rho} \left[\mu_{\mathrm{r}}(\rho') - \mu_{\mathrm{r}}(\rho)\right] \mathrm{d}\rho' \tag{14.5}$$

In order to exploit this equation for the calculation of the pressure, we performed a series of bulk simulations in the Grand–Canonical ensemble. As in the case of the inhomogeneous system, we have also organized these simulations in cycles. As before, each cycle consists in N trial MC moves. The only difference is that we do not perform full chain configurational bias regrowth but Grand–Canonical configurational bias chain insertion/deletion. Each type of move is chosen with a probability of 20%, 40%, and 40% for center of mass displacements, partial configurational bias chain regrowth, and Grand–Canonical configurational bias chain insertion/deletion, respectively. Typically, we run between 10 and 20 thermodynamic states from the ideal gas limit to the supersaturated vapor. Each state is equilibrated for 5×10^4 MC cycles, and averages of density are determined over a further period of 4×10^5 MC cycles. The production stage is divided into M blocks. We consider $M = 50$ for all the states (different chemical potentials and temperatures) and chain lengths considered here. With this choice, the density at each chemical potential has been obtained from an average of 50 uncorrelated or statistically independent blocks (8×10^3 cycles per block). The residual chemical potential, as a function of density, was then fitted to a polynomial of 2nd up to 5th order and integrated up to the coexistence vapor density. We have checked that our fitting procedure is essentially independent of the degree of the polynomial fit. Once the function $\mu_r = \mu_r(\rho)$ has been obtained, the vapor pressure can be readily calculated from Eq. (14.5). The statistical uncertainty associated with the thermodynamic integration of the equation of state given in Eq. (14.5) has been estimated from the *synthetic analysis* proposed recently by de Miguel. [221] In particular, we have generated 10^6 synthetic data sets according to the de Miguel's prescription, [221] obtaining a Gaussian-like distribution for the vapor pressure at each temperature. Our final results, including the statistical uncertainty of vapor pressure are presented in Table 14.1.

Fig. 14.3 shows the simulation results obtained for the vapor pressure of the chains studied. The results are compared also with the simulation results obtained by Chapela and Alejadre. As can be seen, agreement between both results is excellent in all the cases and in the whole range of coexistence. Differences in the error bars of both results can be observed comparing the data obtained in this work, shown in Table 14.1, and in the original work of Chapela and Alejandre [122]. As can be

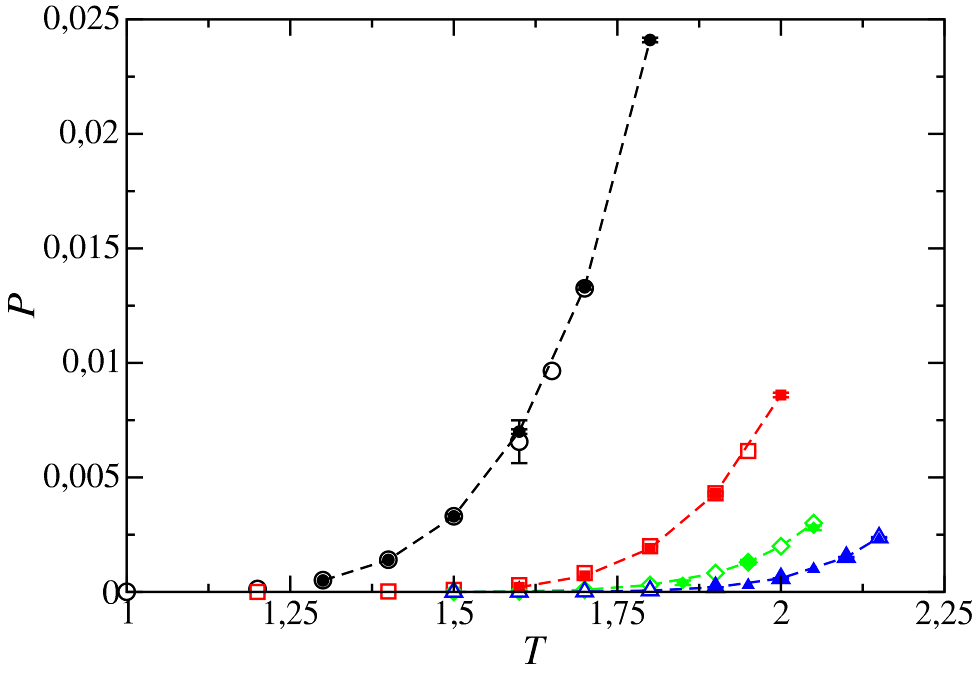

Figura 14.3: Vapor pressure P, as a function of the temperature for fully-flexible SW chains with potential range $\lambda = 1.5$. The meaning of the symbols is the same as in Fig. 14.2b. The curves are included as guides to the eye.

seen, uncertainties obtained in this work are of one or two orders of magnitude lower than those corresponding to the work of Chapela and Alejandre. This is an expected results since the method for calculating the vapor presusre is very accurate and robust, in comparison with that used by Chapela and Alejandre, which is based on the average of the normal component of the pressure tensor along the vapor-liquid interface.

Another interesting property obtained from our analysis is the 10-90 interfacial thickness (cf. Table 14.1). For a given chain length, t is seen to increase with temperature, which simply reflects the fact that the interfacial region gets correspondingly wider. This can be observed in Fig. 14.1 for the case of SW chains form from 4 spherical segments. At low temperatures the density profiles exhibit a sharp interface, which corresponds to a low value of the interfacial thickness. As the temperature is increased toward the critical value, the interfacial region becomes wider, and hence, the value of the interfacial thickness increases and diverges to infinity as $T \to T_c$. The same behavior is also observed in the case of longer chains. The variation of interfacial thickness with temperature for different chain lengths is illustrated in Fig. 14.4. According to the figure, increasing the chain length results in a decrease of the thickness of the interface at fixed temperature, which is consistent with the fact that the systems of longer molecules have a larger cohesive energy. This behavior is consistent with that found for the shape of the vapor-liquid phase envelopes. It is interesting to note that the variation of t with chain length at constant temperature is more significant for a change from the $m = 4$ to the $m = 8$ system than in the rest of the cases. This is again related with the aforementioned asymptotic limit.

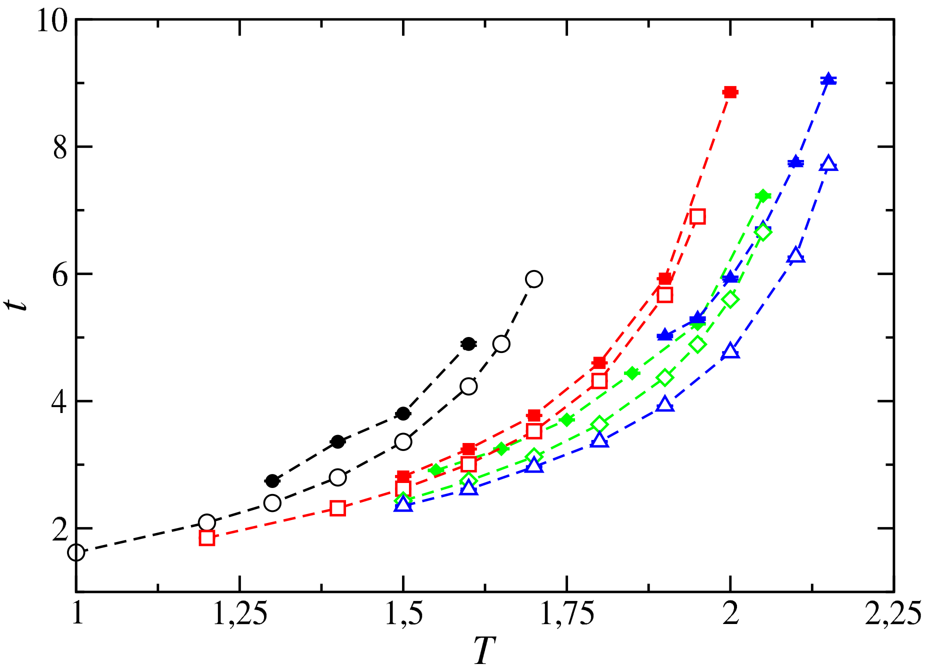

Figura 14.4: 10-90 Interfacial thickness, t, as a function of the temperature for fully-flexible SW chains with potential range $\lambda = 1.5$. The meaning of the symbols is the same as in Fig. 14.2b. The curves are included as guides to the eye.

As in the case of the coexistence densities and vapor pressures of SW chains considered in this work, we have also compared the results obtained in this work with those calculated by Chapela and Alejandre [122] for nearly the same molecular model. As can be seen, the results obtained by these authors show the same qualitative behavior. However, as can be seen in Fig. 14.4, the interfacial thickness values obtained by Chapela and Alejandre are systematically higher, at the same temperature and for the same chain length, than those obtained in this work. It seems, from the inspection of the Figure, that this deviation is approximately the same, for a given chain, at all temperatures. Why is happing this? Apart from the fact that both molecular models are not exactly the same, we think the reason of this disagreement between both results arises due to the difference in surface area, $\mathcal{A}$, employed in the simulations. In this work, the surface area is always $\mathcal{A} = L_x L_y = 11 \times 11$ (in reduced units). However, Chapela and Alejandre use different values (see Tables of their work for further details).

Finally, the temperature dependence of the surface tension for the SW chains is shown in Fig. 14.5. At any given temperature, the interfacial tension is larger for longer chains. Once again, this is consistent with the larger cohesive energy in systems consisting of long chains. As can be seen from Fig. 14.5, an essentially linear behavior is found for the range of temperatures considered here, with a slight curvature close to the critical point for each system. The effect of chain length on the slope of the surface tension curves is remarkable. At a given temperature, this slope becomes less negative as m is increased, a trend which is also exhibited by the first members of the n-alkane series. [199] The same qualitative behavior has been previously found by Bryk and collaborators. [200] One should keep in mind, however, that a fully-flexible SW chain model is not the most appropriate representation of

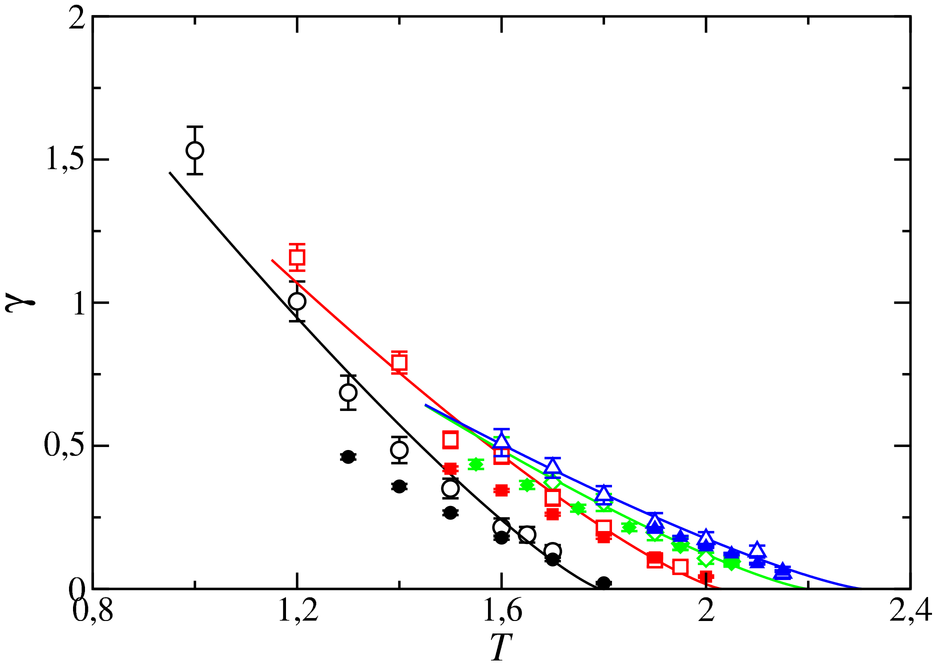

Figura 14.5: Surface tension as a function of the temperature for fulle-flexible SW chains with potential range $\lambda = 1.5$. The meaning of the symbols is the same as in Fig. 14.2b. The curves represent the fits of the simulation data to the scaling relationship of the surface tension near to the critical point given by Eq. (14.6), with $\mu = 1.258$.

real n-alkanes.

It is also interesting to compare our computed values of the surface tension with those reported by Chapela and Alejandre *et al.* [122] for nearly the same molecular model of fully-flexible SW chains with potential range $\lambda = 1.5$. Although the models are similar, as we have discussed previously in this work, the model used by Chapela and Alejandre has a slightly smaller intramolecular length between the spherical segments forming the SW chains. This difference should results in slightly lower values of the interfacial tension for this model at low temperatures. In addition to that, the values of the interfacial tension obtained by Chapela and Alejadre are similar than ours at the intermeditate and high temperatures.

The computed values of the surface tension allow us to obtain an independent estimate of the critical temperature for each chain length from the scaling relation

$$\gamma = \gamma_0 \left(1 - T/T_c\right)^{\mu} \ , \tag{14.6}$$

where γ is the surface tension at temperature T, γ_0 is the "zero-temperature" surface tension, μ is the corresponding critical exponent, and T_c is the critical temperature. Here, we fix μ to the universal value of $\mu = 1.258$ as obtained from renormalization-group theory. [5] Our estimates for the critical temperatures are collected in Table 14.2. The overall agreement between these values and those obtained from an analysis of the coexistence densities is satisfactory.

14.4 Conclusion

We have simulated the interfacial properties of the vapor-liquid interface of fully-flexible chains formed from tangentially bonded SW monomers with potential range $\lambda = 1.5$. Chains formed by four, eight, twelve, and sixteen monomers are considered. Both intermolecular and intramolecular segment-segment interactions are taken into account explicitly in this work. We use Monte Carlo NVT simulation of the inhomogeneous system containing two vapor-liquid interfaces. The surface tension is evaluated using the wandering interface method (WIM). We have examined the density profiles, interfacial thickness, and surface tension in terms of the temperature and the number of monomers forming the chains. In addition, we have also calculated the coexistence phase envelope and the vapor pressure, including the location of the critical point from an analysis of the density profiles and the surface tension.

The effect of the chain length on the density profiles, coexistence densities, vapor pressures, critical temperature and density, interfacial thickness, and surface tension has been investigated. The vapor-liquid interface is seen to sharpen with increasing chain length corresponding to an increase in the width of the coexistence phase envelope, and an accompanying increase in the surface tension. The coexistence phase envelope, the interfacial thickness and the surface tension are seen to exhibit an asymptotic limiting behavior as the chains get longer.

Finally, we have also compared the results obtained in our simulations with simulation data obtained independently by Escobedo and de Pablo and Chapela and Alejandre several years ago, including vapor-liquid coexistence densities, vapor pressures, interfacial thickness, and surface tension. In the case of the coexsitence densities and vapor pressures, agreement between our simulation results and those taken from the literature are excellent in all cases. Slightly differences at high temperatures, close to the critical point, can be observed in coexistence densities. This is probably due to the difference in the molecular models. Whereas in the model we use here the segments forming the fully flexible chains are strickly tangent, in the other simulations the SW chains are modeled as either using a bead spring model or as vibrating chains in which the intramolecular distance between consecutive segments is 0.97 (and not 1.0) in reduced units. However, interfacial thickness and surface tension exhibit differences between our simulation results and those taken fro mthe literature. In the first case, this is probably due to the differences in surface areas used in the simulations. However, in the case of the surface tension, probably the most sensitive property to the molecular details, we think the disagreement observed between the simulation results are due to differences between the molecular models employed.

ACKNOWLEDGMENT

F.J.M.R., F.J.B., and A.I.M.-V.B. acknowledge Ministerio de Economía y Competitividad of Spain for financial support from project FIS2013-49620-C2-1-P, cofinanced with EU Feder funds. Additional support from Universidad de Huelva and Junta de Andalucía is also acknowledged.

Capítulo 15

Universal scaling behaviour of surface tension of molecular chains

The Journal of Chemical Physics 137, 024702 (2012)

F. J. Blas[1], F. J. Martínez-Ruiz[1], A. I. Moreno-Ventas Bravo[2], and L. G. MacDowell[3]

[1]Departamento de Física Aplicada, Universidad de Huelva, 21071, Huelva, Spain
[2]Departamento de Geología, Facultad de Ciencias Experimentales, Universidad de Huelva, 21071 Huelva, Spain
[3]Departamento de Química Física, Facultad de Ciencias Químicas, Universidad Complutense, 28040 Madrid, Spain

---

We use and extend the universal relationship recently proposed by Galliero [G. Galliero, *J. Chem. Phys.* **133**, 074705 (2010)], based on a combination of the corresponding-states principle of Guggenheim [E. A. Guggenheim, *J. Chem. Phys.* **13**, 253 (1945)] and the parachor approach of Macleod [J. Macleod, *Trans. Faraday Soc.* **19**, 38 (1923)], to predict the vapour-liquid surface tension of fully flexible chainlike Lennard-Jones molecules. In the original study of Galliero, the reduced surface tension of short-chain molecules formed by up to five monomers is expressed as a unique function of the difference between the liquid and vapour coexistence densities. In this work, we extend the applicability of the receipe and demonstrate that it is also valid for predicting the surface tension of two different chainlike molecular models, namely, linear tangent chains that interact through the Lennard-Jones intermolecular potential and fully flexible chains formed by spherical segments interacting through the SW potential. Computer simulation data for vapour-liquid surface tension of fully flexible and rigid linear Lennard-Jones, and fluid flexible square-well chains is taken from our previous works. Our results indicate that the universal scaling relationship is able to correlate short- and long-chain molecules with different degrees of flexibility and interacting through different intermolecular potentials.

15.1 Introduction and theoretical background

Among the thermodynamic and structural properties associated to interfaces, surface tension is undoubtedly the most important quantity. An accurate knowledge of this property is essential to understand the phenomenology associated to practically any interface, including the formation of micelles by amphiphilic surfactant molecules, wetting transitions in systems involving solid substrates, optoelectronic devices, such as liquid crystals, industrial proceses such as oil-reservoir engineering applications, etc.

During the last years, an intensive development of reliable and predictive modelling techniques are being developed by different groups [7, 8]. See the recent works of Bryk and MacDowell [222] and Jackson and coworkers for a description of the most relevant and novel methodologies introduced recently [148, 223, 224]. Although a variety of sophisticated and very accurate methods are being proposed and applied to predict the interfacial properties of complex systems from a molecular perspective, other simple and old methodologies, less theoretical-based but also able to provide an accurate description of the interfacial properties with particular emphasis on the surface tension, are being used during last years.

One of the most popular family of correlations for estimating the vapour-liquid surface tension of real substances is based on the so-called parachor approach, introduced by Macleod in 1923 [107]. In this empirical method, the vapour-liquid surface tension is correlated with the difference of the bulk coexistence densities,

$$\gamma = C(\rho_L - \rho_V)^p \tag{15.1}$$

Here γ is the vapour-liquid surface tension, ρ_L and ρ_V are the bulk liquid and vapour coexistence densities, respectively, and $p = 4$. C is a constant for each substance and has to be found by fitting to available experimental data, usually in the temperature range from the melting-point to the critical temperature. Despiste its empirical base, the former relation is found to fit the experimental data for many substances with remarkable accuracy for the whole range of temperatures. Sugden [108], following the approach of Macleod, wrote Eq. (15.1) as,

$$\frac{M\gamma^{1/4}}{(\rho_L - \rho_V)} = P \tag{15.2}$$

where M is the molecular weight of the substance. Sugden calls P the *parachor*, and the exponent $p = 4$ in Eq. (15.1) is usually called the parachor exponent. In the original works of Macleod and Sugden the parachor exponent was equal to 4, although several authors have considered different values, obtained either from theoretical approaches or simply as empirical adjustments, leading to a *fauna* of parachor relationships which are usually written in the general form [115,225], not only valid for pure systems but also for describing fluid-fluid interfacial tension of mixtures [226]. Despiste its simplicity and empirical basis, a great research effort has been devoted to improve the accuracy of the parachor methodology by optimising the values of the parachor exponent p and the parachor P, which strongly depends on the parachor exponent value. Although the parachor method originally proposed by Macleod is based on an empirical approach, Fowler [227] showed that Eq. (15.1), with $p = 4$, can be derived as an explicit function of the intermolecular potential in the case of a stepwise density profile, which is a reasonable assumption far away from the critical point.

Other popular approaches are based on the corresponding-states principle of Guggenheim [105], probably one of the most useful results of the van der Waals equation of state. The corresponding-states principle of Guggenheim, applicable to different kind of substances, states that many properties including the critical state, the density coexistent phases, and the vapour pressure of the liquid among many others, can be described using universal functions when are expressed in terms of reduced magnitudes with respect to their critical values. In particular, the corresponding-states principle was extended by Guggenheim to deal with surfaces assuming that the excess free energy due to the presence of an interface of surface area $\mathcal{A}$ containing N_s molecules is given by a universal function that only depends on the reduced temperature $T^* = k_B T/\epsilon_0$ and surface area per molecule $\mathcal{A}^* = A/N_s R_0^2$, with ϵ_0 the minimum intermolecular potential energy and R_0 a measure of the intermolecular potential range [105]. Using this extension of the corresponding-states principle, Guggenheim proposed a simple form for an empirical relationship between the surface tension γ and the temperature T. The approach of Guggenheim is able to correlate the vapour-liquid surface tension of a number of substances in excellent agreemnent with experimental data [105],

$$\gamma = \gamma_0 \left(1 - T/T_c\right)^{11/9} \tag{15.3}$$

where γ_0 represents the "zero-temperature" surface tension. As we will see below, this expression is not in exact agreement with the relation of Macleod [107]. In particular, Guggenheim estimated the parachor exponent as $p = 11/3$, a value lower than the 4 obtained by Macleod (and corrobotated from a theoretical point of view by Fowler assuming restricted approximations), and that provides a better description of the surface tension dependence on density than this latter approach.

Although both the Macleod and the corresponding-states principle of Guggenheim are clearly empirical approaches, their functional expressions have a theoretical basis founded in the more fundamental and modern Renormalization Group Theory (RGT). According to that, a fluid close to the critical region exhibits large density fluctuations that could be quantified by the correlation length of density fluctuations (correlation length of the distribution function) [5], $\xi \sim |1-t|^{-\nu}$, where t is the reduced temperature to the critical temperature, $t = T/T_c$, and ν is the well-know correlation length critical exponent. The most accurate experimental values for this critical exponent gives $\nu \approx 0.629\,(3)$ according to recent works [5,228]. RGT indicates that the vapour-liquid surface tension should vanish as $T \to T_c^-$ following the well-known scaling relationship [5],

$$\gamma \sim |1-t|^{\mu} \tag{15.4}$$

where μ is the critical exponent associated to the vapour-liquid surface tension. μ is related with other critical exponents associated to the correlation length of density fluctuations through the hyperscaling relation proposed by Widom in the sixties [106], $\mu = (d-1)\nu$. Here d is the dimensionality of the system, and since we are dealing with three dimensional systems, $d = 3$ and $\mu = 1.258\,(6)$ when the value of the correlation length critical exponent, $\nu = 0.629\,(3)$, is used. Note that this value is very close to that found by Guggenheim in 1945 [105], $\mu \approx 1.22$, using the empirical corresponding-states correlation previously presented in Eq. (15.3).

It is possible to write the scaling law given by Eq. (15.4) in terms of the difference between the vapour and liquid densities. This allows to understand, from a more fundamental point of view, the parachor relation proposed by Macleod in 1923 [107]. Probably, the best-known scaling law near the vapour-liquid critical point is given by the difference in densities as a function of the temperature [5], i.e.,

$$\rho_L - \rho_G \sim |1-t|^{\beta} \tag{15.5}$$

where β is the vapour-liquid critical exponent given by $\beta \approx 0.326(2)$ according to the current experimental estimates [228]. The vapour-liquid surface tension can be expressed in terms of the difference of vapour and liquid densities combining Eq. (15.4) and (15.5), i.e.,

$$\gamma \sim |1-t|^{\mu} \sim \left(\rho_L - \rho_V\right)^{\mu/\beta} \sim \left(\rho_L - \rho_V\right)^{(d-1)\nu/\beta} \tag{15.6}$$

The comparison between the previous expression and Eq. (15.1) gives the parachor exponent in terms of the critical exponents obtained from RGT, $p = (d-1)\nu/\beta = 3.86\,(3)$, which is similar to that proposed by Macleod in 1923 [107] ($p = 4$) and with that found by Guggenheim [105] in its seminal work on the corresponding-states principle, $p = 11/3 \approx 3.67$.

Although it is important to understand and justify the functional form and exponent values of the parachor of Macleod from a fundamental point of view, another interest question arises from the ensuing discussion. Is it possible to use the above description to find a universal relationship to describe the behaviour of the vapour-liquid surface tension of several substances? Different studies carried out in the past have showed that the relations previously introduced here are essential, although an additional ingredient must be included. In the seminal work of the corresponding-states principle [105], Guggenheim argues that not the vapour-liquid surface tension but the surface tension reduced with respect to two critical properties should be a universal function of t, the reduced temperature to the critical temperature ($t = T/T_c$). The particular choice of Guggenheim, widely used in the literature, is given by [105, 113]

$$\gamma_r = \gamma\,(k_B T_c)^{-1}\,(M/\rho_c)^{-3/2} = \frac{\gamma}{k_B T_c\,(M/\rho_c)^{3/2}} \tag{15.7}$$

where ρ_c and T_c are the critical density and temperature of a substance, and M is the molecular mass of the substance. A slightly different but equivalent reduced surface tension could be obtained by reducing it with respect to critical temperature T_c and pressure P_c, as suggested recently by Galliero [113]. This author, as well as Garrabos *et al.* [115], have shown that this universal scaling approach is also able to deal with real fluids, except for systems with specific interactions, such as hydrogen bonding.

Galliero [113] has also proposed a different but useful way of reducing the surface tension using the critical temperature, T_c, and pressure, P_c, as

$$\gamma_r = \gamma^*\,(k_B T_c)^{-1/3}\,P_c^{-3/2} = \frac{\gamma^*}{(k_B T_c)^{1/3}\,P_c^{3/2}} \tag{15.8}$$

Although both receipes provide similar results, as pointed by Galliero [113], we have only used the approach given by Eq. (15.7) since we have not calculated the critical pressure of the systems under consideration.

The reduced surface tension receipe given by Eq. (15.7) is a universal function of t for spherical fluids with different potential parameters, as pointed by several authors [92, 105, 111, 112]. Unfortunately, it is not able to predict a universal behaviour of the surface tension of LJ chainlike molecules of different length when the surface tension is represented as a function of t. However, as pointed recently by Galliero [113], a combination of the scaling proposed originally by Guggenheim and the Macleod's parachor approach, i.e., plotting the surface tension reduced according to Eq. (15.7) as a function of $(\rho_L - \rho_V)/\rho_c$, accounts for a universal behaviour of short-chain LJ molecules with different length. Here we show that this approach can be also exploited to fit into the same universal master curve the properties of different types of chainlike molecules.

In a previous work, we have determined the interfacial properties of fully flexible (FF) Lennard-Jones (LJ) chains with different chainlengths [13, 14]. We have studied the effect of the cutoff distance of the intermolecular potential on interfacial properties, with particular emphasis on surface tension.

Additionally, we have extended and improved the inhomogeneous long-range corrections proposed by Janeček [15] to deal with molecular systems. In all cases, the Test-Area (TA) approach of Gloor *et al.* [4] and the Wandering Interface Method (WIM) of MacDowell and Bryk [10] have been used to determined the vapour-liquid surface tension of these systems.

More recently, we have also determined the interfacial properties of a similar but slightly different molecular chain model, namely, the rigid linear (RL) LJ chainlike model [144]. The flexible model has neither bending nor torsional potentials between the monomers in a chain. Contrary, in rigid linear chains the bond length, bond angles, and internal degrees of freedom are fixed. In other words, whereas in the first model the molecules can adopt any bond angle or torsional state, as corresponds to flexible molecules, these degrees of freedom are frozen in the rigid linear chain. In this latter case, we have used the TA methodology [4] and the inhomogeneous long-range corrections following the MacDowell and Blas receipe [14] (based on the Janeček's method [15]) to determine the vapour-liquid surface tension of RL chains formed by 3, 4, and 5 monomers that interact through the LJ intermolecular potential.

We have also determined the interfacial properties of FF square-well (SW) chains with a potential range $\lambda = 1.5\sigma$ and chain lengths equal to 4, 8, 12, and 16 monomers [143] using the TA methodology and the WIM approach. Recently, Chapela and Alejandre [122] have also determined the surface tension of SW chains formed by several chain lengths and intramolecular bond lengths.

The goal of this work is to extend the approach proposed by Galliero [113] to deal with longer FFLJ chains (up to molecules formed by sixteen segments), short RLLJ molecules, and SW chains. The surface tension data corresponding to Lennard-Jones and SW chains are taken from our previous works [13, 14].

15.2 Results

Following the previous work of Galliero [113], we have first reduced the vapour-liquid surface tension of FFLJ chains obtained by MacDowell and Blas [14] using the TA and WIM approaches for molecules formed by different chainlengths using the original receipe of Guggenheim given by Eq. (15.7). In addition to that, we have also reduced the surface tension of RLLJ chainlike molecules of different chain lengths as obtained by Moreno-Ventas Bravo *et al.* [144]. We have then represented the reduced surface tension of LJ chainlike molecules (both FF and RL) as a function of the different between liquid and vapour coexistence densities (reduced with respect to the critical density). The critical temperature T_c and density ρ_c have been obtained using the standard technique, i.e., the simulation results for the vapour and liquid coexistence data and the scaling relation for the width of the coexistence curve given by Eq. (15.5) and the law of rectilinear diameters,

$$\frac{\rho_L + \rho_V}{2} = B + CT \tag{15.9}$$

where B and C are constants. A universal value of $\beta = 0.326$ is assumed here [5]. See the works of Blas, MacDowell, and collaborators [13, 14] for further details.

As can be seen in Fig. 15.1, the reduced surface tension of FFLJ and RLLJ long-chain molecules exhibits a universal behaviour as a function of $(\rho_L - \rho_V)/\rho_c$. We have not included the data corresponding to short-chain molecules presented by Galliero for clarity. Since our data also includes

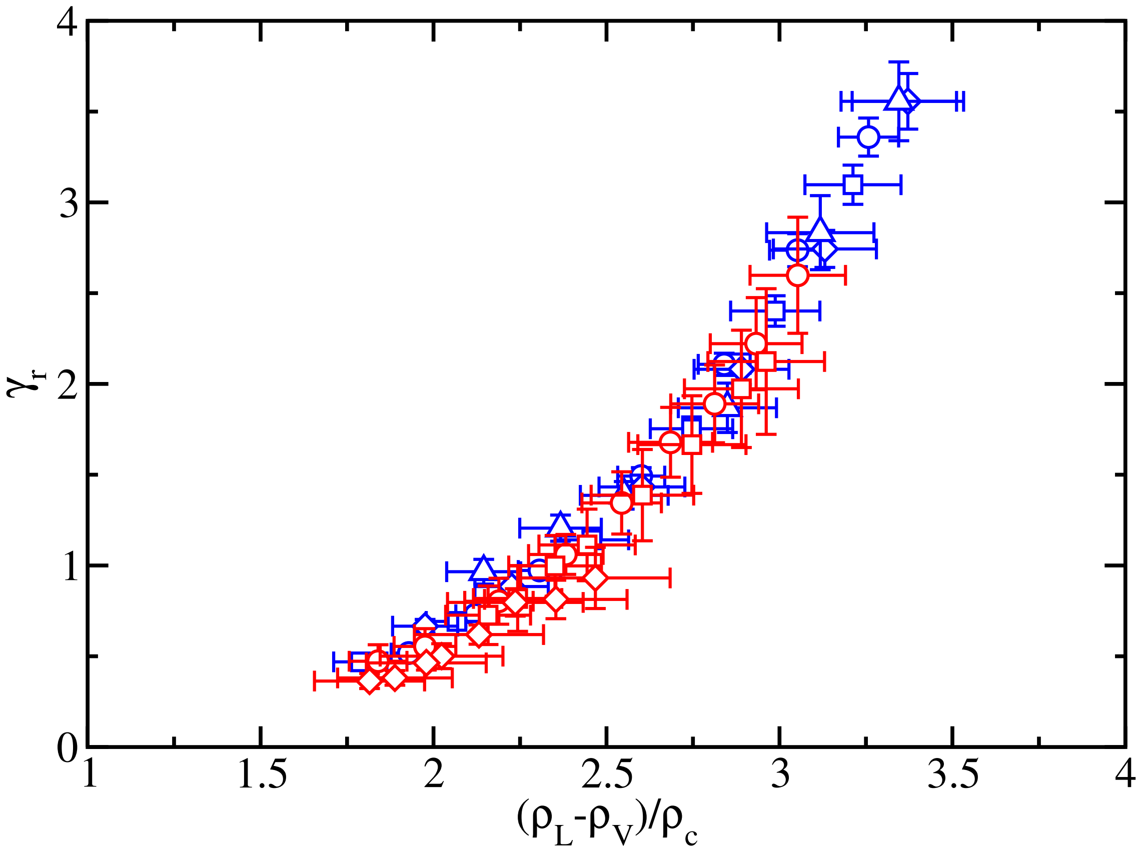

Figura 15.1: Reduced vapour-liquid surface tension of LJ chains with different chain lengths as a function of the difference between the vapour and liquid coexistence densities with respect to the critical density. The reduced surface tension is calculated according to Eq. (15.7). Blue symbols represent the surface tension values of FFLJ chains with 4 (circles), 8 (squares), 12 (diamonds), and 16 (triangles) monomers, and the red symbols are the surface tension values of RLLJ chains with 3 (circles), 4 (squares), and 5 (diamonds) segments.

the case of chains formed by 4 segments, a system that is also studied by Galliero [113], the surface tension of long-chain molecules exhibits the same universal behaviour previously shown in reference [113].

It is interesting to remark that the universal behaviour for the vapour-liquid surface tension is applicable to different molecular models, FFLJ and RLLJ chains, that are indeed radically different. Although both models interact through the same intermolecular potential, their hamiltonians are radically different, producing differences in their vapour-liquid coexistence curves. Galindo *et al.* [186] have demonstrated several years ago that the vapour-liquid phase diagram of RLLJ chains are slightly thicker than that of FFLJ chains with the same chainlength. As a consequence of this, the vapour-liquid surface tension of RL molecules is higher than the corresponding to the FF model with the same chain length.

Although the results shown in Fig. 15.1 are very satisfactory since indicate a universal scaling relationship between the surface tension of short- and long-chain RLLJ and FFLJ molecules, there is still a remaining question. Is it possible to describe the surface tension, as a universal function of $(\rho_L - \rho_V)/\rho_c$ for a third (different) molecular model? We have used the vapour-liquid surface tension data corresponding to FFSW chains obtained recently by us [143] and represent the reduced surface tension of Guggenheim given by Eq. (15.7) as a function of the difference between the liquid and

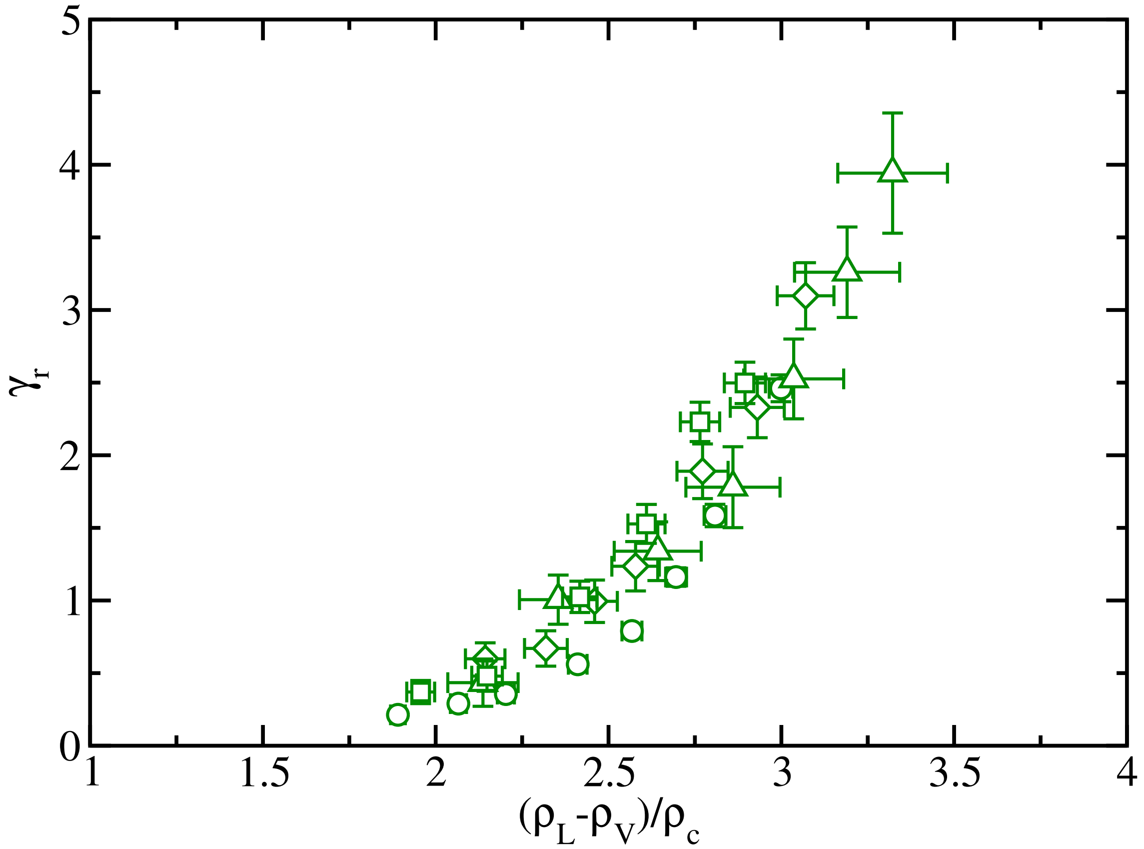

Figura 15.2: Reduced vapour-liquid surface tension of FFSW chains of different chain lengths as a function of the difference between the vapour and liquid coexistence densities with respect to the critical density. The reduced surface tension is calculated according to Eq. (15.7). Green symbols represent the surface tension values of chains with 3 (circles), 4 (squares), and 5 (diamonds) monomers.

vapour densities. As can be seen in Fig. 15.2, the same scaling relationship is able to predict a universal scaling relation between the surface tension and $(\rho_L - \rho_V)/\rho_c$. Comparison between the results corresponding to LJ and SW systems indicate that the dispersion in the case of SW chains is larger than for LJ chainlike molecules, especially for the longest molecules. This is expected since the interfacial properties of systems interacting through discontinuous intermolecular potentials, particularly the SW, are difficult to obtain with the same accuracy than for systems interacting with continuous potentials (LJ). This is especially true in the case of the surface tension, a property very sensitive to the interface stability, size of the system, and length of the simulation run (number of microstates sampled along the simulation).

We have represented the surface tension data for the three molecular models considered in this work in the same figure to assess the adequacy of the proposed relationship in predicting the same universal surface tension as a function of the difference in liquid and vapour densities. As can be seen in Fig. 15.3, the surface tension of the three molecular models seems to correlate in a unique and universal curve, although results corresponding to the FFSW systems deviate slightly from the universal behaviour at the region of low density differences. Our results suggest that both models obey approximately the same equation, indicating that the reduced surface tension as a function of the difference in liquid and vapour coexistence densities results from a more fundamental universal scaling behaviour in which intermolecular details are irrelevant at this level, including intermolecular potential (LJ and SW) and molecular architecture (FF and RL).

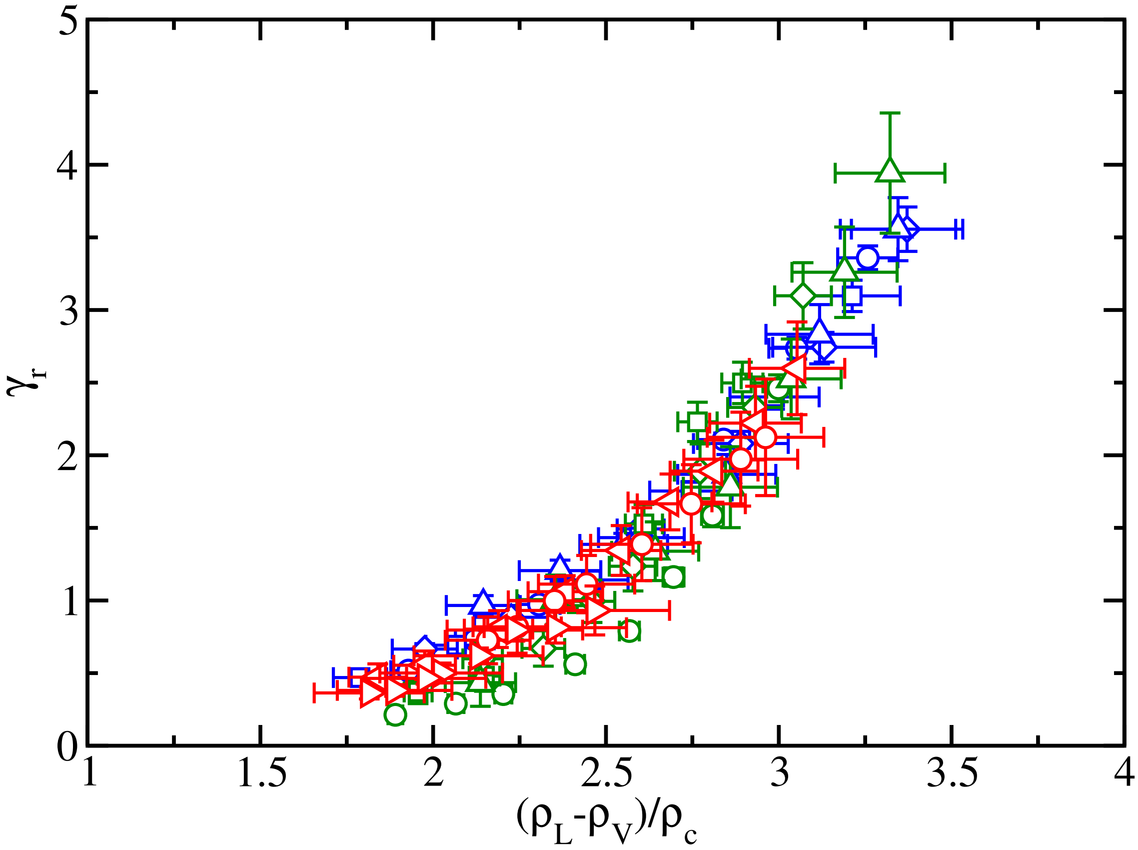

Figura 15.3: Reduced vapour-liquid surface tension of FFLJ, RLLJ, and FFSW chains with different chain lengths as a function of the difference between the vapour and liquid coexistence densities with respect to the critical density. The reduced surface tension is calculated according to Eq. (15.7). Blue symbols represent the surface tension values of FFLJ chains with 4 (circles), 8 (squares), 12 (diamonds), and 16 (triangles) monomers, red symbols are the surface tension values of linear tangent (rigid) Lennard-Jones chains with 3 (circles), 4 (squares), and 5 (diamonds) segments, and the green symbols correspond to the surfacet tension values of FFSW chains with 4 (circles), 8 (squares), 12 (diamonds), and 16 (triangles) monomers.

15.3 Conclusions

We have extended the approach proposed recently by Galliero, in which an appropriate reduced vapour-liquid surface tension, orginially proposed by Guggenheim, can be represented as a universal function of the difference between the vapour and liquid coexistence densities for several chainlike molecular models. In particular, we have considered long-chain FFLJ chains, RLLJ molecules, and FFSW chains with several chain lengths. Our results indicate that the universal scaling relationship used by Galliero is able to describe, as a unique function, the vapour-liquid surface tension of longer FFLJ chains. In addition to that, we have also applied the same universal scaling relationship to account for the surface tension of linear tangent Lennard-Jones chains and FFSW chains of different chain lengths. All the interfacial tension data seems to correlate in the same universal curve, confirming that the universal relationship is able to describe three different molecular models.

15.4 Acknowledgements

The authors would like to acknowledge helpful discussions with B. Mendiboure, D. Bessières, F. Plantier, and M. M. Piñeiro. This work was supported by Ministerio de Ciencia e Innovación (MICINN, Spain) through Grants Nos. FIS2010-14866 and FIS2010-22047-C05-05. Further financial support from Proyecto de Excelencia from Junta de Andalucía (Grant No. P07-FQM02884), Comunidad Autónoma de Madrid (Grant No. MODELICO-P2009/EPS-1691), and Universidad de Huelva are also acknowledged.

Capítulo 16

Conclusiones

En este capítulo de cierre de la memoria de tesis se sintetizan brevemente las conclusiones alcanzadas en los capítulos 9 al 15. En esta recapitulación final no se aportan ideas nuevas, pero es necesaria con objeto de hacer una puesta en valor de los problemas tratados, además de establecer el estado en cuestión de la línea de trabajo. La limitación temporal, de un proyecto de tesis realista, ha hecho que sea necesario acotar en nuestro caso los sistemas objeto de estudio, lo cual no significa, que no sea necesario continuar en el futuro ampliando el conocimiento sobre alguno de los sistemas planteados, bien dentro del contexto de la simulación Monte Carlo o en el contexto de otros escenarios en los que el grupo de investigación ha entrado durante estos 5 años de realización de la tesis doctoral.

Las conclusiones finales de una tesis pueden redactarse de muchas maneras, pero entendiendo que una tesis doctoral no es meramente un evento administrativo para lograr una promoción profesional, ni es tampoco un proceso exclusivamente científico, de pura investigación. Tanto en el camino de trabajo como en la redacción final he tenido siempre presente que una tesis tiene sobre todo una finalidad de aprendizaje. Es por lo que antes de pasar a comentar las conclusiones finales he dedicado un breve apartado a mi propia autoevaluación como doctorando.

16.1 Breve reflexión de autoevaluación del doctorando

Pienso que el primer fruto de mi tesis doctoral es mi crecimiento personal que parte de un compromiso personal dentro del grupo de investigación. Solamente después de un proceso como el desarrollado en estos 5 años de estudio, he sido capaz de escribir una tesis doctoral con la que pretendo acreditar mi competencia investigadora y mostrar mi capacidad de comunicar, a la comunidad que trabaja en este campo de investigación, el trabajo desarrollado.

Evidentemente mi experiencia científica inicial, como estudiante de doctorado, era necesariamente limitada, situación que se ha resuelto con la adecuada integración dentro de un trabajo en equipo. Valoro muy positivamente el haber desarrollado una competencia de trabajo en equipo. Al comienzo de mi actividad investigadora este modelo de trabajo ha permitido resolver un exceso de confianza de mis posibilidades reales. Posteriormente he comprendido que el trabajo en equipo desarrollado por un grupo de investigación, aún con un número pequeño de integrantes, es un punto clave que lo posiciona en una clara ventaja competitiva. En este trabajo en equipo he desarrollado un conjunto de habilidades y comportamientos que me han permitido realizar las tareas fijadas en los objetivos de tesis de forma altamente eficaz. Mencionar que mi actividad profesional principal no ha sido la investigación, sino la docencia como profesor de enseñanzas medias, por lo que la adecuada gestión de los tiempos ha sido en mi proceso una cuestion vital.

La capacidad de diseñar y crear códigos propios de simulación molecular Monte Carlo me ha permitido adoptar un proceso de creación que me facilitará, en un futuro próximo, la transición hacia códigos comerciales como GROMACS para Dinámica Molecular (integrado en estos dos últimos años en las líneas de trabajo del grupo de investigación).

El proceso de investigación ha contribuido a ampliar mi capacidad de integrar el conocimiento, en especial estableciendo conexiones entre física estadística, termodinámica y simulación molecular. Además me ha permitido desarrollar una comprensión sistemática del campo de la simulación molecular Monte Carlo, así como el dominio de las metodologías de simulación presentadas en la Parte I de este trabajo de tesis.

Valoro muy positivamente el haber adoptado la decisión, en los inicios del trabajo de tesis, de realizar una defensa de la tesis doctoral por artículos. Este modelo de trabajo, aunque ha supuesto un esfuerzo extra, me ha permitido desarrollar la capacidad de comunicación con la comunidad científica internacional de mi campo de estudio. Aunque en ocasiones, se contempla la intervención de los *referees* como un elemento que nos retrasa la publicación del artículo, debo reconocer que valoro esta intervención, ya que la interacción me ha aportado en ocasiones nuevas ideas y/o consejos sobre el campo de estudio.

Por último, comentar que considero que he mejorado mis destrezas para desarrollar en contextos donde hay poca información específica. El mejor ejemplo es el de ser capaz de integrar una metodología no propia en tu código de simulación. Aunque las metodologías están bien descritas en los trabajos de la bibliografía, estas descripciones suelen redactarse en general bastante conceptualizadas y condensadas, existiendo un *gap* que superar para transportarlas a los código de programación.

16.2 Resumen de las conclusiones de los trabajos realizados y *status questionis*

En ningún momento se pretende, en estas conclusiones, volver a repetir innecesariamente las detalladas conclusiones recogidas en cada uno de los artículos. Estas conclusiones que se exponen a continuación, como cierre del trabajo de tesis, pretenden poner en valor los aspectos y aportaciones más relevantes de cada uno de los trabajos desarrollados, comentar algunas dificultades y valorar el estado de la cuestión, al cierre de la redacción de esta memoria, con objeto de establecer futuras líneas de transición a partir de este trabajo.

Trabajo 1. **Effect of dispersive long-range corrections to the pressure tensor: The vapor-liquid interfacial properties of Lennard-Jones system revisited (Capítulo 9).** En el trabajo de este artículo se recogen los resultados de la líneas de trabajo del objetivo general **Obj 1. (a, b, c ,d y e)**.

Uno de los logros principales de este trabajo ha sido el poder extender la versión mejorada por MacDowell y Blas de las correcciones de largo alcance (LRC) de Janeček, para el potencial de Lennard-Jones, sobre el cálculo de las componentes microscópicas del tensor de presiones usando la ruta mecánica (virial), en el contexto de la elección de Irving-Kirkwood.

Se ha producido un código Monte Carlo NVT Lennard-Jones depurado, que cierra una línea de trabajo de programación del grupo de investigación, y que permite calcular las componentes del tensor de presiones tanto por una ruta termodinámica como por el virial (componentes microscópicas). Este código contiene también la metodología de Test-Area.Ttener un código absolutamente testeado ha sido esencial para su posterior extensión a cálculos con más de un componente.

Es de destacar el cálculo del perfil, a lo largo de la componente z de la caja de simulación, de las componentes del tensor de presiones. El perfil microscópico ha permitido tener una clara información visual que ha mejorado nuestra comprensión tanto de la equilibración de la interfase (complementando la información que nos ofrece el perfil de la densidad) como del comportamiento interfacial de la presión. El perfil microscópico del tensor de presiones ha sido un elemento fundamental para poder comprender el efecto de la contribución impulsiva que aparece al cortar el potencial de interacción molecular.

Se presenta una revisión que aporta una visión del cálculo de la tensión superficial haciendo uso de tres metodologías diferentes sobre un rango de diferentes radios de corte. Se ha realizado un análisis del efecto de aumentar el radio de corte (a una temperatura fija) sobre la presión de vapor y sobre las propiedades interfaciales. La convergencia de las diferentes metodologías nos confirma la adecuada incorporación a los algoritmos de las LRC, siendo una excelente decisión en la simulación $r_c = 3\sigma + LRC$.

Por último, poner en valor el análisis realizado, complementando así las aportaciones de Trokhymchunk y Alejandre (1999) y de de Miguel y Jackson (2006), sobre el efecto de la contribución impulsiva a la presión debido a la discontinuidad en el potencial intermolecular cuando es cortado (pero no desplazado) en r_c. El no tener en cuenta esta contribución tiene efectos realmente críticos sobre las componentes del tensor de presiones, proporcionado valores no adecuados de las componentes, así como una estructura equivocada de la interfase líquido-vapor. Este efecto es tanto más drástico cuanto menores son las distancias de corte, ya que el salto en la discontinuidad en r_c es mayor.

Este trabajo también ha servido de inspiración, en el grupo de investigación, para extender las metodologías comentadas al potencial de Yukawa.

Trabajo 2. **Determination of interfacial tension of binary mixtures from perturbative approaches (Capítulo 10).** En el trabajo de este artículo se recogen los resultados de la líneas de trabajo del objetivo general **Obj 2. (a, b y c)**.

Se ha abordado la determinación de propiedades interfaciales de mezclas binarias, de moléculas esféricas Lennard-Jones, mediante la simulación de la coexistencia directa líquido-vapor. El tensor de presiones se ha obtenido haciendo uso de una ruta mecánica (virial) y una ruta termodinámica (VP). La tensión superficial líquido-vapor ha sido calculada haciendo uso de las tres metodologías ya implementadas en el trabajo anterior, metodo de Irving-Kirkwood (virial), diferencia de las componentes macroscópicas del tensor de presiones (método VP) y el Test-Area. La intencionalidad de poner en juego todas las metodologías de trabajo anterior ha sido la de poder chequear la validez de la extensión de las LRC, de MacDowell y Blas, en sistemas de mezclas binarias. Ante el problema de no disponer en la literatura de datos, para poder comparar con los sistemas simulados, se ha hecho realizando una comparación con diagramas de fases obtenidos mediante la aproximación Soft-SAFT, obteniéndose una correspondencia de los datos de simulación con los proporcionados por la ecuación de estado Soft-SAFT realmente excelentes.

Los sistemas simulados son de moléculas del mismo tamaño y diferentes valores del parámetro dispersivo de la energía, $\epsilon_{22}/\epsilon_{11} = 1.5, 1.75$, and 2.0. Al aumentar el parámetro la mezcla se hace más asimétrica, siendo realmente apreciable el efecto tanto en el perfil total de la densidad como en los perfiles de cada uno de los componentes. Los perfiles totales de la densidad se hacen más abruptos (mayor pendiente en la zona interfacial). La absorción en la superficie del componente menos volátil de la mezcla aumenta, mostrando un máximo relativo en la zona interfacial, y se obtiene el comportamiento usual de mezclas binarias de moléculas esféricas que presentan diferencias significativas en los valores de interacción dispersiva de moléculas diferentes. Se ha estudiado, además del efecto del parámetro dispersivo, el efecto de la presión en estos sistemas sobre la tensión superficial y la anchura interfacial.

El estado de la cuestión es que hubiera sido deseable estudiar el efecto del tamaño molecular en la mezcla, manteniendo el mismo parámetro dispersivo de la energía. En el momento presente el doctorando se encuentra trabajando sobre $\sigma_{22}/\sigma_{11} = 1.6$, 2.0, y 2.3 en un rango de presiones para una temperatura dada ($T = 1.20$), vislumbrándose que en estos sistemas las fluctuaciones hacen que los métodos perturbativos no sean tan agradecidos, presentado mayores incertidumbres. Una visión realista, de los tiempos de trabajo, ha hecho que tenga que posponer este trabajo para después de la defensa de la tesis doctoral.

Para la realización de este trabajo, se ha extendido el código Monte Carlo NVT Lennard-Jones anterior para trabajar con más de un componente. Además se ha diseñado una versión reducida de este código para el colectivo NPT. La combinación de la simulación en el colectivo NPT, junto con las predicciones obtenidas mediante Soft-SAFT, ha sido necesaria para las preparaciones de las fases vapor y líquido con las que construir el sistema inhomogeneo para su simulación en coexistencia directa. Este código quedó a disposición del grupo de investigación, sirviendo de base inicial para la implementación del algoritmo *Reactive Monte Carlo* para simular mezclas de moléculas esféricas que reaccionan con ordenes sencillos de reacción.

El grupo de investigación, desde hace aproximadamente 2 años, está aumentado de forma muy rápida su nivel del experiencia en el programa de dinámica molecular GROMACS, y este código puede aportar un elemento de comparación de resultados a la hora de implementar en GROMACS sistemas interfaciales de moléculas esféricas Lennard-Jones.

Trabajo 3. **Liquid-liquid interfacial properties of a symmetrical Lennard-Jones binary mixture (Capítulo 11).**En el trabajo de este artículo se recogen los resultados de la líneas de trabajo del objetivo general **Obj 2. (d)**.

Siguiendo en la línea de chequear la implementación de las LRC, en el cálculo de las componentes del tensor de presiones, se decide estudiar el comportamiento interfacial de una mezcla líquido-líquido. El poder construir diagramas de fases, mediante la aproximación Soft-SAFT, ha permitido una adecuada selección tanto de los parámetros moleculares como de las condiciones termodinámicas del sistema objeto de estudio. Se determinan así propiedades interfaciales de una mezcla binaria simetrica de moléculas del mismo tamaño $\sigma_{11} = \sigma_{22}$, pero diferente energía dispersiva entre moléculas de diferentes especies, $\epsilon_{12} = 0.5\epsilon_{11}$. Esta elección del parámetro ϵ_{12} conduce a un diagrama de fases tipo

III con heteroazeotropía (en la clasificación de Scott y Konynenburg) y nos posicionamos a una $T = 1.5$ (por encima del punto tricrítico) que nos garantiza que en la mezcla se induce la separación de fases, exhibiendo la inmiscibilidad líquido-líquido buscada.

Después de ensayar los $r_c = 3\sigma$, $r_c = 4\sigma$ y $r_c = 3\sigma + LRC$, concluimos que la elección 3σ con correcciones de largo alcance proporciona una excelente aproximación, de los datos de simulación, al diagrama de fases de la aproximación Soft-SAFT.

Particularmente interesante fue la aparición de un mínimo relativo en el perfil total de la densidad de la mezcla simétrica objeto de estudio. Este mínimo está relacionado con la desorción de moléculas en la interfase, una consecuencia directa de la combinación de las débiles interacciones dispersivas entre especies diferentes y la presencia de una región interfacial que separa dos fases líquidas inmiscibles en coexistencia. Cabe mencionar que este comportamiento ha sido observado, por el grupo de investigación, reproduciendo el mismo sistema de estudio en simulaciones de dinámica molecular con GROMACS. Desde una perspectiva de equilibrios de fase, la adsorción o desorción de uno de los componentes de una mezcla heterogénea puede también comprenderse en términos de fenómenos de barotropía molar y presencia de estados isopícnicos. Realmente no ha sido un objetivo el investigar este interesante, a la vez que delicado efecto, pero sin duda nos abre todo un campo de aprendizaje en este tipo de sistemas en el futuro, especialmente después de enriquecernos con las aportaciones realizadas por D. José Matias Garrido (Universidad de Concepción - Chile) durante su estancia en el grupo de investigación.

Trabajo 4. Effect of molecular flexibilty of Lennard-Jones chains on the vapour-liquid interfacial properties (Capítulo 12). En el trabajo de este artículo se recogen los resultados de la líneas de trabajo del objetivo general **Obj 3. (a y b)**.

En gran parte el hilo conductor, de este trabajo de tesis, ha sido la implementación de la versión mejorada por MacDowell y Blas de las correcciones de largo alcance (LRC) de Janeček, para el potencial de LJ, para chequear su validez sobre un amplio número de sistemas. En este caso se utilizan estas correcciones sobre cadenas de monómeros, seleccionando un $r_c = 3\sigma$, donde σ es a la longitud de enlace entre monomeros tangentes.

El trabajo sigue una línea de tiempo que se inicia en el año 2008 con la publicación de un trabajo del grupo de investigación, en colaboración con el Dr. Jackson (Imperial College London) y con el Dr. MacDowell (Universidad Complutense de Madrid), donde se determina la tensión superficial líquido-vapor, de cadenas flexibles LJ en interfases planas, haciendo uso del método WIN y del Test-Area [13]. En este trabajo no se incorporan LRC y se estudia el efecto de aumentar el radio de corte. En 2009, MacDowell y Blas [14] proponen la mejora de las LRC de Janeček y hacen uso del TA en sistemas de cadenas flexibles, analizando la elección de $r_c = 3\sigma + LRC$ frente a $r_c = 4\sigma$. La presión de vapor de estos sistemas es obtenida mediante la combinación de la integración termodinámica y la simulación en GCMC. En 2012, Blas et al. [144] extienden, estos estudios de propiedades interfaciales, a cadenas rígidas LJ.

En este trabajo la tensión superficial se ha calculado haciendo uso exclusivamente del Test-Area y de las LRC. Se han determinado propiedades interfaciales de cadenas de monómeros flexibles completando el rango de longitudes ya estudiadas en otros trabajos a $m = 3, 5, y\, 6$. El aumento de la longitud de cadena tiene un inmediato efecto, los perfiles de densidad se hacen más abruptos y le acompaña un aumento de la tensión superficial. Con la selección, de longitudes de cadena corta, cubrimos el rango de datos necesario para poder comparar con el trabajo de Blas et al. (2012) [144] de cadenas rígidas. La comparación ha permitido comprender el efecto de la flexiblidad sobre las densidades de coexistencia, sino también sobre los perfiles de la densidad, anchura interfacial y tensión superficial líquido-vapor. Los efectos de la flexibilidad son analizados tanto desde el punto de vista termodinámico (densidades de coexistencia y temperatura crítica) como desde el punto de vista de la región interfacial.

El campo de exploración en el tema de cadenas es realmente extenso, pero siguiendo la trayectoria del grupo de investigación, sería deseable hacer estudios basados en la función de distribución con objeto de analizar la orientación de la moléculas a lo largo de la interfase. En el caso de cadenas completamente flexibles, por razones de simetría, no existe ninguna una dirección preferencial molecular. En el caso de las cadenas lineales, sin embargo, es plausible esperar efectos entrópicos que tiendan a orientar las moléculas paralelamente a lo largo de la interfase.

Trabajo 5. **Interfacial properties of binary mixtures of square-well molecules from Monte Carlo simulation (Capítulo 13).**En el trabajo de este artículo se recogen los resultados de la líneas de trabajo del objetivo general **Obj 2. (e y f)**.

Se ha completado el estudio sobre mezclas binarias analizando el efecto del parámetro dispersivo de la energía en otro potencial, el potencial de SW, con tamaõs moleculares idénticos en ambas especies. Se seleccionaron los mismos valores de $\epsilon_{22}/\epsilon_{11}$ que para el potencial de Lennard Jones. En este caso la aproximación SAFT-VR nos ha permitido obtener el diagrama de fases completo de las mezclas objeto de estudio, y hemos podido seleccionar las condiciones termodinámicas más adecuadas para el estudio. Los resultados obtenidos en las simulaciones Monte Carlo realizadas concuerdan muy bien con la predicción SAFT-VR, lo que nos permite validar la implementación del cálculo del tensor de presiones. Destacar también que se obtiene un comportamiento interfacial muy similar, al variar el parámetro dispersivo, que en las mezclas binarias Lennard-Jones.

El implementar el cálculo de las componentes microscópicas del tensor de presiones nos ha permitido también analizar la estructura de $P_N(z)$ y $P_T(z)$ en la región interfacial, así como la influencia en dicha estructura de la variación del parámetro dispersivo de la energía.

En cuanto al estado de la cuestion, sería deseable el poder completar el estudio analizando el efecto de la variación del alcance del potencial λ_{ij} sobre las propiedades interfaciales. Para la realización de este trabajo se ha construido un nuevo código de mezclas NVT para el potencial de SW. En este código se ha implementado el cálculo de las componentes microscópicas del tensor de presiones mediante el virial, promediando solapamientos de moléculas mediante cambios virtuales de volumen, metodología que desde el primer momento hemos considerado como un valor seguro. Las mezclas binarias SW son sistemas bastante más delicados que un sistema inhomogeneo puro, o que las mezclas de un potencial continuo LJ, obteniéndose incertidumbres demasiado grandes en el cálculo de las componentes macroscópicas del tensor de presiones mediante la metodología termodinámica VP de de Miguel y Jackson (2006) [16]. En el momento actual, se está ensayando una ligera modificación sobre el método VP, haciendo que los cambios virtuales en el volumen de la caja de simulación se distribuyan uniformente en un determinado rango aleatorio según el esquema planteado por Vörtler y Smith (2000) [208], de forma que la variación en el factor de Boltzmann es acumulada en un histograma. Aunque este esquema aumenta el tiempo de computación, puede minimizar las incertidumbres.

Otra acción futura, que realmente complementará el cálculo de la tensión superficial en sistemas SW, es la implementación para dicho cálculo del *Expanded Ensamble*, ya que contamos con el nivel experiencial suficiente, en nuestro grupo de investigación, al ser utilizado en la determinación de energías libres en sólidos. La implementación se contemplará tanto para sistemas de mezclas de moléculas esféricas SW como para sistemas especialmente delicados como son las cadenas SW.

Trabajo 6. **Vapor-liquid interfacial properties of fully flexible square well chains from simulation and theory (Capítulo 14).** En el trabajo de este artículo se recogen los resultados de la líneas de trabajo del objetivo general **Obj 3. (c, d y e)**.

Se han simulado propiedades interfaciales del equilibro líquido-vapor de cadenas SW, de 4, 8, 12 y 16 monómeros, con un potencial de rango $\lambda = 1.5$. El incremento de la longitud de cadena lleva asociado un claro aumento de la tensión superficial. Los datos de simulación obtenidos han sido comparados con la literatura, obteniéndose muy buenos acuerdos en las densidades de coexistencia y presiones de vapor. La sensibles diferencias, cerca del punto crítico, pensamos que son atribuibles a diferencias en los modelos moleculares utilizados. Sin embargo, aparecen diferencias en la tensión superficial y distancia interfacial, ambas propiedades muy sensibles en la simulación tanto a los modelos moleculares utilizados como al valor del área interfacial.

Se valora muy positivamente los buenos resultados obtenidos, comparados con la literatura, para la presión de vapor mediante el método de integración propuesto por nuestro grupo de investigación y el Dr. MacDowell (Universidad Complutense de Madrid).

También se valora muy positivamente los buenos acuerdos entre los valores de la temperatura crítica, obtenidos mediante en análisis de las densidades de coexistencia, y los valores obtenidos a partir de aplicar la relación de escalado universal a los valores obtenidos de la tensión superficial haciendo uso del exponente crítico obtenido por la teoría de grupo de renormalización.

En cuanto al estado de la cuestión, sería deseable continuar este estudio analizando la dependencia de las propiedades interfaciales con el alcance del potencial ($\lambda = 1.75$ y 2.0). Además la tensión superficial ha sido obtenida haciendo uso de la metodología WIM, no descartando en un futuro inmediato su determinación mediante *Expanded Ensamble*.

Trabajo 7. **Universal scaling behaviour of surface tension of molecular chains (Capítulo 15). Obj 3. (f)**

El disponer de un número suficiente de datos de la tensión superficial, para diferentes longitudes, de cadenas de monómeros LJ totalmente flexibles y rígidas LJ, así como de cadenas totalmente flexibles SW, ha permitido ampliar el trabajo de Galliero (2010) [113], mostrando que la tensión superficial es una propiedad que exhibe un comportamiento de escalado universal cuando es reducida con respecto a dos propiedades críticas. Es de destacar que la relación de universalidad correlaciona, en la misma curva de universalidad, tres modelos moleculares diferentes.

Este trabajo, pone broche final a la memoria de tesis, y aunque no sea una valoración propiamente científica, me permito la licencia de destacar su marcado carácter didáctico. El curso anterior un alumno de primero de bachillerato me preguntaba: ¿por qué la vida tiene aproximadamente 100 millones de años, y no un millón de años?. A lo que yo le conteste: ¿y por qué no unas solas semanas?, ¿y por qué un elefante duerme sólo 3 horas y el ratón que se subió al reloj duerme 18 horas? . . . Al día siguiente intenté mostrarles en clase el significado de las leyes de escala en el Universo y este trabajo acabó proyectado en la pizarra. Lo más importante es que lo entendieron y además comenzamos a trabajar en experiencias relacionadas con la tensión superficial.

Bibliografía

[1] J.P. Hansen and I.R. McDonald. *Theory of Simple Liquids with Applications to Soft Matter. Fourth Edition*. Elsevier, 2013.

[2] M. P. Allen and D. J. Tildesley. *Computer Simulation of Liquids*. Oxford University Press, 1987.

[3] D. Frenkel and B. Smit. *Understanding Molecular Simulations*. 2nd ed. Academic, San Diego, 2002.

[4] G .J. Gloor, G. Jackson, F. J. Blas, and E. de Miguel. *J. Chem. Phys.*, 123:134703, 2005.

[5] J. S. Rowlinson and B. Widom. *Molecular Theory of Capillarity*. Claredon Press, 1982.

[6] G. J. Gloor, G. Jackson, F. J. Blas, E. Martín del Río, and E. de Miguel. *J. Chem. Phys.*, 121:12740, 2004.

[7] R. Evans. *Density Functionals in the Theory of Nonuniform Fluids. In Fundamentals of Inhomogeneous Fluids*. Dekker, New York, 1992.

[8] H. T. Davis. *Statistical Mechanics of Phases, Interfaces, and Thin Films*. VCH, Weinheim, 1996.

[9] A. Trokhymchuk and J. Alejandre. *J. Chem. Phys.*, 111:8510, 1999.

[10] L. G. MacDowell and P. Bryk. *Phys. Rev. E*, 75:061609, 2007.

[11] J. R. Errington and D. A. Kofke. *J. Chem. Phys.*, 127:174709, 2007.

[12] E. de Miguel. *J. Phys. Chem. B*, 112:4647, 2008.

[13] F. J. Blas, L. G. MacDowell, E. de Miguel, and G. Jackson. *J. Chem. Phys.*, 129:144703, 2008.

[14] L. G. MacDowell and F. J. Blas. *J. Chem. Phys.*, 131:074705, 2009.

[15] J. Janeček. *J. Phys. Chem. B*, 110:6264, 2006.

[16] E. de Miguel and G. Jackson. *J. Chem. Phys.*, 125:164109, 2006.

[17] M. S. Wertheim. *J. Stat. Phys.*, 35:19, 1984.

[18] M. S. Wertheim. *J. Stat. Phys.*, 35:35, 1984.

[19] M. S. Wertheim. *J. Stat. Phys.*, 42:459, 1986.

[20] M. S. Wertheim. *J. Stat. Phys.*, 42:477, 1986.

[21] F. J. Blas and L. F. Vega. *Mol. Phys.*, 92:135, 1997.

[22] F. J. Blas and L. F. Vega. *Ind. Eng. Chem. Res.*, 37:660, 1998.

[23] J. de la Rubia Pacheco and J. J. Brey Abalo. *Introducción a la mecánica estadística*. Ediciones del Castillo, 1978.

[24] P. Ehrenfest and T. Ehrenfest. *The Conceptual Foundations of the Statistical Approach in Mechanics*. Dover Publications, 2002.

[25] G. D. Birkhoff. *Proc. Natl. Acad. Sci.*, 17:656, 1931.

[26] F. Reif. *Fundamentals of statistical and thermal physics*. McGraw-Hill, 1965.

[27] D.A. McQuarrie. *Statistical Mechanics*. Harper & Row, 1976.

[28] P. Attard. *Thermodynamics and Statistical Mechanics: Equilibirium by Entropy Maximisation*. Academic Press, 2002.

[29] N. Metropolis, A. W. Rosenbluth, M. N. Rosenbluth, A. H. Teller, and E. Teller. *J. Chem. Phys.*, 21:1087, 1953.

[30] Richard J. Sadus. *Molecular Simulation of Fluids. Theory, Algorithms and Object-Orientation*. Elsevier, 2002.

[31] L. Verlet. *Phys. Rev.*, 159:98, 1967.

[32] K.E. J.J. Nicolas, W.B. Gubbins, Streett, and D.J. Tildesley. *Mol. Phys.*, 37:1429, 1979.

[33] J. K. Johnson, J. A. Zollweg, and K. E. Gubbins. *Mol. Phys.*, 78:591, 1993.

[34] G. A. Chapela, G. Saville, S. M. Thompson, and J. S. Rowlinson. *J. Chem. Soc. Faraday Trans.*, 73:1133, 1977.

[35] J.P.R.B. Walton, D.J. Tildesley, J.S. Rowlinson, and J.R. Henderson. *Mol. Phys.*, 48:1357, 1983.

[36] M. J. P. Nijmeijer, A. F. Bakker, C. Bruin, and J. H. Sikkenk. *J. Chem. Phys.*, 89:3789, 1988.

[37] C.D. Holcomb, P. Clancy, S.M. Thompson, and J.A. Zollwegg. *Fluid Phase Equil.*, 75:185, 1992.

[38] M. Mecke, J. Winkelmann, and J. Fischer. *J. Chem. Phys.*, 107:9264, 1997.

[39] L. J. Chen. *J. Chem. Phys.*, 103:10214, 1995.

[40] D. Henderson, W. G. Madden, and D. D. Fitts. *J. Chem. Phys.*, 64:5026, 1976.

[41] D. Henderson, O. H. Scalise, and W. R. Smith. *J. Chem. Phys.*, 72:2431, 1980.

[42] B. J. Alder, D. A. Young, and M. A. Marx. *J. Chem. Phys.*, 56:3013, 1972.

[43] G. Guo, W. Wang, and H. Lu. *Fluid Phase Equil.*, 60:221, 1990.

[44] J. R. Elliott and L. Hu. *J. Chem. Phys.*, 110:3043, 1999.

[45] A. L. Benavides, J. Alejandre, and F. del Río. *Mol. Phys.*, 74:321, 1991.

[46] G.A. Chapela, S.E. Martinez-Casas, and C. Varea. *J. Chem. Phys.*, 86:5683, 1987.

[47] L. Vega, E. de Miguel, L. F. Rull, G. Jackson, and I. A. McLure. *J. Chem. Phys.*, 96:2296, 1992.

[48] G.A. Chapela, S.E. Martinez-Casas, and C. Varea. *Phys. Rev. E*, 55:1347, 1997.

[49] P. Orea, Y. Duda, and J. Alejandre. *J. Chem. Phys.*, 118:5635, 2003.

[50] E. de Miguel and G. Jackson. *Mol. Phys.*, 104:3717, 2006.

[51] P. E. Brumby, A. J. Haslam, E. de Miguel, and G. Jackson. *Mol. Phys.*, 109:169, 2010.

[52] J. Delhommelle and P.Millié. *Mol. Phys.*, 99:619, 2001.

[53] T. M. Reed. *J. Phys. Chem.*, 59(5):425, 1955.

[54] T. M. Reed. *J. Phys. Chem.*, 59:428, 1955.

[55] G.C. Maitland, M. Rigby, E.B. Smith, and W.A. Wakeham. *Forces Their Origin and Determination*. Clarendon Pres, Oxford, 1981.

[56] J.S. Rowlinson. *Liquids and Liquid Mixtures*. 2nd ed., Butterworth, London, 1961.

[57] F. London. *J. Chem. Soc. Faraday Trans.*, 33:8b, 1937.

[58] A. J. Haslam, A. Galindo, and G. Jackson. *Fluid Phase Equil.*, 226:105, 2008.

[59] G.H. Hudson and J.C. McCoubrey. *J. Chem. Soc. Faraday Trans.*, 56:761, 1960.

[60] W. R. Smith, D. Henderson, and Yoshio Tago. *J. Chem. Phys.*, 67:5308, 1977.

[61] G. Jiménez-Serratos, C. Vega, and A. Gil-Villegas. *J. Chem. Phys.*, 137:204104, 2011.

[62] J. H. Irving and J. G. Kirkwood. *J. Chem. Phys.*, 18:817, 1950.

[63] A. Harasima. *Adv. Chem. Phys.*, 1:203, 1958.

[64] J. G. Kirkwood and F. P. Buff. *J. Chem. Phys.*, 17:338, 1949.

[65] A. Ghoufi, F. Goujon, V. Lachet, and P. Malfreyt. *Phys. Rev. E*, 77:031601, 2008.

[66] P. Schofield and J. R. Henderson. *Proc. R. Soc. London, Ser. A*, 379:231, 1982.

[67] E.M. Blokhuis and D. Bedeaux. *J. Chem. Phys.*, 97:3576, 1992.

[68] B. Hafskjold and T. Ikeshoji. *Phys. Rev. E*, 66:011203, 2005.

[69] J. Alejandre, D. Tildesley, J. Dominic, and G.A. Chapela. *J. Chem. Phys.*, 102:4574, 1995.

[70] J. Sonne, F.Y. Hansen, and G.H. Peters. *J. Chem. Phys.*, 122:124903, 2005.

[71] H. T. Davies and L. E. Scriven. *Adv. Chem. Phys.*, 49:357, 1982.

[72] H. Heinz, W. Paul, and K. Binder. *Phys. Rev. E*, 72:066704, 2005.

[73] F. Varnik, J. Baschnagel, and K. Binder. *J. Chem. Phys.*, 113:4444, 2000.

[74] F. Goujon, P. Malfreyt, A. Boutin, and A. H. Fuchs. *J. Chem. Phys.*, 116:8106, 2002.

[75] F. Biscay, A. Ghoufi, V. Lachet, and P. Malfreyt. *J. Chem. Phys.*, 131:124707, 2009.

[76] A. Ghoufi and P. Malfreyt. *Mol. Simul.*, 39:603, 2013.

[77] M. Rao and B. J. Berne. *Mol. Phys.*, 37:455, 1979.

[78] E. M. Blokhuis, D. Bedeaux, C. D. Holcomb, and J. A. Zollweg. *Mol. Phys.*, 95:665, 1995.

[79] M. Mecke, J. Winkelmann, and J. Fischer. *J. Chem. Phys.*, 110:1188, 1999.

[80] G.F. Teletzke. *Journal of Colloid and Interface Science*, 87:550, 1982.

[81] A. R. Imre, G. Mayer, G. Hazi, R. Rozas, and T. Kraska. *J. Chem. Phys.*, 128:114708, 2008.

[82] A. Mejía, J.C. Pamies, D. Duque, H. Segura, and L. F. Vega. *J. Chem. Phys.*, 123:034505, 2005.

[83] A. Ghoufi, F. Goujon, V. Lachet, and P. Malfreyt. *J. Chem. Phys.*, 128:154716, 2008.

[84] C. H. Bennett. *J. Comput. Phys.*, 22:245, 1976.

[85] J. Miyazaki, J. A. Barker, and G. M. Pound. *J. Chem. Phys.*, 64:3364, 1976.

[86] E. Salomon and M. Mareschal. *J. Phys. Condens. Matter*, 3:3645, 1991.

[87] A. P. Lyuvartsev, A. A. Martsinovski, S. V. Shevkunov, and P. N. Vorontsov-Velyaminov. *J. Chem. Phys.*, 96:1776, 1992.

[88] C. Ibergay, A. Ghoufi, F. Goujon, P. Ungerer, A. Boutin, B. Rousseau, and P. Malfreyt. *Phys. Rev. E*, 75:051602, 2007.

[89] C. Vega and E. de Miguel. *J. Chem. Phys.*, 126:154707, 2007.

[90] E.A. Müller and A. Mejía. *Fluid Phase Equil.*, 282:68, 2009.

[91] J. G. Sampayo, F. J. Blas, E. de Miguel, E. A. Müller, and G. Jackson. *J. Chem. Eng. Data*, 55:4306, 2010.

[92] G. Galliero, M. M. Piñeiro, B. Mendiboure, C. Miqueu, T. Lafitte, and D. Bessières. *J. Chem. Phys.*, 130:104704, 2009.

[93] J. G. Sampayo, A. Malijevský, E. A. Müller, E. de Miguel, and G. Jackson. *J. Chem. Phys.*, 132:141101, 2010.

[94] R. Eppenga and D. Frenkel. *Mol. Phys.*, 52:1303, 1984.

[95] V. I. Harismiadis, J. Vorholz, and A. Z. Panagiotopoulos. *J. Chem. Phys.*, 105:8469, 1996.

[96] F. Biscay, A. Ghoufi, F. Goujon, and P. Malfreyt. *J. Phys. Chem. B*, 112:13885, 2008.

[97] F. Biscay, A Ghoufi, F. Goujon, V. Lachet, and P. Malfreyt. *J. Chem. Phys.*, 130:184710, 2009.

[98] H.B. Callen. *Thermodynamics and an Introduction to Thermostatistics (2nd ed)*. John Wiley & Sons, 1985.

[99] V.I. Kalikmanov. *Statistical Physics of Fluids. Basics Concepts and Applications*. Springer-Verlag, 2001.

[100] H.J. Butt, K. Graf, and M. Kappl. *Physics and Chemistry of Interfaces*. Wiley-VCH Verag GmbH and Co, 2006.

[101] S. Fisk ann B. Widom. *J. Chem. Phys.*, 50:3219, 1969.

[102] K.G. Wilson. *Scientific American*, 1979.

[103] H.E. Stanley. *Reviews of Modern Physics, The American Physical Society*, 71:358, 1999.

[104] M.E. Fisher. *Reviews of Modern Physics, The American Physical Society*, 70:653, 1998.

[105] E. A. Guggenheim. *J. Chem. Phys.*, 13:253, 1945.

[106] B. Widom. *J. Chem. Phys.*, 43:3892, 1965.

[107] D. B. Macleod. *Trans. Faraday Soc.*, 19:38, 1923.

[108] S. Sugden. *J. Chem. Soc.*, 168:1177, 1924.

[109] S. A. Mumford and J. W. C. Phillips. *J. Chem. Soc.*, 159:2112, 1929.

[110] A.I. Vogel. *J. Chem. Soc.*, 159:98, 1948.

[111] P. Orea, Y. Reyes-Mercado, and Y. Duda. *Phys. Lett. A*, 372:7024, 2008.

[112] P. Orea and Y. Duda. *J. Chem. Phys.*, 128:134508, 2008.

[113] G. Galliero. *J. Chem. Phys.*, 133:074705, 2010.

[114] B.E. Poling, J.M. Prausnitz, and J.P. OConnell. *Forces Their Origin and Determination*. McGraw-Hill, New York, 2001.

[115] Y. Gabarros, F. Palencia, C. Lecoutre, and D. Broseta. *Phys. Rev. E*, 76:061109, 2007.

[116] J. M. H. L. Sengers. *Physica*.

[117] W. C. Carter and W. C. Johnson. *The Selected Works John W. Cahn*. TMS (The Minerals, Metals & Materials Society), 2005.

[118] D. Y. Ivanov. *Critical Behavior of Non-Ideal Systems*. Wiley-VCH Verlag GmbH and Co, 2008.

[119] L. G. MacDowell, J. Benet, and N. A. Katcho. 111:047802, 2013.

[120] L. G. MacDowell, J. Benet, N. A. Katcho, and J. M. Palanco. *Adv. Colloid Interface Sci.*, 206:150, 2014.

[121] J. Alejandre and G. A. Chapela. *J. Chem. Phys.*, 132:014701, 2010.

[122] G. A. Chapela and J. Alejandre. *J. Chem. Phys.*, 135:084126, 2011.

[123] G. A. Chapela, E. Día-Herrera, J. C. Armas-Pérez, and J. Quintana-H. *J. Chem. Phys.*, 138:224509, 2013.

[124] J. C. Armas-Pérez, J. Quintana, and G. A. Chapela. *J. Chem. Phys.*, 139:024505, 2013.

[125] J. C. Neyt, A. Wender, V. Lachet, and P. Malfreyt. *J. Phys. Chem. C*, 116:10563, 2012.

[126] J. C. Neyt, A. Wender, V. Lachet, A. Ghoufi, and P. Malfreyt. *J. Chem. Phys.*, 139:024701, 2013.

[127] J. M. Míguez, D. González-Salgado, J. L. Legido, and M. M. Piñeiro. *J. Chem. Phys.*, 132:184102, 2010.

[128] E. de Miguel, N. G. Almarza, and G. Jackson. *J. Chem. Phys.*, 127:034707, 2007.

[129] C. Miqueu, J. M. Míguez, M. M. Piñeiro, T. Lafitte, and B. Mendiboure. *J. Phys. Chem. B*, 115:9618, 2011.

[130] F. Biscay, A. Ghoufi, V. Lachet, and P. Malfreyt. *Phys. Chem. Chem. Phys.*, 11:6132, 2009.

[131] J. C. Neyt, A. Wender, V. Lachet, A. Ghoufi, and P. Malfreyt. *J. Chem. Theory Comput.*, 10:1887, 2014.

[132] J. Benet, L. G. MacDowell, and C. Menduiña. *J. Chem. Eng. Data*, 55:5465, 2010.

[133] R. de Gregorio, J. Benet, N. A. Katcho, F. J. Blas, and L. G. MacDowell. *J. Chem. Phys.*, 136:104703, 2012.

[134] F. J. Martínez-Ruiz, F. J. Blas, L. G. MacDowell, and A. I. Moreno-Ventas Bravo. Vapor-liquid interfacial properties of square-well chains.

[135] E. M. Blokhius, D. Bedeaux, C. D. Holcomb, and J. A. Zollweg. *Mol. Phys.*, 15:665, 1995.

[136] K. C. Daoulas, V. A. Harmandaris, and V. G. Mavrantzas. *Macromolecules*, 38:5780, 2005.

[137] M. Guo and B. C.Y. Lu. *J. Chem. Phys.*, 106:3688, 1997.

[138] J. Janeček, H. Krienke, and G. Schmeer. *J. Phys. Chem. B*, 110:6916, 2006.

[139] V. K. Shen, R. D. Mountain, and J. R. Errington. *J. Phys. Chem. B*, 111:6198, 2007.

[140] J. Janeček, H. Krienki, and G. Schmeer. *Condens. Matt. Phys.*, 10:415, 2007.

[141] J. Janeček. *J. Chem. Phys.*, 131:124513, 2009.

[142] F. J. Martínez-Ruiz, F. J. Blas, B. Mendiboure, and A. I. Moreno-Ventas Bravo. *J. Chem. Phys.*, 141:184701, 2014.

[143] F. J. Blas, F. J. Martínez-Ruiz, A. I. Moreno-Ventas Bravo, and L. G. MacDowell. *J. Chem. Phys.*, 137:024702, 2012.

[144] F. J. Blas, A. I. Moreno-Ventas Bravo, J. M. Míguez, M. M. Piñeiro, and L. G. MacDowell. *J. Chem. Phys.*, 137:084706, 2012.

[145] F. J. Blas, A. I. Moreno-Ventas Bravo, J. Algaba Fernández, F. J. Martínez-Ruiz, and L. G. MacDowell. *J. Chem. Phys.*, 140:114705, 2014.

[146] J. M. Míguez, M. M. Piñeiro, and F. J. Blas. *J. Chem. Phys.*, 138:034707, 2013.

[147] F. J. Blas and B. Mendiboure. *J. Chem. Phys.*, 138:134701, 2013.

[148] F. Llovell, A. Galindo, G. Jackson, and F. J. Blas. *J. Chem. Phys.*, 133:024704, 2010.

[149] Robert L. Scott and Peter H. van Konynenburg. *Discuss. Faraday Soc.*, 49:87, 1970.

[150] P. H. van Konynenburg and R. L. Scott. *Phil. Trans.*, A298:495, 1980.

[151] F. J. Martínez-Ruiz and F. J. Blas. *Mol. Phys.*, 113:1227, 2015.

[152] E. A. Müller and K. E. Gubbins. *Ind. Eng. Chem. Res.*, 40:2193, 2001.

[153] I. G. Economou. *Ind. Eng. Chem. Res.*, 41:953, 2002.

[154] Patrice Paricaud, Amparo Galindo, and George Jackson. *Fluid Phase Equil.*, 194:87, 2002.

[155] S. P Tan, H. Adridharma, and M. Radosz. *Ind. Eng. Chem. Res.*, 47:8063, 2008.

[156] C. McCabe and A. Galindo. *pplied Thermodynamics of Fluids*. Ed. A. R. H. Goodwin, J. V. Sengers and C. J. Peters (Royal Society of Chemistry, Cambridge), 2010.

[157] George Jackson. *Mol. Phys.*, 72(6):1365, 1991.

[158] C. Vega and L. G. MacDowell. *Mol. Phys.*, 98:1295, 2000.

[159] S. Toxvaerd and J. Stecki. *J. Chem. Phys.*, 102:7163, 1995.

[160] E. Día-Herrera, J. Alejandre, G. Ramírez-Santiago, and F. Forstmann. *J. Chem. Phys.*, 110:8084, 1999.

[161] P. Geysermans, N. Elyeznasni, and V. Russier. *J. Chem. Phys.*, 123:204711, 2005.

[162] I. Napari, A. Laaksonen, V. Talanquer, and D. W. Oxtoby. *J. Chem. Phys.*, 110:5906, 1999.

[163] S. Quiñones-Cisneros. *Fluid Phase Equil.*, 135:103, 1997.

[164] S. Quiñones-Cisneros. *Fluid Phase Equilibria from Minimization of the Free Energy*. PhD thesis, University of Minnesota, 1987.

[165] M. E. Flores, M. J. Tardón, C. Bidart, A. Mejía, and H. Segura. *Fluid Phase Equil.*, 313:171, 2012.

[166] M. J. Tardón, J. M. Garrido, H. Quinteros-Lama, A. Mejía, and H. Segura. *Fluid Phase Equil.*, 336:84, 2012.

[167] D. Henderson. *Fundamentals of Inhomogeneous Fluids*. Dekker, New York, 1992.

[168] K. Binder. *Z. Phys. B Condensed Matter*, 43:119, 1981.

[169] A. Aguado, W. Scott, and P. A. Madden. *J. Chem. Phys.*, 115:8612, 2001.

[170] E. de Miguel, F. J. Blas, and E. Martín del Río. *Mol. Phys.*, 104:2919, 2006.

[171] F. Goujon, P. Malfreyt, A. Boutin, and A. H. Fuchs. *Mol. Simul.*, 27:99, 2001.

[172] F. Goujon, P. Malfreyt, J. M. Simon A. Boutin, B. Rousseau, and A. H. Fuchs. *J. Chem. Phys.*, 121:12559, 2004.

[173] B. Smit, S. Karaborni, and J. I. Siepmann. *J. Chem. Phys.*, 102:2126, 1995.

[174] B. Smit, S. Karaborni, and J. I. Siepmann. *J. Am. Chem. Soc.*, 115:6454, 1993.

[175] B. Smit, S. Karaborni, and J. I. Siepmann. 365:330, 1993.

[176] J. I. Siepmann, M. G. Martin, C. Mundy, and M. L. Klein. *Mol. Phys.*, 90:687, 1997.

[177] M. G. Martin and J. I. Siepmann. *J. Am. Chem. Soc.*, 119:8921, 1997.

[178] M. G. Martin and J. I. Siepmann. *J. Phys. Chem. B*, 102:2569, 1998.

[179] C. Vega and A. L. Rodríguez. *J. Chem. Phys.*, 105:4223, 1996.

[180] A. López-Rodríguez, C. Vega, and J. J. Freire. *J. Chem. Phys.*, 111:438, 1999.

[181] S. K. Nath, F. A. Escobedo, and J. J. de Pablo. *J. Chem. Phys.*, 108:9905, 1998.

[182] Y. J Sheng, A. Z. Panagitopoulos, S. K. Kumar, and I. Szleifer. *Macromolecules*, 27:400, 1994.

[183] Y. J Sheng, A. Z. Panagitopoulos, and S. K. Kumar. *Macromolecules*, 29:4444, 1996.

[184] F. Escobedo and J. J. de Pablo. *Mol. Phys.*, 87:347, 1996.

[185] D. Duque, J. C. Pàmies, and L. F. Vega. *J. Chem. Phys.*, 121:11395, 2004.

[186] A. Galindo, C. Vega, E. Sanz, L. G. MacDowell, E. de Miguel, and F. J. Blas. *J. Chem. Phys.*, 120:3957, 2004.

[187] J. J. de Pablo, M. Laso, and U. W. Suter. *J. Chem. Phys.*, 96:2395, 1992.

[188] J. M. Míguez, M. M. Piñeiro, A. I. Moreno-Ventas Bravo, and F. J. Blas. *J. Chem. Phys.*, 136:114707, 2012.

[189] J. M. G. Palanco. *Termodinámica Estadística de Fluidos Moléculares y sus Interfases*. PhD thesis, Universidad Complutense de Madrid, 2013.

[190] G. D. Birkhoff. *Rev. Prog. Phys.*, 50:783, 1987.

[191] B. Wilding. *Phys. Rev. E*, 52:602, 1995.

[192] B. Wilding, M. Müller, and K. Binder. *J. Chem. Phys.*, 105:802, 1996.

[193] G. J. Pauschenwein, J. M. Caillol, D. Levesque, J. J. Weis, E. Scholl-Paschinger, and G. Kahl. *J. Chem. Phys.*, 126:014501, 2007.

[194] E. Luijten and K. Binder. *Phys. Rev. E*, 58:R4060, 1998.

[195] F. J. Blas and L. F. Vega. *J. Chem. Phys.*, 115:4355, 2001.

[196] L. G. MacDowell, P. Virnau, M. Müller, and K. Binder. *J. Chem. Phys.*, 117:6360, 2002.

[197] C. Vega and L. G. MacDowell. *J. Chem. Phys.*, 114:10411, 2001.

[198] C. Vega, F. J. Blas, and A. Galindo. *J. Chem. Phys.*, 116:7645, 2002.

[199] G. J. Gloor, G. Jackson, F. J. Blas, E. Martín del Río, and E. de Miguel. *J. Phys. Chem. C*, 111:15513, 2007.

[200] P. Bryk, K. Bucior, S. Sokolowski, and G. Zukocinski. *J. Phys. Condens. Matter*, 16:8861, 2004.

[201] M. P. Allen. *J. Chem. Phys.*, 124:214103, 2006.

[202] T. Boublik. *Mol. Phys.*, 27:1415, 1974.

[203] M. P. Allen, G. T. Evans, D. Frenkel, and B. M. Mulder. *Adv. Chem. Phys.*, 86:1, 1993.

[204] F. J. Martínez-Ruiz, A. I. Moreno-Ventas Bravo, and F. J. Blas. *J. Chem. Phys.*, 143:104706, 2015.

[205] A. Gil-Villegas, A. Galindo, P. J. Whitehead, S. J. Mills, G. Jackson, and A. N. Burgess. *J. Chem. Phys.*, 106:4168, 1997.

[206] A. Galindo, L. A. Davies, A. Gil-Villegas, and G. Jackson. *Mol. Phys.*, 93:241, 1998.

[207] M. Müller and L. G. MacDowell. *Macromolecules*, 33:3902, 2000.

[208] H. L. Vörtler and W. R. Smith. *J. Chem. Phys.*, 112:5168, 2000.

[209] K. Binder. *Phys. Rev. A*, 25:1699, 1982.

[210] P. Virnau and M. Müller. *J. Phys. Chem.*, 120:10925, 2004.

[211] A. I. Milchev and A. A. Milchev. *Europhys. Lett*, 56:695, 2001.

[212] P. Virnau, M. Müller, L. G. MacDowell, and K. Binder. *J. Chem. Phys.*, 121:2169, 2004.

[213] B. M. Mognetti, L. Yelash, P. Virnau, W. Paul, K. Binder, M. Müller, and L. G. MacDowell. *J. Chem. Phys.*, 128:104501, 2008.

[214] C. Vega, E. P. A. Paras, and P. A. Monson. *J. Chem. Phys.*, 96:9060, 1992.

[215] D. Frenkel, G. C. A. M. Mooij, and B. Smit. *J. Phys. Condens. Matter*, 3:3053, 1991.

[216] J. I. Siepmann and D. Frenkel. *Mol. Phys.*, 75:59, 1992.

[217] B. Smit. *Mol. Phys.*, 85:153, 1995.

[218] L. G. MacDowell, C. Vega, and E. Sanz. *J. Phys. Chem.*, 115:6220, 2001.

[219] K. G. Honnell, C. K. Hall, and R. Dickman. *J. Chem. Phys.*, 87:664, 1987a.

[220] L. G. MacDowell. *J. Chem. Phys.*, 119:453, 2003.

[221] E. de Miguel. *J. Chem. Phys.*, 129:214112, 2008.

[222] P. Bryk and L. G. MacDowell. *J. Chem. Phys.*, 135:204901, 2011.

[223] A. Georgiadis, F. Llovell, A. Bismarck, F. J. Blas, A. Galindo, G. C. Maitland, J. P. M. Trusler, , and G. Jackson. *J. Supercrit. Fluids*, 55:743, 2010.

[224] N. Mac Dowel, F. E. Pereira, F. Llovell, F. J. Blas, G. Jackson C. S. Adjiman, and A. Galindo. *J. Phys. Chem. B*, 115:8155, 2011.

[225] D. Broseta, Y. Meleán, and C. Miqueu. *Fluid Phase Equilib.*, 233:86, 2005.

[226] C. Miqueu, D. Broseta, J. Satherley, B. Mendiboure, J. Lachaise, and A. Gracia. *Fluid Phase Equilib.*, 172:169, 2000.

[227] R. D. Fowler. *Proc. R. Soc. London, Ser. A*, 159:229, 1937.

[228] J. V. Sengers, R. F. Kayser, C. J. Peters, and J. M. J. White. *Equations of State for Fluids and Fluids Mixtures. Part I, Experimental Thermodynamics*. Elsevier, 2000.